UNIVERSITY OF LIVERPOOL

Investigation of Adsorbates on Metal Single Crystal Electrodes

by

Nikolaos Antonatos

Stephenson Institute for Renewable Energy,
University of Liverpool

This thesis is submitted in accordance with the requirements of the University of Liverpool for the degree of Doctor of Philosophy

September 2018

CONTENTS

ACKNOWLEDGEMENTS

First and foremost, I would like to thank my two supervisors. I have to thank Dr. Yvonne Gründer, my primary supervisor, for introducing me to the interesting research area of fundamental electrochemistry and Surface X-Ray Diffraction. Yvonne has allowed me to proceed at my own pace throughout my Ph.D. and as a result of this approach, I have learned valuable skills for the future, such as being an independent researcher and presenting my work at conferences. Then, I would like to thank Professor Christopher A. Lucas, my secondary supervisor, who presented me with the opportunity of exploring a different scientific path by investigating silicene, which I found of huge interest and also provided me with valuable feedback for the structure of this thesis.

Then, I would like to thank each member of the research group individually. I was fortunate enough to work with Dr. Angeline Kasina who was constantly going through my thesis and helping me properly constructing my chapters. I would also like to thank Lisa Rhodes-Martin firstly, for countless backgammon games and coffee sessions and giving me strength to finish my Ph.D. The time spent for organising the ECS Student Chapter Conference and during the conference in Birmingham was very entertaining. Then, to Joshua J. Fogg, thank you for being there in the tiring Synchrotron trips where I had someone to talk to and for all the CTR analysis we did together. To Liz Cocklin, thank you for all the help in the Silicene analysis and constant help in my first years of my Ph.D. To Jack Beane, I really enjoyed our countless Wednesday football games and music discussions. I wish you see Norwich winning the Premier League one day. To Lena Reichenbach, thank you for keeping me company in the lab during our electrochemical experiments and your helpful input on my work. Finally, to the "outsider" of our group, Graeme O'Dowd, thanks for being so calm and told me not to worry about anything. Without you guys, my Ph.D. would have been a lot harder and I will never forget our group meals, the Poker night and the Sugar and Dice day.

Then, my sincere gratitude to Dr. David Martin and the beamline staff of I-07 at Diamond Light Source and especially Dr. Matt Forster who helped me the most with the silicene experiments and was a great companion throughout all the days I spent in Diamond, despite being an Everton fan.

I want also to thank all the people in the Stephenson Institute for all the good times we had together, the Wednesday footy, the FIFA sessions with Giorgos, the Pokémon Go Raids with Pete and many thanks to all the players in the Wavertree Friday Football.

Επίσης, είμαι αναγκασμένος να ευχαριστήσω όλους μου τους φίλους στην Ελλάδα: τον κουμπάρο μου κι αμετάκλητο γκρινιάρη Παναγιώτη, τον μόνο καλό βάζελο Τάσο, το Γιώργο που θέλει να δει τη Λίβερπουλ πρωταθλήτρια, το Χρήστο που όσο μπόι του λείπει τόσο εξαιρετικό παιδί είναι, τον αιώνιο πελάτη στο Fantasy της Πρεμιερ Λιγκ Αντώνη και τον Γιώργο, που πρόσφατα έγινε πατέρας, εύχομαι να δει την κόρη του να γερνάει. Στον Ηλία και το Θάνο πολλά ευχαριστώ για το καταπληκτικό ταξίδι στο Παγκόσμιο Κύπελλο της Ρωσίας το 2018 και τις απίστευτες εμπειρίες που αποκτήσαμε. Τέλος, πολλά ευχαριστώ στην Μαρία Κουκουβιτάκη που επί 4 χρόνια ήταν στο πλάι μου και με υπέφερε αδιαμαρτύρητα δίνοντας μου συνεχώς ατελείωτη υποστήριξη για να εκπληρώσω τους στόχους μου.

Τέλος, θα ήθελα μέσα από την καρδιά μου να ευχαριστήσω την αγαπημένη οικογένεια μου: τη μητέρα μου Λήδα, τον πατέρα μου Χρήστο και τον αδερφό μου Κωνσταντίνο που με υποστήριξαν τα μέγιστα και κυρίως ψυχολογικά σε όλες τις δύσκολες στιγμές αυτά τα 4 χρόνια. Χωρίς την ατελείωτη υποστήριξη τους αυτό το διδακτορικό δε θα μπορούσε να εκπαιρεωθεί. Εύχομαι στον αδερφό μου κάθε επιτυχία στο δύσκολο ταξίδι που ετοιμάζεται να ξεκινήσει στο Μάστερ του στην Αγγλία.

DECLARATIONS

I, Nikolaos Antonatos, declare this thesis contains an account of my research carried out in Stephenson Institute for Renewable Energy at the University of Liverpool between October 2014 and September 2018 under the supervision of Dr. Yvonne Gründer and Professor Christopher A. Lucas. The research reported hereby is a presentation of my own work, unless specified. It has not been previously submitted, either wholly or in part, in this or any other academic institution for admission to a higher degree.

Figures 2.7, 2.8 and *2.9* have been taken from Dr. Gary Harlow's thesis. The CTR analysis presented in *Sections 6.3.2.2.* and *6.4.2.2.* have been analysed by Joshua J. Fogg. The Silicene deposition on Ag(111) was performed at the I07 beamline at Diamond Light Source and part of this research has been reported in Dr. Elizabeth Cocklin's thesis, although all the experimental data were obtained and analysed by the author. The silicene in NaOH solution data collection mentioned in *Section 7.6* were performed by Joshua J. Fogg and Grace Chrichton in a separate beamtime at DLS. All the remaining data collection and calculations were performed by the author. The data analysis and interpretation was all performed by the author.

Nikolaos Antonatos

September 2018

The following articles based on this research are in preparation:

Antonatos, N., Cocklin, L., Forster, M., Hussein, H., Rawle, J., Nicklin, C., Martin, D. and Lucas, C.A.

Comparing the (4 x 4) Silicene Structure at Different Temperatures

Antonatos, N., Fogg, J.J., Lucas, C.A. and Gründer, Y.

Orientation of Acetonitrile on Copper (111) and Silver (111) Electrode Surfaces Studied by Surface X-Ray Diffraction

Antonatos, N., Fogg, J.J., Lucas, C.A. and Gründer, Y.

Kinetics of copper UPD on Au(111) in sulphuric acid under the presence of Acetonitrile

The author has presented the research reported in this thesis at the following conferences:

Influence of Acetonitrile on Copper Under-Potential Deposition (oral presentation), Electrochem 2017, September 2017, University of Birmingham, Birmingham, U.K.

Silicene on Ag(111): A Surface X-Ray Diffraction Study (poster presentation), Graphene 2017, March 2017, Centre de Convencions Internacional de Barcelona, Barcelona, Spain

Chronoamperometric study of Cu UPD on Au(111) in acidic media (poster presentation), ECS Northwest Student Chapter Conference, June 2017, Stephenson Institute for Renewable Energy, University of Liverpool, Liverpool, U.K.

INVESTIGATIONS OF ADSORBATES ON METAL SINGLE CRYSTAL ELECTRODES

Nikolaos Antonatos

ABSTRACT

The aim of this thesis is to provide a detailed investigation of the behaviour of several adsorbates on noble metal single crystal electrodes. The effect of these adsorbates on structural changes of the underlying substrate is discussed as well. For this research surface X-ray diffraction (SXRD) and electrochemical techniques have been mainly employed.

The study of the atomic structure of silicon and silver atoms forming the (4 x 4) silicene structure on Ag(111) single crystal in room temperature revealed a honeycomb structure with a buckling of the Si atoms of 0.76 Å. Furthermore, the buckling of silicene produces a distortion effect upon the top two Ag layers of the crystal which is dependent of the temperature. Additional investigations were carried out to examine the orientation of acetonitrile (CH_3CN) on the Cu(111) and Ag(111) single crystal electrodes in perchloric acid via *in situ* SXRD techniques. This was studied as a function of acetonitrile concentration and electrochemical potential to determine how these factors affect the adsorbate structure at the interface. The results indicate acetonitrile orients perpendicular to the Cu(111) surface with the CN group of the molecule bonding with the surface atoms. It was further shown that due to acetonitrile, copper atoms dissolute from the crystal surface and are redeposited in a different orientation to the substrate. At high acetonitrile concentrations, the molecule decomposes to the $–CH_3$ and -C≡N groups where the latter complexes with the copper atoms. On the other hand, acetonitrile orients parallel to the Ag(111) surface interacting weakly with the top silver atoms via the π orbital of the nitrile group. Therefore, it is established that the impact of acetonitrile on Cu(111) is much more prominent than on Ag(111). The influence of acetonitrile is further examined on the under-potential deposition (UPD) of copper on Au(111) in sulphuric acid over a wide range of acetonitrile concentrations by cyclic voltammetry and chronoamperometry. The influence of acetonitrile on the resulting copper

structure and coverage is discussed based on the electrochemical results and *in situ* SXRD. The presence of the organic molecule is found to affect the deposition behaviour, strongly enhance the resulting copper coverage deposited on Au(111) and alter the final copper structure.

ABBREVIATIONS AND COMMON SYMBOLS

2D	Two-dimensional
3D	Three-dimensional
AcN	Acetonitrile
CE	Counter Electrode
CTR	Crystal Truncation Rod(s)
CV	Cyclic Voltammetry / Voltammogram
DLS	Diamond Light Source
DFT	Density Functional Theory
DWF	Debye-Waller Factor
FOR	Fractional Order Rod(s)
fcc	Face-centred cubic
GIXRD	Grazing Incidence X-Ray Diffraction
HOMO	Highest Occupied Molecular Orbital
IHP	Inner Helmholtz Plane
IR	Infrared
LEED	Low Energy Electron Diffraction
LINAC	Linear Accelerator
LUMO	Lowest Unoccupied Molecular Orbital
ML	Monolayer
OHP	Outer Helmholtz Plane
RE	Reference Electrode
rms	root-mean-square
SHE	Standard Hydrogen Electrode
STM	Scanning Tunnelling Microscopy
SXRD	Surface X-Ray Diffraction

UHV	Ultra-High Vacuum
UPD	Under-Potential Deposition
WE	Working Electrode
XPS	X-ray Photoelectron Spectroscopy

α	Thermal Expansion Coefficient
β	Roughness Factor
ε_{ij}	Distance between layers
Θ	Coverage
$\Delta_{atom1/atom2}$	Interlayer spacing
σ_i	rms roughness
d	Distance from electrode surface
d_{atom}	Atom lattice constant
E	Electrochemical Potential
E_F	Fermi level
F	Faraday constant: 96495.3 C mol^{-1}
R	Universal gas constant: 8.314 J mol^{-1} K^{-1}

LIST OF FIGURES

LIST OF TABLES

CHAPTER 1

Introduction

Adsorption is a surface phenomenon occurring at the interface of two phases, in which forces such as Van der Waals forces or hydrogen bonding act between the molecules of all substances irrespective of their state of aggregation. Surface forces or unbalanced forces at the phase boundary cause changes in the concentration of molecules at the solid/liquid interface. The substance adsorbed on a solid surface is referred to as adsorbent and the material where the adsorption occurs is referred to as adsorbate. Adsorption may be due to a physical process generally referred to as physical adsorption, or physisorption, caused by Van der Waals forces, or a chemical process referred to as chemical adsorption or chemisorption, involving valency forces. Adsorbent substances can be restored to original conditions by a desorption process usually involving the application of heat, except in some cases chemisorption processes may be irreversible. Depending upon adsorbate and adsorbent phases, adsorption systems may be classified as gas/solid, gas/liquid, liquid/liquid, liquid/solid and solid/solid. This thesis will focus on the last two adsorption systems.

Electrochemistry is vital in a wide range of important technological applications. It is involved in the production of materials by processes called electrodeposition and electrorefining as well as destruction of materials by corrosion. In most electrochemical systems there is an interface between two conductors: a solid metal – the working electrode – and a solution containing ions – the electrolyte. The region where these two conductors meet is characterised as the electrochemical interface or simply the double layer. The structure and electronic composition of the interfacial double layer dictate various properties important for the aforementioned applications. The interface plays a critical role in various physical and chemical properties, such as in electrics, mechanics and carrier transportation of a material. Many crucial properties of a material in technological applications are strongly affected and determined by the presence of interfaces. The physical and chemical properties of a material

can be modified or changed significantly around the interface. One of the aims in surface science is to facilitate material manufacture of technological importance by optimising the materials' properties based on a comprehensive understanding of the fundamentals of the interactions between materials. A deep understanding of the interfaces is crucial to advances in many technological fields where many of them rely upon electrochemical systems.

The second Chapter dwells on the principles of the techniques employed throughout the whole thesis. The basic electrochemical technique used is cyclic voltammetry (CV) where the current is measured as a function of potential. This technique enables the understanding of electron transfer across the double layer. The other technique is chronoamperometry where the current is plotted against time. A major drawback to electrochemical techniques is the inability to give away any structural information. Nevertheless, if electrochemistry is combined with spectroscopic or imaging techniques measurements, we can obtain a full structural analysis of the electrolyte interface across the whole potential window, providing that these techniques are surface sensitive. Moreover, it is essential to perform these measurements *in situ*, in a modified electrochemical cell, in order to have full potential control. However, most optical and imaging techniques such as Low Energy Electron Diffraction (LEED), Infra-Red (IR) and Raman spectroscopy are able to provide detailed information about the electrode surface. On the other hand, *in situ* surface x-ray diffraction (SXRD) is capable of providing information about the structural rearrangements of the surface of the electrode and the layers underneath. Before every measurement some procedures need to be undertaken. These methods include solution and single crystal preparation and the experimental setups employed. Chapter 3 focuses on the procedures needed to be undertaken before every experiment and the principles behind a synchrotron and the beamlines.

Silicene, the silicon-based analogue of graphene, is an emerging two-dimensional material with very attractive electronic properties and in comparison to the planar structure of graphene silicene has a buckled structure, However, it cannot exist as a free standing layer and is grown almost exclusively on Ag(111). [1] and it has been reported that the underlying substrate hinders these potentially intriguing electronic properties, that can surpass those of graphene. [2, 3] Therefore, it crucial to establish the precise interaction of this novel 2D material with its underlying substrate by determining the atomic positions of the silicon and silver atoms. In Chapter 4, after initial characterisation from LEED, SXRD was used to determine the atomic positions of the silicon atoms at the (4 x 4) silicene structure and also

the silver atoms on the top three Ag layers of the crystal at room temperature. The formation of other co-existing silicene structures at monolayer and multilayer coverage is discussed and the behaviour of the material in an electrolyte solution is briefly examined. The results revealed that the interlayer spacing between silicon atoms in the buckled silicene layer is similar to theoretical and other experimental reports. Moreover, silicene produces a buckling of the top two silver layers. On the other hand, the atom spacing on the substrate layers was calculated to be smaller than the analysis of Curcella *et al.* [4] which was performed at growth temperature and was attributed to the large thermal expansion coefficient of silver.

Surface X-Ray Diffraction is not only a very powerful tool for the analysis of the interaction between a solid and another solid material but this technique can be extended for the detailed study of the interaction of a liquid on a solid surface under electrochemical potential control. The liquid/solid interface plays a fundamental role in diverse fields and helps with an understanding of the physical phenomena and structural knowledge of the interface, at the atomic scale, for example in catalysis, crystal growth, lubrication, fundamental electrochemistry, colloidal system, and in many biological reactions. Unraveling the atomic structure at the solid/liquid interface is, therefore, one of the major challenges facing the surface science today to understand the physical processes in model systems.

Non-aqueous electrolytes have been extensively studied across many biological and energy storage systems and play a crucial role in energy technologies. Acetonitrile (CH_3CN) is a liquid used in electrochemistry as an aprotic solvent which can solvate noble metal ions via electron transfer from the cyanide group of the molecule, an important process in the organometallic complex formation of transition metals. Moreover, it has been shown that AcN molecules compete for adsorption sites on metal electrodes. [5] However, compared to water, very little information exists on the interaction of this polar molecule with solid electrode surfaces. The role of solvent molecules at the electrochemical interface is very important to understand fundamental processes such as electron transfer at solid / solution interface. Molecular details of this interface are especially lacking partly due to the limited methods of studying this interface. Chapter 5 investigates the effect of potential and the effect of acetonitrile concentration on the structure and bonding of acetonitrile at the Cu(111), Ag(111) and single crystal electrodes. Surface x-ray diffraction is well suited to investigate these systems since the technique is sensitive to the bulk solvent and can provide atomic scale structural information. It was revealed that acetonitrile interacts strongly with the Cu(111) surface, bonding with the top copper atoms via the lone pair orbital of the nitrile group, while

this interaction is weaker with the Ag(111) crystal. In Cu(111) the orientation of the acetonitrile molecules is perpendicular to the surface while in Ag(111) the molecules are oriented parallel to the surface.

Since the presence of small organic molecules can significantly affect the electrochemical reactivity of a metal electrode at a liquid/solid interface it can also affect the formation of metal adlayer on a foreign metal substrate. The latter phenomenon occurs when the deposition takes place at potentials more positive than the Nernst potential, known as Under-Potential Deposition (UPD), [6] a technique important for the semiconductor fabrication process. Furthermore, a prominent effect of the interaction between metal ions and anions is the influence on the kinetics of the metal layer formation. [7] For the investigation of the influence of organic molecules on metal deposition nucleation, growth and kinetics it is vital to comprehend their mechanism. In Chapter 6, it is presented how different acetonitrile concentrations show a systematic change in the Cu UPD formation on Au(111) in the presence of sulphate anions. Through initial characterisation by cyclic voltammetry, the alteration of the kinetics of the system is examined by modelling chronoamperometry transients through the Avrami model as well as showing structural changes between potentials by the use of X-Ray Voltammetry. The results showed that the increase of acetonitrile concentration from 10 mM up to 4 M enhanced Cu deposition and moreover, chronoamperometry analysis showed that the final Cu coverage in sulphuric drastically increased in the presence of acetonitrile. Experimental analysis showed that without acetonitrile, copper deposits in two separate processes, both with instantaneous nucleation. On the other hand, in the presence of acetonitrile, it was observed that copper deposits in one stage where the nucleation is instantaneous at high underpotentials and gradually becomes progressive. Additionally, acetonitrile enhances the kinetics and the deposition rate of copper on Au(111). Surface x-ray diffraction further confirmed the enhancement of the copper deposition rate with the possibility of a complex formation.

References

1. Guzmán-Verri, G.G., Lew Yan Voon, L.C., *Phys. Rev. B,* **2007,** *76,* 075131
2. Takeda, K., Shirashi, K., *Phys. Rev. B,* **1994,** *50,* 14916-14922
3. Liu, C.-C., Feng, W., Yao, Y., *Phys. Rev. Lett.,* **2011,** *107,* 7680
4. Curcella, A., Bernard, R., Borensztein, Y., Resta, A., Lazzeri, M., Prevot, G., *Phys. Rev. B,* **2016,** *94,* 165438
5. Rudnev, Molodkina, E.B., Danilov, A.I., Polukarov, Y.M., Berna, A., Feliu, J.M., *Electrochim.Acta,* **2001,** *101,* 1987-1930
6. Herrero, E., Bueller, L.J., Abruña, H.D., *Chem. Rev.,* **2001,** *101,* 1897-1930
7. Rudnev, Molodkina, E.B., Danilov, A.I., Polukarov, Y.M., Feliu, J.M., *Electrochim. Acta,* **2009,** *54,* 3692-3699

CHAPTER 2

Theoretical Background

2.1. Electrochemistry

Electrochemistry is the study of charge transfer processes at an electrode / solution interface, either in equilibrium at the interface or under kinetic control. Most of the charge transfer processes are transfer of electrons described by the following reaction

$O + ne^- \leftrightharpoons R$

where O is the oxidant and R is the reductant species and all together they form a redox couple. Both reduction and oxidation must occur, due to the law of conservation of energy. In its simplest variation, an electrochemical cell consists of two electrodes and a supporting electrolyte. The electrode where electrons transfer from the electrolyte is called the anode while the other electrode, where electrons are transferred to the electrolyte, is called the cathode. Therefore, in an electrochemical cell there are two half-reactions occurring: an oxidation reaction at the anode and a reduction reaction at the cathode. [1]

Whether an electrochemical reaction can happen depends on the Fermi level, E_F. For a reduction, electrons in the electrode must have a minimum energy in order to be transferred from the electrode and for the oxidation the energy of the electrons must be equal or higher than the electrode's Fermi level in order to be transferred to the electrode (*Figure 2.1*). These electron energies correspond to the electrode potentials and consequently the corresponding energies in an O/R pair are their redox potentials. [2]

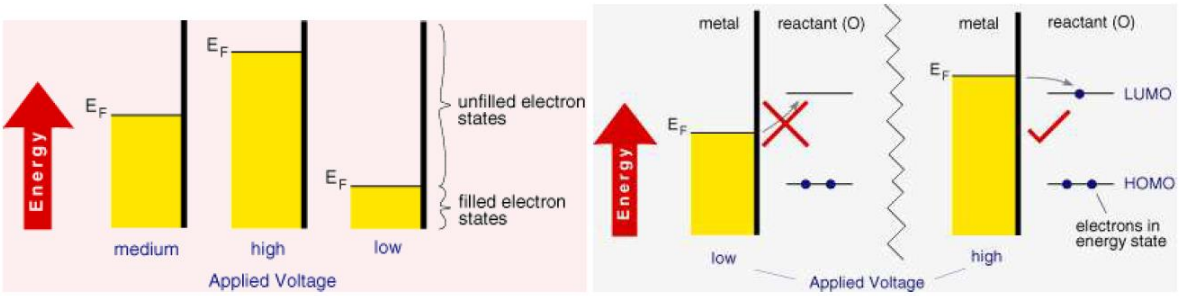

Figure 2.1 a) *Representation of the Fermi-level in a metal at three applied voltages.* ***b)*** *Schematic representation of the reduction of a species (O) in a solution and the Fermi-level, E_F within a metal along the highest occupied molecular orbital (HOMO) and lowest unoccupied molecular orbital (LUMO). If the E_F has a lower value than the LUMO of O it is thermodynamically unfavourable for an electron to jump from the electrode to the molecule. However, if the E_F is above the LUMO of O, it is thermodynamically favourable for the electron transfer to occur, in this case the reduction of O.*
Source: [3]

Electrode potentials cannot be directly measured and instead they are compared against a reference electrode. The Nernst equation (*Equation 2.1*) is used to describe the direction of a cell reaction that is thermodynamically favoured and calculate the resulting electrochemical potential. [1, 4]

$$E_{eq.} = E^0 + \frac{RT}{nF} ln \frac{a_{ox.}}{a_{red.}} \qquad (2.1)$$

where $\alpha_{ox./red.}$ are the activities of the oxidised and reduced species respectively, R the universal gas constant and T the temperature (K). E^0 is the standard electrode potential, distinctive for all redox reactions measured against the hydrogen reduction: [5]

$2H^+ + 2e^- \leftrightharpoons H_2$, $E^0 = 0.000$ V

2.1.1. Electrolyte Double Layer

Prior to describing the electrochemical techniques employed in this thesis, it is vital to describe the metal / electrolyte interface, simply known as the interfacial region. One of the most important goals of physical electrochemistry has been the elaboration of the metal / electrolyte interface in order to provide detailed information of general electrochemical processes. The interfacial region is the region where electrode reactions occur and potential differences across the electrical circuit appear. If we consider an inert metal electrode and an applied potential, a net charge will appear at the surface of the electrode which will attract ions of opposite polarity.

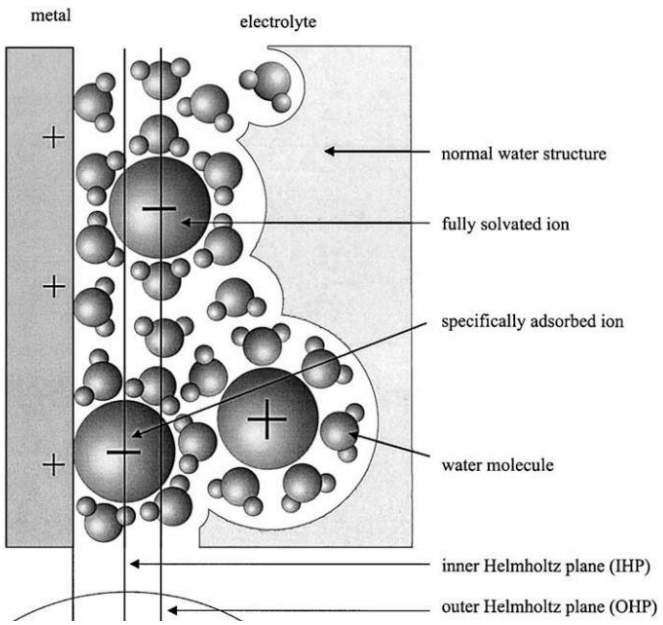

Figure 2.2 *Schematic of the metal / electrolyte interface structure. Source: [1]*

This charge separation indicates a capacity associated with the interfacial region which is also widely known as the double layer because of this charge separation on either side of the metal / electrolyte contact plane. Many theoretical suggestions for this double layer have been proposed, but the most widespread concept is the Helmholtz model depicted in *Figure 2.2* with the formation of numerous layers on top of the metal layer, specifically the inner Helmholtz plane (IHP), which comprises of specifically adsorbed anions, the outer Helmholtz plane (OHP) consisting of non-specifically adsorbed ions and the diffuse double layer.

Figure 2.2 shows fully solvated ions along with partially solvated ions. Fully solvated ions are held in place by electrostatic forces and such ions are characterised as "non-specifically adsorbed". "Specifically adsorbed" ions are defined as the ions which contain weakly bound solvation shells, such as halide anions that may donate part of the solvation shell and form a chemical bond with the electrode surface. In order for electrode reactions to happen, the reactant species needs to be in close proximity to the electrode surface for electron transfer to happen and usually this involves the displacement of either solvent molecules or adsorbed ions from the surface. [1, 6]

Another parameter that needs to be taken into account is the nature of the metal electrode as it influences the distribution of electrons in the material and is directly associated with the energy needed to remove an atom from the surface. Finally, it is essential that the interfacial region is as thin as possible for the electron reactions to occur. This is achieved by employing high concentrations of the supporting electrolyte.

2.1.2. Electrodeposition

Electrodeposition is an electrochemical process where a metal is deposited on top of an electrode surface using changes in potential across an electrochemical cell to drive electron

transfer reactions. The deposition occurs when ions in a solution are reduced to a lower oxidation state and afterwards adsorb on the surface substrate. This method allows the deposition of metallic layers with a thickness ranging from a few nm to mm. [7, 8]

Electrodeposition takes place at the interface of an electrolyte and the electrode surface. When a metallic electrode is dipped into an electrolyte solution containing metal ions, M^{n+}, the reaction mentioned in *Section 2.1* becomes:

$M^{n+} + ne^- \leftrightharpoons M$

and consequently, the Nernst equation (*Equation 2.1*) converts to:

$$E_M = E_M^0 + \frac{RT}{nF} ln \frac{a_M{}^{n+}}{a_M} \quad (2.2)$$

Metallisation by electrodeposition is a well-established technological method used to obtain functional layers and it has also been employed for decorative applications. [9] Moreover, electrodeposition has been used to deposit layers of non-equilibrium compositions and structures, oxides, intermetallic compounds, etc. [10] Furthermore, electrodeposition is a technique with various advantages over other techniques: [11, 12]

- It provides a cheap alternative for materials formation (metals, alloys and compositionally modulated alloys and composites) either as freestanding objects such as foils and wires or as coatings.
- Particle size can be manually controlled by monitoring the charges passed during the deposition process.
- Deposition rates of several tens of microns per hour can be accomplished.
- Low processing temperature (room temperature).
- Electrodeposition can be employed with modified electroplating baths to produce small nanoparticles.

2.1.3. Under-Potential Deposition

Under-Potential Deposition (UPD) is a method to electrochemically deposit a monolayer on a different metal electrode. The potential mentioned in *Equation 2.2* refers to the potential for the metal to be reduced to bulk. When the potential is higher, i.e. more positive, than the Nernst potential, a metal ion can still reduce and deposit on a foreign metallic substrate. [13, 14]

In 1974, Gerischer, Kolb and Przasnyski studied the chemisorption of metal atoms on metal surfaces in correlation to work function differences. [13] It was made clear that the binding energy of the adatoms on the substrate was exceeding the binding energy of the atoms in the respective bulk crystal. Later, electrodeposition of metal atoms onto foreign metal electrodes at under-potentials were studied in aqueous and non-aqueous solutions and it was found out that UPD is a general phenomenon and can be performed even at a solid-vacuum interface. Therefore, it has been realised that this phenomenon is independent of concentration or scan rate and relies upon the plane orientation and the physical properties of the metal of the electrode. [14]

Since then, extensive studies of under-potential deposition of various metals on single crystal [15] and polycrystalline surfaces [16] have been made.

2.1.4. Nucleation, Growth and Phase Formation of Electrodeposited Layers

The nucleation and the early stages of layer growth are of great fundamental and theoretical importance. When a layer is formed, the nucleation processes can determine the physical properties of the layer. [17] Therefore, the understanding of the earliest stages of the layer growth and the influence of the deposition parameters is very crucial for the development process. The potential deposition, the electrolyte composition and the hydrodynamic condition play an important role on the nucleation and the further growth of the layers. [18]

At the initial stages of electrocrystallisation the metal ions in the bulk electrolyte are hydrated and diffuse towards the electrode surface partially losing their hydration sphere. In the Helmholtz layer these ions completely lose their hydration sphere and are discharged and form an adatom adsorbed on the surface of the electrode. For the adsorption of the adatoms, energetically favourable sites on the electrode surface must be present, achieved by surface diffusion. The preferred deposition sites are surface defects such as dislocations or vacancies. [19]

As the metal ions begin to reduce, they group together on the electrode surface and grow as more metal ions are reduced. Once nuclei of sufficient size have developed these clusters begin to grow more rapidly and their stability increases with the addition of more material. Two different kinds of nucleation can be distinguished: i) instantaneous and ii) progressive nucleation. In the case of the former, if the nucleation rate is fast, the maximum number of nuclei is formed on the surface substrate simultaneously right after the induction time. If the

centres begin to overlap, a layer is produced while the rest of the substrate continues to be covered and the nucleation is called "progressive". [20, 21]

2.1.5. Cyclic Voltammetry

Cyclic voltammetry (CV) is considered the most versatile technique in dynamic electrochemistry. Its versatility and effectiveness rely upon its ability to observe the electrochemical processes which occur at an electrode surface. Such processes involve electron transfer across the interface, ionic adsorption and changes in ordering of adsorbate layers. In CV a typical three electrode experimental setup is utilised consisting of a working, a reference, and a counter electrode.

A potential, *E* is applied between the working and the reference electrodes from E_1 and E_2 in a linear fashion and after it reaches a specific value the direction is reversed and the potential continues in the opposite direction (*Figure 2.3a*). Throughout the whole procedure the resultant current is measured between the working and the counter electrode in such a way that the reference electrode's potential and stability is not affected.

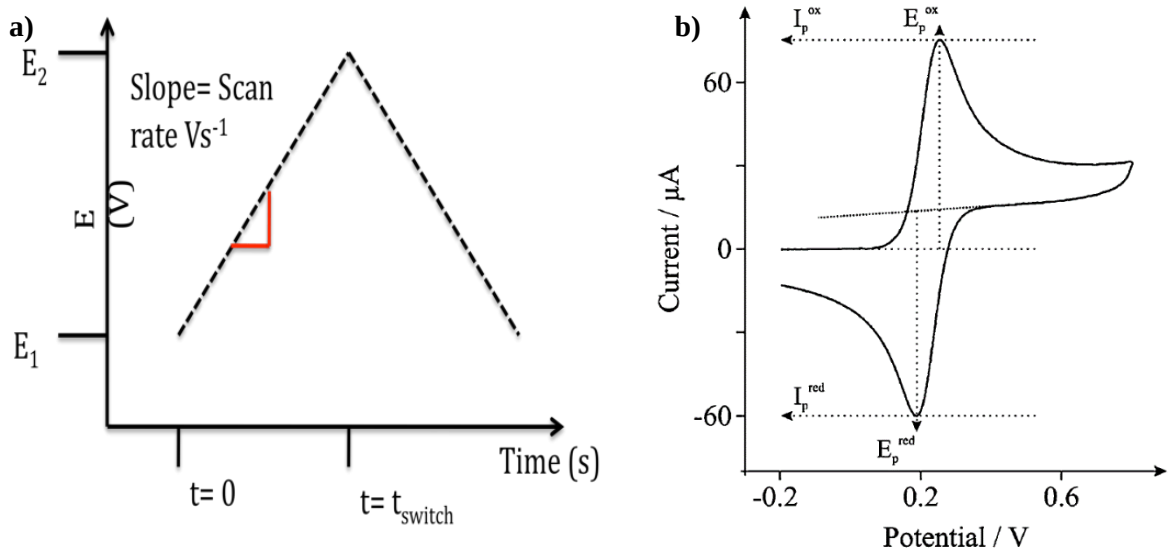

Figure 2.3 *A typical schematic depiction of a CV.* ***a)*** *Potential waveform applied to the working electrode. The potential of the electrode is initially set at E_1, at $t = 0$ and is linearly increased at a constant rate to E_2 until $t = t_{switch}$. The potential is then reversed and scanned back to the original value, E_1.* ***b)*** *The resulting voltammogram. When the potential is scanned from E_1 to E_2 the current starts at $I = 0$ and increases until a maximum current value, I_p^{ox}, at a potential of E_p^{ox} which is between E_1 and E_2 signifying the oxidation of the analyte. Then the potential is reversed from E_2 back to E_1 and the current values exhibits a minimum value, I_p^{red} at E_p^{red} potential indicating the reduction of the redox analyte.*
Source: [1]

During a typical reversible one electron-transfer reaction, the initial potential, V_1, is chosen in a potential region where no reaction of the analyte can occur. Ideally, no faradaic current is observed near E_1, but as the potential increases towards E_2 an increase in faradaic current is

observed indicating the oxidation of the analyte (*Figure 2.3b*). Then, a current maximum (peak), I_p^{ox}, is measured. Following that, the potential direction is reversed and the reduction of the redox analyte is measured in a similar way, producing another peak – a current minimum, I_p^{red}.

The difference between these two peaks is 59.16/n mV for a reversible reaction as given by the Nernst equation. Apart from the reversibility of a redox couple, CV can also provide information, based on the Randles – Sevcik equation (*Equation 2.3*), on the concentration, electrode area and the diffusion coefficient.

$$i_p = 2.69x10^5\ n^{3/2}\ A\ D^{1/2}\ C\ v^{1/2} \quad (2.3)$$

where i_p is the current maximum (A), n the number of electrons transferred, A the electrode area (cm^2), D the diffusion coefficient ($cm^2\ s^{-1}$), C the concentration (mol cm^{-3}) and v the scan rate of the applied potential (V s^{-1}).

It is important to point out that the difference as long as the dependency between Nernst and Randles – Sevcik equations. (*Equations 2.1* and *2.3*) The current passing through the electrode is limited by the diffusion of the analyte on the electrode surface and the diffusion flux is influenced by the concentration of the analyte and how fast the species can diffuse through solution as set by the Randles – Sevcik equation. By changing the applied potential, the concentration of the analyte at the electrode surface is also affected as set by the Nernst equation. Therefore, faster voltage sweep results in a higher concentration gradient leading to higher currents.

Adsorbed species produce changes in the shape of the CV, since they do not have to diffuse to the electrode surface. Specifically, if only adsorbed species are present in the solution and possess fast kinetics the resulting voltammogram is symmetrical, with oxidation and reduction peaks occurring at, approximately, the same potential. (*Figure 2.4*)

If the kinetics become slower, peak separation becomes noticeable. Nevertheless, in *Equation 2.4* the expression of a reversible reaction in which only the adsorbed species O and R contribute to the total current which is proportional to v (in comparison to $v^{1/2}$ in *Equation 2.3*).

$$i_p = \frac{n^2 F^2 v A \Gamma_{O,i}}{4RT} \quad (2.4)$$

where $\Gamma_{O,i}$ is the initial surface concentration of the adsorbed species *i*. [1]

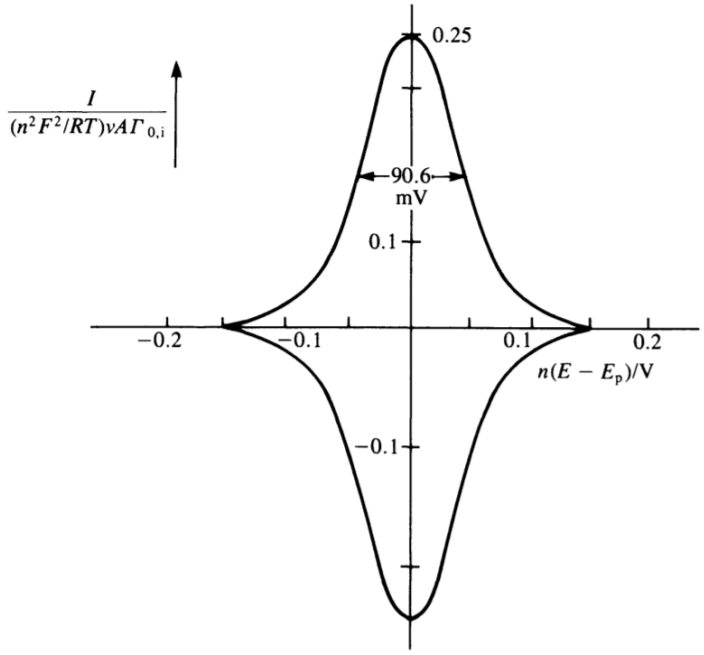

Figure 2.4 *An example of a cyclic voltammogram of the reversible reaction of a surface adsorbed species. If O and R are adsorbed with the same strength, $E_p = E^0$ from the Nernst equation.*
Source: [1]

2.1.6. Chronoamperometry

Chronoamperometry is an electrochemical technique where the potential of the working electrode is stepped and the resulting faradaic current occurring at the electrode, because of electron transfer, is recorded as a function of time.

Prior to the beginning of the process, the working electrode is kept at a potential E_0 where usually no reaction occurs. At t = 0 s, the potential changes to a new value, E_1. Then, the high charging current generated at t = 0 s reduces exponentially with time due to the sudden potential change.

Generally, the change in electric current when the potential is stepped is described by Cottrell equation created by Frederick Gardner Cottrell in 1903. [22]

$$i = \frac{nFAc_j^0\sqrt{D_j}}{\sqrt{\pi t}} \qquad (2.5)$$

where, n is the number of electrons needed to reduce or oxidise one molecule of analyte j, F is the Faraday constant, A is the area of the electrode in cm^2, c_j^0 is the initial concentration of the analyte, j, in mol cm^{-3}, D_j the diffusion coefficient of a species, j, in $cm^2\ s^{-1}$ and t the time.

Deviations from linearity in the plot of i vs $t^{-1/2}$ sometimes indicate that the redox event is associated with other processes, such as association of a ligand, dissociation of a ligand, or a change in geometry. Practically, *Equation 2.5* is simplified to

$$i = kt^{-1/2} \quad (2.6)$$

where k is the collection of constants for a given system (n, F, A, c_j^0, D_j). [23]

Chronoamperometry is the best experimental technique to study in detail the stages of a metal layer deposition. The nucleation and stages of growth can be studied by the analysis of the *i(t)* transients obtained in a chronoamperometric experiment. Fleischmann and Trick, modified the Avrami model [25, 28] (*Equation 2.6*) and established this method after observing maxim followed by a current decay in the *i(t)* transients, caused by sudden potential steps applied to the electrode. They proposed the nucleation rate law, where it is indicated that the nuclei at the active sites are formed according to an exponential decay (*Equation 2.7*)

The Avrami model follows the equation:

$$y = 1 - exp^{-kt^n} \quad (2.7)$$

And subsequent modification by Fleischmann and Trick leads to:

$$N(t) = N_0[1 - \exp(-At)] \quad (2.8)$$

where N(t) is the number of nuclei at a time, t, N_0 is the number of nuclei at saturation and A the nucleation rate constant.

In *Equation 2.8* two instances can be distinguished: first, if A>>1 the equation becomes N(t) = N_0 and the nucleation becomes instantaneous, where all nuclei are activated at the same time, t → 0 and second, if A<<1 the equation becomes N(t) = N_0At and the nucleation is progressive. Later on, Deutscher and Fletcher claimed that in *Equation 2.8* it is presumed that the whole surface of the electrode has the same nucleation activity but at the same time, it allows N_0 to be potential dependant. [26] Thus, the activity distribution of the site activity was incorporated to the nucleation rate law as "nucleation rate dispersion".

With respect to the formation of one monolayer, we have nuclei growth in two directions and therefore a two-dimensional electrocrystallisation is assumed.

$$i = nFk2\pi rh \tag{2.9}$$

Equation 2.9 describes the growth current per nuclei, with r and h being the radius and height of the nuclei, assuming they are disc-shaped, and k is the rate of incorporation of the adspecies. [27] The charge of a nucleus is given by:

$$Q(r) = \frac{\pi r^2 hnF\rho}{M} \tag{2.10}$$

where M and ρ are the molecular weight and density, respectively, of the deposited material. Since the charge is the rate of the current flowing, i over a period of time, t, *Equation 2.10* can be rewritten as:

$$i(r,t) = \frac{2\pi r(t)hnF\rho}{M}\frac{dr(t)}{dt} \tag{2.11}$$

By equating *Equations 2.9* and *2.11* we obtain:

$$\frac{dr(t)}{dt} = \frac{Mk}{\rho} \Leftrightarrow r(t) = \frac{Mk}{\rho}t \tag{2.12}$$

Then, by incorporating *Equation 2.12* to *2.9*:

$$i(t) = \frac{2nFk^2\pi rhM}{\rho}t \tag{2.13}$$

For metal layers growth, we must take into consideration the growth of all nuclei and the interaction between them. In crystallisation processes, impinging nuclei adhere to each other leading to growth discontinuance while other nuclei continue to grow. Thus, Avrami introduced a model where the current density for all nuclei would be:

$$j(t) = i(t)N(t) \tag{2.14}$$

Therefore, depending on the type of nucleation and after incorporating *Equation 2.13*, *Equation 2.14* becomes:

$$j_{ex}(t) = \frac{2nFk^2\pi rhMN_0}{\rho}t \text{ for instantaneous nucleation and 2D growth} \tag{2.15}$$

$$j_{ex}(t) = \frac{2nFk^2\pi rhMAN_0}{\rho}t^2 \text{ for progressive nucleation} \tag{2.16}$$

Now, we must take into account the covered area of the deposited metal. The Avrami theorem can be stated as:

$$S = 1 - e^{-S_{ex}} \tag{2.17}$$

where S is the normalised area with respect to the normalised extended area, S_{ex}. Substituting $\pi r^2 = 1$ for a full monolayer in *Equation 2.10*, we can determine the charge density of a monolayer:

$$Q_{ML} = \frac{hnF\rho}{M} \tag{2.18}$$

Next, the extended charge density, Q_{ex} is defined as:

$$Q_{ex} = \int_0^t j_{ex} dt = S_{ex} Q_{ML} \tag{2.19}$$

Thus,

$$j_{ex} = Q_{ML} \frac{dS_{ex}}{dt} \text{ and } j = Q_{ML} \frac{dS}{dt} \tag{2.20}$$

And through the relationship of *Equation 2.17*

$$j = j_{ex} e^{-S_{ex}} = j_{ex} e^{-\frac{Q_{ex}}{Q_{ML}}} \tag{2.21}$$

Therefore, after also calculating Q_{ex} from *Equation 2.19*, *Equations 2.15* and *2.16* become:

$$j(t) = \frac{2nFk^2\pi rhMN_0}{\rho} t\, e^{-\frac{\pi k^2 M^2 N_0}{\rho^2 t^2}} \text{ for instantaneous nucleation and 2D growth} \tag{2.22}$$

$$j(t) = \frac{2nFk^2\pi rhMAN_0}{\rho} t^2 e^{-\frac{\pi k^2 M^2 N_0 A}{3\rho^2 t^3}} \text{ for progressive nucleation} \tag{2.23}$$

For ease of use, *Equations 2.22* and *2.23* can be generalised in *Equation 2.24*

$$j_n(t) = S_n k_n m_n t^{(m_n - 1)} e^{(-k_n t^{m_n})} \tag{2.24}$$

This will be referred as the Avrami Equation, where it will be exploited to quantitatively determine the final transferred charge $S_n = Q_{ML}$ (*Equation 2.18*), the electron transfer rate of the process, k_n and the type of the nucleation, m_n. The latter parameter needs to be an integer value which in return will dictate nucleation and growth of the process: 1 for instantaneous

nucleation and 2D growth combined with surface diffusion, 2 for instantaneous and 3 for progressive nucleation. [28-30]

2.2. X-Ray Diffraction

In addition to electrochemical techniques, experiments in this thesis contain X-Ray Diffraction (XRD) techniques, which occur when x-rays are scattered from periodic crystal structures. All experiments were centred on a well-defined (111) face centred cubic (*fcc*) single crystal surface.

2.2.1. Crystal Lattice and Unit Cell

A crystal is a periodic array of atoms with long range order, where in space lattice terms is a group of atoms attached to each lattice point. The lattice is defined by three vectors, **a**, **b**, and **c** in such way that an integer number of translations in these directions from any point on the lattice will locate a similar lattice point. A unit cell is defined as the smallest group of particles in a material that comprises a repeating pattern, defined by the sides of length **a**, **b**, and **c** and angles of α, β and γ between them. (*Figure 2.5*)

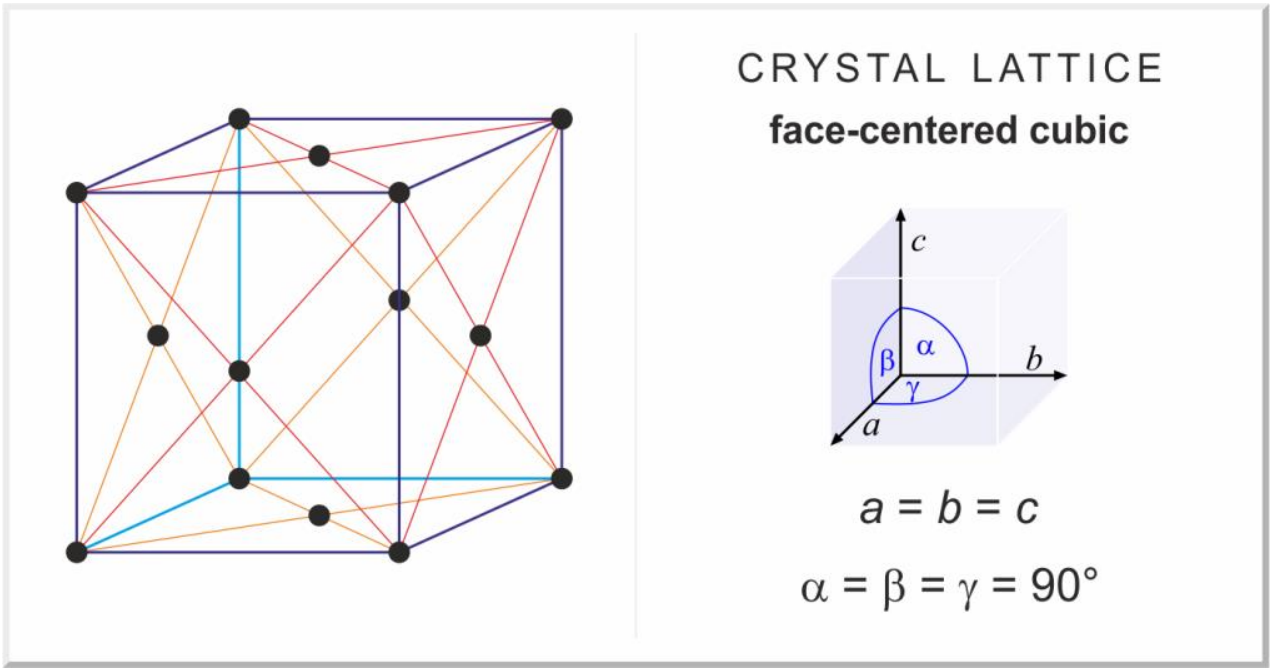

Figure 2.5 *The face centered cubic (fcc) crystal structure. This is a cubic lattice with a four atom basis where a = b = c and α = β = γ = 90°.*
Source: [31]

The repetition of the unit cell over space in all three directions of the vectors completes the crystal structure. There are an infinite number of parallel 2D planes associated with the 3D

lattice that are expressed by Miller indices as (hkl), introduced by William Hallowes Miller. The Miller indices indicate the family of planes orthogonal to $h\mathbf{a}_1 + k\mathbf{a}_2 + l\mathbf{a}_3$, where $\mathbf{a}_i$ are the basis of the reciprocal lattice vectors. Miller indices are stemmed from the intercepts of the plane with three axes in terms of the lattice vectors **a**, **b**, and **c**. The reciprocals of the intercepts are taken and multiplied by the lowest common factor necessary to provide integer values for (hkl). For simple cubic crystals, the lattice vectors are orthogonal and of equal length, **a** and the lattice spacing, d for parallel planes can be calculated as:

$$d_{hkl} = \frac{a}{\sqrt{h^2+k^2+l^2}}$$

2.2.2. Bragg's Law

Figure 2.6 depicts a diagram showing X-rays scattering from adjacent parallel planes separated by a distance d. Each plane of atoms scatters just a small fraction of the X-rays so that multiple layers of bulk crystal contribute to the observed diffraction.

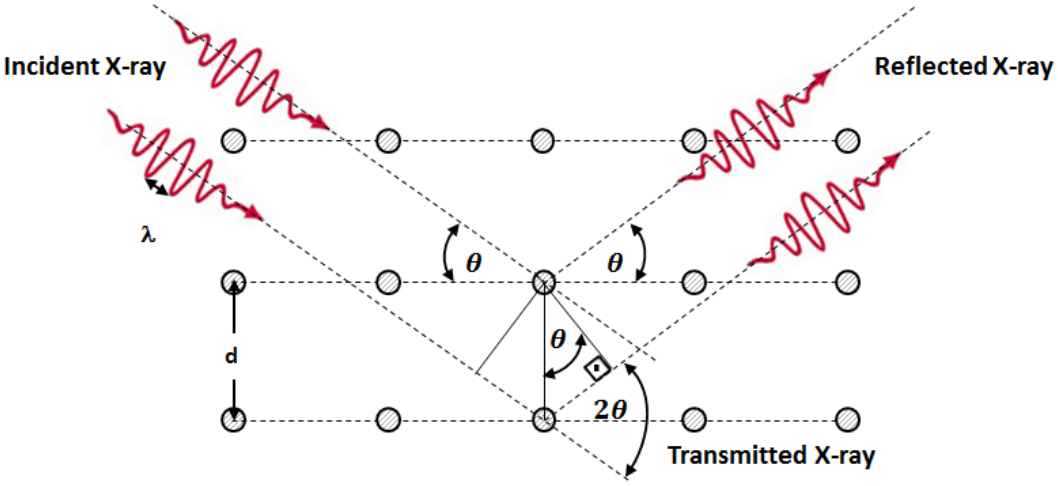

Figure 2.6 *Schematic of an X-ray scattering from a series of parallel planes separated by a distance d. X-rays scattering from planes of atoms exhibit interference effects leading to angles where reflections are observed.*
Source: [32]

If the wave scattering is equal to an integer number of wavelengths, nλ, the distance is equal to dsinθ from trigonometric calculations and Bragg's law can be stated as:

$$n\lambda = 2d\sin\theta \qquad (2.25)$$

Bragg's law produces the conditions for diffraction from parallel atomic planes, without considering the scattering power of the crystal atoms, which is vital for a complete structural

analysis. In the next sections, we will build up the stages of scattering from one electron up to a crystal with N unit cells in all three dimensions. [33]

2.2.3. Momentum Transfer

The momentum transfer is the vector difference between the incident wave-vector $\mathbf{k_i}$ and the outgoing vector $\mathbf{k_f}$, ($q = k_f - k_i$) (*Figure 2.7*). When elastic scattering occurs $|\mathbf{k_i}| = |\mathbf{k_f}| = |\mathbf{k}| = 2\pi/\lambda$.

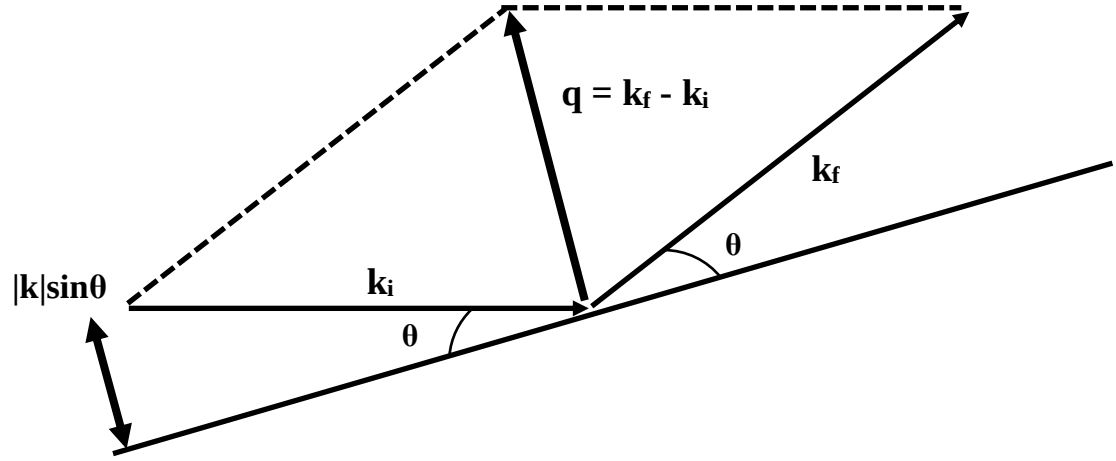

Figure 2.7 *Illustration of how momentum transfer, **q**, is calculated. This is the fundamental quantity in elastic scattering*

From this equation Bragg's law can be expressed in terms of momentum transfer and wave-vector:

$$|\boldsymbol{q}| = 2|k|\sin\left(\frac{1}{2}2\theta\right) = \frac{4\pi}{\lambda}\sin(\frac{1}{2}2\theta) \qquad (2.26)$$

2.2.4. X-Ray Diffraction Principals

Primarily, we must take into consideration the form of a scattered wave from a single electron. When an incident X-Ray comes in contact with an electron, it begins to oscillate and then, the electron radiates a spherical wave with the same wavelength as the incident plane wave.

The process where electrons reflect X-rays is known as Thompson scattering and is the result of X-rays triggering an electron to oscillate and radiate a secondary spherical wave with equal wavelength. [34] Thompson equation [34] describes the amplitude of a scattered wave A_e, at a distance r_e as a function of the incident wave amplitude, A_i.

$$A_e e^{-i(k_f r_e)} = A_i \frac{e^2}{4\pi\varepsilon_0 mc^2} \frac{1}{R_0} e^{-i(k_i r_e)} \quad (2.27)$$

The Thompson scattering length, r_0 is defined as

$$r_0 = \frac{e^2}{4\pi\varepsilon_0 mc^2} \quad (2.28)$$

Taking into account *Equation 2.28* and the definition of momentum transfer, $q = k_f - k_i$, rearranging *Equation 2.27* is expressed in terms of the incident amplitude and the momentum transfer

$$A_e = A_i \frac{r_0}{R_0} e^{-i(q r_e)} \quad (2.29)$$

Scattering from an atom originates from the constructive interference of the scattering amplitude of every electron of this atom.

Thus, the contribution to the scattering from a single atom, A_a is given by aggregating every electron contribution and changing the electron position vector into *Equation 2.30*

$$A_a = A_i \frac{r_0}{R_0} \int_{-\infty}^{+\infty} \rho(r') e^{-iq\,(R_n + r_j + r')} d^3 r' = A_i \frac{r_0}{R_0} f(q) e^{-iq(R_n + r_j)} \quad (2.30)$$

With f(q) is the atomic form factor expressed as:

$$f(q) = \int_{-\infty}^{+\infty} \rho(r') e^{-iqr'} d^3 r' \quad (2.31)$$

From *Equation 2.30* it is shown that the scattering power of each atom is directly related to the momentum transfer, q. If the value q is close to zero, the atomic form factor is equal to the number of electrons in the atom. As q increases, electrons begin to scatter out of phase, causing destructive interference and f(q) = 0 when $q = \infty$. Every atomic form factor has been calculated for every element. [35]

Consequently, the scattering amplitude of one unit cell, A_u is the sum of the A_a of all the atoms comprising the unit cell. Since a unit cell may contain atoms of various elements, a separate atom form factor for each element needs to be introduced. Therefore, if the unit cell contains N_C atoms, then the scattered amplitude is given by:

$$A_u = A_i \frac{r_0}{R_0} \sum_{j=1}^{N_c} f_j(q) e^{(iq\,(R_n + r_j)} = A_i \frac{r_0}{R_0} F(q) e^{(iq\,R_n)} \quad (2.32)$$

With F(q) being the structure factor expressed as:

$$F(q) = \sum_{j=1}^{N_c} f_j(q) e^{i(q\, r_j)} \quad (2.33)$$

Finally, we mentioned earlier that a crystal is consisted of a periodic array of a specific unit cell. A crystal is defined as comprising of N_1, N_2 and N_3 unit cells along the **a**, **b** and **c** vectors respectively. The position of each unit cell is given by:

$R_n = n_1\mathbf{a} + n_2\mathbf{b} + n_3\mathbf{c}$

And the scattering amplitude of a crystal is given by:

$$A_c = A_i \frac{r_0}{R_0} F(q) \sum_{n_1=0}^{N_1-1} \sum_{n_2=0}^{N_2-1} \sum_{n_3=0}^{N_3-1} e^{i(q\,(n_1 a + n_2 b + n_3 c))} \quad (2.34)$$

Therefore, it becomes evident that the scattered amplitude from a crystal is dependent on the amplitude from the structure factor from *Equation 2.33* and the total sum over the lattice of unit cells in three dimensions. If we consider one of the terms from *Equation 2.34*:

$$S_{N_1}(q) = \sum_{n_1=0}^{N_1-1} e^{i(q(n_1 a))}$$

This is the sum of a geometric progression that after rearrangement gives

$$S_{N_1} = \frac{1-e^{iN_1 qa}}{1-e^{iqa}} = \frac{e^{iN_1 q\frac{a}{2}}(e^{-iN_1 q\frac{a}{2}} - e^{-iN_1 q\frac{a}{2}})}{e^{iq\frac{a}{2}}(e^{-iq\frac{a}{2}} - e^{iq\frac{a}{2}})} \quad (2.35)$$

For diffraction measurements we are interested in the scattered intensity, which is proportional to the square value of $S_{N1}(q)^*$. Therefore, considering that $e^{i\theta} = \cos\theta + i\sin\theta$, the contribution to scattered intensity is given by:

$$\left|S_{N_1}(q)\right|^2 = \frac{sin^2(N_1 q\frac{a}{2})}{sin^2(q\frac{a}{2})}$$

This is similar to an N-slit interference function, producing maxima of magnitude N^2 with a distance of 2π in q**a** units. The value of $\left|S_{N_1}(q)\right|^2$ takes its maximum value when $^{qa}/_{2} = n\pi$, with n being an integer. Performing the same calculations for the other two respective parameters of *Equation 2.34* we obtain the scattered intensity from a large 3D crystal (*Equation 2.36*)

$$I(q) = I_i \left(\frac{r_0}{R_0}\right)^2 |F(q)|^2 \frac{sin^2\left(\frac{1}{2}N_1 qa\right) sin^2\left(\frac{1}{2}N_2 qb\right) sin^2\left(\frac{1}{2}N_3 qc\right)}{sin^2\left(\frac{1}{2}qa\right) sin^2\left(\frac{1}{2}qb\right) sin^2\left(\frac{1}{2}qc\right)} \quad (2.36)$$

Equation 2.36 reaches its maximum value when the Laue conditions for diffraction are met:

q**a** = 2πh

q**b** = 2πk

q**c** = 2πl

where h, k and l have integer values. All three conditions are satisfied by the vector

$$q = h\mathbf{a}^* + k\mathbf{b}^* + l\mathbf{c}^* \quad (2.37)$$

where a^*, b^* and c^* are related to the real space vectors by:

$$\boldsymbol{a}^* = 2\pi \frac{\boldsymbol{b} \times \boldsymbol{c}}{\boldsymbol{a} \cdot (\boldsymbol{b} \times \boldsymbol{c})}, \boldsymbol{b}^* = 2\pi \frac{\boldsymbol{c} \times \boldsymbol{a}}{\boldsymbol{a} \cdot (\boldsymbol{b} \times \boldsymbol{c})}, \boldsymbol{a}^* = 2\pi \frac{\boldsymbol{a} \times \boldsymbol{b}}{\boldsymbol{a} \cdot (\boldsymbol{b} \times \boldsymbol{c})} \quad (2.38)$$

Replacing integer values of h, k and l into *Equation 2.37* forms a 3D lattice of q values that satisfy the Laue conditions. This is termed as the reciprocal lattice and outlined by the reciprocal lattice vectors stated by the *Equations 2.38*. The points on the reciprocal lattice show the position of the maximum scattered intensity, termed as Bragg peaks, and labelled by h, k and l. Since the units of the real space vectors are expressed in Å, the reciprocal lattice vectors are expressed as $Å^{-1}$.

To conclude, the diffracted intensity from a large 3D crystal has discrete values of momentum transfer that lie on the reciprocal lattice. Therefore, in a diffraction experiment the scattered intensity is measured as a function of momentum transfer (*Equation 2.39*) and we can determine the real space unit structure of the unit cell.

$$I_{hkl} = I_i \left(\frac{r_0}{R_0}\right)^2 |F(h\boldsymbol{a}^* + k\boldsymbol{b}^* + l\boldsymbol{c}^*)|^2 \, N_1^2 N_2^2 N_3^2 \quad (2.39)$$

2.2.5. Surface X-Ray Diffraction (SXRD)

In *Section 2.2.4* the calculation of diffracted intensity from a large 3D crystal was determined. However, in the case of diffraction from a crystal surface, *Equation 2.39* needs to be transformed.

Primarily, for an isolated 2D monolayer (*Figure 2.6a*), N_3 is set at $N_3 = 1$, where the **c** vector is along the surface normal and **a** and **b** vectors are along the plane of the surface. Hence, the diffraction depends exclusively on the component of the momentum transfer along the plane

of the surface (q**a** and q**b**). Thus, when the Laue conditions are met in the plane of the surface, for integer values of h and k, intensity is observed for all the values of l. The resulting diffraction is depicted in *Figure 2.6a* where scattering is entirely diffuse in the direction normal to the crystal surface.

These "rods" of scattering are superimposed on the scattering from 3D crystal passing through bulk reflections shown in *Figure 2.6b.* In the case of a real crystal, the diffraction is similar to the one shown in *Figure 2.6c* where the diffracted intensity is spread between the Bragg peaks along the l direction producing the Crystal Truncation Rods (CTRs).

The intensity profile of a CTR is calculated by modification of *Equation 2.39*. We consider a crystal extending infinitely in the directions defined by the **a** and **b** in-plane vectors with a finite thickness of N_3**c**. When the in-plane Laue conditions are met, the scattered intensity is given by:

$$I_{CTR} = I_0 \left(\frac{r_0}{R_0}\right)^2 |F(q)|^2 \, N_1^2 N_2^2 \frac{1}{2sin^2(q\frac{c}{2})} \tag{2.40}$$

Equation 2.40 produces sharp peaks in intensity for values $q \cdot \mathbf{c} = 2\pi l$, defined as Bragg peaks. Between Bragg peaks the intensity is spread along the surface normal direction. (*Figure 2.8*)

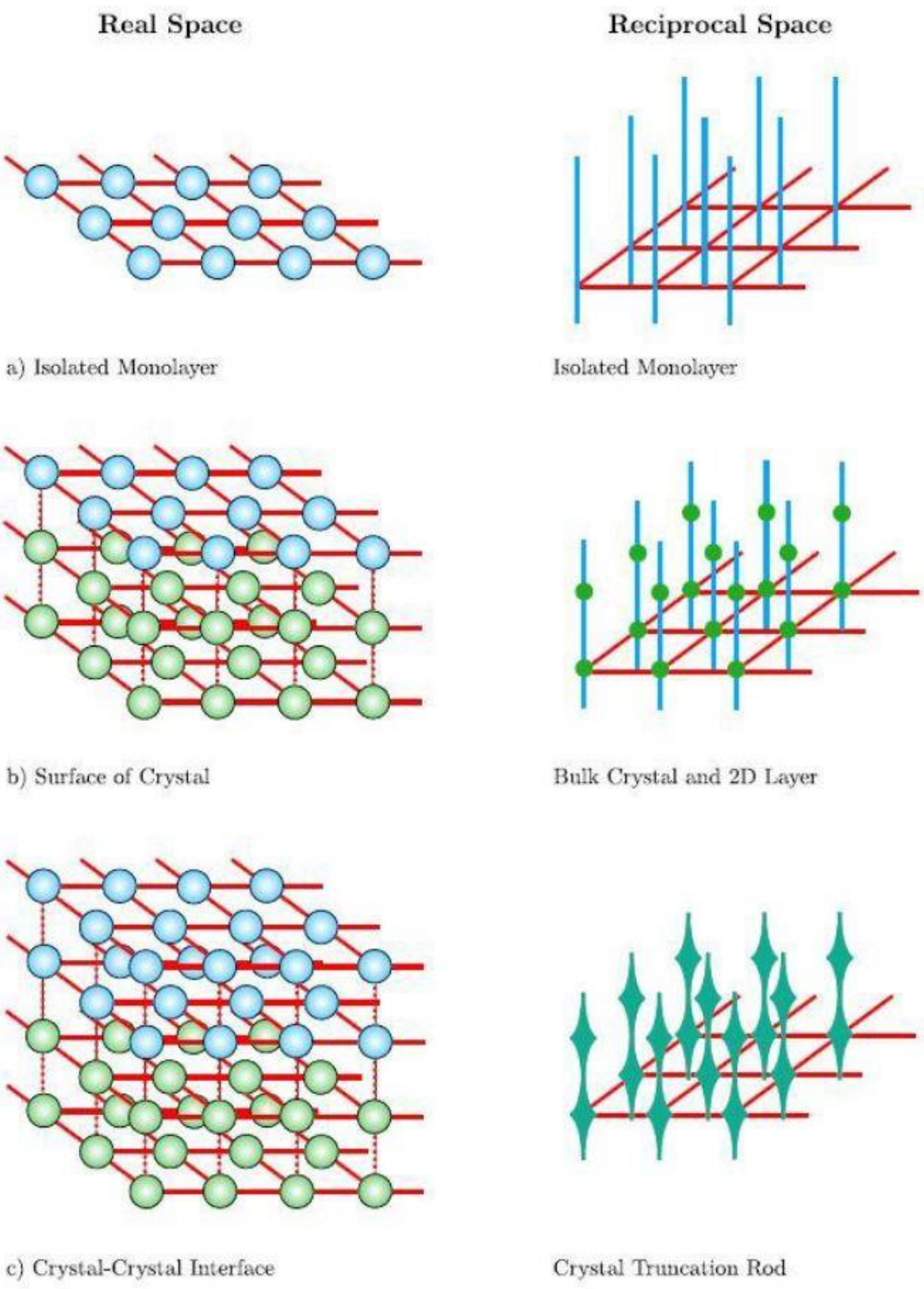

Figure 2.8 *Real space and corresponding reciprocal space diffraction pattern for a) a two dimensional monolayer, b) crystal surface and c) crystal-crystal interface.*
Source: [33]

2.2.6. Modelling Surface Structure

The calculation of the scattered intensity along the CTRs (*Equation 2.40*) is assuming a defect-free, perfectly terminated surface. In real cases coverage, surface relaxation and roughness have an effect on the CTR profile and need to be taken into consideration to model the scattered intensity.

The surface normal component of momentum transfer CTR is defined as the specular CTR at (0 0 l). The non-specular CTR have an additional in-plane component of momentum transfer for integer values of h and k. Measurement of these CTRs is sensitive to the registry of surface and bulk layers of the crystal. However, if the surface layer has a different symmetry from the bulk termination structure, scattering from the surface can be observed. Modelling all CTRs (specular and non-specular) leads to a detailed three-dimensional model for the surface structure.

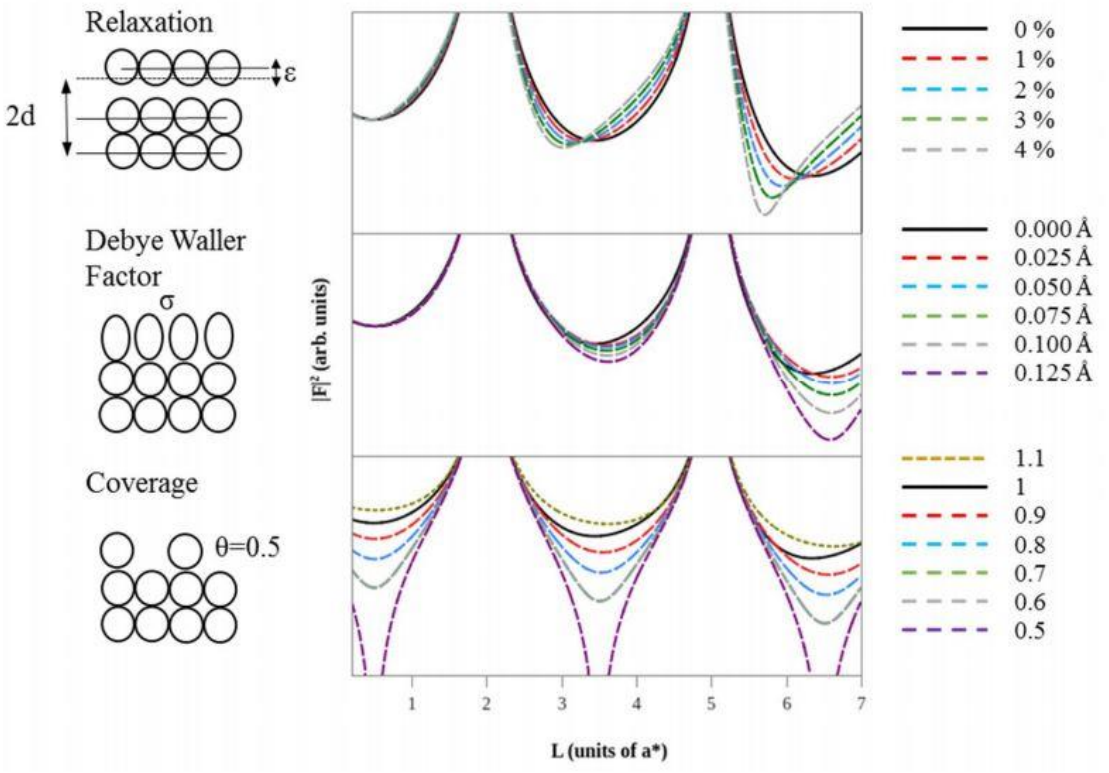

Figure 2.9 *Schematic depiction of how relaxation (top), roughness (middle) and coverage (bottom) of the topmost layer of a surface crystal can alter the shape of a CTR.*

Figure 2.9 illustrates the effects of coverage, relaxation and roughness of the top surface layer. Coverage decrease causes the intensity at the anti-Bragg positions to drop more sharply while surface relaxation produces an asymmetry at said positions. Roughness, calculated

through the Debye Waller factor (DWF), is told apart from a change in coverage as the effect is more pronounced at higher momentum transfer, **q**.

Figure 2.10 depicts how coverage percentage of a layer and its distance from the crystal can affect the CTR profile. Firstly, it becomes evident that even adlayers with a small coverage can significantly alter a CTR profile. Also, a change in layer height has an impact on a CTR as it affects the path difference of the interfering waves.

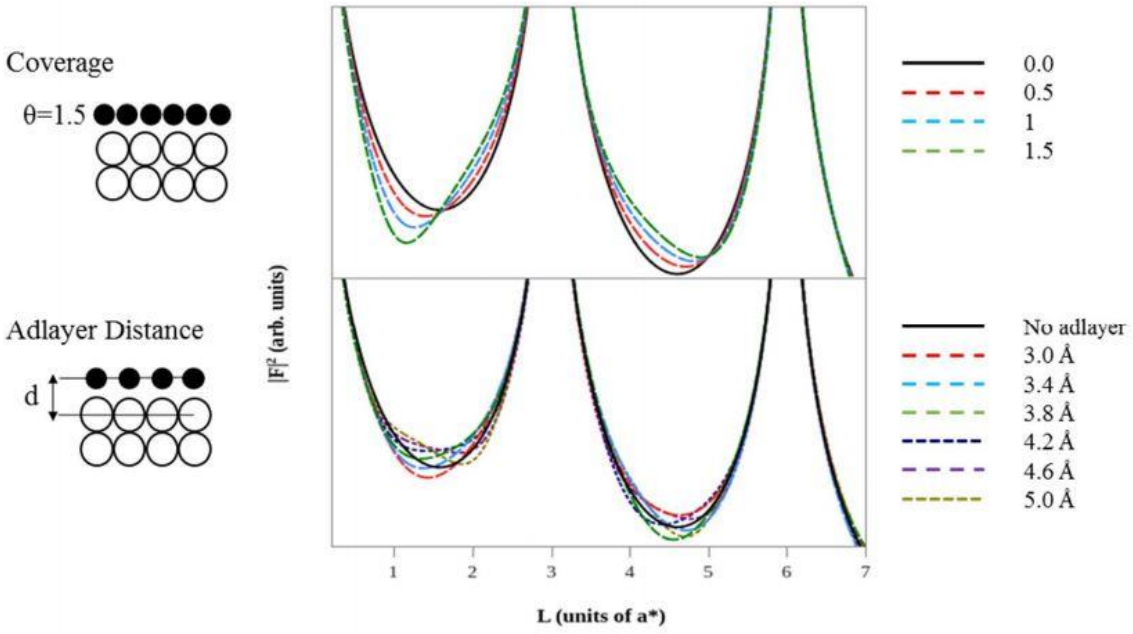

Figure 2.10 *Schematic depiction of how coverage (top) and distance (bottom) of an adlayer can alter the shape of a CTR.*

Finally, another parameter which must be considered is the effect of a liquid structure when modelling CTRs in aqueous or non-aqueous solutions. There are two methods of modelling the liquid structure: the error function and the layered liquid model. *Figure 2.11a* depicts how the form of a CTR is affected by the liquid components and in *Figure 2.11b* it is shown the contribution each model makes to the structure factor.

The error function alters the CTR at low q but then falls off quickly, while the layered liquid model has a quasi-Bragg peak because of the layering. The liquid layer model works well for water at charged mineral interfaces [39] but is not ideal for electrochemical interfaces with adsorbed species. [40]

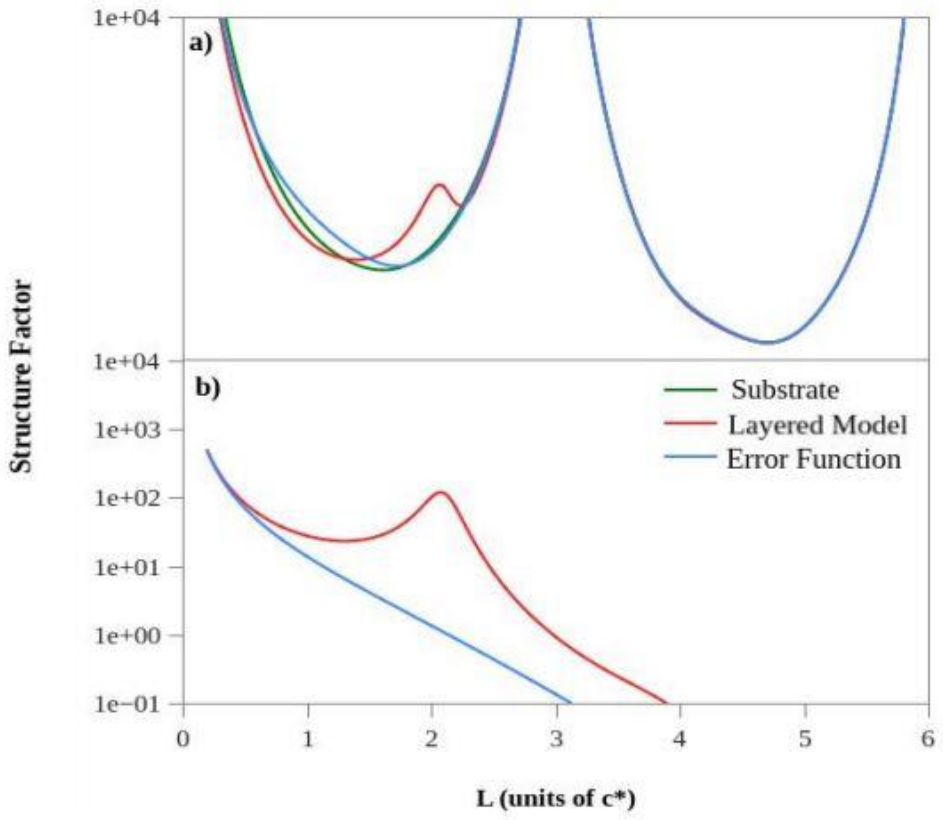

Figure 2.11 *Comparison of the effect a layered liquid model and the error function have on the structure factor.*

2.2.7. The (111) Surface

This thesis is focused solely on the low index face of (111) of fcc metal surfaces. This section will detail the real space unit cell and the corresponding reciprocal space lattice. The h and k directions are in the plane of the surface, while l along the surface normal direction hence, the specular CTR is always with respect to the surface normal direction.

The (111) surface is the most densely packed of the three low index faces and has an hexagonally close packed (hcp) surface structure. In *Figure 2.12* a top and side view of a (111) crystal are presented. The **a** and **b** vectors are equal to the nearest neighbour spacing with an angle of 120^{o}. The unit cell consists of three atomic layers, due to the ABC stacking, terming the **c** lattice parameter as shown in *Figure 2.12a*.

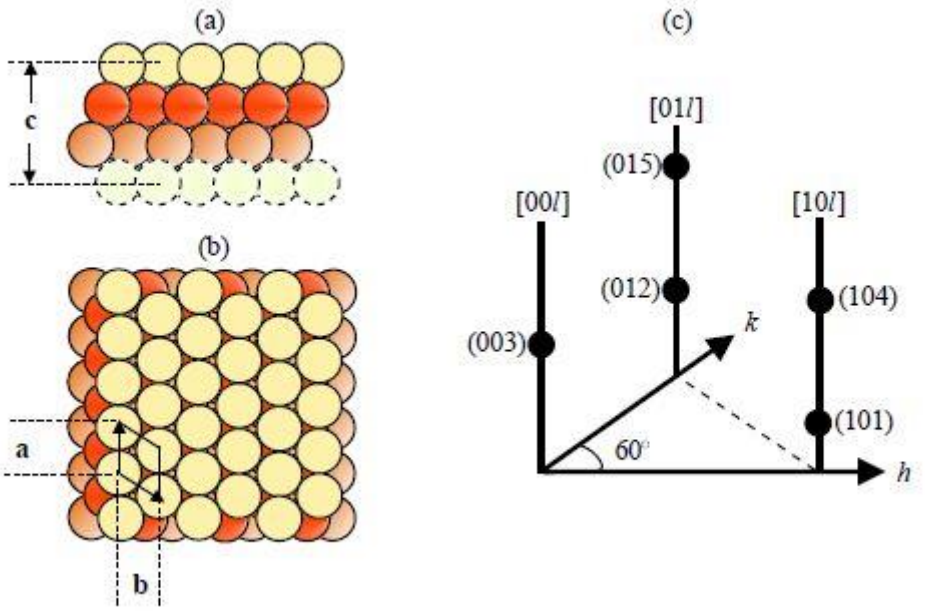

Figure 2.12 *Surface structure of fcc(111).* ***a)*** *side and* ***b)*** *top view.* ***c)*** *Reciprocal space lattice*

The h, k, l unites are defined as:

$$a^* = b^* = \frac{4\pi}{\sqrt{3}\alpha_{NN}}, c^* = \frac{2\pi}{\sqrt{6}\alpha_{NN}}$$

The Bragg peaks marked as circles in *Figure 2.12c* are separated by three points of l because of the three atomic layer repetition of the unit cell. The surface notation is related to the cubic notation by the transformations:

$$h_C = \frac{2}{3}h_S - \frac{2}{3}k_S + \frac{1}{3}l_S$$

$$k_C = \frac{2}{3}h_S + \frac{4}{3}k_S + \frac{1}{3}l_S$$

$$l_C = -\frac{4}{3}h_S - \frac{2}{3}k_S + \frac{1}{3}l_S$$

Such as the (111) Bragg peak is identified as the (003) in the surface notation.

For a clean (111) surface the bulk structure factor is calculated as:

$$F_{bulk} = f\ DW_{bulk} \sum_{n=0}^{\infty} e^{in\left[2\pi\left(\frac{h}{3}-\frac{k}{3}-\frac{l}{3}\right)\right]} = \frac{f\ DW_{bulk}}{1-e^{2\pi i\left(\frac{h}{3}-\frac{k}{3}-\frac{l}{3}\right)}} \quad (2.41)$$

Where f is the atomic form factor depending on the momentum transfer, q and

$$DW_{bulk} = e^{-\frac{1}{2}(q\sigma)^2}$$

DW_{bulk} is termed as the Debye-Waller factor that stands for thermal disorder, either in-plane, or out-of-plane, which depends on the thermal vibration root-mean-square (rms) displacement of the atom about their average position (σ). Similarly to the atomic structure factor, the Debye temperature has been tabulated for every element and can be found in the International Tables for Crystallography. The unit for σ are in Ångstroms and thus, usually the Debye-Waller factor is in $Å^2$.

Additionally, scattering from surface layers of the crystal contribute to the overall structure factor and is regarded as a continuation of the bulk crystal.

$$F_{surface} = f\ \Theta_n\ DW_n\ e^{2\pi i\left[n\left(-\frac{h}{3}+\frac{k}{3}+l[\frac{1}{3}+\varepsilon_n]\right)\right]}, for\ n = 1,2,3 \quad (2.42)$$

In this instance, the DWF are considered separately for each of the top three surface layers (DW_n) due to differences between bond strengths and distances between the layers in comparison to the bulk layers. Θ_n accounts for the occupation of each surface layer respectively and ε_n for displacement of the surface layer along the surface normal.

The total scattered intensity is expressed as:

$$I_{Total} = |F_{Total}|^2 = \left|F_{bulk} + F_{surface}\right|^2 \quad (2.43)$$

2.2.8. X-Ray Voltammetry

X-ray Voltammetry (XRV) is a powerful technique to observe the structural changes that are characterised by potentiostatic CTR measurements. It is a combination of X-ray diffraction and cyclic voltammetry techniques. By measuring the reflected intensity at a fixed (hkl) value sensitive to surface relaxation or adsorption processes we can acquire an understanding of any structural effects occurring and the potential range of any modified surface structures. By comparison of XRV data with cyclic voltammograms it is possible to relate electrochemical measurements and observations to atomic scale structural characteristics of the surface. XRV measurements can be extremely valuable when monitoring surface structures such as an ordered adsorbate layer or a reconstructed surface layer with a different symmetry to the underlying substrate.

2.3. Low Energy Electron Diffraction (LEED)

Low Energy Electron Diffraction (LEED) is a powerful technique for surface analysis. It is largely utilised in materials science research to study surface structure, bonding and the effects of a structure on surface processes.

LEED was first demonstrated by Davisson and Germer. [41] In this technique, electrons originating from an electron gun collide upon a surface where they are elastically backscattered and analysed in a range between 20 – 200 eV. Electrons in this range are excellent probes of a surface structure for two reasons:

a. Their inelastic mean free paths are between approximately 5 – 20 Å, translating to a penetration of a few atomic layers into the surface
b. Their de Broglie wavelengths are of the same order of magnitude as the interatomic spacing between the atoms at a surface and therefore, may undergo diffraction if they are periodically arranged.

LEED is a surface sensitive diffraction technique that works by firing a beam of electrons at the surface and collecting the scattered electrons on a photo-fluorescent screen. The screen will show a diffraction pattern caused by the interference of electrons. The surface sensitivity is a result of the strongly interacting nature of the electrons which do not penetrate far into the sample. Sharp spots on a LEED pattern indicate a well ordered surface. For example single crystal surfaces such as Au(111), reconstruct and if there are sharp satellite spots due to the reconstruction then this is good sign of a clean well-ordered surface. [42]

Figure 2.12 depicts a simplistic perspective of how an electron beam is diffracted from an ordered array of atoms separated by a distance d. If two incident parallel beams, k_i, diffract off the surface then the path difference, Δs, between the two is given by:

$$\Delta s = d(\sin\psi - \sin\varphi) \tag{2.44}$$

In the case of coherent interference between incident beams, the path difference must be an integer value of wavelengths. So, equation 2.44 becomes:

$$n\lambda = d(\sin\psi - \sin\varphi) \tag{2.45}$$

If n = 1 and the values of ψ and φ are known, then the separation of atoms, d, can be determined.

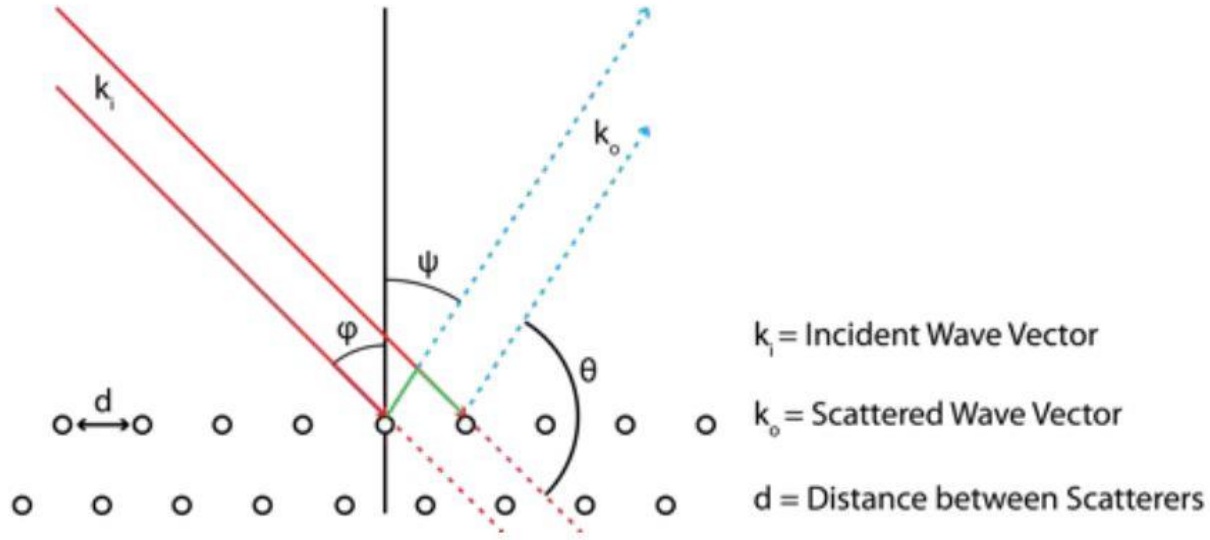

Figure 2.13 *A simplistic perspective of the diffraction of two incident parallel beams, k_i, from an ordered array of atoms. ψ and φ are the angles of the incident and diffracted beam, respectively. θ is the angle of diffraction between the incident beam, k_i and the diffracted beam, k_0.*

For the determination of the surface structures, LEED can be used:

a. Qualitatively, where the spot positions of the diffraction pattern provide information of the diffraction pattern, symmetry and any rotational domains of the unit cell of the adsorbate with respect to the substrate
b. Quantitatively, where the intensities of the spots of the structure are monitored as a function of the electron beam energy to create I-V curves, which in comparison with theoretical I-V values from Density Functional Theory (DFT) may provide detailed information on atomic positions.

The major difference between Surface X-Ray Diffraction and Low-Energy Electron Diffraction is that low-energy electrons are strongly scattered in a crystal, while X-rays are scattered weakly. This leads to LEED having a low penetration depth and high surface sensitivity and a high yield. However, it is difficult to interpret the scattered intensity because -rays have a high penetration depth, low yield – hence the requirement for synchrotron radiation – and the advantage of a straightforward interpretation of the intensity owing to the absence of multiple scattering. [43]

2.4. References

1. Brett, C.M.A., Brett, A.M.O., *Electrochemistry: Principles, Methods and Applications,* Oxford University Press, Oxford, 2000
2. Khan, S.U.M., Kainthia, R.C., Bockris, J.O'M., *J. Phys. Chem.,* **1987,** *91,* 5974-5977
3. Andrienko, D., *Cyclic Voltammetry,* John Wiley & Sons Inc.: New York, **2008**
4. Wahl, D., *Galvanotechnik,* **2005,** *96,* 1820-1828
5. IUPAC, Compendium of Chemical Terminology, 2nd ed. (the "Gold Book"). Compiled by McNaught, A.D. and Wilkinson, A. Blackwell Scientific Publications, Oxford (1997).
6. Grahame, D.C., *Chem. Rev.,* **1947,** *41,* 441-501
7. Jayakrishnan, D.S., *Corrosion Protection and Control Using Nanomaterials,* **2012,** 86-125
8. Casella, I.G., Contursi, M., *Electrochim. Acta,* **2007,** *52,* 7028-7034
9. Hegemann, D., Amberg, M., Ritter, A., Heuberger, M., *Materials Technology,* **2009,** *24,* 41-45
10. Cavallotti, P.L., Nobili, L., Vicenzo, A., *Electrochim. Acta,* **2005,** *50,* 4557-4565
11. Robertson, A., Erb, U., Palumbo, G., *Nanostruct. Mater.,* **1999,** *12,* 1035-1040
12. Anderson, P.M., Li, C., *Nanostruct. Mater.,* **1995,** *5,* 349-362
13. Gerischer, H., Kolb, D.M., Przasnyski, M., *Surface Science,* **1974,** *43,* 662-666
14. Kolb, D.M., Przasnyski, M., Gerischer, H., *Electroanal. Chem. Interfac. Electrochem.,* **1974,** *54,* 25-38
15. Herrero, E., Buller, L.J., Abruña, H.D., *Chem. Rev.,* **2001,** *101,* 1897-1930
16. Van Huong, C.N., Gonzalez-Tejera, M.J., *J. Electroanal. Chem.,* **1988,** *244,* 249-259
17. Armstrong, R.D., Fleischmann, M., Thirsk, H.R., *J. Electroanal. Chem.,* **1966,** *11,* 208-223
18. Astley, D.J., Harrison, J.A., Thirsk, H.R., *Trans. Faraday Soc.,* **1968,** *64,* 192-201
19. Abyaneh, M.Y., *Electrochim. Acta,* **1982,** *27,* 1329-1334
20. Paunovic, M., Schlesinger, M., *Fundamentals of Electrochemical Deposition,* Wiley: New York, 2nd edition, **2006**
21. Scharifker, B., Hills, G., *Electrochim. Acta,* **1983,** *28,* 879-889
22. Cottrell, F.G., *Z. Phys. Chem.,* **1903,** *42,* 385
23. Bard, A. J., Faulkner, L. R. *Electrochemical Methods: Fundamentals and Applications,* Wiley: New York, 2nd edition, **2000**

24. Hölzle, M.H., Apsel, C.W., Will, T., Kolb, D.M., *J. Electrochem. Soc.*, **1995,** *142*, 3741-3749
25. Fleischmann, M., Thirsk, H.R., *Electrochim. Acta*, **1960,** *2*, 22-49
26. Deutscher, R.L., Fletcher, S., *J. Electroanal. Chem.*, **1990,** *277*, 1-18
27. Pletscher, D., Greef, R., Peat, R., Peter, L.M., Robinson, J., *Instrumental Methods in Electrochemistry*, Horwood Publishing Limited, **2006**
28. Avrami, M., *Journal of Chemical Physics*, **1939,** *7*, 1103
29. Avrami, M., *Journal of Chemical Physics*, **1940,** *8*, 212
30. Avrami, M., *Journal of Chemical Physics*, **1941,** *9*, 177
31. Kot, M., *In-operando hard X-ray photoelectron spectroscopy study on the resistive switching physics of HfO_2-based RRAM*, Ph.D. thesis, Brandenburgische Technische Universität Cottbus
32. Generalic, E., https://glossary.periodni.com/glossary.php?en=face-centered+orthorhombic+lattice
33. Robinson, I.K., Tweet, D.J., *Rep. Prog. Phys.*, **1992,** *55*, 599-651
34. Warren, B.E., *X-Ray Diffraction*, Dover Publications, New York, **1990**
35. Ibers and Hamilton, *International Tables for Crystallography, Volume IV*, Kluwer Academic Publishers, **1974**
36. Hyde, M.E., Klymenko, O.V., Compton, R.G., *J. Electroanal. Chem.*, **2002,** *534*, 13-17
37. Floate, S., Hyde, M., Compton, R.G., *J. Electroanal. Chem.*, **2002,** *523*, 49-63
38. Lucas, C.A., Markovic, N.M., *Structure Relationships in Electrochemical Reactions*, Encyclopaedia of Electrochemistry, **2007**
39. Fenter, P., Sturchio, N.C., *Geochim. Cosmochim. Acta*, **2012,** *97*, 58-69
40. Fenter, P., Sturchio, N.C., *Prog. Surf. Sci.*, **2004,** *77*, 171-258
41. Davisson, C., Germer, L.H., *Phys. Rev.*, **1927,** *30*, 705
42. Held, G., *Low-Energy Electron Diffraction (LEED,*. In Surface and Thin Film Analysis (eds Friedbacher, G., Bubert, H.,), **2011**
43. Duke, C.B., Plummer Ward, E., *Frontiers in Surface Science and Interface Science*, Wiley: New York, **2002**

CHAPTER 3

Methods and Techniques

This Chapter consists of the preparation procedures for each experiment presented in the thesis. Details include the preparation for each single crystal, description of the electrochemical cells and solution making and finally, details about the Ultra-High Vacuum chamber will be explained.

3.1. Sample Surface Preparation Methods

For all electrochemical measurements it is important to be able to prepare well-ordered single crystal surfaces. Otherwise, the interpretation of the experimental results might be inaccurate or even misleading. A well-ordered surface must be atomically flat and possess as little surface defects as possible.

Smooth single crystal surfaces can be prepared through various methods. Commonly, they are prepared in ultra-high vacuum (UHV) by cycles of argon ion bombardment and high-temperature annealing. [1,3.5 2] By employing surface science techniques such as LEED, AES or XPS the surface structure can be examined in UHV straight after preparation. However, the transfer to an electrochemical cell after the preparation can be achieved only through the use of a glove bag filled with an inert gas such as nitrogen or argon in order to avoid any surface oxidation.

Another method is by electropolishing the crystal by anodising the sample surface in a specific polishing solution. Electropolishing of single crystal electrodes has attracted attention due to its quickness and its practicality. Despite the considerable amount of experimental works reported in literature, the exact mechanisms responsible for the limiting behaviour during dissolution of copper, important for successful polishing, is currently unknown. [3]

An alternative method was fabricated by Clavilier *et al.* where they developed the cheap, fast and convenient flame annealing method to handle platinum single crystal electrodes without the use of UHV techniques. [4] Later on, the flame annealing method was utilised for the preparation of gold single crystal electrodes. [5] Single crystals are annealed in the oxidising part of a Bunsen burner, hydrogen or butane flame to remove any contaminants and / or to reorder the surface atoms. Usually, the annealing time is approximately five minutes, a time period long enough to prepare reconstructed surfaces. Nevertheless, long-time annealing in a small furnace at a controlled temperature is necessary for incredibly disordered surfaces. Finally, it must be noted that heating the crystal above the melting point will result in permanent damage. Therefore, it is vital to constantly move the flame around the crystal.

3.1.1. Electropolishing of Cu(111)

The Cu(111) single crystal (Mateck, 10 mm diameter) was prepared by electropolishing. Cu(111) was immersed in orthophosphoric acid (H_3PO_4, 70% w/w concentration) at 2 V for 10 seconds and repeated three times after rinsing repeatedly with MilliQ water (18.2 MΩ). Afterwards, the surface was protected from oxidation and / or contamination by air by covering it in an overpressure of nitrogen during the transfer in the electrochemical cell.

3.1.2. Surface annealing of Ag(111) in UHV

The surface of Ag(111) (Mateck, 10 mm diameter) was prepared under UHV chamber. The surface was cleaned through three cycles of argon ion sputtering (4×10^{-5} Torr, 20 min) and annealing (450 ^{o}C, 40 min). The confirmation of a clean Ag(111) surface was obtained through LEED images. For the experiment of the acetonitrile adsorption on Ag(111), the crystal was transferred in the electrochemical cell via the aid of a nitrogen filled glove bag to prevent any surface oxidation.

3.1.3. Flame annealing of Au(111)

The single crystal of Au(111) (Mateck, 10 mm diameter) was annealed in a blue butane gas flame for approximately 5 minutes until glowing red and then, the crystal was left to cool down in air. This process was repeated three times before immersing the crystal inside the electrochemical cell.

3.2 Electrochemical Cells

3.2.1. Conventional Electrochemical cell

For all electrochemical measurements a conventional electrochemical cell was employed and is shown in *Figure 3.1*. The glass cell was covered with a Teflon lid that contained sockets for the three electrodes and the gas tube. The sample was placed inside a collet and screwed inside a Teflon tube which was screwed in on the central hole of the Teflon lid. A wire was entering from the other side of the tube so it could go in contact with the crystal from its back. The single crystal was mounted inside the cell carefully in a hanging meniscus orientation, so only its surface would be in contact with the electrolyte. The working electrode (WE) presented in this thesis was a Au(111) single crystal, the reference electrode (RE) was an Ag/AgCl and all potentials in all electrochemical measurements are written with respect to this electrode and a Au wire was used as the counter electrode (CE).

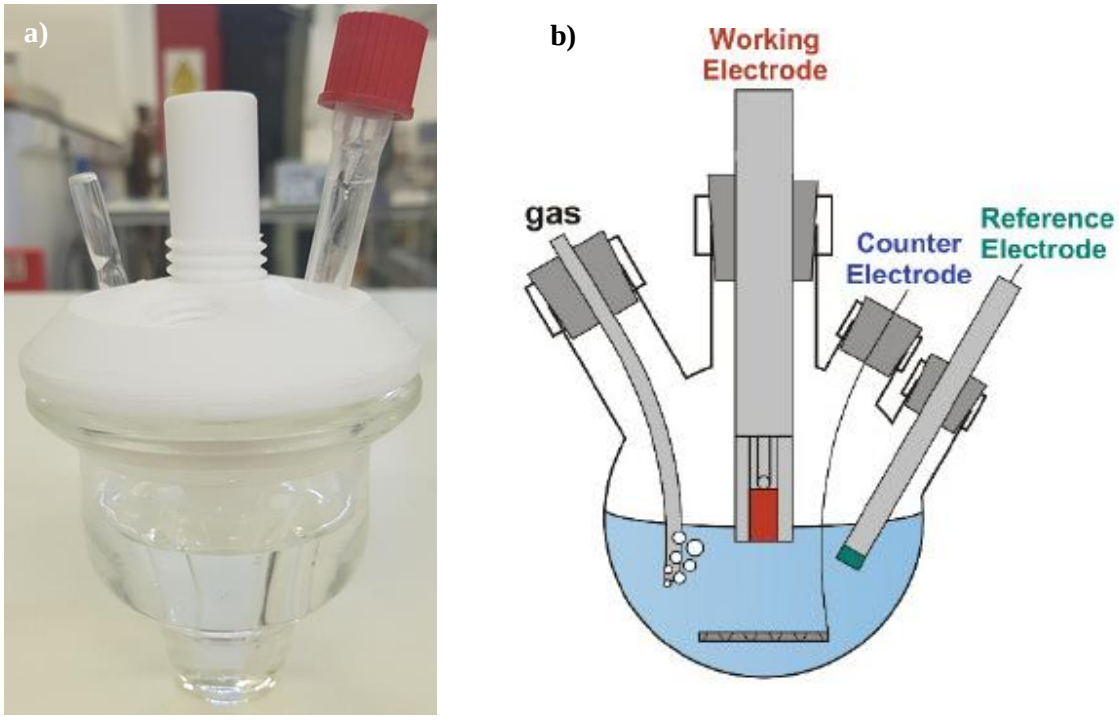

Figure 3.1 a) *Picture and* ***b)*** *Schematic of the conventional three electrode electrochemical cell used in all electrochemical measurements.*

3.2.2. Electrochemical X-Ray cell

A depiction of the electrochemical cell, which was employed in all X-ray scattering related experiments is shown in *Figure 3.2*. With the aim of ensuring chemical inertness, in the same manner with the bench electrochemical cell, the X-Ray cell and all of its parts, with the exception of the polypropylene film and the O-ring were made of Teflon. It consists of a conical shaped centre collet for sample holding and side ports for electrodes and wires.

The cell uses the standard three-electrode system that has been modified to be utilised on diffractometers. The sample is carefully mounted in a collet which is located into the centre of the cell so that only the surface of the crystal is exposed. The collet ensures a tight seal around the crystal. The counter electrode is connected at the side of the cell and lies around a circular cavity which surrounds the sample. The reference electrode is placed in a straight through connector in the same cavity as the counter electrode to complete the setup. A thin polypropylene film (~10 μm, Chemplex) covers the top of the cell and is held stable by a tightly fitted O-ring around the cell. At each side of the cell, Teflon tubes are linked with one side connected to an electrolyte reservoir while the other to a syringe for pulling fresh electrolyte into the system.

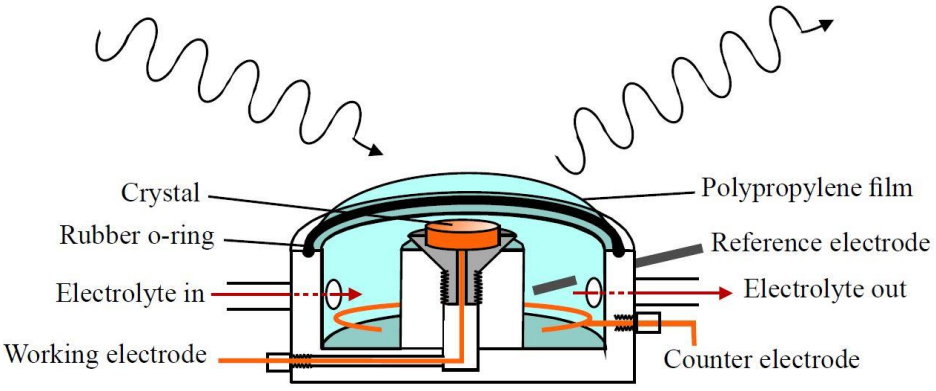

Figure 3.2 *Schematic of the electrochemical X-Ray cell.*

A gold, copper or silver wire, depending on the nature of the experiment, was used as a counter electrode and it must be long enough (~ 10 cm) to enter inside the cell. A Ag/AgCl electrode was used in all X-Ray experiments and all the potential values are quoted with respect to this reference electrode. Finally, to remove all contamination from dissolved gases, the electrolyte is purged with nitrogen, an inert gas, through another tube.

The cell is operated in two modes. Firstly, when the film is raised where the cell operates as a conventional electrochemical cell where CVs can be obtained for comparison to those measured in conventional electrochemical cells to confirm the cleanliness and condition of the crystal surface. Secondly, when the film is lowered where a thin layer of electrolyte is formed on the surface of the crystal which is thick enough for X-rays to penetrate it to perform X-ray scattering experiments.

A white light beam enters the beamline and a monochromator crystal is used to select the preferred wavelength of radiation. Then, applying focus optics the beam is focused on the centre of the diffractometer. An attenuator may be required as the scattered intensity can be in excess of the detector onset (e.g. in the case of the satisfaction of the Bragg conditions). Next, the beam passes through an ion chamber that calculates the number of photons per second. Finally, the beam passes through a set of slits that enable the user to handle the incident beam size according to their requirements.

3.3 Experimental Procedures

3.3.1 Glassware cleaning

In order to remove any unwanted contamination associated with impurities, proper cleaning was required. All glassware as well as the Teflon parts of the electrochemical cells were dipped into an acid bath consisting of concentrated sulphuric and nitric acids in a 1:1 ratio and were left overnight. Afterwards, everything was rinsed with MilliQ water, followed by a submerging into MilliQ water and boiled for approximately 20 minutes and repeated three times.

3.3.2 Chemicals

All solutions mentioned in this thesis were prepared with the highest grade of chemicals available. In *Table 3.1*, the list of all the chemicals used is stated.

Chemical	Formula	MW / g mol^{-1}	Purity	Supplier
Acetonitrile	CH_3CN	41.05	99.8%	Sigma – Aldrich
Copper (II) Sulphate Pentahydrate	$CuSO_4 \cdot 5H_2O$	249.69	≥ 98%	
Copper (II) Perchlorate Hexahydrate	$Cu(ClO_4)_2 \cdot 6H_2O$	370.54	98%	
Sulfuric Acid	H_2SO_4	98.08	99.999%	
Perchloric Acid	$HClO_4$	100.46	99.999%	
Nitric Acid	HNO_3	63.01	70%	
Phosphoric Acid	H_3PO_4	98.00	85%	

Table 3.1 *List of all chemicals used.*

3.3.3 Solution Preparation

All solutions were prepared in clean flasks of 100 or 250 mL. Each amount of the respective chemical was added to the flask and afterwards was filled with MilliQ water up to the desired concentration.

3.3 Ultra-High Vacuum

The Ultra-High Vacuum (UHV) system used in this work is from Diamond Light Source's (DLS) I-07 beamline and is displayed in *Figure 3.3*. This UHV system contains a large 2 + 3 diffractometer to study *in situ* grown samples and includes a large environmental chamber on the diffractometer. It is a three-vessel system, containing primarily, a load lock for the samples input, a buffer chamber for up to four samples storage and finally, a preparation and analysis chamber.

The buffer chamber houses the ion gun for the sputtering and annealing procedures and LEED optics in addition to scanning probe microscope for . The analysis chamber includes a second LEED system, an X-Ray source to perform XPS. X-Rays are directed to the sample through a small beryllium window and come out from another larger beryllium window and the diffracted intensity is collected in a Pilatus 100K area detector.

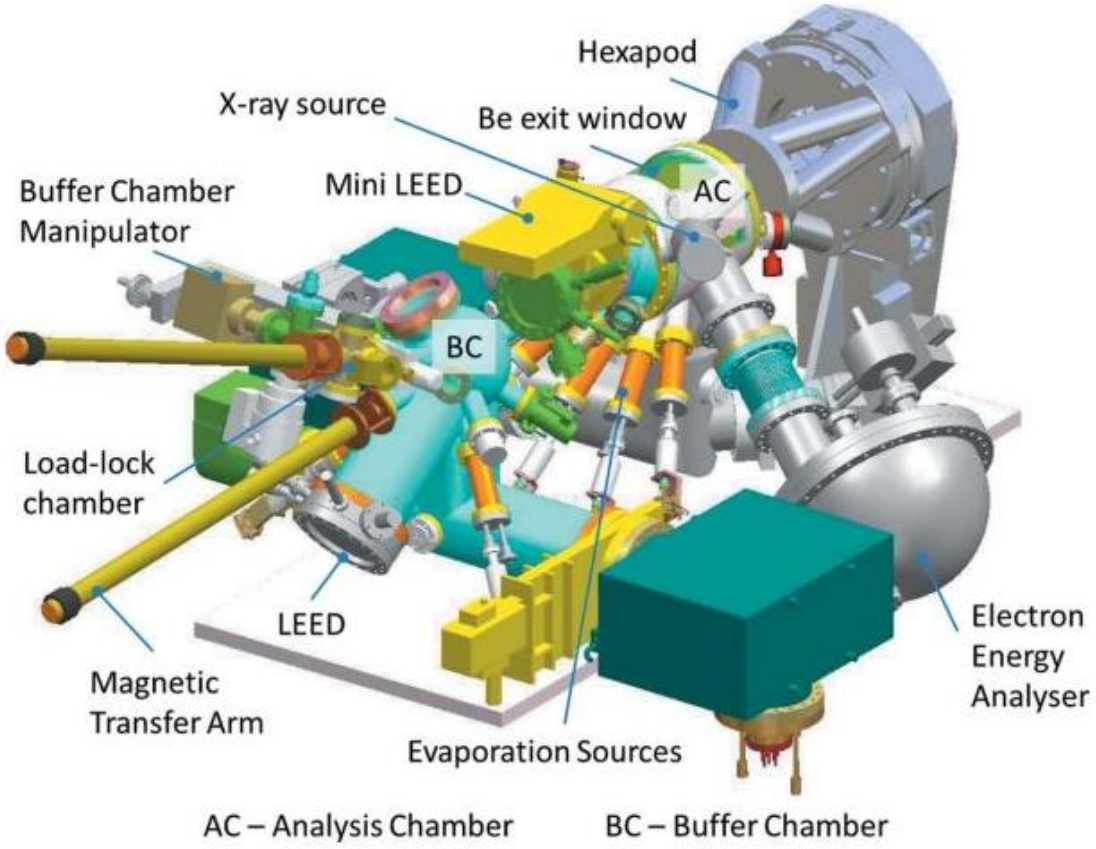

Figure 3.3 *Schematic outline of the UHV chamber from the I-07 beamline*
Source: *[6]*

3.4 Synchrotron and Beamlines

Scattering along a Crystal Truncation Rod (CTR) is approximately 10^5 times less than that from a Bragg peak. In addition to the need to penetrate a liquid layer it becomes apparent that an extremely high photon flux is mandatory. Laboratory-based X-ray sources are not widely available and do bot provide fluxes high enough for *in-situ* SXRD measurements and thus, synchrotron-based X-ray sources are the best option as they also have the advantage of having tunable energy output.

The acceleration of relativistic charged particles on a curved path through a magnetic field causes the emission of synchrotron radiation. In *Figure 3.4* a schematic of the arrangement of a third-generation light source is depicted. An electron beam is produced and then accelerated in a linear accelerator (LINAC) and afterwards, it passes around a booster synchrotron to reach the required energy. The electrons then enter the storage ring which is made up of straight sections and bending magnets that are used to curve the beam between the sections.

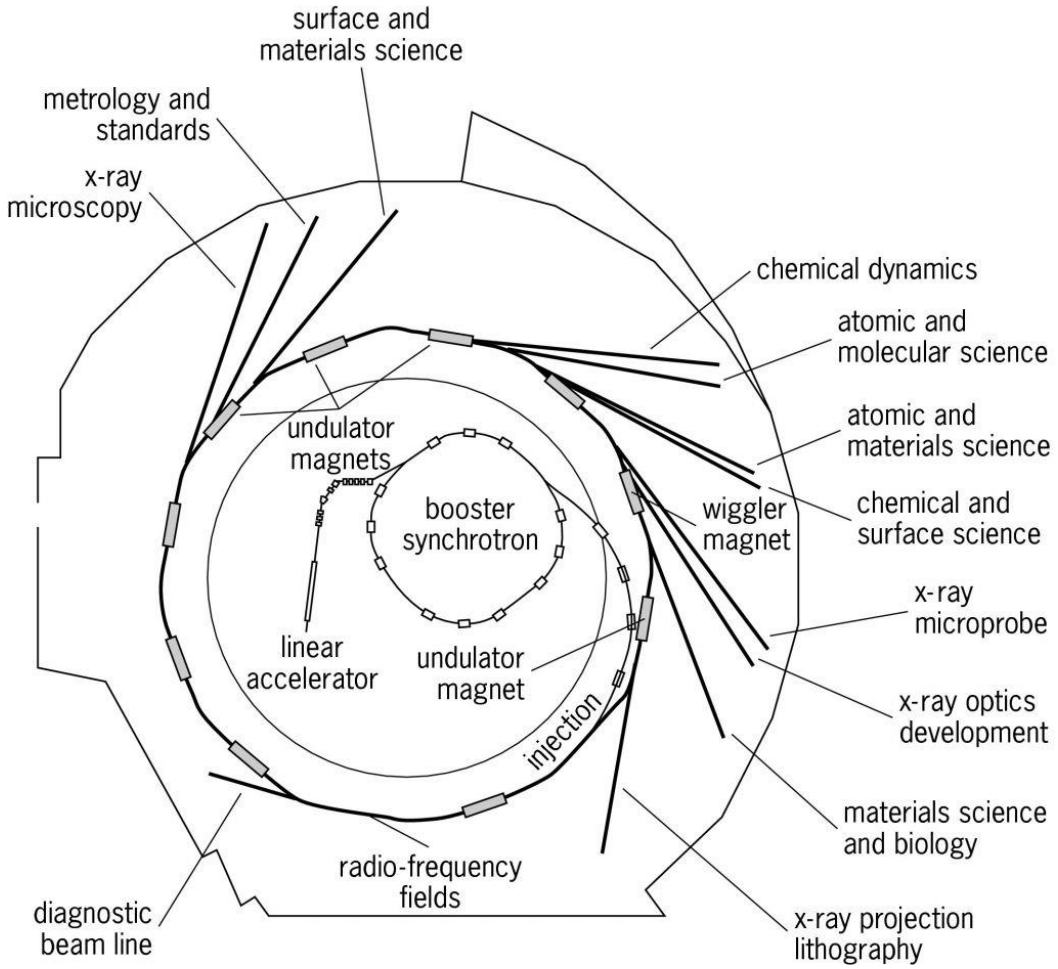

Figure 3.4 *Schematic of a third-generation synchrotron layout. The picture is taken from the Lawrence Berkeley National Laboratory synchrotron website to better demonstrate the main parts of the synchrotron. Also depicted are the different beamlines of the synchrotron.*
Source: [7]

As the electron beam passes through the various components in the storage ring it may lose energy. Radio frequency fields boost the electrons to not allow the loss of energy. Around the storage ring several beamlines are located, either at a bending magnet where synchrotron radiation is already produced or next to a straight section where a different device is needed to generate X-rays. Such devices are known as insertion devices and there are two types: undulators and wigglers. An undulator has a periodic arrangement of magnets that trigger the generated radiation to add up constructively, providing a brightness enhancement. A wiggler is a series of magnets like a bending magnet that periodically deflect the electron beam and causes emission of synchrotron radiation,

The generated fan of synchrotron X-rays then enters a beamline where there are generally three hutches: an optics hutch, an experimental hutch and a control hutch (*Figure 3.5*). In the optics hutch, the synchrotron radiation is monochromatised by a pair of monochromating

crystals and then it is focused by focusing lenses and mirrors. Afterwards, the focused monochromatic beam enters the experimental hutch. Generally, a series of attenuators are employed to reduce the intensity of the beam prevent damaging the sample or the detector. A beam monitor, such as an ion chamber, monitors the intensity of the beam which can be used to normalise the experimental data and adjustable slits are used to define the intensity of the beam which will reach the sample. Finally, the diffracted beam from the sample is measured by a detector.

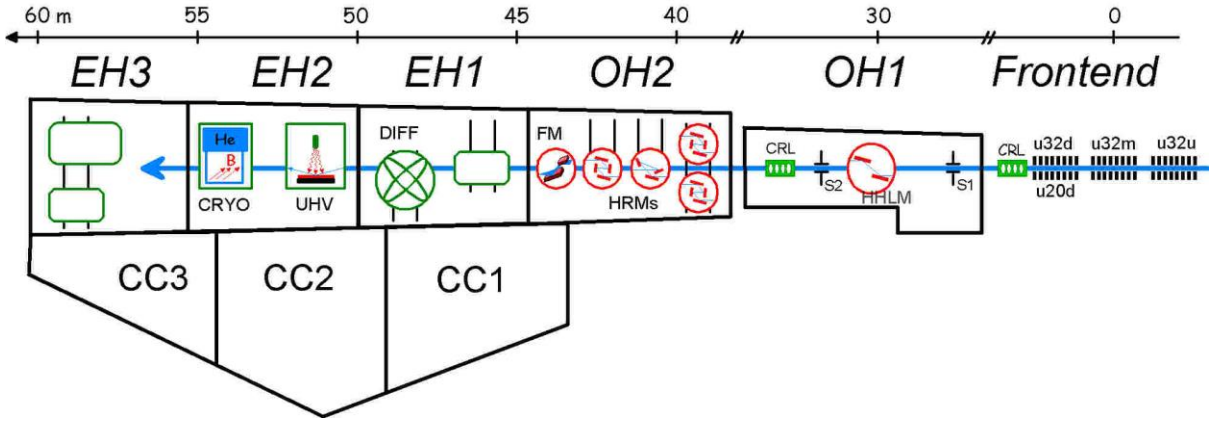

Figure 3.5 *Schematic layout of a typical beamline. The image has been taken from the ID18 beamline from the European Synchrotron Radiation Facility. Abbreviations of the main parts: OH: optical hutch, EH: experimental hutch, CC: control cabin, S: slit system, HHLM: high heat load monochromator, CRL: compound refractive lenses, HRM: high resolution monochromator, FM: focusing monochromator, DIFF: diffractometer.*
Source: [8]

3.5 References

1. Hubbard, A.T., Chem. Rev., **1988,** *88,* 633-656
2. Soriaga, M.P., Progr. Surf. Sci., **1992,** *39*, 325-443
3. Glarum, S.H., Marshall, J.H., *J. Electrochem. Soc.*, **1985,** *132,* 2872-2878
4. Clavilier, J., Faure, R., Guinet, G., Durand, R., *J. Electroanal. Chem.*, **1980,** *107,* 205-209
5. Hamelin, A., Doubova, L., Wagner, D., Schirmer, H., *J. Electroanal. Chem.*, **1987,** *220,* 155-160
6. Nicklin, C., Arnold, T., Rawle, J., Warne, A., *J. Synchroton Rad.*, **2016,** *23*, 1245-1253
7. https://encyclopedia2.thefreedictionary.com/synchrotron+radiation
8. http://www.esrf.eu/home/UsersAndScience/Experiments/MEx/ID18/beamline_layout/id18_layout.html

CHAPTER 4

Silicene Growth on Ag(111)

4.1. Introduction

The discovery of the fascinating properties of graphene, [1] a zero-overlap semimetal with very high electrical conductivity and electronic mobility, largely motivated the theoretical and experimental investigation of two-dimensional (2D) materials and particularly 2D honeycomb materials. [2] More specifically, elements of the IV-group of the periodic table, the same group as carbon, received significant attention (Si, Ge, Sn). [3] Remarkably, the energetic stability of 2D forms of silicon and germanium were predicted by Takeda and Shiraishi in 1994 with first principles density functional theory (DFT). [4] Later, after being coined the terms "silicene" [5] and "germanene" [6] for the silicon and germanium based counterparts of graphene respectively, these 2D materials attracted most of the attention. [7] It must be noted that the term "silicene" refers to a honeycomb lattice consisting of six Si atoms

Theoretical investigations showed that freestanding silicene can be stable and obtain massless Dirac fermion features [8] and quantum spin Hall effects [22] much like graphene. Moreover, the spin-orbit coupling of Si is much larger than that of carbon and opens large energy gaps at the Dirac cone establishing silicene as a promising 2D topological insulator, with its properties surpassing those of graphene. [9-11] Additionally, silicene has the advantage of better compatibility with current silicon-based technologies in microelectronics. [12] Thus, it can be stated that silicene is not just a continuation of graphene but rather a novel material beyond graphene.

Nevertheless, in contrast to graphene, pure free-standing silicene cannot be found in nature and it cannot be synthesised either. Another major difference between these two materials is

their structure: Silicene comprises a buckled structure where two atoms in the unit cell are displaced perpendicularly to the basal plane in comparison to the planar structure of graphene (*Figure 4.1*). [3, 4, 7, 8, 13] These differences originate from the dissimilarity in hybridisation between silicon and carbon.

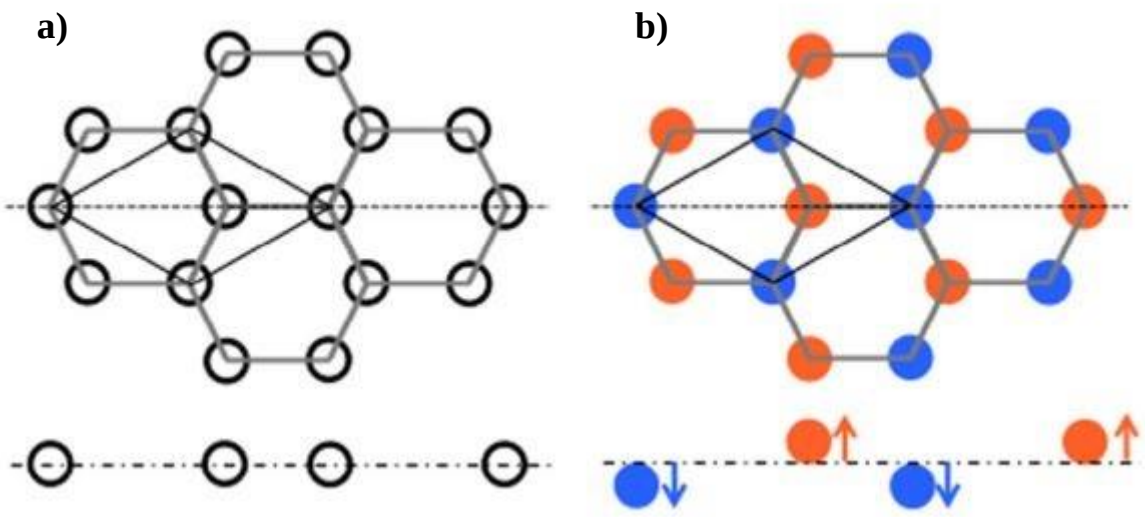

Figure 4.1 *Models of* ***a)*** *graphene – planar honeycomb structure,* ***b)*** *silicene – buckled honeycomb structure.*
Source: *[13]*

Silicon undergoes sp^3 hybridisation that results in a 3D tetrahedral configuration. The Si-Si bond length in silicene is bigger than the C-C bond in graphene, a phenomenon that prevents the full sp^2 hybridisation of the silicene structure. [14]

As mentioned above, free-standing silicene cannot be synthesised and for this reason a suitable substrate is required to grow it. It has been reported that 2D silicon structures can be grown on different substrates such as MoS_2, [15] $ZrBr_2(0001)$, [16] Ir(111) and [17] Au(110). [18] However, the majority of the reports are focused on growing silicene on silver single crystals and specifically Ag(111) and Ag(110). [7, 9, 12-14, 19-22] Silver has been found out to be the most appropriate substrate as: 1) Ag and Si lattice constants have a ¾ ratio, [23] 2) their close electronegativity values indicates small charge transfer between the silicon layer and the silver substrate [24] and 3) silver and silicon have a low tendency to alloy since the Ag/Si phase diagram shows no miscibility of the solid phases. [25] A major issue that has been addressed is the fact that joint experimental studies and DFT calculations have shown a non-negligible interaction between silicon and silver where the underlying substrate is hindering

the potentially fascinating electronic properties of the silicene. [9, 19, 26] Nonetheless, the extent of this interaction is still under debate.

The first report on experimentally grown silicene was presented by Lalmi *et al.* where they observed a $(2\sqrt{3}$ x $2\sqrt{3})$R30^o structure on Ag(111). [27] In succeeding studies it was discovered that silicene growth is highly dependent on deposition rate and substrate temperature and for this reason various other structures have been observed: (4 x 4), [7, 9, 13, 14, 19, 21, 22, 28, 29] $(\sqrt{13}$ x$\sqrt{13})$R13.9^o, [9, 13, 21, 22, 30] $(\sqrt{19}$ x $\sqrt{19})$R23.4^o, [31] (3.5 x 3.5)R26^o, [21] $(\sqrt{7}$ x $\sqrt{7})$R19.1^o [32] where many of these may co-exist. [13, 19, 21, 27] Each of these structures has been reported as a single silicon layer. Beyond one monolayer (ML) a $(4/\sqrt{3}$x $4/\sqrt{3})$ structure emerges which remains stable at higher coverages and has been proposed as "multilayer silicene". [9, 21, 33] High resolution Scanning Tunnelling Microscope (STM) images have revealed that silicene structures on Ag(110) are in the form of isolated nanoribbons [34] while on Ag(111) it is a continuous, almost defect free, sheet of silicene. [27]

The (4 x 4) structure is by far the most examined structure and it has been agreed that is the most stable epitaxial structural arrangement of the silicon atoms on Ag(111). [13] (4 x 4) is the only structure that it can appear as a single phase depending on the growth conditions. In a structural model presented by Lin *et al.* [35] and Vogt *et al.* [22] by combining DFT calculations and I-V curves from LEED they showed that there are 18 silicon atoms in the unit cell, comprising a honeycomb lattice, 6 of them are displaced upward with respect to the remaining 12 Si atoms. (*Figure 4.2*) In the same model, substrate relaxation was important in order to fully characterise the structure and it is shown that silver atoms in the first two substrate layers are also shifting upward perpendicularly to the surface. Thus, this structural model which has been convincingly established describes that the (4 x 4) silicene structure is buckled and that the interface couplings between the silicene layer and the Ag(111) substrate are not negligible.

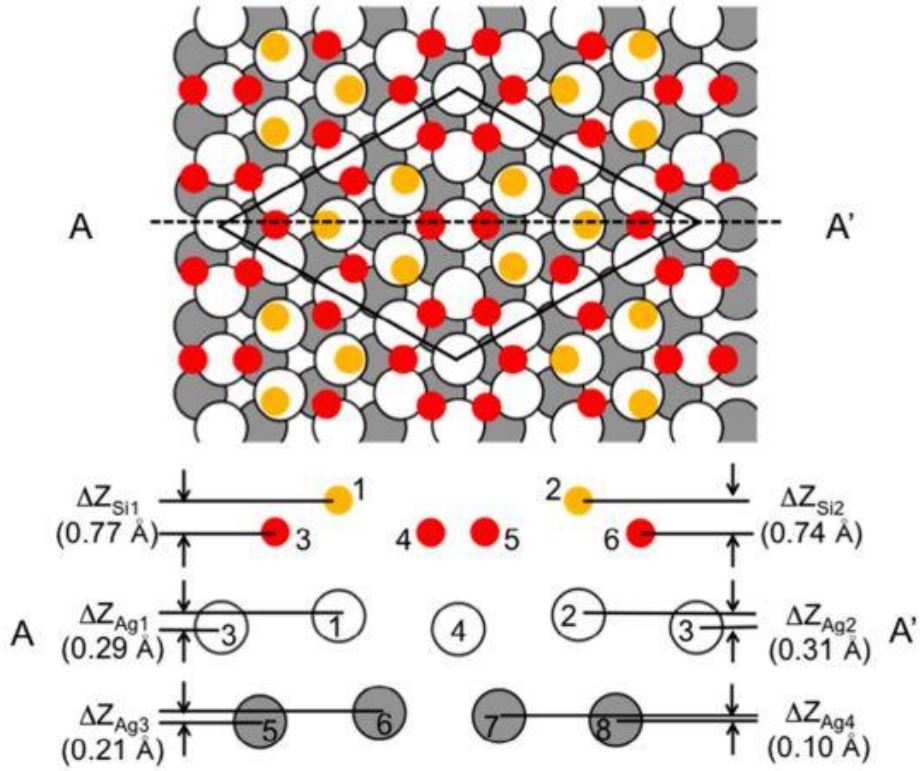

Figure 4.2 *Top and side views of the best-fit structural model for the (4 x 4) structure. The side views depict the positions of the atoms in a basal plane marked as an AA' line*
Source: *[35]*

Although, there has been enough evidence and detailed information on the grown structures, it still remains unclear from probe microscopy data what the preferred structure is. Also, a further limitation with STM data is the lack of information on the Ag substrate directly underneath the silicene layer.

Recently, Curcella *et al.* published a paper, where they determined the atomic structure of the (4 x 4) silicene phase through Grazing Incidence X-Ray Diffraction (GIXRD) measurements and DFT calculations at the growth temperature. They analysed several Fractional Order Rods (FORs) resulting from scattering from the (4 x 4) structure. [33] However, no CTRs were included in the analysis and their study was performed at 570 K compared to the study presented here that was analysed at room temperature.

The aim of this Chapter is the investigation and growth of silicene structures on Ag(111) and the precise interaction of the substrate at room temperature (25 ^{o}C) by deriving a detailed structural model through surface x-ray diffraction (SXRD) measurements. Knowledge of the precise structure of the silicene layer and its interaction with the Ag substrate will be crucial to understanding the electronic properties of the 2D material.

4.2. Experimental Procedure

Silicene synthesis and SXRD experiments were carried out at the I-07 beamline at Diamond Light Source.

The synthesis of silicene on Ag(111) was performed in a series of interconnected ultrahigh-vacuum (UHV) chambers equipped with LEED optics. The surface of Ag(111) crystal was cleaned through three cycles of argon ion sputtering ($4x10^{-5}$ Torr, 20 min) and annealing (450 ^{o}C, 40 min). The confirmation of a clean Ag(111) surface was obtained through LEED images after sharp LEED (1 x 1) spots were acquired. The deposition of Si was carried out by e-beam evaporation from a silicon rod heated to 240 ^{o}C temperature for 60 and 75 minutes employing a Specs electron bombardment evaporator with an integrated flux monitor, to maintain a constant deposition rate. The temperature was monitored by a thermocouple located between the sample and the filament.

LEED spot intensities were extracted from LEED images using the ImageSXM analysis software written by Dr. Steve Barrett from University of Liverpool with the help of LEEDpat software analysis. [36]

Silicene was synthesised under UHV conditions and characterised *in situ* with SXRD. For the SXRD experiments an X-Ray beam of 20 keV of energy was established and a grazing incidence of 0.3^{o}. The surface coordinates for Ag(111) were a = b = 2.887 Å, c = 7.076 Å, $\alpha = \beta = 90^{o}$ and $\gamma = 120^{o}$. For the collection of structure factor data for structure analysis the IgorPro program (Wavemetrics, Lake Oswego, OR, U.S.A.) was used.

Fitting analysis of Fractional Order and Crystal Truncation Rods was accomplished with the use of the ROD program. [37]

4.3. Structure Characterisation by LEED

LEED was the primary technique employed to optimise the growth conditions and, afterwards, characterise the silicene structures grown on Ag(111).

In *Figure 4.3* LEED images of *a)* clean Ag(111) surface and *b)* with deposited silicene are presented at 60 eV energy. The deposition of Si atoms clearly leads to extra spots in the diffraction pattern. The complex LEED pattern in *Figure 4.3.b.* hints the presence of multiphase structures with large unit cells. The substrate spots originating from Ag(111) surface were brighter than the silicene superstructure spots, as the scattering power of Si is considerably smaller than that of Ag, rendering it extremely difficult to extract any significant LEED-IV curves. For this reason, images from 25 to 100 eV energies with a 5 eV interval were obtained in order to enable us to identify each structure.

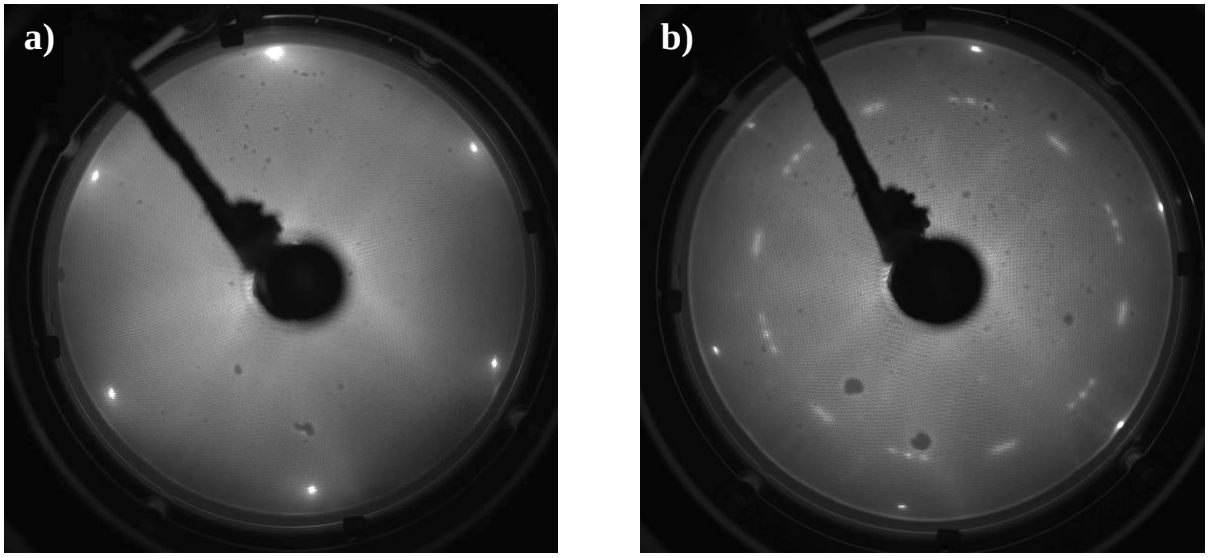

Figure 4.3 *LEED images of* ***a)*** *Pure Ag(111) surface and* ***b)*** *Silicene on Ag(111)*
Growth conditions: *T = 240 °C, deposition time = 60 min, flux = 1.50 nA*
Energy: *60 eV.*

We observed various superstructures that depend on the growth conditions for Si deposition. The deposition rate was controlled by the temperature of the sample. At a 240 °C temperature and deposition time of 60 minutes with a 1.50 nA flux two co-existing structures were identified. (*Figure 4.4.)*

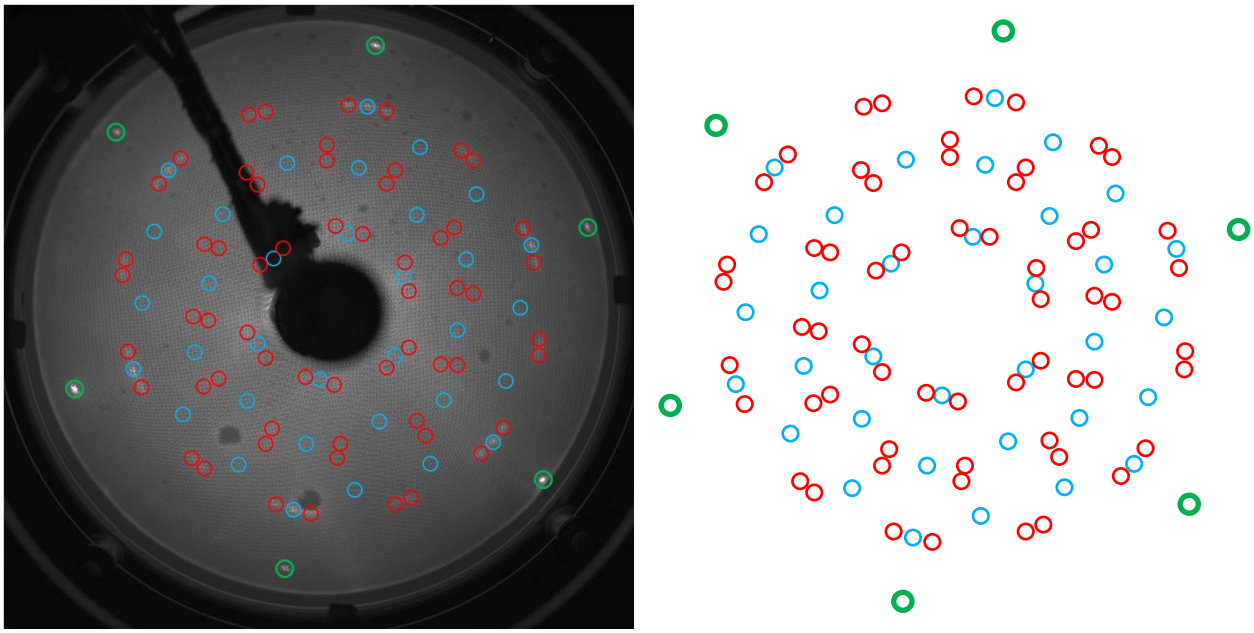

Figure 4.4 *LEED pattern of two co-existing silicene structures on Ag(111)*
Si deposition conditions: T = 240 ºC, t = 60 min, flux = 1.50 nA
LEED Energy = 60 eV
Legend: O Ag, O 4 x 4, O $(\sqrt{13} \times \sqrt{13})R13.9^{o}$

By observing all eleven acquired LEED images we mapped every spot associated with the (4 x 4) structure. The coordinates are presented in *Table 4.1* and therefore we can verify the presence of this structure. The second structure was more complex and more difficult to identify. Judging by the phase diagram of Arafune *et al.* [21] and based on the growth conditions, we assign the second structure to $(\sqrt{13}\text{x}\sqrt{13})\text{R13.9}^{o}$.

LEED Spot	Coordinates		LEED Spot	Coordinates		LEED Spot	Coordinates	
	h	k		h	k		h	k
(3 0)	0.77	0.02	(3 -1)	0.76	-0.24	(2 0)	0.5	0.02
(0 3)	0.00	0.79	(-1 -2)	-0.26	-0.53	(0 2)	0.01	0.51
(-3 3)	-0.75	0.77	(1 -3)	0.25	-0.77	(-4 1)	-1.02	0.23
(-3 0)	-0.77	-0.01	(2 -3)	0.51	-0.77	(-3 -1)	-0.75	-0.25
(0 -3)	0.01	-0.77	(1 1)	0.26	0.29	(-1 -3)	-0.25	-0.75
(3 -3)	0.77	-0.77	(-1 2)	-0.26	0.55	(1 -4)	0.25	-0.99
(-3 1)	-0.78	0.24	(-2 1)	-0.53	0.27	(3 -4)	0.75	-1.01
(-3 2)	-0.76	0.54	(-1 -1)	-0.27	-0.29	(4 -1)	1	-0.25
(-2 3)	-0.51	0.78	(1 -2)	0.26	-0.52	(3 1)	0.76	0.25
(-1 3)	-0.25	0.80	(-2 2)	-0.5	0.51	(1 3)	0.26	0.76
(1 2)	0.26	0.52	(-2 0)	-0.49	0.01	(-1 4)	-0.25	1.01
(2 1)	0.53	0.27	(0 -2)	0.01	-0.47	(-3 4)	-0.74	1.01

Table 4.1 *Structure coordinates for the (4 x 4) Silicene structure obtained by ImageSXM*

With increase of the deposition time by 10 minutes, more spots start to appear in the LEED images along with those associated with the two aforementioned structures. The points on the LEED images associated with these structures have become fainter, indicating the formation of multilayer silicene. (*Figure 4.5*) Structure analysis from Image SXM determined that these spots are associated with an emerging $(4/\sqrt{3}\text{x } 4/\sqrt{3})$ structure layer. The coordinates for this structure are presented in *Table 4.2*

LEED Spot	**Coordinates**	
	h	**K**
1	0.43	0
2	-0.01	0.44
3	-0.43	0.44
4	-0.43	-0.01
5	0	-0.44
6	0.44	-0.43

Table 4.2 *Structure coordinates for the* $(4/\sqrt{\mathbf{3}}$ *x* $4/\sqrt{\mathbf{3}})$ *Silicene structure obtained by ImageSXM*

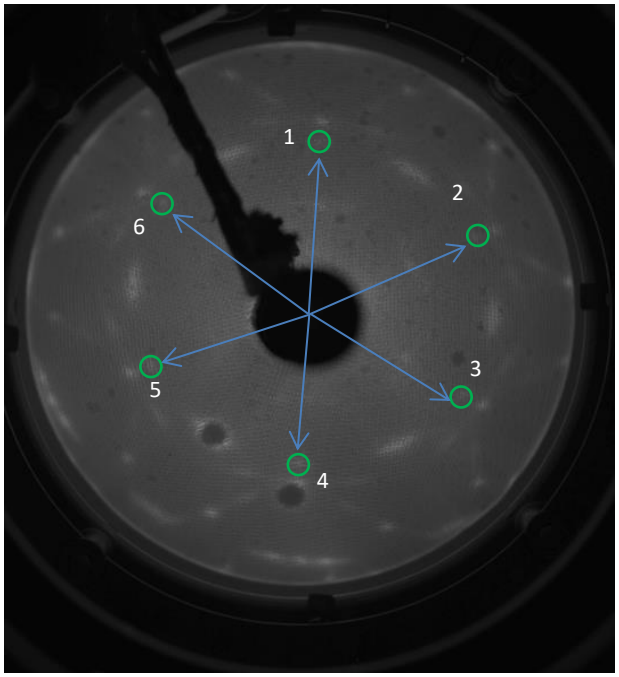

Figure 4.5 *LEED image after 70 minutes Si deposition at 240 ºC. Green spots indicate the* $(4/\sqrt{\mathbf{3}}$ *x* $4/\sqrt{\mathbf{3}})$ *emerging structure. Energy: 50 eV*

These results are in agreement with those presented in the literature, where they show that at a lesser deposition time two co-existing structures are present: (4 x 4) and ($\sqrt{13}$x$\sqrt{13}$)R13.9º at monolayer coverage. [13, 14, 19, 21, 22, 33] Moreover, at a higher deposition time, a different structure appears which is attributed to the formation of a second layer of silicene formed by islands of ($4/\sqrt{3}$x $4/\sqrt{3}$) structure. [21, 33] It can be concluded that the greater the deposition time, the higher the complexity of the analysis becomes and thus, the structures at a smaller deposition time were preferable for subsequent analysis. Finally, we have simulated the three observed silicene structures via the LEEDpat program and presented them in *Figure 4.6*.

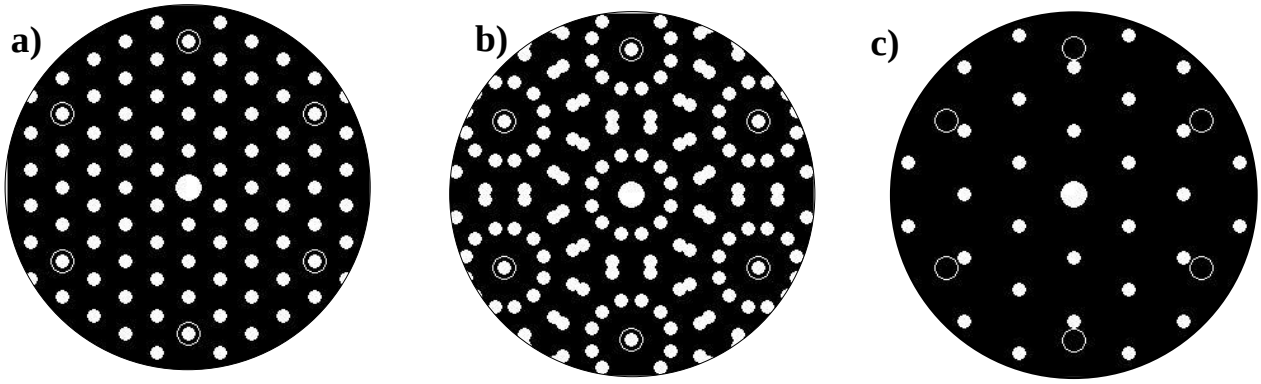

Figure 4.6 *Simulated LEED images from LEEDpat. The open white circles are attributed to the Ag(111) substrate. Closed with circles are the respective silicene structures. a) (4 x 4) and b) ($\sqrt{13}$ x $\sqrt{13}$)R13.9º structures and c) ($4/\sqrt{3}$ x $4/\sqrt{3}$)*

4.4. Surface X-Ray Diffraction Analysis

This section focuses solely on the (4 x 4) structure as determined in *Section 4.3.* The reasons for this are that this structure has been the most studied one owing to being assured to be the most stable epitaxial structural arrangement of the silicon atoms on the Ag(111) and the fact that (4 x 4) is the only structure that can appear as a single phase. Moreover, it is easier to analyse compared to the $(\sqrt{13}\ \text{x}\ \sqrt{13})\text{R}13.9^{o}$ structure that contains two rotational domains. Due to the high resolution of the of the SXRD technique, scattering exclusive to the (4 x 4) structure can be separated to any scattering originating from another structure, despite the presence of other structures.

4.4.1. Pure Ag(111)

In order to better understand the influence of silicene to the underlying substrate, the CTRs of the pure silver surface were fit first. For the fitting process, the top Ag layers and the respective in-plane Debye-Weller factors were left as free parameters.

The CTR fitting analysis showed an *inwards* relaxation of the top three Ag layers. In *Figure 4.7* the CTR fits are shown the summary of them is presented in *Table 4.3*.

Ag Layer	**Displacement / Å**	**Displacement Percentage**	**In-Plane D-W Factor / Å²**	**Out-of-Plane D-W Factor / Å²**
Top	-0.014 ± 0.003	(-0.586 ± 0.16) %	0.263 ± 0.02	1.028 ± 0.09
Second	-0.009 ± 0.003	(-0.361 ± 0.12) %	0.262 ± 0.03	0.375 ± 0.09
Third	-0.004 ± 0.002	(-0.183 ± 0.09) %	0.169 ± 0.02	0.088 ± 0.02

Table 4.3 *Summary of the parameters obtained following the fits of the CTRs for clean Ag(111) surface.*

The displacement values of the top three Ag layers are in good agreement with the literature. [38, 39]

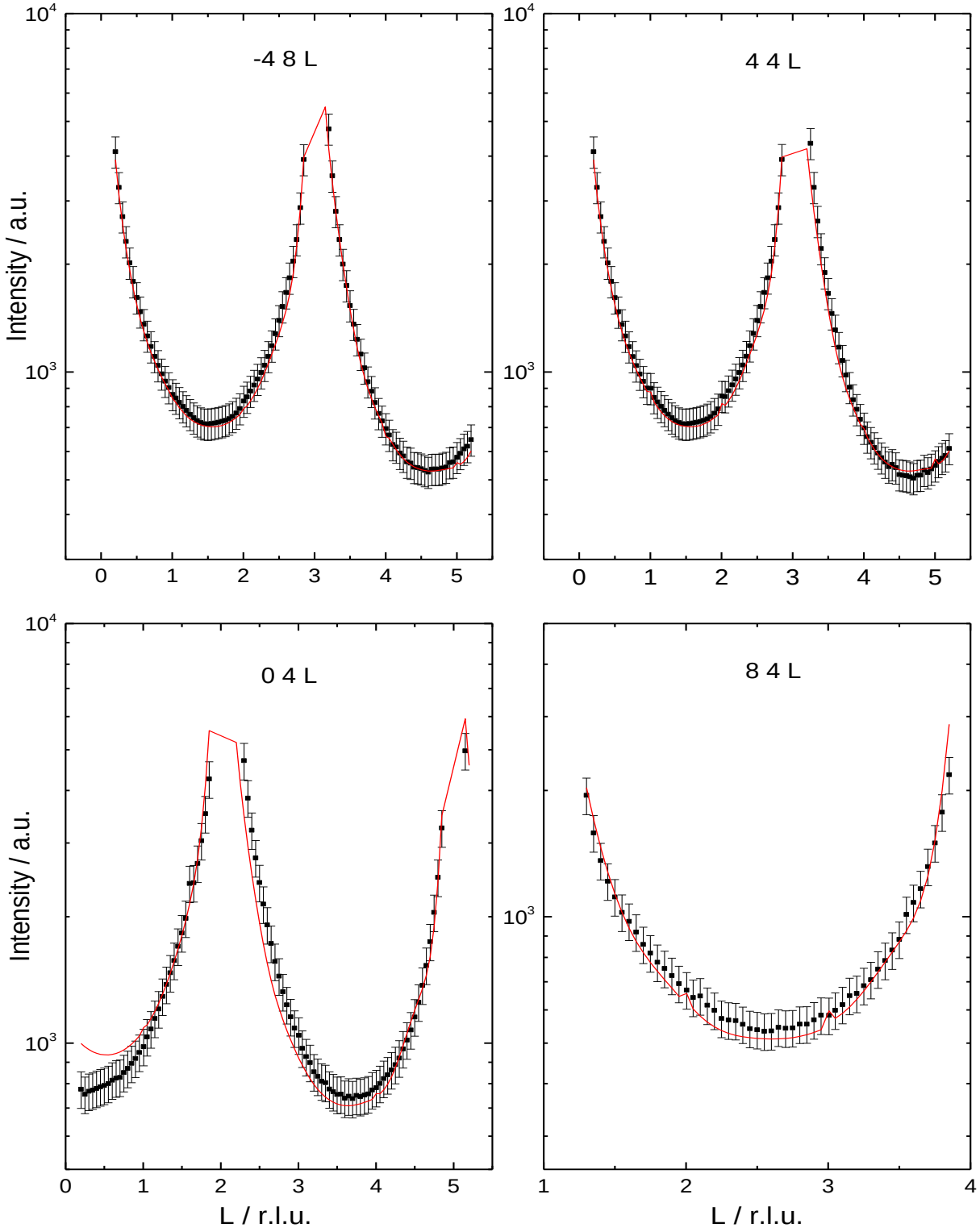
-4 8 L
4 4 L
0 4 L
8 4 L
Intensity / a.u.
L / r.l.u.

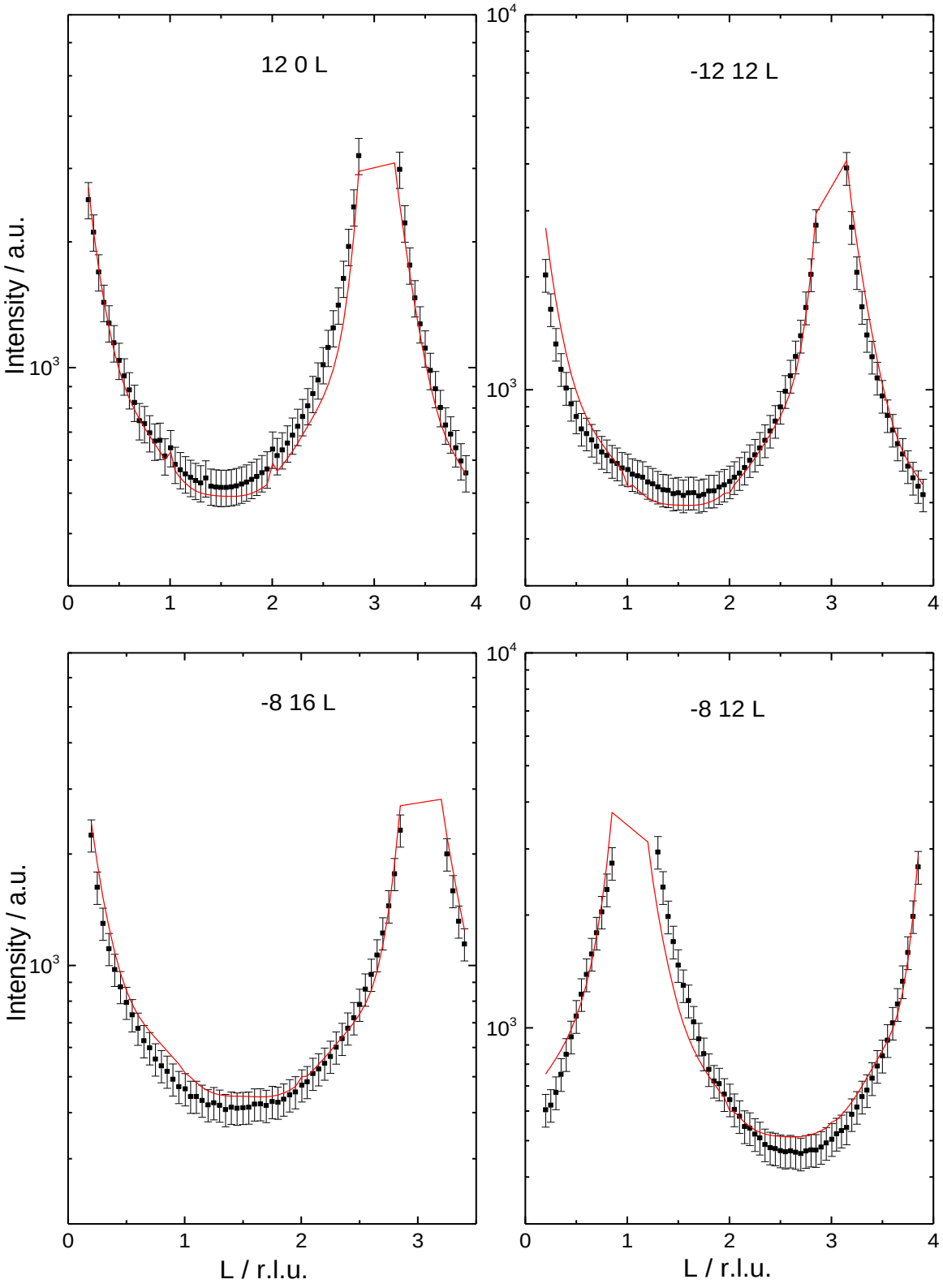

Figure 4.7 *Comparison between experimental data (black dots with error bars) and the theoretical fit data (continuous red line) along eight crystal truncation rods for clean Ag(111) surface.*

4.4.2. In-plane scans

In-plane scans along the h and k directions were obtained to observe any scattering peaks occurring from the silicene structures and more specifically from the (4 x 4). In *Figures 4.8* and *4.9* an in-plane scan along the k axis on pure Ag(111) and on Si/Ag(111) are presented for comparison to emphasise the peaks that occur as a result of the grown silicene.

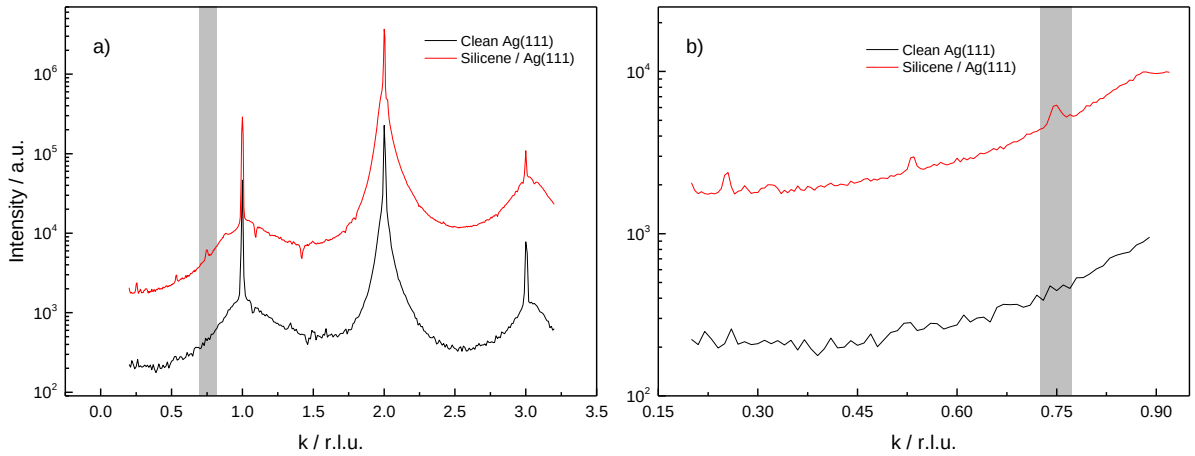

Figure 4.8 a) *In-plane scans (h=0) along the k direction comparison between the clean surface and Si/Ag(111).* ***b)*** *Smaller scale to exhibit the rising peak at k = 0.75 due to the (4 x 4) structure.*

As depicted in *Figures 4.8a* and *4.9a*, the intensity of the diffraction peaks originating from the Ag(111) surface found at integer values (e.g. k = 1, 2, etc..) dominate the measured signal. This occurrence is due to the fact that the scattering power of Si is significantly smaller than Ag and therefore, any peaks that result from silicene are comparatively small.

Additionally, scans along the (h, 0), (h, k), and (-h, -k,) were also recorded. Peaks due to the (4 x 4) structure were detected at (0.75, 0), (0, 0.75), (0.75, 0.75) and (0.75, -0.75) (*Figure 6.10*). All the aforementioned scans were recorded at l = 0.8.

Finally, other peaks due to the (4 x 4) structure were observed at k = 0.25 and k = 0.50 (*Figure 4.10*), while arising peaks found at k = 0.28 and k = 0.55 (*Figure 4.9b*), are attributed to the existence of the $(\sqrt{13}x\sqrt{13})R13.9^{o}$ structure.

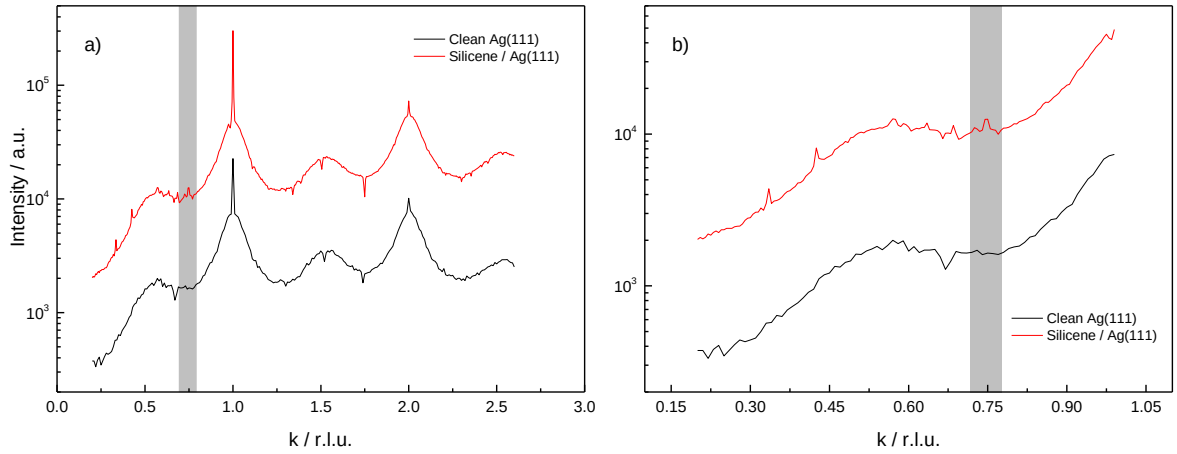

Figure 4.9 a) *Scan comparison along the hk direction between the clean surface and Si/Ag(111).* ***b)*** *smaller scale to empasise the rising peak at h=k = 0.75 due to the (4 x 4) structure.*

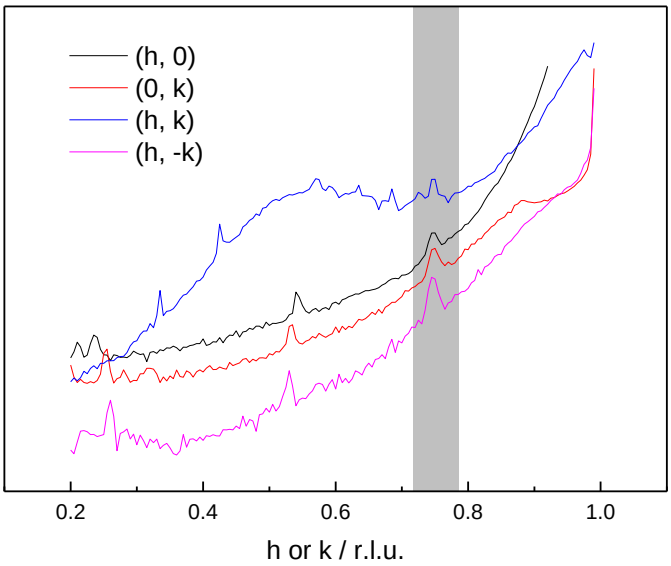

Figure 4.10 *Scans along the h or k direction of the Silicene/Ag(111) system. All four scans reveal a peak at 0.75 caused by the (4 x 4) structure.*

An in-plane map of the reciprocal space for the (4 x 4) silicene structure has been simulated via WinRod program and presented in *Figure 4.11*. The program has multiplied the reciprocal positions by a factor of 4 due to the (4 x 4) structure, e.g. the position at (0.75, -0.75) is the (3. -3). It can be clearly seen that the superstructure peaks at integer values of 3, which correspond to 0.75 are most prominent and for this reason can be observed during the in-plane scans.

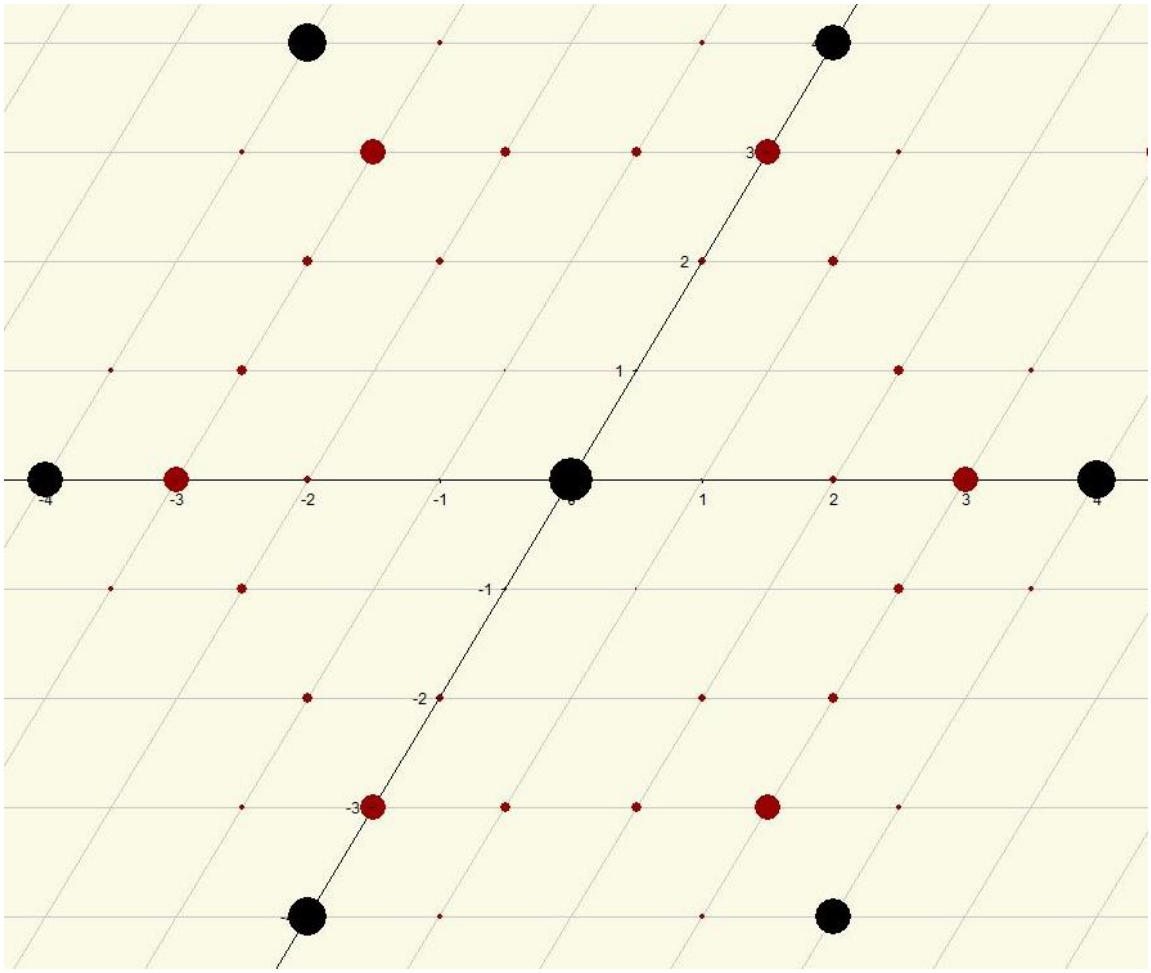

Figure 4.11 *In-plane map of the reciprocal space for the (4 x 4) silicene reconstruction. Red and black circles indicate the position of superstructure peaks for silicene and Ag(111) respectively.*

4.4.3. *In situ* Silicene deposition study

After observing a peak intensity during an h scan at the (h, 0, 0.8) position we examined the progression of the silicene layer growth. Having ascertained the existence of the peak due to the (4 x 4) structure, we fixed the h and k positions at 0.75 and 0 respectively and recorded the intensity change during *in situ* silicene deposition. The growth conditions remained similar (T = 240 ^{o}C, flux = 1.50 nA).

In *Figure 4.12* scans along the h axis in reciprocal space are shown at different time intervals. At the (0.75, 0, 0.8) position, at 0 minutes just before the deposition of silicene began there is no intensity with a small bump noted which is attributed to the background signal. As the deposition time is increased the formation of a peak and the increase in intensity become more prominent with the development of a full peak being observed at 55 minutes. At 70

minutes the intensity of the peak has been stabilised. This saturation of intensity is indicative of the formation of a full silicene monolayer.

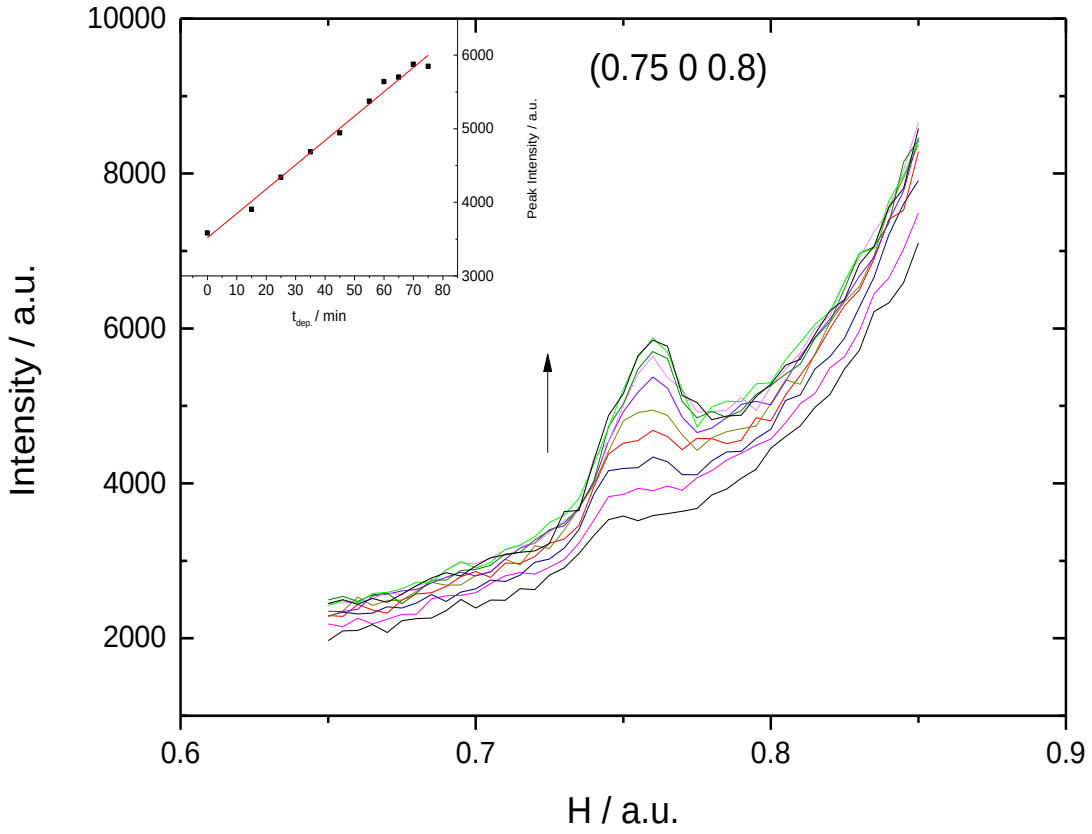

Figure 4.12 *Scans measured through the (h, 0, 0.8) direction with increasing deposition time of Si with the intensity of the (0.76, 0, 0.8) peak with increasing deposition time (inset graph).*
Deposition conditions: T =240 ºC, flux = 1.50 nA

The deposition rate was calculated at 0.014 ML / min. The linear deposition rate is consistent with the report of Vogt et al. [22] which was at 0.016 ML / min and they similarly generated a (4 x 4) structure but nevertheless without any additional structures present. Despite the similar growth conditions, a single (4 x 4) structure could not be observed through LEED images; this phenomenon confirms the difficulty and sensitivity of silicene growth.

It should be stated that at 70 minutes deposition time under same growth conditions, a different structure appeared on LEED images. Therefore, it can be postulated that firstly, one hour is required in order to obtain a full silicene monolayer under these particular growth conditions and then, only after the completion of a full monolayer consisting of two co-existing structures, the (4 x 4) and the $(\sqrt{13}$ x $\sqrt{13})$R13.9º, a third structure, the $(4/\sqrt{3}$x $4/\sqrt{3})$ begins to develop.

4.4.4. Fractional Order Rods (FORs)

Rocking scans were performed at superstructure peak positions. These peaks were found at intervals in reciprocal space of ¾. In order to simplify the analysis, we multiplied them by a factor of four because the study was performed with respect to the (4 x 4) structure. These rocking scans were obtained at the (6 -3 L), (3 -6 L), (0 -3 L), (-3 6 L), (3 -3 L) and (3 3 L) positions. The rocking scans which were measured along the L direction at intervals of L values were fit to a Lorentzian curve to produce the Fractional Order Rods (FORs). An example of such fit is presented in *Figure 4.13*.

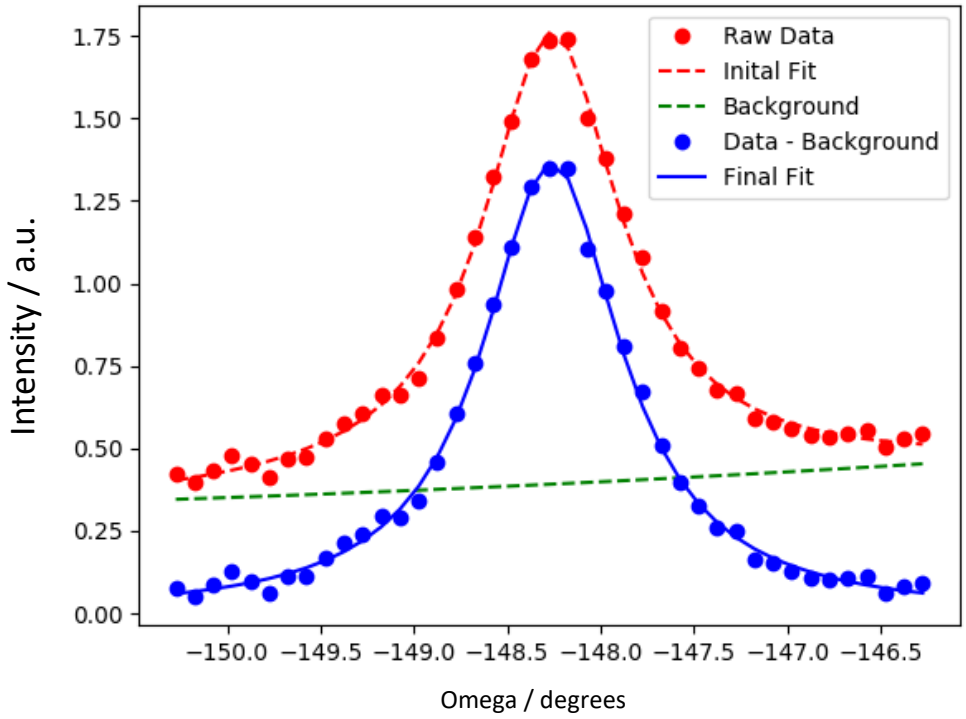

Figure 4.13 *Rocking scan performed at the (0 -3 0.5) superstructure position at room temperature*

Curcella *et al.* measured rocking scans at the (4 x 4) superstructure peaks at substrate temperatures of 520 and 570 K, [33] in comparison to this study where the rocking scan measurements were performed at room temperature substrate. Following the peak integration, the intensity of all the FORs was fit with the ROD program. [37]

For the fitting analysis, the scale factor, the roughness value, β, the vertical displacement of the top three Ag layers along with the in-plane and out-of-plane Debye-Waller factors for both the Si and surface Ag atoms were left as free parameters and allowed to vary. The Ag atoms in the fourth and fifth layers were fixed in their bulk positions. Finally, the Si layer was

included in the fit model file as an adlayer. For the final rocking scans the error was calculated through the integration of the curves.

Initially, the planar silicene model structure which was first proposed by Kawahara *et al.* [13, 19] was tested. This analysis produced a poor fit to the data, giving $\chi^2 = 14.34$. Afterwards, the model of Feng *et al.* [29] was investigated and despite the improvement of the reduced χ^2 value to 5.43, this was still considered a large value.

After that, the model presented by Lin *et al.*, [35] Vogt *et al.*, [22] and Curcella *et al.* [33] was examined. It is worth mentioning that, to date, this has been the most universally accepted model. This model gave the best fits to our data as shown in *Figure 4.14* producing a reduced χ^2 value of 1.848.

The good fit of this model to the experimental data is used to propose a structural model as discussed in *Section 4.5.*

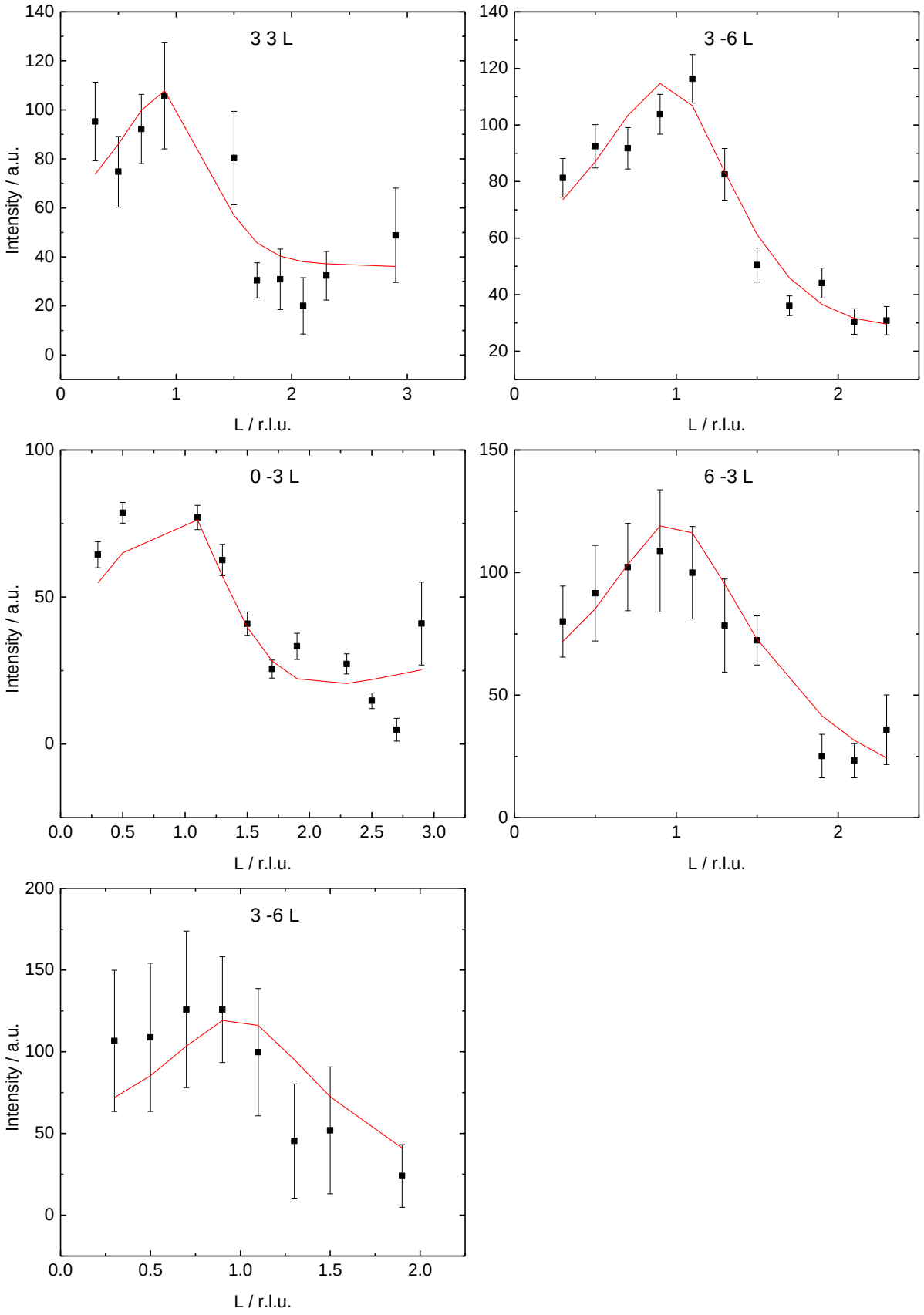

Figure 4.14 *Comparison between experimental data (black dots with error bars) and the theoretical fit data (continuous red line) along five superstructure rods.*

4.4.5. Specular Crystal Truncation Rod (CTR)

On a subsequent step, we focus on the analysis of the specular CTR, which, even though is not sensitive to in-plane atomic positions and not exclusively specific to the (4 x 4) structure, in contrast to the FORs, it gives a good indication of the average Si and Ag layer positions. The specular CTR was fitted keeping the parameter's values obtained from the FORs analysis and produced a χ^2 value of 1.579. (*Figure 4.15*).

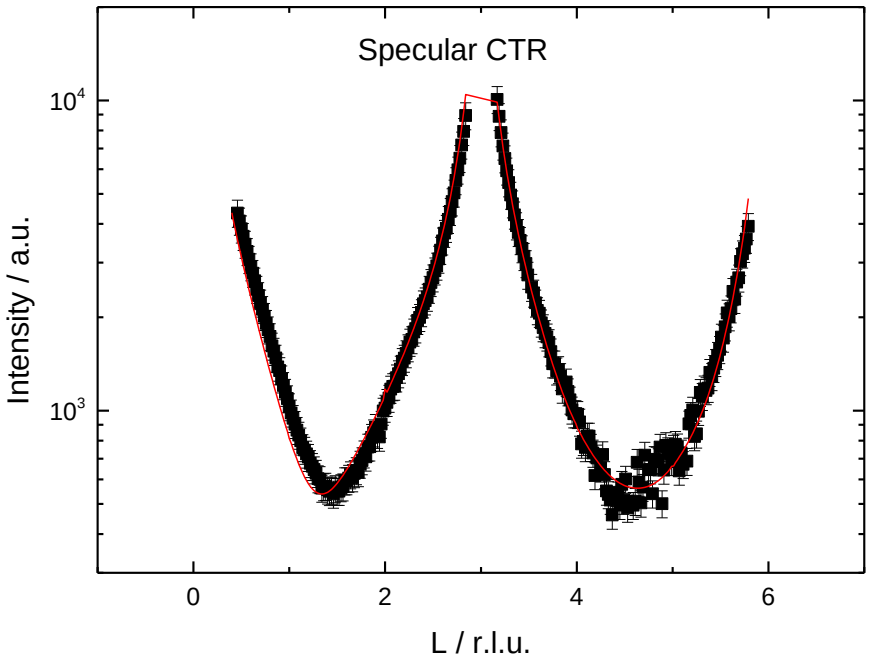

Figure 4.15 *Comparison between experimental data (black dots with error bars) and the theoretical fit data (continuous red line) along the specular CTR for the Si/Ag(111) system.*

4.4.6. Non-Specular Crystal Truncation Rods

Following thisξ, the parameters file from the FORs and the specular CTR fitting analysis was incorporated to the ROD program and was applied for the non-specular CTR analysis. Ten CTRs were also measured in order to obtain a complete structural model for silicene. It must be noted at this point, however, that while the FORs are exclusively associated with the (4 x 4) silicene structure, the CTRs contain the contributions of the second structure, the $(\sqrt{13}\ x\sqrt{13})R13.9^o$ and thus, a non-perfect fit is expected.

All ten CTRs were fitted simultaneously by the ROD program, keeping the parameters' values obtained from the FORs fitting analysis and produced a χ^2 value of 1.787 after incorporating a 10 % error to the data. (*Figure 4.16*).

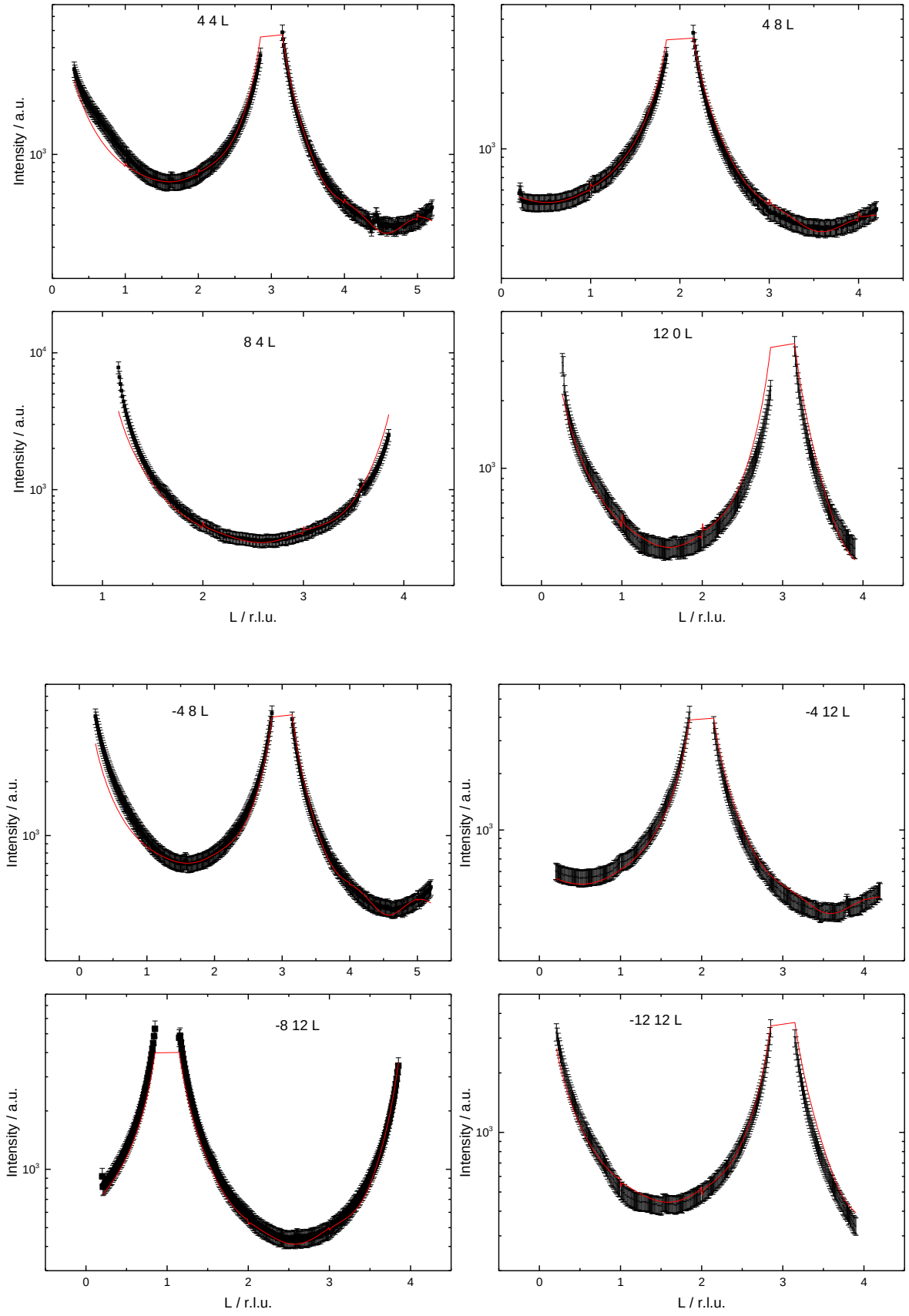

Figure 4.16 *Comparison between experimental data (black dots with error bars) and the theoretical fit data (continuous red line) along ten crystal truncation rods.*

4.5. Structural Model

Based on the SXRD fitting analysis, presented in the previous sections a structural model has been determined. (*Figure 4.17*)

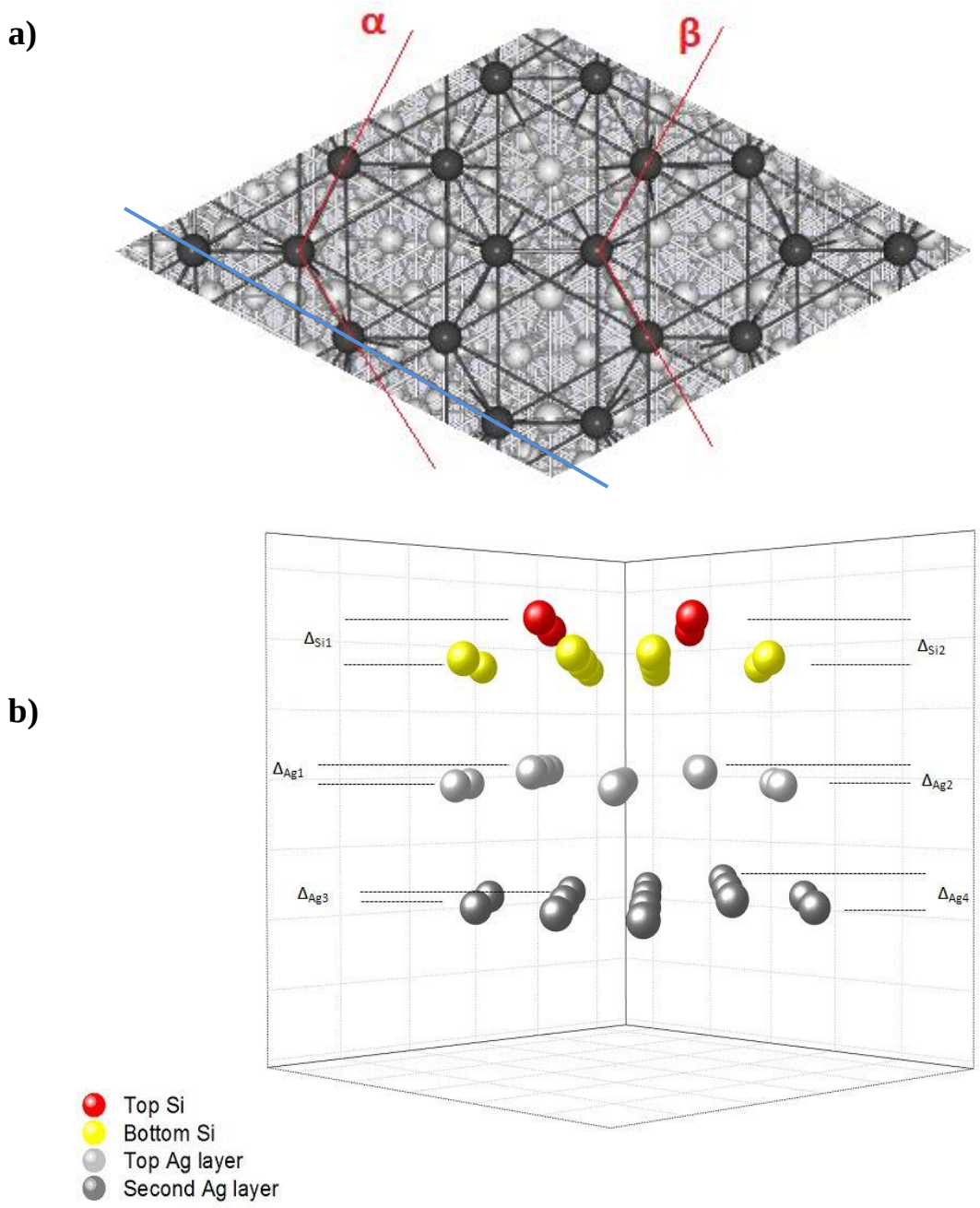

Figure 4.17 *Schematic representation of the structural model of silicene on Ag(111)*
a) *Top view and* ***b)*** *side view of the (4 x 4) structure.*

First of all, the results confirmed the existence of 1 ML of silicon on top of the Ag(111) substrate. Moreover, there is further evaluation of the buckling of the silicene layer with an interlayer spacing of $\Delta_{Si1/Si2}$ = 0.76 Å and since the latter value is small, we can attribute it to the buckling of the Si layer, instead of a bilayer of silicene. The unit cell of silicene comprises of eighteen atoms that constitute an hexagonal honeycomb lattice, where six Si atoms are displaced upwards with respect to the plane formed by the other twelve atoms (*Figure 4.17a*). This observation is consistent with the structural models that have been published in the literature. [13, 22, 33, 35]

Layer	**In-Plane D-W Factor / Å^2**	**Out-of-Plane D-W Factor / Å^2**
Si	3.96 ± 1.64	7.98 ± 2.20
Top Ag	0.415 ± 0.01	2.35 ± 0.04
Second Ag	0.076 ± 0.01	1.19 ± 0.05
Third Ag	0.025 ± 0.01	0.847 ± 0.04

Table 4.4 *Summary of the Debye-Waller factors for each separate layer obtained from the rocking scans and the Crystal Truncation Rods for Si on Ag(111).*

Another interesting observation was that deposition of silicon results in a deformation of the top two Ag layers. The silver atoms of the top layer that are located directly below the top Si atoms (red spots in *Figure 4.17b*) are pulled upwards off the plane of the layer with a spacing of Δ_{Ag1} = 0.188 Å and Δ_{Ag2} = 0.198 Å resulting in an *outwards* relaxation in comparison with the *inwards* relaxation occurring at clean Ag(111) [38]. This occurrence is also observed on the second Ag layer with a spacing of Δ_{Ag3} = 0.0012 Å and Δ_{Ag4} = 0.0014 Å. On the other hand, the third Ag layer was downwards displaced by Δ_{Ag3} = 0.0085 Å and at the fourth layer and beyond the contribution and effects become negligible.

The Debye-Waller factor (DWF) is a term which describes how thermal fluctuations extinguish scattering intensity and create disorder as the atoms oscillate about their equilibrium positions. [40] Therefore, the large out-of-plane DWF values as opposed to their in-plane counterparts can be attributed to the distortion of the silicene and the top two Ag layers. (*Table 4.2*). For the same reason, the DWF values are larger than the respective ones for the clean Ag(111) which were presented in *Table 4.4.* Also, the surface roughness was calculated at β = 0.29 indicating a smooth Ag(111) surface.

	T / K	d_{Si} / Å	$\Delta_{Si1/Si2}$	$\Delta_{Ag1/2}$ / Å	$\Delta_{Ag3/4}$ / Å	θ_1/θ_2
DFT – GGA [41]			0.75	0.4		110°/118°
LEED [19]	550	2.29 – 2.31	0.77/0.74	0.29/0.31	0.10/0.21	
DFT – GGA / GIXD [33]	520 / 570	2.30 – 2.33	0.77	0.25/0.27	0.05/0.24	108.6°/111.1°
SXRD	298	2.29	0.76/0.76	0.19/0.20	0.001/ 0.001	110.1°/120.6

Table 4.5 *Comparison between structural model parameters obtained in this work from SXRD and those reported in the literature from LEED, from first principles DFT calculations and GIXD for Si/Ag(111). The parameters in question are 1) the temperature the measurements were taken, T 2) The silicene lattice constant, $d_{Si,}$ 3) The interlayer spacing between silicon atoms, $\Delta_{SiX,}$ and silver atoms, Δ_{AgX} and 4) the bond angles between silicon atoms.*

In *Table 4.5* different model parameters found in literature are summarised and are compared to the analysis reported in this Chapter. It is evident, that while the interlayer spacing between the top and bottom silicon atoms is in good agreement with the study of Curcella *et al.* [33], there are notable differences regarding the spacing between Ag atoms on the top two layers.

Our analysis revealed an interlayer spacing of $\Delta_{Ag1/2}$ = 0.19/0.20 Å for the top Ag layer and $\Delta_{Ag3/4}$ = 0.0012/0.0014 Å for the second layer. As mentioned in the introduction, the lattice constants of bulk silver and silicon have a ¾ ratio. Both elements have a closed pack face-centred cubic unit cell, where the nearest neighbour distance is calculated by $\frac{\alpha}{\sqrt{2}}$. The thermal expansion of an element is expressed as:

$$dL = L_0 \alpha \Delta T \quad (4.1)$$

where dL is the change of length, α the thermal expansion coefficient and ΔT the change in temperature. Taking into consideration the thermal expansion coefficients (*Table 4.6*), at the silicene growth temperatures, between 543 – 563 K, the two lattices match since three Si atoms correspond to four Ag atoms (*blue line – Figure 4.16a*).

	Lattice / Å	Thermal exp. coeff. α, x 10^{-6} / K^{-1}	Ref.
Ag bulk	4.085	18.9	[38]
Ag(111)	2.359	22.0	[38]
Si bulk	5.431	2.6	[42]
Silicene	3.860	-1.0, -5.3, -7.2	[43], [44], [45]

Table 4.6 *Comparison of lattices and thermal expansion coefficients α of bulk Ag and Si, Ag(111) and silicene.*

Therefore, for bulk Ag:

$$\frac{4.085\ \text{Å}+dL_{Ag}}{\sqrt{2}} = 2.888\ \text{Å}$$

And for bulk Si:

$$\frac{3}{4}\ \frac{5.431\ \text{Å}+dL_{Si}}{\sqrt{2}} = 2.882\ \text{Å}$$

We have calculated that the above two values match and for this reason silicene can grow on Ag(111). In our analysis, we waited for the Si/Ag(111) system to cool down to room temperature before performing the SXRD analysis presented previously. In *Table 4.6* the large difference in the thermal expansion coefficients between silver and silicon is presented. Hence, when cooled down, Ag contracts approximately seven times more than silicon. Therefore, this fact can explain why the buckling of the Ag atoms on the top two silver layers is smaller than the analysis of Curcella *et al.* [33] and why at the same time the buckling of the Si atoms at the silicene layer has not changed.

The bond angles in the silicon atoms were calculated at θ_1 = 110.1° and θ_2 = 120.6°. The values of the bond angles are very close to those in reported in the theoretical calculations [38] and suggest that the hybridisation of the system is closer to sp_2. Comparatively, in Curcella *et al.*, the bond angles are somewhat smaller (θ_1 = 108.6° and θ_2 = 111.1°).

4.6. Specular CTR Comparison

Further to the data already shown in the previous sections, two separate sets of CTR and FOR measurements were additionally taken. The first set was taken after 75 minutes of silicon deposition and the second set was taken after the Si/Ag(111) system was transferred in a thin layer cell and dipped in 0.1 M NaOH.

In *Figure 4.18* the specular CTR profile of both sets is compared with their counterparts of clean Ag(111) and silicene deposition of 60 minutes.

The shape of the CTR for 75 minutes deposition time closely resembles the profile of 60 minutes deposition time with the difference that the former contains oscillations along the profile. These oscillations are a further indication of the existence of a silicene multilayer as mentioned in *Sections 4.3.* and *4.4.3.* On the other hand, the shape of the CTR of silicene in 0.1 M NaOH is more similar to that of the clean Ag(111) rather than the silicene ones. These sets of data have been analysed but useful conclusions have not been extracted yet, as for the 75 minutes deposition time, it is very difficult to determine a structural model, due to the existence of multiple structures, which some of them contain rotational domains and different silicene layers.

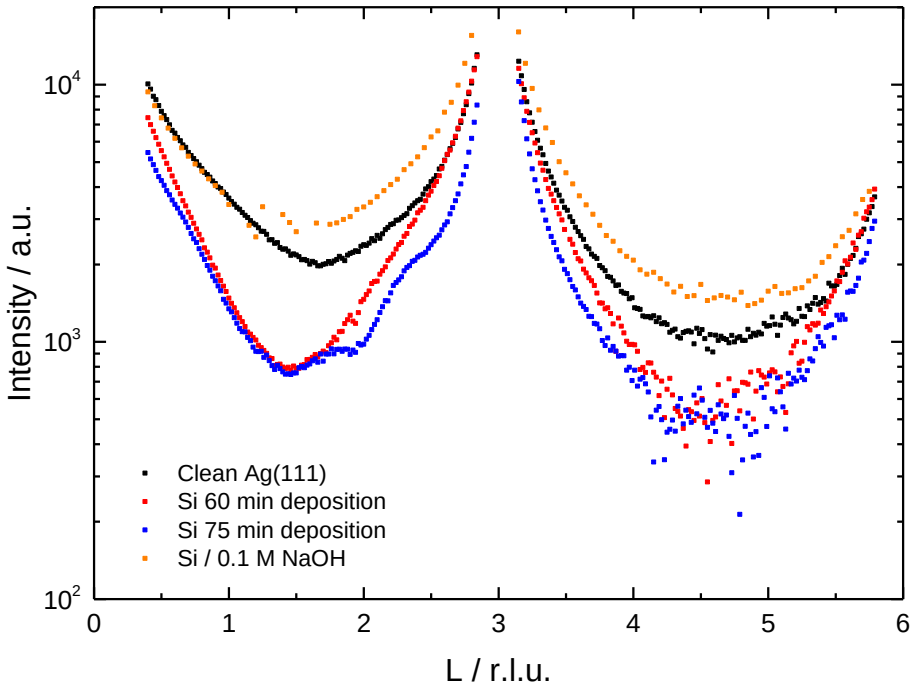

Figure 4.18 *Specular CTR profile of the clean Ag(111) surface (black), 60 minutes (red) and 75 minutes (blue) of Si deposition and in 0.1 M NaOH at -550 mV (orange).*

Regarding the measurements of silicene in 0.1 M NaOH, CTRs were recorded at three different potentials with respect to the potential window of sodium hydroxide and presented in *Figure 4.19*.

By comparing the three CTRs in 0.1 M NaOH, we notice an increase in intensity as the electrochemical potential is scanned towards more negative potentials. However, this increase is due to OH^- adsorption. [46] Despite the notable differences among the three CTRs, it must be mentioned again that their profile is more alike to the clean Ag(111) rather than the silicene. This is an indication that any deposited silicene on the Ag surface was lost during the transfer from the UHV chamber to the alkaline solution or that silicene was dissolved inside the alkaline solution. This was further confirmed by LEED images where no silicene spots had been observed.

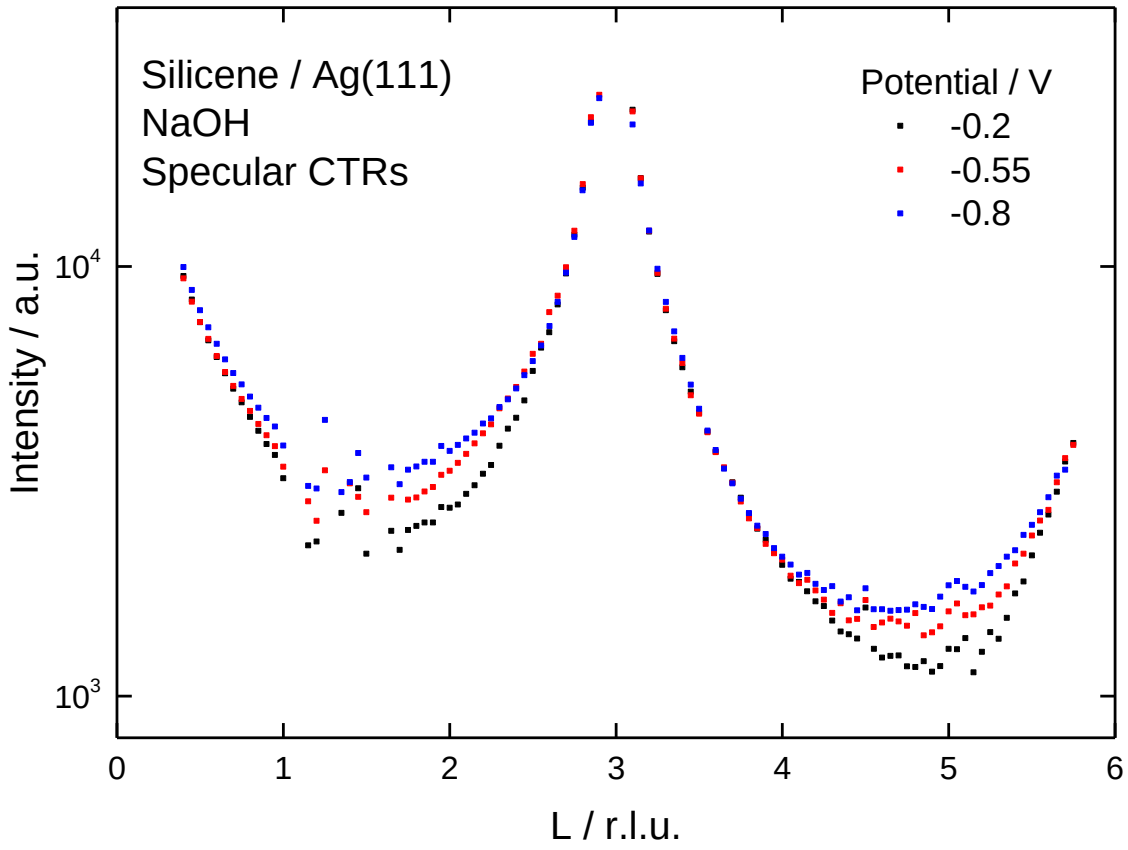

Figure 4.19 *Specular CTR profile of silicene in 0.1 M NaOH at -200 mV (black), -550 mV (red) and -800 mV (blue).*

Also, the increase in intensity observed between the clean Ag(111) CTR and the respective one in 0.1 M NaOH is due to the liquid layer since the latter experiment was performed in aqueous solution.

4.7. Summary

Silicene structures were successfully grown on the Ag(111) substrate. The Si/Ag(111) system is consisted of two co-existing structures at monolayer coverage, namely (4 x 4) and ($\sqrt{13}$ x$\sqrt{13}$)R13.9^{o} with a deposition rate of 0.014 ML / min. After completion of a full monolayer, a second layer comprised of a single ($4/\sqrt{3}$ x $4/\sqrt{3}$) structure is formed. Afterwards, we employed SXRD to probe in detail the atomic positions of the (4 x 4) structure, which is widely considered the most dominant structure of silicene and the easiest to model.

In conclusion, we have accurately determined the (4 x 4) silicene structure on Ag(111) substrate at room temperature. We have, also, verified that the (4 x 4) silicene layer corresponds to a buckled honeycomb layer consisting of eighteen silicon atoms in the unit cell, where six out of them are displaced perpendicularly relatively to the plane formed by the remaining twelve silicon atoms, as suggested initially by Vogt *et al.* [22], with an interlayer spacing of 0.76 Å. Moreover, we have further confirmed that the deposition of silicene has a clear effect on the surface of Ag(111) as it undergoes modifications that result in an *outwards* metal relaxation of specific atoms on the top two surface metal layers.

However, in comparison with a similar study [33] that was performed at the growth temperature of silicene instead of the room temperature there was a distinct difference. While the buckling at the silicene layer was the same, the interlayer spacing of the Ag atoms on the top two silver layers had smaller values. This was justified by taking into consideration the large difference of the thermal expansion coefficient between silver and silicon.

Finally, CTR measurements were also taken after silicene on Ag(111) was taken out of the UHV chamber and placed inside a thin layer cell containing 0.1 M NaOH. The CTR profile indicated that silicene had either evaporated during the transfer from UHV to the cell or dissolved inside the alkaline solution.

4.8. References

1. Geim, A.K., Science, **2009,** *324,* 1530-1534
2. Xu, M., Liang, T., Shi, M., Chen, H., *Chem. Rev.,* **2013,** *113,* 3766
3. Cahangirov, S., Topsakal, M., Aktürk, E., Şahin, H., Ciraci, S., *Phys. Rev. Lett.,* **2009,** *102,* 236804
4. Takeda, K., Shiraishi, K., *Phys. Rev. B,* **1994,** *50,* 14916-14922
5. Guzmán-Verri, G.G., Lew Van Yoon, L.C., *Phys. Rev. B,* **2007,** *76,* 075131
6. Bianco, E., Butler, S., Jiang, S., Restrepo, O.D., Windl, W., Goldberger, J.E., *ACS Nano,* **2013,** *7,* 4414-4421
7. Kara, A., Enriquez, H., Seitsonen, A.P., Lew Yan Voon, L.C., Vizzini, S., Aufray, B., Oughaddou, H., *Surface Science Reports,* **2012,** *67,* 1-18
8. Huang, S., Kang, W., Yang, L., *Appl. Phys. Lett.,* **2012,** *102,* 133106
9. Liu, C.-C., Feng, W., Yao, Y., *Phys. Rev. Lett.,* **2011,** *107,* 7680
10. Kane, C.L., Mele, E.J., *Phys. Rev. Lett.,* **2005,** *95,* 146802
11. Ando, Y., *J. Phys. Soc. Jpn.,* **2013,** *82,* 3045
12. Chen, L., Liu, C.C., Feng, B., He, X., Cheng, P., Ding, Z., Meng, S., Yao, Y.G., Wu, K.H., *Phys. Rev. Lett.,* **2012,** *109,* 056804
13. Takagi, N., Lin, C.L., Kawahara, K., Minamitani, E., Tsukahara, N., Kawai, M., Arafune, R., *Progress in Surface Science,* **2015,** *90,* 1-20
14. Oughaddou, H., Enriquez, H., Tchalala, M.R., Yildirim, H., Mayne, A.J., Bendounan, A., Dujardin, G., Ali, M.A., Kara, A., *Progress in Surface Science,* **2015,** *90,* 46-83
15. Chiappe, D., Scalise, E., Cinquanta, E., Grazianetti, C., van den Broek, B., Fanciulli, M., Houssa, M., Molle, A., *Adv. Mater.,* **2014,** *26,* 2096
16. Fleurence, A., Friedlein, R., Ozaki, T., Kawai, H., Wang, Y., Yamada-Takamura, Y., *Phys. Rev. Lett.,* **2012,** *108,* 245501
17. Meng, L., Wang, Y., Zhang, L., Du, S., Wu, R., Li, L., Zhang, G., Li, G., Zhou, H., Hofer, W.A., Gao, H.-J., *Nano Lett.,* **2013,** *13,* 685
18. Enriquez, H., Mayne, A.J., Kara, A., Vizzini, S., Roth, S., Lalmi, B., Seitsonen, A.P., Aufray, B., Greber, T., Belkhou, R., Dujardin, G., Oughaddou, H., *Appl. Phys. Lett.,* **2012,** *101,* 021605
19. Kawahara, K., Shirasawa, T., Arafune, R., Lin, C.-L., Takahashi, T., Kawai, M., Takagi, N., *Surf. Sci.,* **2014,** *623,* 25

20. Lalmi, B., Oughaddou, H., Enriquez, H., Kara, A., Vizzini, S., Ealet, B., Aufray, B., *Appl. Phys. Lett.,* **2010,** *97,* 45802
21. Arafune, R., Lin, C.L., Kawahara, K., Tsukahara, N., Minamitani, E., Kim, Y., Takagi, N., Kawai, M., *Surface Science,* **2013,** *608,* 297-300
22. Vogt, P., De Padova, P., Quaresima, C., Avila, J., Frantzeskakis, E., Asensio, M.C., Resta, A., Ealet, B., Le, G., *Phys. Rev. Lett.,* **2012,** *108,* 155501
23. Lubarda, V.A., *Mechanics of Materials,* **2003,** *35,* 53-68
24. Butler, K.T., Vullum, P.E., Muggerud, A.M., Cabrera, E., Harding, J.H., *Phys. Rev. B,* **2011,** *83,* 235307
25. Olesinski, R.W., Gokhale, A.B., Abbaschian, G.J., *Bulletin of Alloy Phase Diagrams,* **1989,** *10,* 635-636
26. Bernard, R., Borensztein, Y., Cruguel, H., Lazzeri, M., Prévot, G., *Phys. Rev. B,* **2015,** *92,* 045415
27. Lalmi, B., Oughaddou, H., Enriquez, H., Kara, A., Vizzini, S., Ealet, B., Aufray, B., *Appl. Phys. Lett.,* **2010,** *97,* 45802
28. Chiappe, D., Grazianetti, C., Tallarida, G., Fanciulli, M., Molle, A., *Adv. Mater.,* **2012,** *24,* 5088-
29. Feng, B., Ding, Z., Meng, S., Yao, Y., He, X., Cheng, P., Chen, L., Wu, K., *Nano Lett.,* **2012,** *12,* 3507
30. Meng, L., Wang, Y., Zhang, L., Du, S., Wu, R., Li, L., Zhang, G., Li, G., Zhou, H., Hofer, W.A., Gao, H.-J., *Nano Lett.,* **2013,** *13,* 685
31. Švec, M., Hapala, P., Ondráček, M., Merino, P., Blanco-Rey, M., Mutombo, P., Vondráček, M., Polyak, Y., Cháb, V., Martín, J.A., Gago, P., Jelínek, P., *Phys. Rev. B,* **2014,** *89,* 201412
32. Resta, A., Leoni, T., Barth, C., Ranguis, A., Becker, C., Bruhn, T., Vogt, P., Le Lay, G., *Sci. Rep.,* **2013,** *3,* 2399
33. Curcella, A., Bernard, R., Borensztein, Y., Resta, A., Lazzeri, M., Prevot, G., *Phys. Rev. B,* **2016,** *94,* 165438
34. Léandri, C., Le Lay, G., Aufray, B., Girardeaux, C., Avila, J., Davila, M.E., Asensio, M.C., Ottaviani, C., Cricenti, A., *Surf. Sci.,* **2005,** *574,* 9–15.
35. Lin, C.-L., Arafune, R., Kawahara, K., Tsukahara, N., Minamitani, E., Kim, Y., Takagi, N., Kawai, M., *Appl. Phys. Express,* **2012,** *5,* 45802

36. LEEDpat, Version 4.2, utility by K.E. Hermann (FHI) and M.A. Van Hove (HKBU), Berlin / Hong Kong, **2014,** see also http://www.fhi-berlin.mpg.de/KHsoftware/LEEDpat/index.html
37. Vlieg, E., *J. Appl Cryst.*, **2000,** *33*, 401-405
38. Soares, E.A., Leatherman, G.S., Diehl, R.D., Van Hove, M.A., *Surf. Sci.*, **2000,** *468*, 129-136
39. Soares, E.A., Nascimento, V.B., de Carvalho, V.E., de Castilho, C.M.C., de Carvalho, A.V., Toomes, R., Woodruff, D.P., *Surf. Sci.*, **1999,** *419*, 89-96
40. Lipkin, H.J., *Physics of Debye-Waller Factors*, **2004,** eprint arXiv:cond-mat/0405023
41. Enriquez, H., Kara, A., Mayne, A. J., Dugardin, G., Jamgotchian, H., Aufray, B., Oughaddou, H., *J. Phys.: Conf. Ser.*, **2014,** *491*, 012004
42. Yim, W.M., Paff, R.J., *J. Appl. Phys.*, **1974,** *45*, 1456-1458
43. Lew Yan Voon, L.C., Sandberg, E., Aga, R.S., Faraijan, A.A., *Appl. Phys. Lett.*, **2010,** *97*, 163114
44. Haung, L.-F., Gong, P.-L., Zeng, Z., *Phys. Rev. B,* **2015,** *91*, 205433
45. Ge, X.-J., Yao, K.-L., Lü, J.-T., *Phys. Rev. B,* **2016,** *94*, 165433
46. Jovic, B.M., Jovic, V.D., Stafford, G.R., *Electrochem. Comm.*, **1999,** *1*, 247-251

CHAPTER 5

Acetonitrile Effect on Single Crystal Electrodes

5.1. Introduction

The adsorption of small organic molecules on metal surfaces has always been an interesting research area in both fundamental studies and industrial application. [1-3] Furthermore, the adlayer structure and conformation of these molecules and the interaction of weak donor ligands with metal surfaces plays a major part of research in electrochemical surface science. [4, 5] In addition, there has been considerable interest in carrying out electrochemical reactions in non-aqueous systems, because of their stability over a wide potential range. [6]

Over the past years the structure and composition features of various organic adlayers on single crystal electrodes have been investigated. [7] These studies involve molecules such as carboxylic acids, [8, 9] amino acids, [10-12] aromatic anhydrides [13] and closed ring structures. [14-16]

Acetonitrile (AcN) (CH_3CN) is one of the most widely used polar aprotic solvents in electrochemistry since it is miscible in aqueous solutions, has a high dielectric constant and a wide potential window of stability. [17] In addition, acetonitrile is a mildly dissociative organic solvent comprised of polar, covalent bonds and functions primarily as a weak Lewis base since acetonitrile possesses a filled orbital containing a lone electron pair which is not involved in bonding and thus, can bond with charge-withdrawing sites such as transition metal centres. [18]

Acetonitrile and other R-CN complexes have been reviewed by Storhoff and Lewis [19] where it was mentioned that it has two possible types of coordination to a metal atom: via the lone pair orbital of nitrogen or via the π orbital of the nitrile group as shown below, where M is a

transition metal. However, it has also been reported another perpendicular orientation of acetonitrile with the methyl group pointing toward the metal surface. [20]

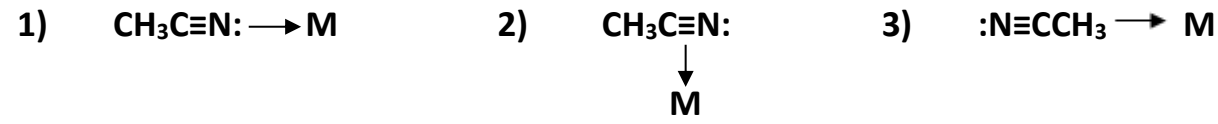

Acetonitrile has been used in surface science as a spectroscopic probe to characterise properties of numerous systems. It can strongly solvate noble metal cations, mainly Cu^+, Ag^+ and Au^+ and Pt^+. The aforementioned metal ions have the ability to strongly back donate their electrons into the cyanide group of the molecule which is a process also very useful in the organometallic complex formation of transition metals. [21]

The effect of acetonitrile in aqueous solutions has been extensively studied on Pt (111), [20, 22, 23] and polycrystalline platinum. [24] In Pt(111) it was found out that acetonitrile molecules orient with the C_3 axis perpendicular with respect to the crystal surface. [20] At positive potentials the nitrile group (CN-) of the molecule faces the crystal surface while at negative potentials the orientation swaps and the methyl group (CH_3-) of the molecule is in contact with the surface of the crystal. [20] Also, adsorbed cyanide ions have been identified in Raman spectroscopy studies. [25]

Not much structural information has been provided for the Cu(111) and Ag(111) single crystals however. Mernagh *et al.* through Raman spectroscopy reported the evidence of cyanocopper(I) species in the interfacial region in 10 M acetonitrile under the presence of perchlorate anions because acetonitrile molecules had decomposed into cyanide and methyl. [26] On the other hand, this phenomenon was not observed for the Ag(111) crystal. [26] No structural information has been provided for these two systems. On polycrystalline gold electrodes through *in situ* vibrational spectroscopy it was presented that two types of adsorption of acetonitrile molecules in the interface; one where the acetonitrile molecules are perpendicular along the C_3 axis on the crystal surface and bonded through the nitrile group and the other are molecules forming a hydrogen bond to chemisorbed water molecules on the surface. [27]

In fundamental electrochemistry the supporting electrolyte plays an integral role in most electrochemical reactions. [21] Their influence on electrochemical processes and reactions are mainly characterised by the strength of their adsorption on metal electrodes. [28] The

adsorption / desorption process of supporting electrolyte ions are involved in important electrochemical processes such as surface reconstruction, surface oxidation and underpotential deposition. [21, 28, 29] The latter process will be explained more thoroughly in Chapter 6.

Perchlorate anions (ClO_4^-) are of special interest, as together with F^- are considered to be the least adsorbing of all the studied anions [28] and in fact, on gold surfaces, perchlorate anion is the weakest adsorbate. [31] Perchloric acid has often been employed as a reference in adsorption studies of other stronger supporting electrolytes such as sulphuric acid. [32] However, the studies on the adsorption of ClO_4^- have been scarce and controversial. [33] In the beginning, perchlorate anions were considered inert that cannot adsorb on single crystal electrodes or, at least, the adsorption was believed to be weak enough to neglect it. [34] Moreover, another significant issue regarding perchloric acid for fundamental electrochemistry has been the reduction of perchlorate to chloride anions, resulting in contamination of the solution that may inhibit the selective adsorption of the perchlorate ions. [35, 36]

Studies of perchlorate anion adsorption has been performed on various metal electrodes such as Pt, [36-40] Cu, [41-43] Ag, [44, 45] Au, [46-49] and Rh. [50]

The cyclic voltammogram of Cu(111) in pure 0.1 M $HClO_4$ is shown in *Figure 5.1a.* The CV depicts a featureless double layer region with a cathodic current associated to hydrogen evolution reaction (HER) that starts to increase at -0.6 V vs. SCE and at potentials more positive than -0.05 V vs. SCE, copper dissolution takes place with an increasing anodic current. [43] Similarly, the CV of 0.1 M $HClO_4$ in Ag(111) (*Figure 5.1b*) does not show any significant features with only a cathodic peak at -0.6 V vs. SCE due to HER, another cathodic peak at 0.28 V caused by the electrochemical deposition of Ag^+ ions formed during the anodic scan and at 0.2 V vs. SCE the anodic dissolution of Ag is observed. [45]

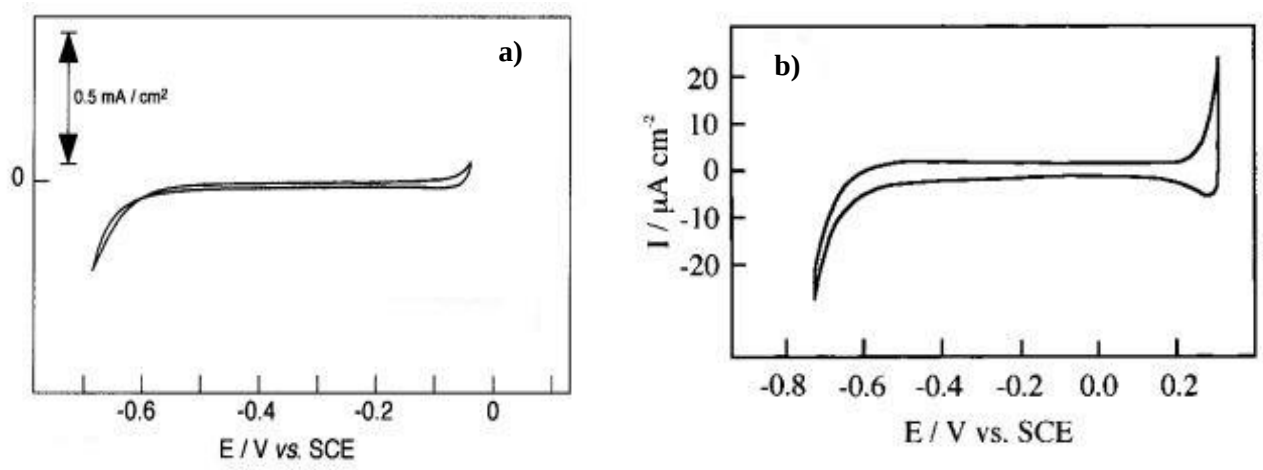

Figure 5.1 *Cyclic Voltammogram of a) Cu(111) and b) Ag(111) in 0.1 M $HClO_4$.*
Scan rate: 5 mV s^{-1}.
Sources: [42], [45]

In this Chapter the adsorption and the bonding of acetonitrile to two different metal single crystal electrodes, namely Cu(111) and Ag(111) in presence of perchloric acid is examined via electrochemical and surface x-ray diffraction techniques.

5.2. Experimental Procedure

Surface x-ray diffraction measurements were performed on the I-07 beamline of the Diamond Light Source in Didcot, Oxfordshire with photon energy of 18.5 keV and a grazing incidence angle of 0.3° employing the thin layer cell, a specifically modified electrochemical cell. Surface coordinates of a) the Cu(111) surface: a = b = 2.556 Å, c = 6.261 Å, α = β = 90°, γ = 120° b) the Ag(111) surface: a = b = 2.887 Å, c = 7.076 Å, α = β = 90°, γ = 120°.

The Cu(111) and Ag(111) crystals have been prepared as outlined in *Section 3.1* of *Chapter 3*. The X-Ray thin layer cell together with the single crystal serving as the working electrode included a silver/silver chloride reference electrode and a Cu or Ag wire, depending on the nature of the single crystal, as the counter electrode. All electrode potentials are reported with respect to the Ag/AgCl (3.4 M KCl) electrode (E = 0.21V vs. SHE).

5.3. Acetonitrile in Cu(111) in Perchloric Acid

5.3.1. Electrochemical Characterisation

Cyclic voltammograms of the Cu(111) single crystal electrode were obtained in 0.1 M $HClO_4$ at various acetonitrile concentrations and are shown in *Figure 5.2*. The first potential scan in each CV was started in the negative direction from 0.2 V to -0.16 V and then cycled to 0.2 V again. The scans were obtained in the thin layer x-ray electrochemical cell and thus, there are expected contributions from the sides and the back of the crystal in the current responses but nonetheless, the CVs can be representative of the behaviour of the Cu(111) crystal.

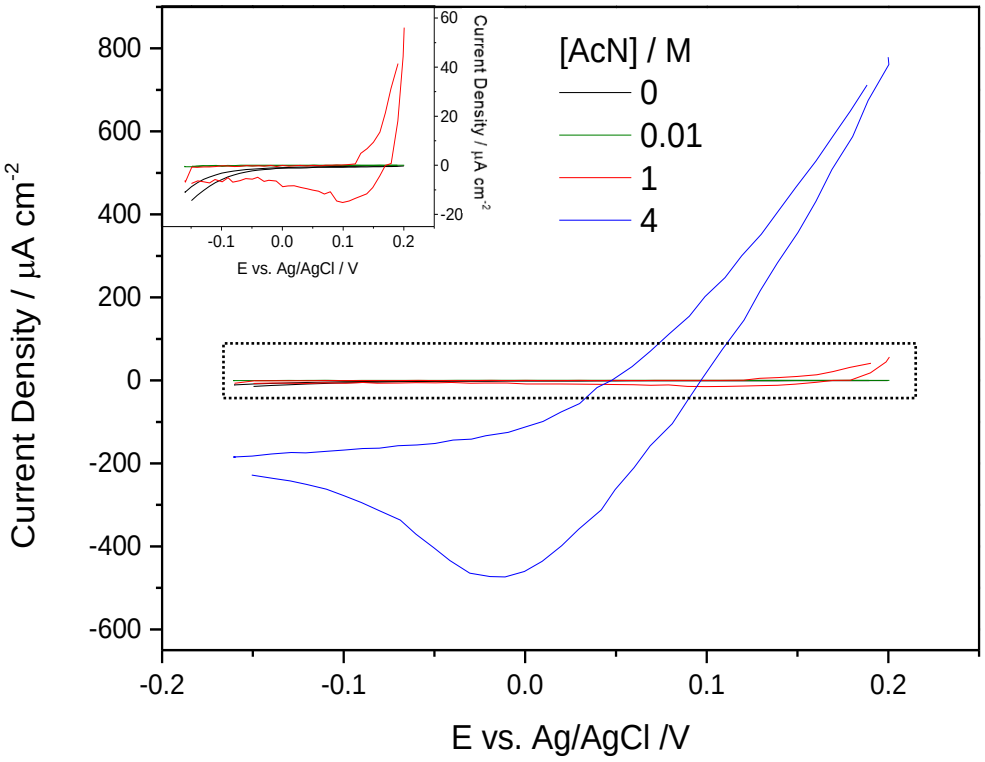

Figure 5.2 *Cyclic voltammograms of Cu(111) in 0.1 M $HClO_4$ in different acetonitrile concentrations. The inset graph shows an enlarged view of the dashed frame.*
Scan rate: 5 mV s^{-1}

In the absence of the organic molecule, a double layer region extends from 0.2 to 0 V. At potentials more negative than 0 V, hydrogen evolution occurs. In presence of 10 mM acetonitrile, the overall shape of the CV is almost the same as the respective one in pure perchloric acid. However, two prominent features are noticeable: firstly, the extension of the potential window and secondly, the electric charge involved in the double layer potential region becomes smaller because of the adsorption of the acetonitrile molecules, [51] but no obvious cathodic peaks were observed. Increase of acetonitrile to 1M and 4 M produced a

broad cathodic peak at 0.1 V and ~ 0 V respectively accompanied by a dissolution peak at 0.15 V and 0.05 – 0.2 V respectively (*Figure 5.2*). The anodic currents at the positive potentials are assigned to surface copper dissolution and consequently, the deposition peaks are assigned to copper re-deposition that have previously been complexed with the acetonitrile atoms. The cyclic voltammogram at 4 M resembles closely the CV reported by Mernagh *et al.* at 10 M acetonitrile, [26] thus it is suggested that the deposition peak observed in the CVs is caused by copper atoms bonded and complexed with cyanide ions after decomposition of the acetonitrile molecules.

In the following section SXRD data obtained in these solutions are analysed where the adsorption process will be thoroughly examined.

5.3.2. Surface X-Ray Diffraction Analysis

5.3.2.1. Crystal Truncation Rods (CTRs)

In order to obtain detailed atomic-scale information on the influence of acetonitrile on the surface structure of the Cu(111) electrode, Crystal Truncation Rods (CTRs) along the specular (0 0 L) and non-specular, (0 1 L) and (1 0 L), directions were measured for pure perchloric acid and all different acetonitrile additions at 200 mV and -160 mV which correspond to the positive and negative ends respectively of the CVs presented in *Figure 5.2*. The potentials were chosen to have the largest separation so that the greatest change could be observed.

All CTRs, specular and non-specular, were modelled at the same time. *Figures 5.3, 5.4, 5.5* and *5.6* show the comparison of each CTR between the two potentials at 0, 0.01, 1 and 4 M acetonitrile concentrations respectively. The solid line in every graph shows the fit to the data using a fit model including the expansion of the layers, the Debye-Waller factors (DWF), σ and distance of the layers. The coverage, Θ of each of the three copper layers was fixed at 1. Every data point presented was background subtracted. However, some data points have been omitted either due to the twinning effect which will be explained in *Section 5.4.2.4.* that were averaging the theoretical fit or due to artificial points from powder lines or because of strong background features providing negative atomic form factor. Each data point has a 10% assumed systematic error.

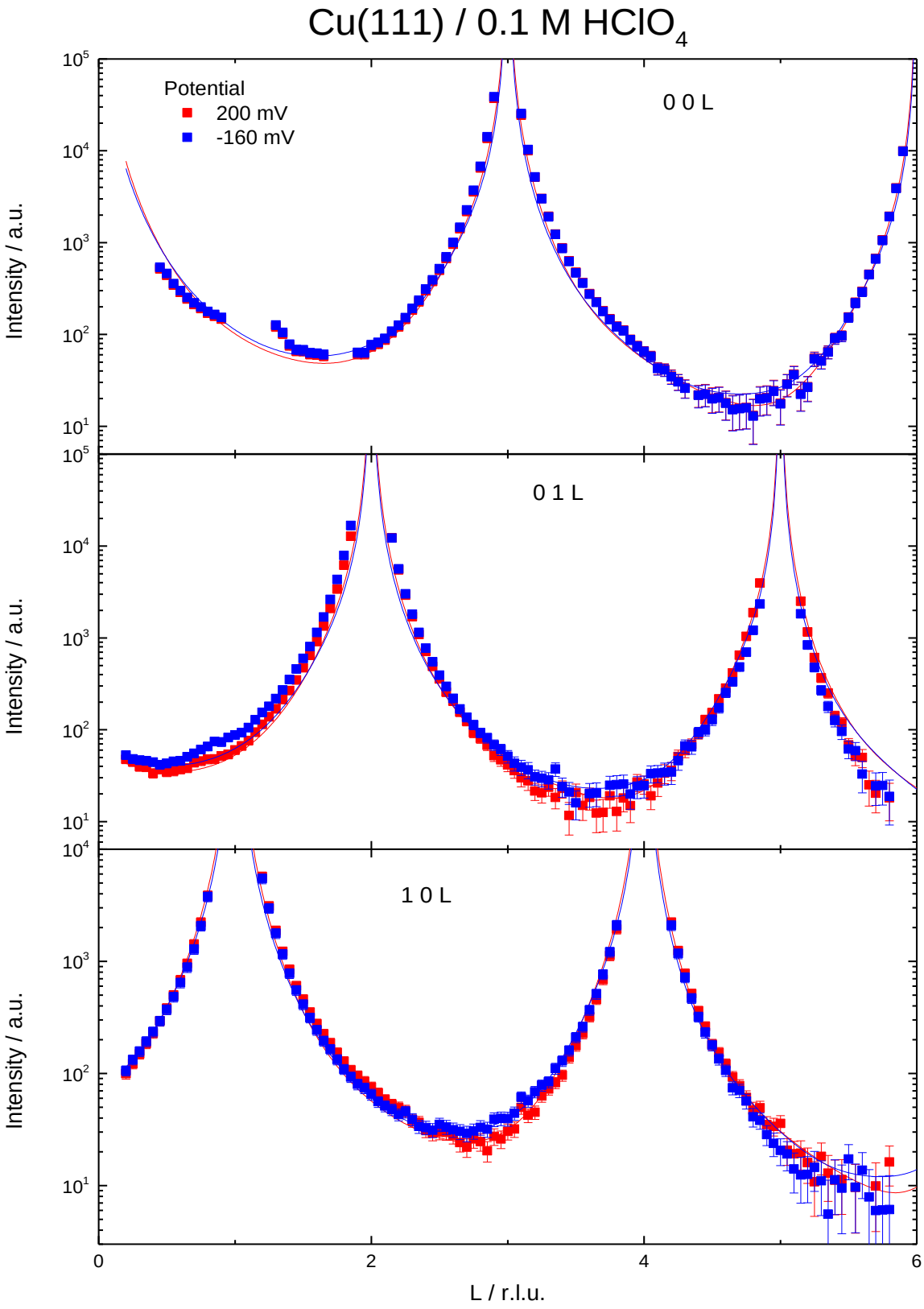

Figure 5.3 *Fits to specular (0 0 L) and non-specular (0 1 L) and (1 0 L) Crystal Truncation Rods for the Cu(111) / 0.1M $HClO_4$ system. The red and blue points correspond to the data measured at 200 and -160 mV respectively. The best fits to these are shown with the respective red and blue solid lines. Error bars include an assumed 10% systematic error.*

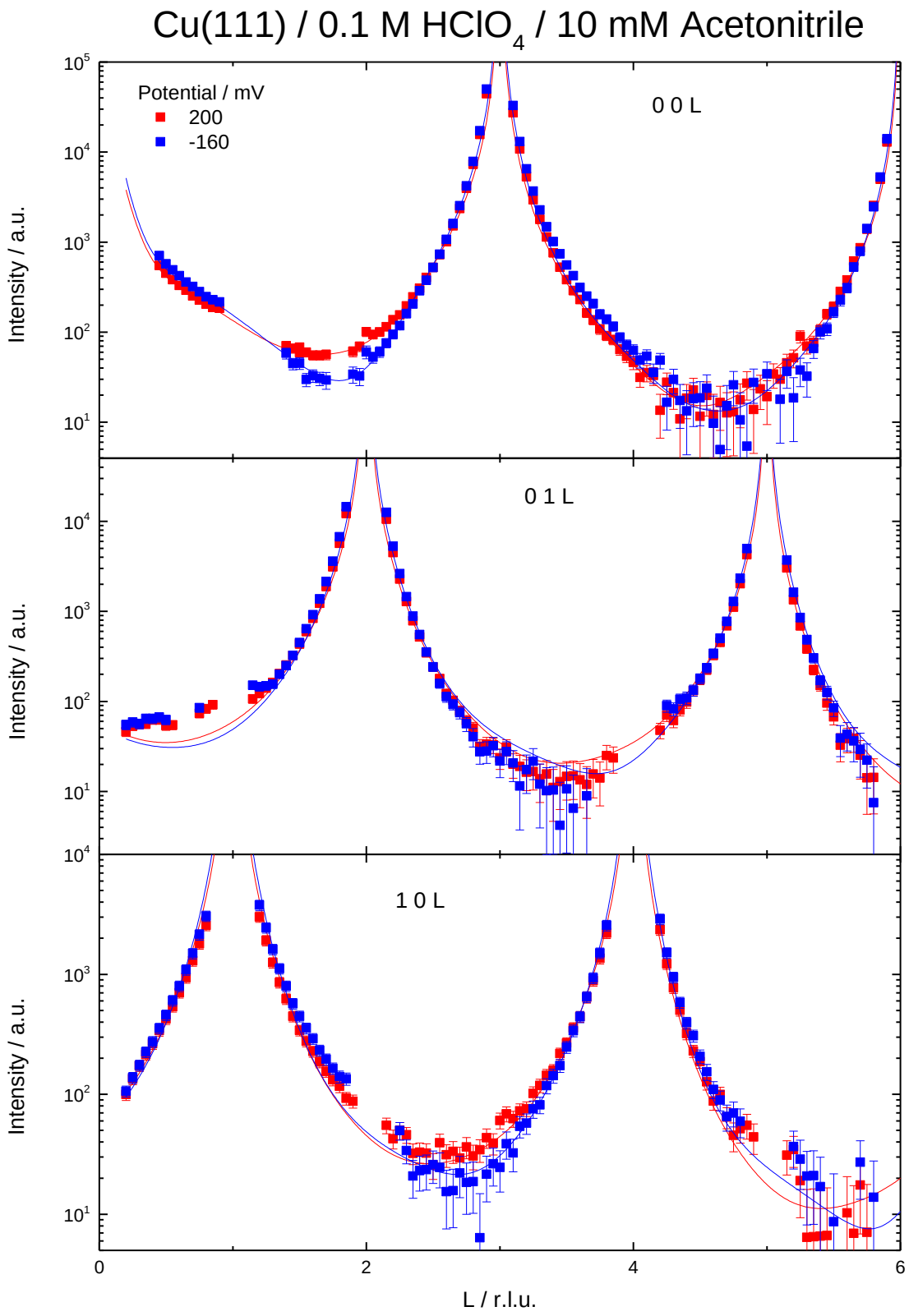

Figure 5.4 *Fits to specular (0 0 L) and non-specular (0 1 L) and (1 0 L) Crystal Truncation Rods for the Cu(111) / 0.1M $HClO_4$ / 10 mM Acetonitrile system. The red and blue points correspond to the data measured at 200 and -160 mV respectively. The best fits to these are shown with the respective red and blue solid lines. Error bars include an assumed 10% systematic error.*

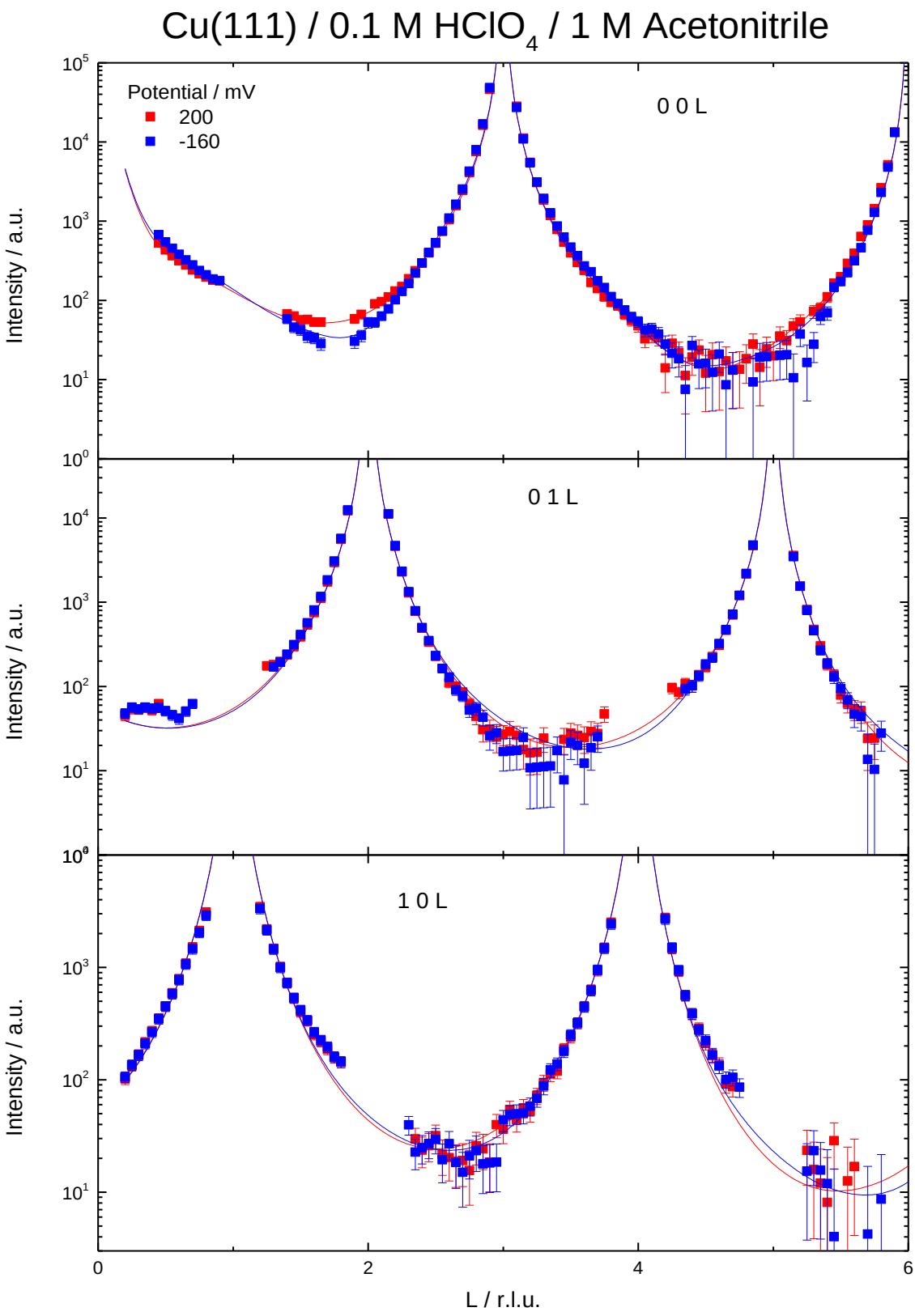

Figure 5.5 *Fits to specular (0 0 L) and non-specular (0 1 L) and (1 0 L) Crystal Truncation Rods for the Cu(111) / 0.1M $HClO_4$ / 1 M Acetonitrile system. The red and blue points correspond to the data measured at 200 and -160 mV respectively. The best fits to these are shown with the respective red and blue solid lines. Error bars include an assumed 10% systematic error.*

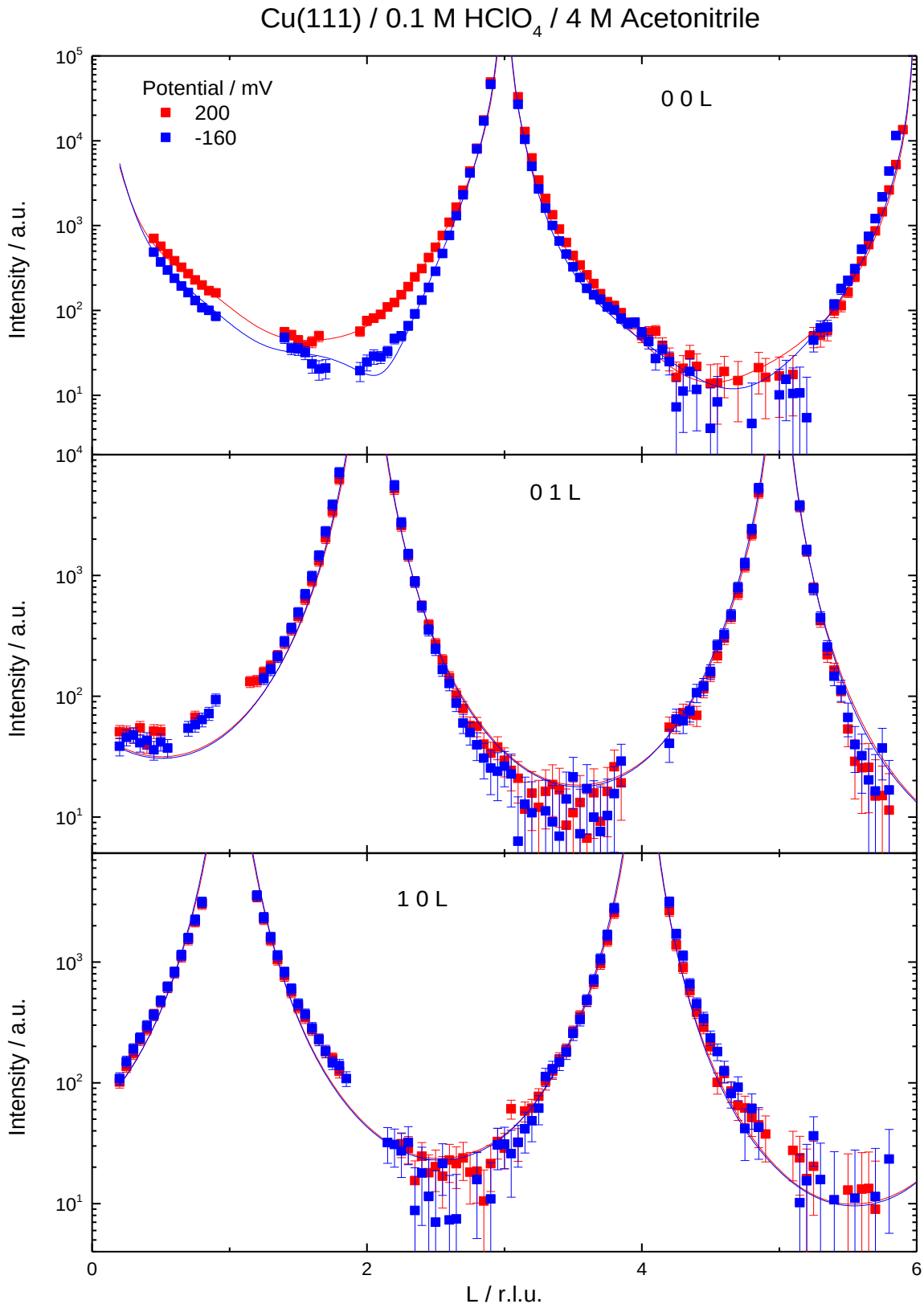

Figure 5.6 *Fits to specular (0 0 L) and non-specular (0 1 L) and (1 0 L) Crystal Truncation Rods for the Cu(111) / 0.1M $HClO_4$ / 4 M Acetonitrile system. The red and blue points correspond to the data measured at 200 and -160 mV respectively. The best fits to these are shown with the respective red and blue solid lines. Error bars include an assumed 10% systematic error.*

5.3.2.2. CTRs Fits Parameters Results

The parameters that gave the best fits from the CTRs presented in *Section 5.3.2.1.* are presented in *Tables 5.1, 5.2, 5.3* and *5.4* for 0, 0.01, 1 and 4 M acetonitrile concentrations respectively. The numbers in italics indicate the values of the parameters that were fixed during the fitting procedure.

a) No acetonitrile

			200 mV	-160 mV
	β		0.331 ± 0.005	0.291 ± 0.007
Metal Layers	Cu_1	Expansion / Å	0.002 ± 0.004	0.006 ± 0.004
	Cu_2	Expansion / Å	0.019 ± 0.003	0.012 ± 0.007
	Cu_3	Expansion / Å	-0.023 ± 0.004	-0.011 ± 0.004
Reduced χ^2			3.62	4.72

Table 5.1 *Parameters giving best fits to the experimental data for the Cu(111) / 0.1 M $HClO_4$ system. The left hand side (red background) show the parameters giving the best fit to the data at 200 mV (positive potential). The parameters on the right hand side (blue background) correspond to the parameters at -160 mV (negative potential).*

b) 10 mM acetonitrile

			200 mV	-160 mV
	β		0.33 ± 0.005	0.34 ± 0.004
Metal Layers	Cu_1	Expansion / Å	0.002 ± 0.003	-0.005 ± 0.006
	Cu_2	Expansion / Å	0.000 ± 0.003	0.018 ± 0.009
	Cu_3	Expansion / Å	0.023 ± 0.004	-0.009 ± 0.007
Carbon Layers	C_1	Θ	0.94 ± 0.11	0.52 ± 0.15
		d / Å	3.35 ± 0.10	3.18 ± 0.27
		σ / Å	*0.35*	*0.35*
	C_2	Θ	1.50 ± 0.18	1.79 ± 0.21
		d / Å	4.87 ± 0.09	4.99 ± 0.11
		σ / Å	*0.35*	*0.35*
Error Function		d / Å	5.44 ± 0.25	5.63 ± 0.30
		σ / Å	*0.5*	*0.5*
Reduced χ^2			2.73	3.51

Table 5.2 *Parameters giving best fits to the experimental data for the Cu(111) / 0.1 M $HClO_4$ / 10mM Acetonitrile system. The left hand side (red background) show the parameters giving the best fit to the data at 200 mV (positive potential). The parameters on the right hand side (blue background) correspond to the parameters at -160 mV (negative potential). Numbers in italics indicate the values of the parameters that were fixed during the fitting procedure.*

c) 1 M acetonitrile

			200 mV	-160 mV
	β		0.35 ± 0.004	0.35 ± 0.004
Metal Layers	Cu_1	Expansion / Å	0.001 ± 0.004	0.003 ± 0.005
	Cu_2	Expansion / Å	0.000 ± 0.006	0.010 ± 0.007
	Cu_3	Expansion / Å	0.016 ± 0.004	-0.005 ± 0.006
Carbon Layers	C_1	Θ	0.99 ± 0.10	0.66 ± 0.01
		d / Å	3.34 ± 0.10	3.09 ± 0.17
		σ / Å	*0.35*	*0.35*
	C_2	Θ	1.53 ± 0.17	1.83 ± 0.15
		d / Å	4.84 ± 0.07	5.01 ± 0.08
		σ / Å	*0.35*	*0.35*
Error Function		d / Å	5.40 ± 0.22	5.76 ± 0.20
		σ / Å	*0.5*	*0.5*
Reduced χ^2			1.90	2.68

Table 5.3 *Parameters giving best fits to the experimental data for the Cu(111) / 0.1 M $HClO_4$ / 1 M Acetonitrile system. The left hand side (red background) show the parameters giving the best fit to the data at 200 mV (positive potential). The parameters on the right hand side (blue background) correspond to the parameters at -160 mV (negative potential). Numbers in italics indicate the values of the parameters that were fixed during the fitting procedure.*

d) 4 M acetonitrile

			200 mV	-160 mV
	β		0.36 ± 0.004	0.37 ± 0.004
Metal Layers	Cu_1	Expansion / Å	0.001 ± 0.004	0.002 ± 0.005
	Cu_2	Expansion / Å	0.000 ± 0.006	0.006 ± 0.008
	Cu_3	Expansion / Å	0.009 ± 0.007	0.013 ± 0.008
Carbon Layers	C_1	Θ	0.87 ± 0.10	1.44 ± 0.30
		d / Å	3.32 ± 0.15	1.98 ± 0.07
		σ / Å	*0.35*	*0.35*
	C_2	Θ	1.29 ± 0.14	1.83 ± 0.15
		d / Å	4.87 ± 0.10	4.66 ± 0.06
		σ / Å	*0.35*	*0.35*
Error Function		d / Å	5.42 ± 0.16	5.76 ± 0.17
		σ / Å	*0.5*	*0.5*
Reduced χ^2			2.75	3.60

Table 5.4 *Parameters giving best fits to the experimental data for the Cu(111) / 0.1 M $HClO_4$ / 4 M Acetonitrile system. The left hand side (red background) show the parameters giving the best fit to the data at 200 mV (positive potential). The parameters on the right hand side (blue background) correspond to the parameters at -160 mV (negative potential). Numbers in italics indicate the values of the parameters that were fixed during the fitting procedure.*

5.3.2.3. Surface Metal Layers Relaxation

By evaluating the obtained parameters presented in the *Tables* above, one of the most prominent changes after addition of acetonitrile is the change of the expansion of the topmost copper layer, Cu_3. In the absence of the organic molecule, an *inwards* relaxation by -0.023 Å is observed which corresponds to -1% relaxation and is in good agreement with literature. [52] In presence of acetonitrile, Cu_3 layer has an *outwards* relaxation, of 0.023 Å, 0.016 Å and 0.009 for 10 mM, 1 M and 4 M acetonitrile, corresponding to a 1%, 0.7% and 0.4%. It has been revealed that the formation of metal-adsorbate bonds weakens the bonds between metal layers [53]. This assumption is further enhanced by the expansion values of the second copper layer, Cu_2. When no acetonitrile is present in the solution, the expansion of the second layer is at 0.019 Å (0.8%) and thus closer to the topmost copper layer and afterwards, at both acetonitrile concentrations present, it changes to practically zero.

However, at -160 mV a different effect was noticed for the top copper layer. Without any AcN Cu_3 has an *inwards* relaxation of -0.011 Å (-0.5%) and in presence of 10 mM and 1 M acetonitrile this value gradually increases to -0.009 Å (-0.4%) and -0.005 Å (-0.2%) respectively. At 4 M acetonitrile this value suddenly increases to 0.013 Å (0.6%) and the relaxation changes to *outwards.* On the other hand, the opposite effect was detected for the second copper layer, Cu_2. This layer has an *outwards* relaxation of 0.018 Å (0.6%) in 10 mM acetonitrile and gradually contracts as the concentration increases obtaining values of 0.010 Å (0.5%) in 1 M and 0.006 Å (0.3%) in 4 M AcN.

Due to the increase of the expansion of the topmost copper layer at -160 mV from -0.5% at no acetonitrile to 0.6% at 4 M acetonitrile, it has become evident that acetonitrile instigates an *outwards* expansion of the top Cu layer which becomes more intense with increase of its concentration. It is postulated that this effect is caused by the bonding of the acetonitrile molecules with the copper atoms via the cyanide (C-N) group simultaneously weakening the interlayer bonding between the top and the second copper layers. This assumption can justify the reason of the gradual *outwards* expansion of the top layer and at the same time the constant decrease of the second copper layer's expansion.

Furthermore, the roughness of the crystal surface, expressed by the β term in this analysis, has been found out to increase with each acetonitrile addition leading to the conclusion that acetonitrile roughens the surface of the Cu(111) crystal.

5.3.2.4. Electrolyte Double Layer Structure

In the previous section, it was proposed that acetonitrile adsorbs on the surface of Cu(111) in presence of perchloric acid. However, in the Chapter introduction two possible methods of coordination of the molecule to the copper atoms were mentioned. In this section, a detailed investigation of the acetonitrile orientation on the copper surface will be presented.

Specular CTRs are sensitive to ordering in the direction perpendicular to the surface and thus, a measure of the vertical electron density. In this model, an error function has been incorporated to model the bulk electrolyte. The atomic form factor of carbon was used for the acetonitrile adlayer since carbon, oxygen and nitrogen have almost similar atomic factors. [54] An error function with 0.5 Å width and maximum electron density equal to the bulk density of AcN of d_{AcN} = 0.786 g mL^{-1} was incorporated to the fit. The height of the error function was left as a free parameter, determined by the best fit to the data. The rms roughness value for each carbon adlayer was fixed at 0.35 Å, a value slightly above that the value of β. The number of the adlayers chosen was based on the impact on the resulting reduced χ^2 value. For both potentials and all acetonitrile concentrations mentioned in this section models with two layers of electron density produced the best theoretical fits.

Figure 5.7 depicts the comparison of the electron density profiles between the two acetonitrile concentrations at 200 and -160 mV. The electron density profile is plotted as a Gaussian function and given by *Equation 5.1*.

$$\rho = \frac{\tau \Theta Z}{[(2\pi)^2 u_{eff}]} \exp\left[-0.5\left(\frac{z-z_0}{u_{eff}}\right)^2\right] \quad (5.1)$$

Where τ is the inverse unit cell area, Θ the coverage, Z the atomic charge and z_0 the position above the surface. It must be noted, however, that since the profiles are laterally averaged, contributions from perchlorate anions present in the electrolyte solution could be possible. However, the cyclic voltammograms presented in *Figure 5.2* showed no perchlorate adsorption.

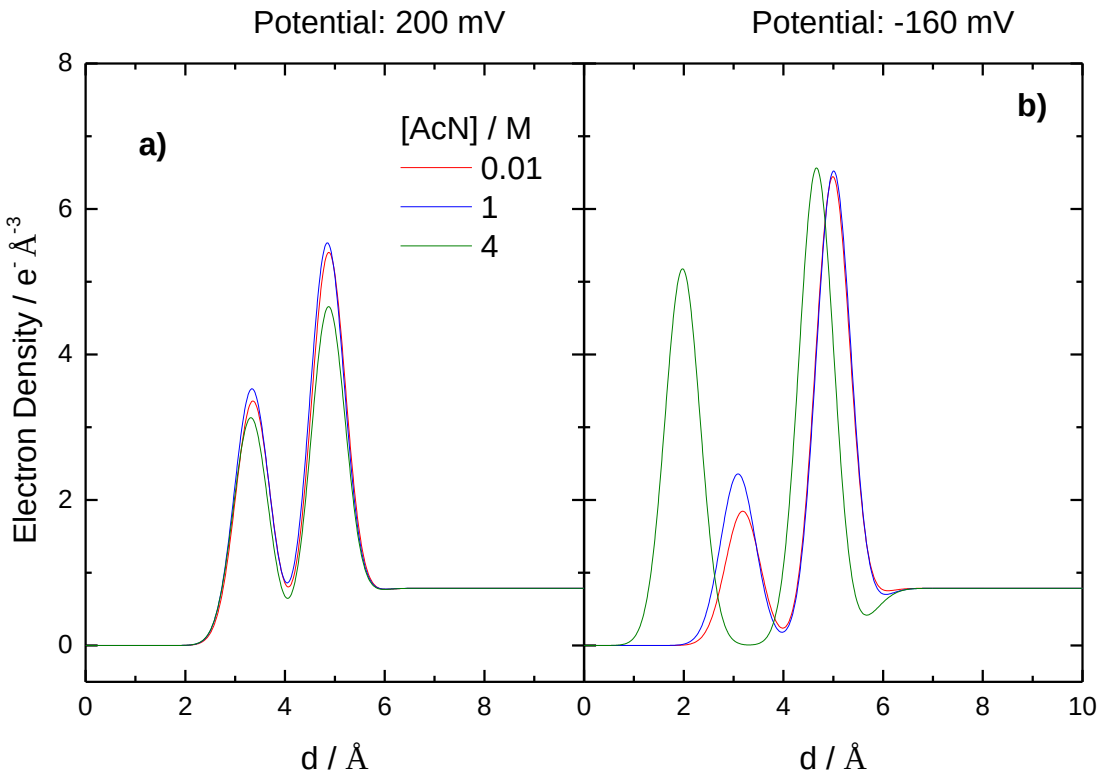

Figure 5.7 *Electron density profiles based on the best fit structure give in Tables 4.2, 4.3 and 4.4. The red, blue and green lines correspond to the 10 mM, 1 M and 4 M Acetonitrile concentrations in the system respectively.* ***a)*** *The calculated electron density profiles at 200 mV for each solution and* ***b)*** *at -160 mV.*

The electron density profile for 200 mV (*Figure 5.7a*) shows that the distance of the carbon atoms from the surface of the crystal is independent of the acetonitrile concentration and situated at 3.3 Å and 4.8 Å signifying that at the positive potential the AcN molecules have the same distance from the Cu(111) surface regardless of the concentration in the electrolyte.

On the other hand, at the negative end, at -160 mV (*Figure 5.7b*) the distance of the first peak from the left slightly decreases as the concentration increases from 10 mM to 1 M and at 4 M the peak distance value is massively reduced to 1.98 Å. Furthermore, the distance of the second peak from the left remains unchanged around 5 Å in 10 mM and 1 M acetonitrile and at 4 M the value drops to 4.66 Å. This observation leads to an assumption that acetonitrile concentration increase leads to a higher attraction of the C≡N group as the potential is scanned towards the negative potential region.

The distance between the two peaks at 200 mV regardless of the concentration is 1.55 Å and based on literature, it is assigned to the C-C distance of the acetonitrile molecule that is reported to be at 1.47 Å. [55]

After having postulated that Acetonitrile molecules adsorb on the Cu(111) surface, judging by the shape of the electron density profiles (*Figure 5.7*) it is proposed here in a model where AcN adsorbs on the surface through the lone pair orbital of nitrogen of the cyanide, (*Figure 5.8*) rather than the π orbital of the nitrile group. The orientation of the Acetonitrile molecules does not change either with potential swap or with varying AcN concentration.

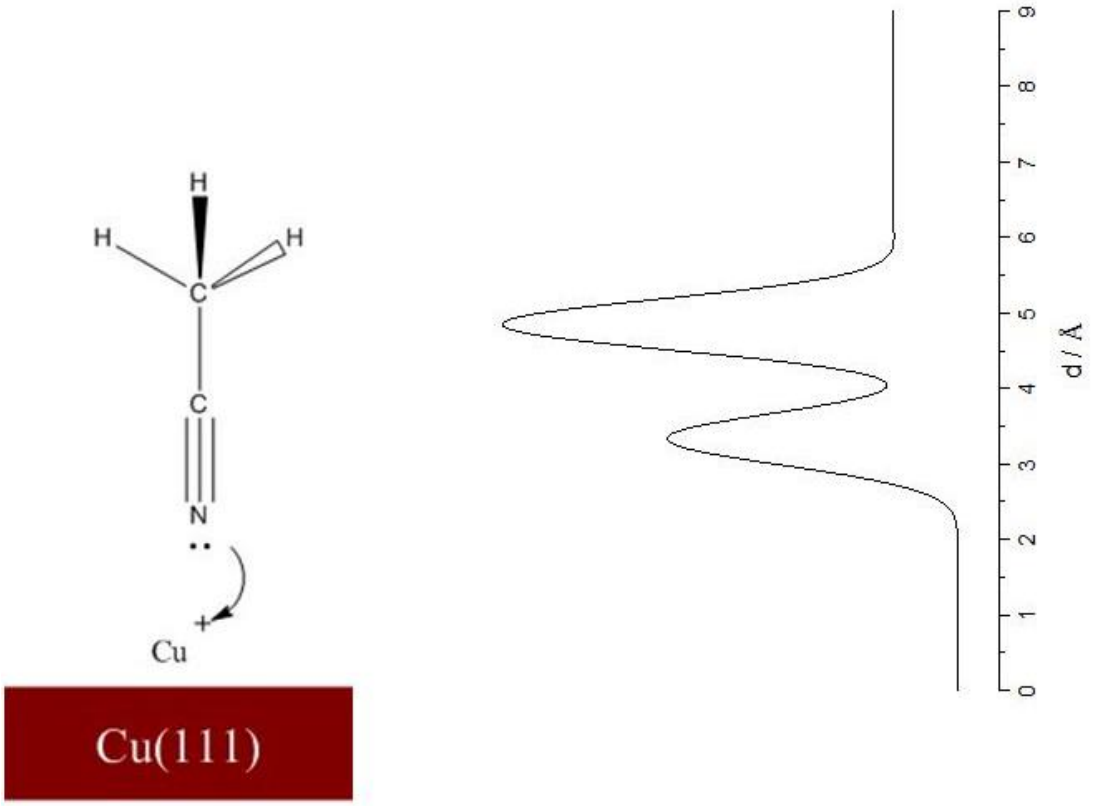

Figure 5.8 *Illustration of the proposed model where Acetonitrile adsorbs on the top copper layer and bonds with the top copper atoms. The graph on the right explains how the electron density corresponds to the carbon atoms of the Acetonitrile molecule.*

However, as previously mentioned, at 4 M acetonitrile concentration and at -160 mV the distance of the first carbon atom is at 1.98 Å from the electrode surface and the C-C distance has increased to 2.69 Å. Based on these observations, it is assumed that at this stage the AcN molecules have dissociated into a methyl radical ($CH_3^{\cdot}$) and a cyanide radical ($C{\equiv}N^{\cdot}$) and the latter has bonded with the copper atoms of the top layer. This assumption is based on firstly, the distance between the two carbon atoms is very large for them to be bonded and secondly, the Cu-N distance in copper complexes with cyanide and acetonitrile has been reported to be at 1.98 Å. [56] Consequently, a different model has been proposed for this stage and depicted in *Figure 5.9* together with the proposed mechanism for the dissociation of the acetonitrile.

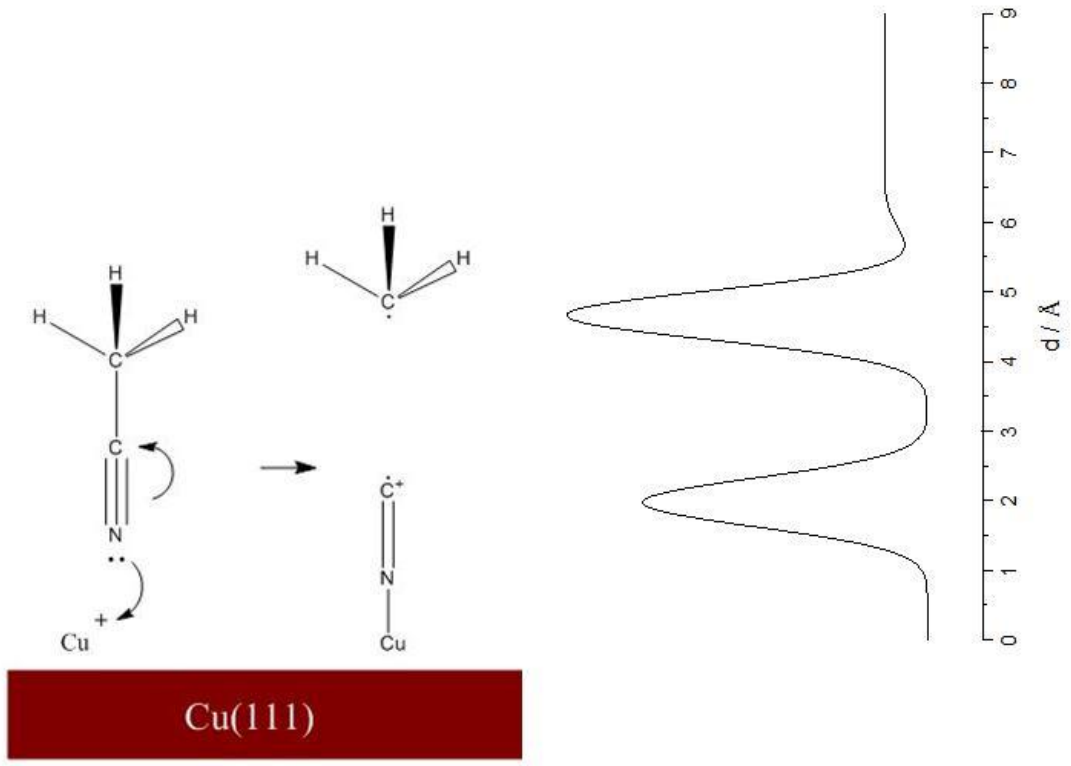

Figure 5.9 *Illustration of the proposed model and mechanism where Acetonitrile dissociates into a methyl and a cyanide group and the CN bonds with the copper atoms on the top layer of the Cu(111) crystal. The graph on the right explains how the electron density corresponds to the carbon atoms of the methyl and the cyanide.*

Dederichs *et al.* have reported that acetonitrile was dissociated into methyl and cyanide in presence of 0.1 M perchloric acid containing 0.025 M Acetonitrile which lead to cyanide adsorption on Pt(111). [57] Thus, it is assumed that in a similar manner AcN dissociates in presence of perchloric acid with the difference being that in Cu(111) it requires at least 4 M instead of 0.025 M of acetonitrile.

5.3.2.5. Twinning Effect

In the previous sections, the twinning effect observed in the Crystal Truncation Rods was briefly mentioned and not shown. As a result, in this section this phenomenon will be explained in more detail.

A twinned crystal is defined as an aggregate where different domains are joined together according to a specific symmetry operation: the twin law. The diffraction patterns derived from different domains are rotated, reflected or inverted with respect to each other depending on the nature of the relationship between the different domains, and weighted according to the quantity of a particular domain present in the crystal. Reflections from different domains

may overlap and twinned crystals fall broadly into two categories in which either all reflections or only certain zones of reflections are affected by overlap. The former occurs when a crystal lattice belongs to a higher point group than the crystal structure itself; the latter frequently occurs when the twin law is a symmetry operation belonging to a higher symmetry supercell. [58]

Minor amounts of an organic additive in a solution have been found to induce dramatic changes in the nucleation properties, growth rate, and the morphology of the crystal. This effect occurs via selective adsorption of the additive molecule on surface sites where a ligand interacts with the crystal surface, followed by inhibition of the regular deposition of oncoming crystal layers. [59]

Figure 5.10 illustrates the peak twinning on the non-specular CTR profiles in the Cu(111) / 0.1 M $HClO_4$ / 1 M Acetonitrile system. At the (0 1 L) CTR a peak is formed at L = 1 and 4 which match to the Bragg peaks of the (1 0 L) CTR and vice versa at (1 0 L) peaks emerge at L = 2 and 5 which correspond to the Bragg peaks of the (0 1 L) CTR.

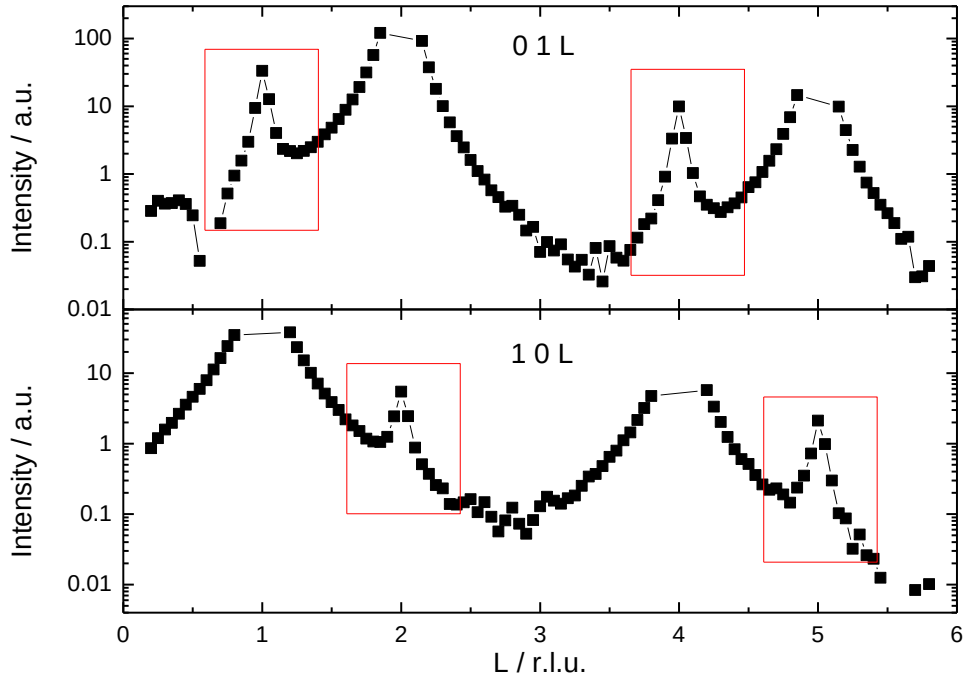

Figure 5.10 *Non-specular CTRs of the Cu(111) / 0.1 M $HClO_4$ / 1 M Acetonitrile at -160 mV. The twin peaks have been highlighted with a red frame*

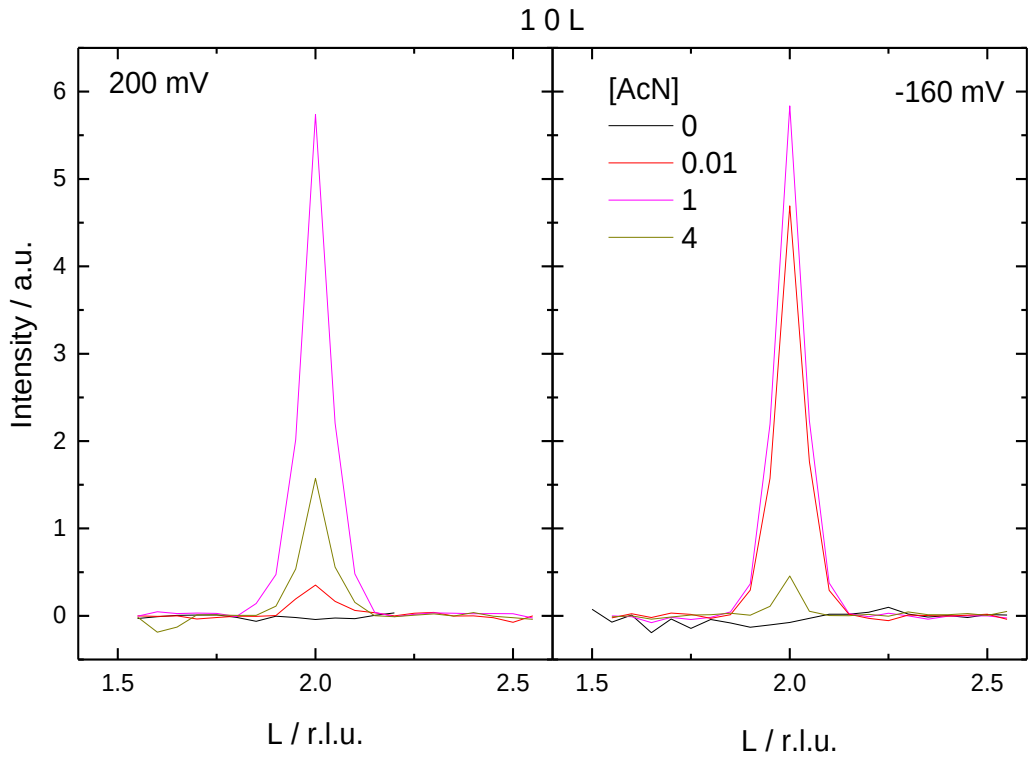

Figure 5.11 *Comparison of the peak formation at (1 0 2) position of reciprocal space between different acetonitrile concentrations at 200 mV (left) and -160 mV (right)*

Figure 5.11 depicts the growth of the twin peak at (1 0 2) position. This position is representative of the growth of the other peaks at (0 1 1), (0 1 4) and (1 0 5) from *Figure 5.10* as well. It must be remarked that the peak twinning phenomenon was not observed in the absence of acetonitrile hence, it can be established that the twinning effect is induced by acetonitrile rather than being an intrinsic property of the Cu(111) crystal.

The twin peaks start to form at 10 mM acetonitrile and increase of acetonitrile concentration to 1 M produces larger peaks which then decrease at 4 M. For this reason, the 1 M AcN concentration was chosen in *Figures 5.10* and *5.11* to highlight this effect.

At this stage, it must be pointed out that the surface of Cu(111) was re-prepared before the additions of 10 mM and 4 M AcN but not for the addition of 1 M AcN. It is implied in *Figure 5.12* that the increase of AcN concentration from 10 mM to 1 M activates more copper atoms to dissolute from the surface and redeposit. For this reason, it would have been expected that increase of AcN concentration to 4 M would lead to more intense twin peaks in the non-specular CTR profiles. Contrary to these expectations, a peak decrease is observed instead. This is attributed to the Cu(111) surface re-preparation carried out before the measurements in 4 M acetonitrile. It is therefore suggested that acetonitrile activates the dissolution of the

surface copper atoms and their complexation with the acetonitrile atoms which subsequently redeposit in a different orientation. The gradual peak increase shown in *Figure 5.11* is independent of the potential and acetonitrile concentration and is due to dissolved copper atoms already present in the solution.

Based on the assumptions discussed in the previous sections the twinning effect is attributed to a percentage of copper atoms on the Cu(111) surface which, after solvation from the AcN molecules, have been removed from the crystal surface, due to a stronger interaction with the molecule than the copper layer underneath, and then are redeposited in a rotated orientation with respect to the electrode surface. The exact orientation of the redeposited copper atoms has not been determined through this analysis.

However, it has been reported on a few occasions that twinning of (111) fcc metals result in a (511) orientation [60-63] The twinning effect can be described by a matrix notation, $T_{(hkl)}$ using *Equation 5.2*: [60]

$$(PQR) = T_{(hkl)}\,(pqr) \tag{5.2}$$

where (PQR) is a the lattice plane in the twinned crystal which corresponds to the lattice plane of the original crystal after twinning on (hkl) expressed as (pqr). [64] The general twin matrix for cubic systems is:

$$T_{(hkl)} = \frac{1}{(h^2+k^2+l^2)}\begin{pmatrix} h^2-k^2-l^2 & 2hk & 2hl \\ 2hk & -h^2+k^2-l^2 & 2kl \\ 2hl & 2kl & -h^2-k^2+l^2 \end{pmatrix} \tag{5.3}$$

For example if twinning occurs on the $(1\bar{1}1)$ axis, for *fcc*(111) crystals it is given by:

$$T_{(1\bar{1}1)} = \begin{bmatrix} -1 & -2 & 2 \\ -2 & -1 & -2 \\ 2 & -2 & -1 \end{bmatrix}\begin{bmatrix} 1 \\ 1 \\ 1 \end{bmatrix} = \begin{bmatrix} -1 \\ -5 \\ -1 \end{bmatrix} \tag{5.4}$$

It has been calculated from above that twinning of *fcc*(111) crystals results in a (511) orientation and thus, for this reason it is assumed here that the redeposited copper atoms obtain the (511) orientation. However, this remains under debate.

5.3.3. Summary

The influence of acetonitrile (AcN), on the Cu(111) surface in presence of 0.1 M perchloric acid ($HClO_4$) has been investigated by cyclic voltammetry and surface x-ray diffraction, which has not been reported yet in the literature. In pure perchloric acid as well as in 10 mM acetonitrile no visible peaks were observed at the CVs. However, in 1 M AcN concentration a deposition peak appears indicating deposition of complexed copper atoms. The aforementioned peak becomes more prominent at 4 M suggesting redeposition of the complexed copper atoms on the Cu(111) surface on a higher rate. Mernagh *et al.* reported the formation of cyanocopper(I) species through Raman spectroscopy at 10 M Acetonitrile. [26] Thus, it can be confirmed that this occurrence can take place for a lesser concentration at 4 M at least.

SXRD analysis indicated that the copper surface atoms of the crystal tend to interact stronger with acetonitrile rather than with the layer underneath. Additionally, it appears that at the negative end of -160 mV, increase of acetonitrile concentration leads to a higher attraction of the organic molecules with the surface atoms. This resulted in dissolution of some copper atoms from the surface and redeposited in a possible (511) structure as suggested by the crystal twinning effect observed in the non-specular CTRs.

Moreover, the electron density profile from SXRD analysis at 4 M acetonitrile concentration and -160 mV potential revealed that instead of the whole molecule of CH_3CN, only the cyanide group, C≡N, is bonded with the copper atoms and deposited as a result of a possible dissociation. A similar occurrence in presence of perchloric acid has also been reported in Pt(111). [57]

5.4. Acetonitrile in Ag(111) in Perchloric Acid

5.4.1. Electrochemical Characterisation

Cyclic voltammograms of the Ag(111) were measured in 0.1 M $HClO_4$ (*Figure 5.12*) in absence of acetonitrile (black line) and in presence of 10 mM and 1 M Acetonitrile (red and blue line respectively). The first potential scan started in the negative region and cycled between 0.5 V and 0 V. Similarly to the electrochemical characterisation in Cu(111) presented in *Section 5.3.1.* the voltammograms were recorded in the X-Ray cell therefore, contributions from the sides and back of the crystal in the shapes of the CV are anticipated. Furthermore, the scans have a large signal-to-noise due to low current density values of the scans but useful information of the behaviour of the Ag(111) crystal can still be deducted.

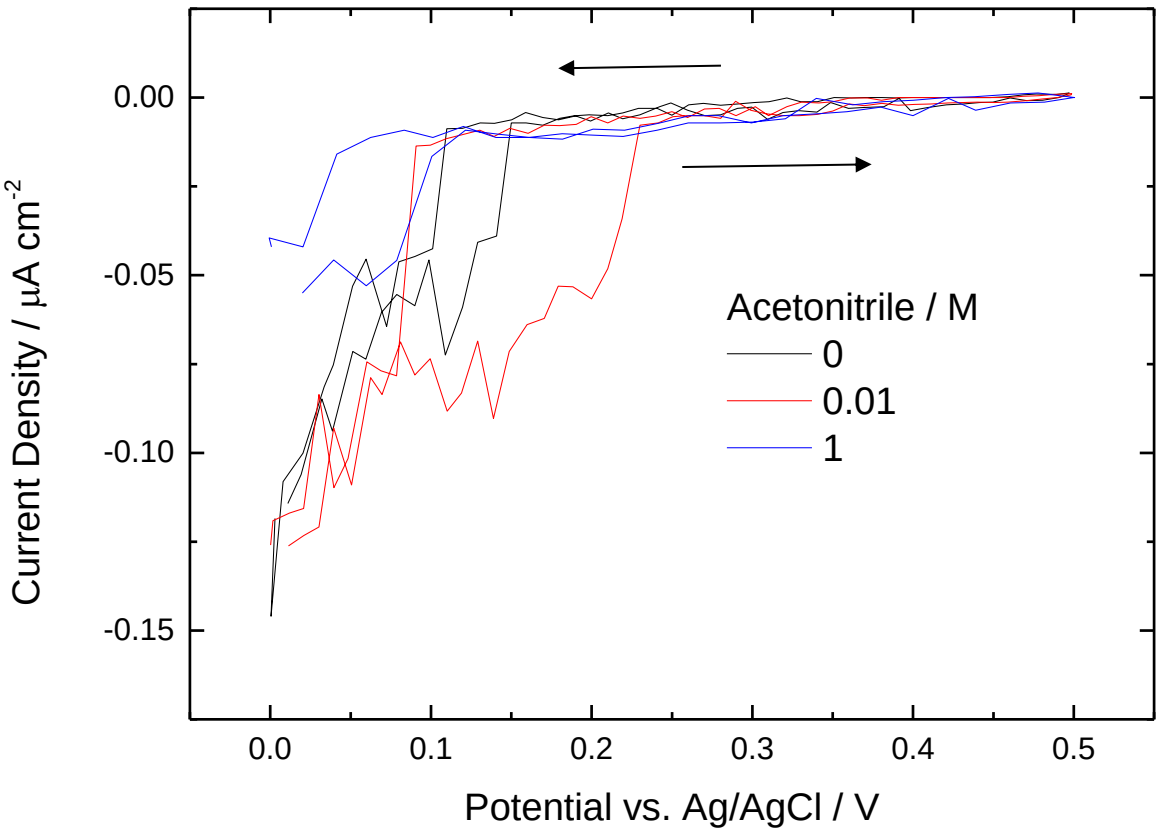

Figure 5.12 *Cyclic voltammograms of Ag(111) in 0.1 M $HClO_4$ in different Acetonitrile concentrations. Scan rate: 5 mV s^{-1}*

Without any acetonitrile in the solution, a double layer region extends from 0.5 to 0.1 V. The cathodic current commencing at 0.1 V is caused by the hydrogen evolution reaction. The CVs obtained in the presence of acetonitrile show an overall profile that is almost the same as the one obtained in the absence of acetonitrile, however there are some significant differences. In

acetonitrile a small hysteresis is observed during hydrogen evolution reaction due to possible interaction of the Ag(111) surface and acetonitrile molecules and the potential window expanded up to 0 V. In contrast to Cu(111) no prominent deposition peaks were observed and upon acetonitrile addition the electric charge involved in the double layer potential region did not exhibit any changes suggesting that there is no interaction of the acetonitrile molecules with the Ag(111) surface or it is weak enough to be negligible.

To obtain a better understanding of any effect acetonitrile has on Ag(111) single crystal, surface x-ray diffraction (SXRD) analysis was performed using both pure 0.1 M $HClO_4$ and in 0.1 M $HClO_4$ + 10 mM acetonitrile. Unfortunately, due to time constraints at the DLS Synchrotron, SXRD data for 1 M acetonitrile were not acquired.

5.4.2. Surface X-Ray Diffraction Analysis

5.4.2.1. Crystal Truncation Rods (CTRs)

For a full atomic-scale information on the influence of acetonitrile on the surface structure of Ag(111) electrode, Crystal Truncation Rods (CTRs) along the specular (0 0 L) and non-specular, (0 1 L) and (1 0 L), directions were measured for pure perchloric and in presence of 10 mM acetonitrile at 500 mV and 0 mV which correspond to the positive and negative ends respectively of the CVs presented in *Figure 5.12*. The potentials were chosen to have the largest separation so that the greatest change could be observed.

All CTRs, specular and non-specular, were modelled at the same time. *Figures 5.13* and *5.14* depict the comparison of each CTR between the two potentials at 0 and 10 mM acetonitrile respectively. The solid line in every graph shows the fit to the data using a fit model including the expansion of the layers, the Debye-Waller factors (DWF), σ and distance of the layers. The coverage, Θ of each of the top silver layers was fixed at 1. Every data point presented was background subtracted. However, some data points have been excluded either due to a twinning effect on the crystals that were averaging the theoretical fit or due to artificial points from powder lines. Each data point has a 10% assumed systematic error.

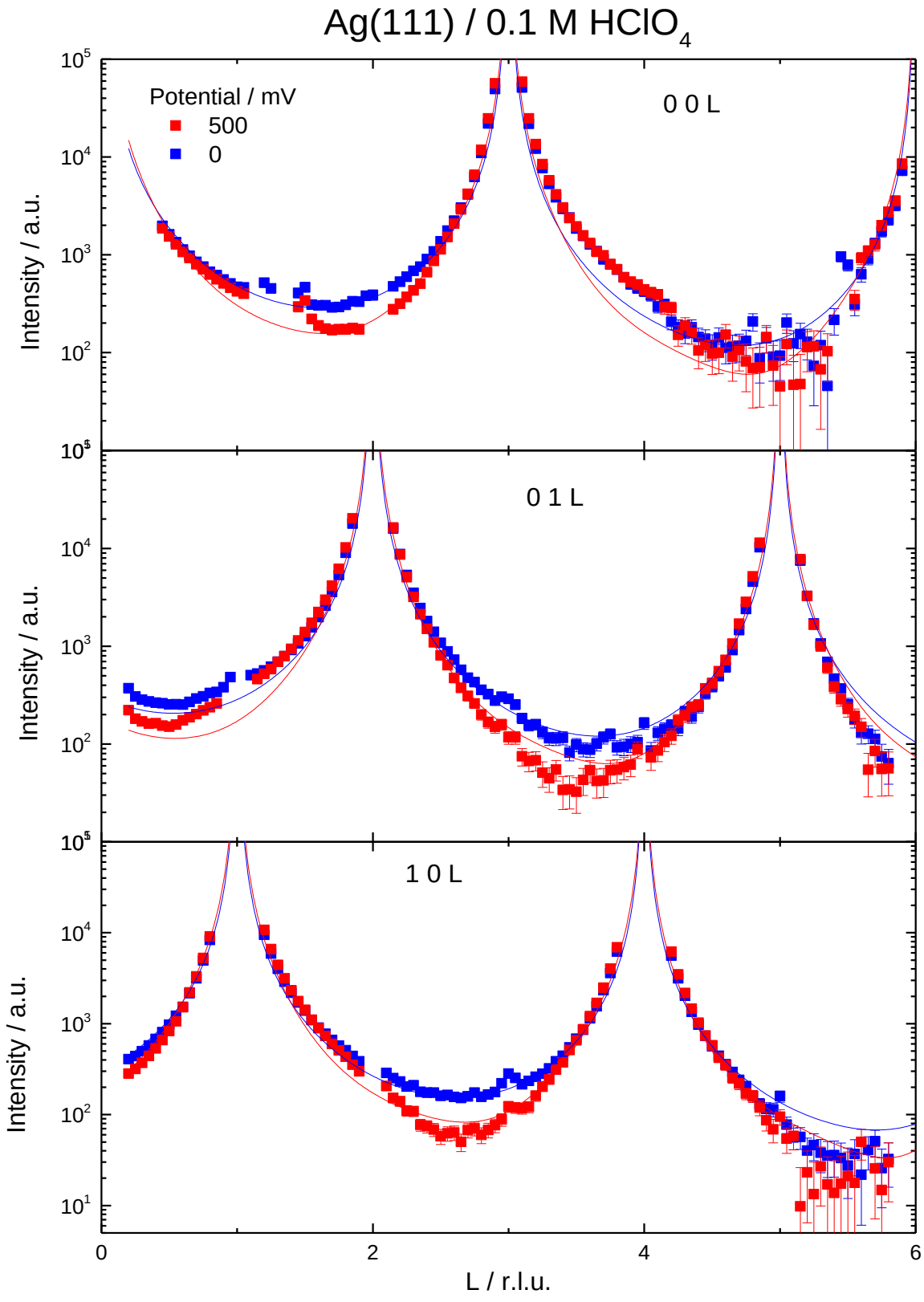

Figure 5.13 *Fits to specular (0 0 L) and non-specular (0 1 L) and (1 0 L) Crystal Truncation Rods for the Ag(111) / 0.1 M $HClO_4$ system. The red and blue points correspond to the data measured at 500 and 0 mV respectively. The best fits to these are shown with the respective red and blue solid lines. Error bars include an assumed 10% systematic error.*

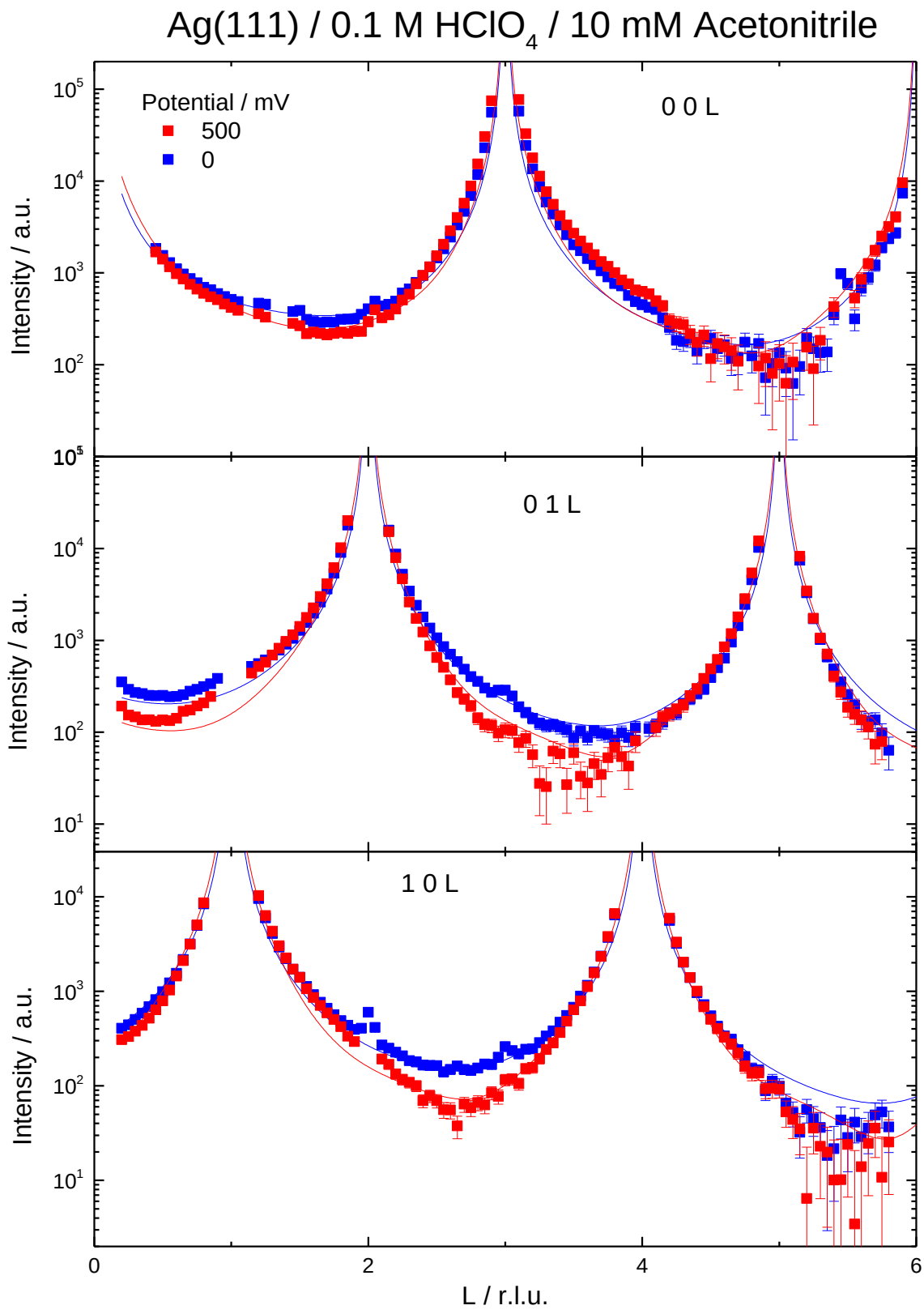

Figure 5.14 *Fits to specular (0 0 L) and non-specular (0 1 L) and (1 0 L) Crystal Truncation Rods for the Ag(111) / 0.1M $HClO_4$ / 10 mM Acetonitrile system. The red and blue points correspond to the data measured at 500 and 0 mV respectively. The best fits to these are shown with the respective red and blue solid lines. Error bars include an assumed 10% systematic error.*

5.4.2.2. CTRs Fits Parameters Results and Discussion

The parameters that gave the best fits from the CTRs presented in *Section 5.4.2.1.* are presented in *Table 5.5*. The numbers in italics indicate the values of the parameters that were fixed during the fitting procedure.

			No Acetonitrile		10 mM Acetonitrile	
			500 mV	0 mV	500 mV	0 mV
	β		0.18 ± 0.012	0.11 ± 0.010	0.19 ± 0.009	0.11 ± 0.010
Metal Layers	Ag_1	Exp. / Å	-0.002 ± 0.003	0.000 ± 0.004	-0.009 ± 0.003	-0.0001 ± 0.006
	Ag_2	Exp. / Å	0.013 ± 0.006	0.002 ± 0.006	0.019 ± 0.006	0.004 ± 0.006
	Ag_3	Exp. / Å	-0.021 ± 0.006	-0.013 ± 0.004	-0.011 ± 0.006	-0.014 ± 0.004
Carbon Layers	C_1	Θ	N/A		3.11 ± 0.87	2.57 ± 0.92
		d / Å			1.42 ± 0.04	1.35 ± 0.07
		σ / Å			*0.25*	*0.25*
Error Function		d / Å			2.74 ± 0.62	3.15 ± 0.36
		σ / Å			*0.5*	*0.5*
Reduced χ^2			5.78	4.59	4.93	4.45

Table 5.5 *Parameters giving best fits to the experimental data for the Ag(111) / 0.1 M HClO4 system (left column) and the Ag(111) / 0.1 M $HClO_4$ / 10 mM Acetonitrile (right column). The left hand side of each column (red background) show the parameters giving the best fit to the data at 500 mV (positive potential). The parameters on the right hand side of each column (blue background) correspond to the parameters at 0 mV (negative potential). Numbers in italics indicate the values of the parameters that were fixed during the fitting procedure.*

First of all, acetonitrile does not show to affect the expansion of the top three silver layers. The topmost Ag layer, Ag_3 possess an *inwards* relaxation and the second Ag layer, Ag_2 an *outwards* relaxation for both potentials, both in the absence and in presence of acetonitrile. Previously it was discussed that metal-adsorbate bonds weakens the bonds between metal layers [53] but, since there are just minor changes in the expansion of the metal layers, it is assumed that acetonitrile is not forming a bond with the top Ag atoms of the Ag(111) crystal. These results are in contrast with those found for the Cu(111) single crystal where the formed bond between the crystal atoms and acetonitrile molecules was stronger than the interlayer bonds.

For the solution containing 10 mM acetonitrile, carbon adlayers and an error function were included in the bulk electrolyte model similarly to the model for Cu(111) explained in *Section 5.3.2.4.* In this instance, the model that gave the best theoretical fit for both potentials had just

one layer of electron density where the rms roughness values for the carbon adlayer was fixed at 0.25 Å.

The shape of the electron density profile produced a single sharp peak at approximately 1.4 Å for both potentials. Therefore, a model is proposed where the C≡N bond of the acetonitrile molecule is parallel to the surface of the crystal and the coordination is via the π orbital of the nitrile group. (*Figure 5.15*)

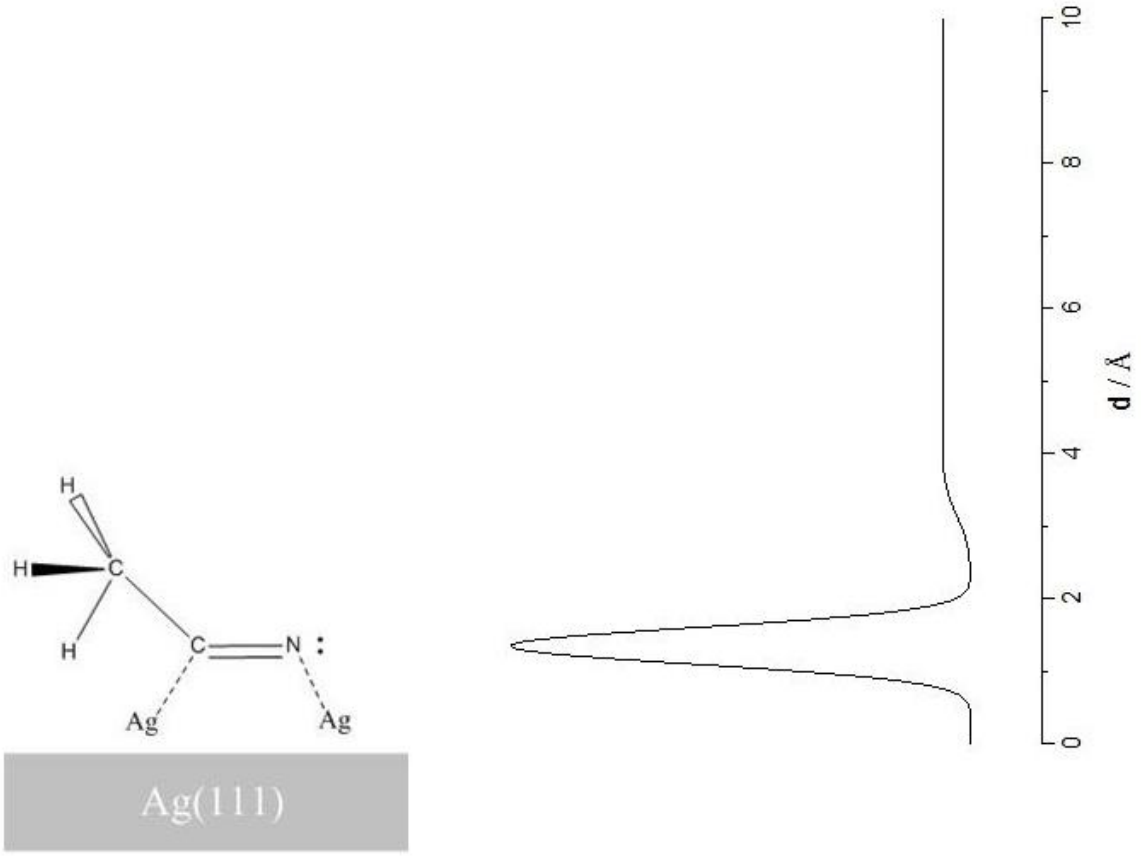

Figure 5.15 *Illustration of the proposed model where Acetonitrile weakly bonds with the atoms on the top silver layer. The graph on the right explains how the electron density corresponds to the acetonitrile molecule.*

This model proposal agrees with the previous reported observations as π bonds are generally less stable than σ bonds [65] and this information can justify the weak interaction of the metal adlayer with the molecule and the lack of any deposition peaks in the cyclic voltammograms of *Figure 5.12*.

Finally, it must be mentioned that the twinning effect observed in the CTRs were more caused by an intrinsic property of the Ag(111) crystal rather than an effect from acetonitrile. This is rationalised by noticing the twinning effect even in pure perchloric acid and the shape of the peaks were not altered even after the addition of 10 mM acetonitrile.

5.4.3. Summary

The effect of acetonitrile on the Ag(111) surface in 0.1 M $HClO_4$ as supporting electrolyte was examined by electrochemical and surface x-ray diffraction techniques. No deposition peaks were observed in either the absence or the presence of the organic molecule.

Analysis of the Crystal Truncation Rods is consistent with the fact that the nitrile group of acetonitrile molecules is positioned parallel to the surface of the Ag(111) crystal where the π orbital of the group is interacting with the top silver atoms of the crystal.

5.5. Summary and Conclusions

In this Chapter the effect of acetonitrile on Cu(111) and Ag(111) has been reported in presence of perchloric acid.

The most significant findings of this study involved the effect of acetonitrile on Cu(111). It was revealed that while perchlorate anions do not adsorb on the single crystal, there is a strong interaction between the top copper atoms of the crystal with the acetonitrile molecules simultaneously weakening the bonds between the copper layers on the crystal. Acetonitrile molecules were oriented with the C_3 axis perpendicular to the Cu(111) surface with the copper atoms forming a bond via the lone pair orbital of nitrogen. The aforementioned interaction was gradually enhanced as the acetonitrile concentration was increasing and at 4 M the acetonitrile molecules were dissociated in the methyl and nitrile groups. It was suggested that some copper atoms from the topmost layer of the single crystal were bonded either with the acetonitrile molecules at low concentrations or the cyanide ions at 4 M and redeposited in a presumably (511) structure.

In contrast to the behaviour in Cu(111) crystal, in the Ag(111) crystal in presence of perchlorate anions the acetonitrile molecules had no significant impact on the top metal layers of the crystals interacting weakly with them. In Ag(111) no adsorption of perchlorate anions was observed either and it was proposed that the orientation of the acetonitrile molecules is parallel to the crystal surface and the top silver atoms form weak bonds with the π orbital of the nitrile group.

The character of molecular adsorption at the IB-group of the periodic table, where the noble metals belong are n between the properties of sp and d metals. Therefore, the interaction of organic molecules with noble metal single crystal electrodes depend on the properties of the

element. It has been reported that the number of d electrons involved in an element strongly affects the interaction of a single crystal with an organic substance. The interaction of acetonitrile with Cu(111) is much stronger than Ag(111), as copper has fewer d electrons and thus, has smaller atomic size than silver and furthermore, Cu(111) single crystals possess more site-specific adsorbate-substrate interactions. [66]

5.6. References

1. Lipkowski, J., Stolberg, L., Yang, D.-F., Pettinger, B., Mirwald, S., Hengelin, F., Kolb, D.M., *Electrochmica Acta,* **1994,** *39,* 1043-1056
2. Barlow, S.M., Raval, R., *Surf. Sci. Reports,* **2003,** *50,* 201-341
3. Kühnle, A., *Current Opinion in Colloid & Interface Science,* **2009,** *14,* 157-168
4. Somorjai, G.A., *Introduction to Surface Chemistry and Catalysis*, John Wiley & Sons Inc.: New York, **1994**
5. Chaki, N.K., Vijayamohanan, K., *Biosens. Bioelectro.,* **2002,** *17,* 1-12
6. Yoshimura, M., Honda, K., Kondo, T., Uchikado, R., Einaga, Y., Rao, T.N., Tryk, D.A., Fujishima, A., *Diamond and Related Materials*, **2002,** *11,* 67-74
7. Barlow, S.M., Raval, R., *Surf. Sci. Reports,* **2003,** *50,* 201-341
8. Netzer, F.P., Ramsey, M.G., *Crit. Rev. Solid State Mater. Sci.,* **1992,** *17,* 397-475
9. Attard, G.A., *J. Phys. Chem. B,* **2001,** *105,* 3158-3167
10. Barlow, S.M., Kitching, K.J., Haq, S., Richardson, N.V., *Surf. Sci.,* **1998,** *401,* 322-335
11. Marti, E.M., Barlow, S.M., Haq, S., Raval, R., *Surf. Sci.,* **2002,** *501,* 191-202
12. Chen, Q., Frankel, D., Richardson, N., *Surf. Sci.,* **2002,** *497,* 37-46
13. Mainka, C., Wegner, H., Schertel, A., Woll, C., Grunze, M., *Z. Phys. Chem.,* **1997,** *198,* 221-244
14. Schluerlein, T.J., Schmidt, A., Lee, P.A., Nebesny, K.W., *J. Appl. Phys., Part I,* **1995,** *34,* 3837-3842
15. Tautz. F.S., Sloboshanin, S., Shklover, V., Scholz, R., Sokolowski, M., Schaefer, J.A., Umblach, E., *Appl. Surf. Sci.,* **2000,** *166,* 363-369
16. Bohringer, M., Schneider, W.D., Berndt, R., *Surf. Rev. Lett.,* **2000,** *7,* 661-665
17. Pons, S., *J. Electroanal. Chem.,* **1983,** *150,* 495-501
18. Marinkovic, N.S., Hecht, M., Loring, J.S., Fawcett, W.R., *Electrochimica Acta,* **1995,** *41,* 641-651
19. Storhoff, B.N., Lewis, H.C., *Coord. Chem. Rev.,* **1977,** *23,* 1-29

20. Baldelli, S., Mailhot, G., Ross, P., Shen, Y.-R., Somorjai, G.A., *J. Phys. B,* **2001,** *105,* 654-662
21. Magnussen, O.M., *Chem. Rev.,* **2002,** *102,* 679-726
22. Morin, S., Dumont, H., Conway, B.E., *Electroanal. Chem.,* **1996,** *412,* 39-52
23. Morin, S., Conway, B.E., Edens, G.J., Weaver, M.J., *Electroanal. Chem.,* **1997,** *421,* 213-220
24. Angerstein-Kozlowska, H., Macdougall, B., Conway, B.E., *J. Electroanal. Chem.,* **1972,** *39,* 287-313
25. Gu, R.A., Caom P.G., Sun, Y.H., Tian, Z.Q., *J. Electroanal. Chem.,* **1980,** *25,* 1597-1601
26. Mernagh, T.P., Cooney R.P., *J. Electroanal. Chem.,* **1984,** *177,* 139-148
27. Faguy, P.W., Fawcett, W.R., Liu, G., Motheo, A.J., *J. Electroanal. Chem.,* **1992,** *339,* 339-353
28. Tripkovic, D.V., Strmcik, D., van der Vliet, D., Stamenkovic, V., Markovic, N.M., *Faraday Discuss,* **2008,** *140,* 25-40
29. Lipkowski, J., Shi, Z., Chen, A., Pettinger, B., Bilger, C., *Electrochimica Acta,* **1998,** *43,* 2875-2888
30. Zhumaev, U.E., Lai, A.S., Pobelov, I.V., Kuzume, A., Rudnev, A.V., *Electrochimica Acta,* **2014,** *146,* 112-118
31. Hamelin, A., *J. Electroanal. Chem.,* 1982, ***138,*** 395-400
32. Herrero, E., Mostany, J., Feliu, J.M., Lipkowski, J., *J. Electroanal. Chem.,* **2002,** *534,* 79-89
33. Conway, B.E., *Progr. Surf. Sci.,* **1995,** *49,* 331-452
34. Uchida, H., Ikeda, N., Watanabe, M., *J. Electroanal. Chem.,* **1997,** *424,* 5-13
35. Ujvári, M., Láng, G., Horányi, G., *J. Appl. Electrochem.,* **2002,** *32,* 581
36. Láng, G.G., Horányi, G., *J. Electroanal. Chem.,* **2003,** *552,* 197-211
37. Lucas, C.A., Markovic, N.M., Ross, P.N., *Phys. Rev. B,* **1997,** *55,* 7964-7971
38. Markovic, N.M., Lucas, C.A., Gasteiger, H.A., Ross, P.N., *Surf. Sci.,* **1996,** *365,* 229-240
39. Orts, J.M., Gómez, R., Feliu, J.M., *J. Electroanal. Chem.,* **1999,** *467,* 11-19
40. Attard, G.A., Brew, A., Hunter, K., Sharman, J., Wright, E., *Phys. Chem. Chem. Phys.,* **2014,** *16,* 13689-13698
41. LaGraff, J.R., Gewirth, A.A., *Surf. Sci.,* **1995,** *326,* L461-L466
42. Inukai, J., Osawa, Y., Itaya, K., *J. Phys. Chem. B,* **1998,** *102,* 10034-10040
43. Wang, D., Xu, Q.-M., Wan, L.-J., Wang, C., Bai, C.-L., *Surf. Sci.,* **2002,** *499,* L159-L163
44. Aloisi, G., Futnikov, A.M., Will, T., *J. Electroanal. Chem.,* **1994,** *370,* 297-300

45. Shimooka, T., Yoshimoto, S., Wakisaka, M., Inukai, J., Itaya, K., *Langmuir,* **2001,** *17,* 6380-6385
46. Zou, S., Gao, X., Weaver, M. J., *Surf. Sci.,* **2000,** *452,* 44-57
47. Sugita, S., Abe, T., Itaya, K., *J. Phys. Chem.,* **1993,** *97,* 8780-8785
48. Ye, S., Ishibashi, C., Uosaki, K., *Langmuir,* **1999,** *15,* 807-812
49. Zhumaev, U.E., Lai, A.S., Pobelov, I.V., Kuzume, A., Rudnev, A.V., Wandlowski, T., *Electrochimica Acta,* **2014,** *146,* 112-118
50. Wan, L.-J., Yau, S.-L., Swain, G.M., Itaya, K., *J. Electroanal. Chem.,* **1995,** *381,* 105-111
51. Wan, L.-J., Itaya, K., *Langmuir,* **1997,** *13,* 7173-7179
52. Lindgren, S.Å., Walldén, L., Rundgren, J., Westrin, P., *Phys. Rev. B,* **1984,** *29,* 576-588
53. Sachtler. W.H.M., van Reijen, L.L., *Catalyst,* **1962,** *4,* 47-65
54. Gullikson, E.M., *X-Ray Data Booklet,* ed. Thompson, A.C., Vaughan, D., Lawrence Berkeley National Laboratory, Chapters 1.6, 1-38 and 1.7, 1-52
55. Karakida, K., Fukuyama, T., Kuchitsu, K., *Bulletin of the Chemical Society of Japan,* **1974,** *47,* 299-304
56. Osako, T., tachi, Y., Taki, M., Fukuzumi, S., Itoh, S., *Inorg. Chem.,* **2001,** *40,* 6604-6609
57. Dederichs, F., Petukhova, A., Daum, W., *J. Phys. Chem. B,* **2001,** *105,* 5210-5216
58. Parsons, S., *Acta Cryst.,* **2003,** *D59,* 1995-2003
59. Edgar, R., Schultz, T.M., Rasmussen, F.B., Feidenhans'l, Leiserowitz, L., *J. Am. Chem. Soc.,* **1999,** *121,* 632-637
60. Sorenson, T.A., Morton, S.A., Waddill, G.D., Switzer, J.A., *J. Am. Chem. Soc.,* **2002,** *124,* 7604-7609
61. Zeng, Y., Zou, Y.L., Alford, T.L., *Thin Solid Films,* **1997,** *307,* 89-95
62. Tomov, I., Adamik, M., Barna, P.B., *Thin Solid Films,* **2000,** *371,* 17-21
63. Rashkov, S., Stoichev, D.S., Tomov, I., *Electrochimica Acta,* **1972,** *17,* 1995-1964
64. Andrews, K.W., Johnson, W., *Br. J. Appl. Phys.,* **1955,** *6,* 92-96
65. Jemmis, E. D., Biswarup, P., Bruce, K.R., Schaefer III, H.F., *Chem. Communications,* **2006,** *20,* 2164-2166
66. Lepper, M., Schmitt, T., Gurrath, M., Raschmann, M., Zhang, L., Stark, M., Hölzel, H., Jux, N., Meyer, B., Schneider, M.A., Steinrück, H.-P., Marbach, H., *J. Phys. Chem. C,* **2017,** *121,* 26361-26371

CHAPTER 6

Influence of Acetonitrile on Copper Under-Potential Deposition in Sulphuric Acid

6.1. Introduction

This Chapter examines the effects acetonitrile has on the process of copper under-potential deposition on the surface of the Au(111) in presence of (bi)sulphate atoms. Cu UPD on Au(111) in sulphuric media has been one of the most studied systems. [1] Numerous characterisation techniques have been utilised for this system, ranging from electrochemical techniques, including voltammetry [2, 3], chronoamperometry [4] and chronocoulometry, [5] to microscopy methods such as *in situ* STM [6, 7] and AFM, [8, 9] and X-Ray techniques. [10-12] All these studies have provided a detailed knowledge of the system establishing it as a principal example for surface electrochemistry and thus it can serve as a reference to subsequent studies.

Initial studies of the copper adlayer structures were performed by Kolb *et al.* [13] using RHEED and LEED. It was revealed that copper UPD on Au(111) in sulphuric acid proceeds in two distinguishable stages as shown in *Figure 6.1*. Toney *et al.* using X-Ray scattering measurements discovered that the copper adlayer at the first stage of the UPD, which can be seen as Peak A in *Figure 6.1*, forms a honeycomb ($\sqrt{3}$ x $\sqrt{3}$)R30^o structure with a 0.67 ML coverage. [12] The co-adsorbing sulphate anions occupy the centres of the honeycomb and, likewise, form a ($\sqrt{3}$ x $\sqrt{3}$)R30^o structure. [4, 8, 12, 14] (*Figure 6.2*)

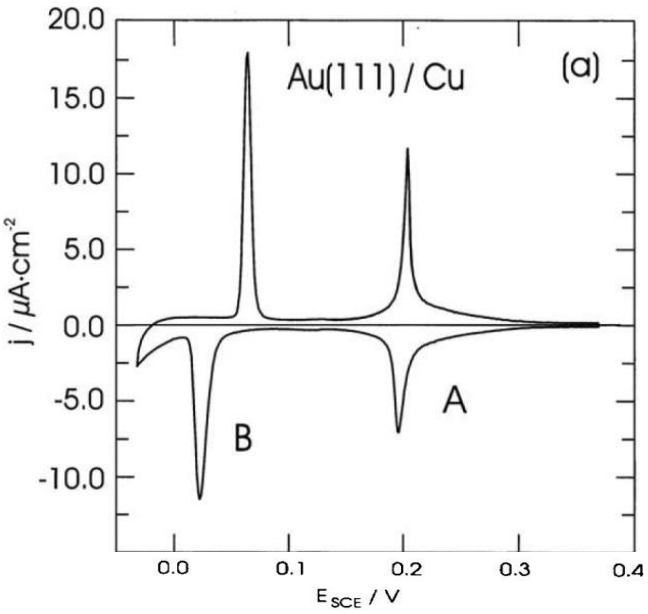

Figure 6.1 *Cyclic Voltammogram of 0.05 M H_2SO_4 + 1 mM $CuSO_4$ showing the UPD of Cu. Scan rate:1 mV s^{-1}.*
Source: *[4]*

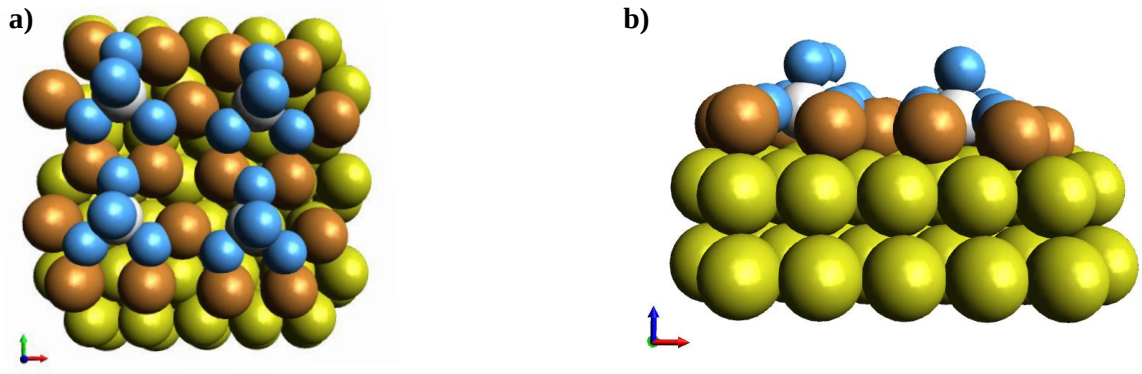

Figure 6.2 *Schematic of the ($\sqrt{3}$ x $\sqrt{3}$)R30° copper structure with the respective sulphate anion structure.* ***a)*** *top view,* ***b)*** *side view. Gold: Au(111), Brown: Copper, White: Sulphur, Blue: Oxygen.*

At the second stage of the UPD the copper atoms replace the sulphur atoms in the aforementioned structure to complete a pseudomorphic (1 x 1) Cu monolayer covered with a sulphate overlayer. (*Figure 6.1 – Peaks B*). It was also confirmed by Watanabe *et al.* employing electrochemical quartz crystal microbalance [15] and Nakamura *et al.* [16] with the use of *in situ* X-Ray scattering showed that this sulphate layer also exhibits a ($\sqrt{3}$ x $\sqrt{3}$)R30° structure. However, a thermodynamic and coulometric investigation by Shi *et al.* had previously revealed that the sulfate anions form a ($\sqrt{3}$ x $\sqrt{7}$)R19.1° on top of the pseudomorphic UPD monolayer of copper [5] which is the same structure observed on both bulk Cu(111) [17] and bulk Au(111) [18] (*Figure 6.3*). This was further confirmed by *in situ* STM studies by Madry *et al.* [19] Furthermore, Auger Electron Spectroscopy (AES)

measurements have indicated that sulphate adsorption on copper adlayers is stronger than on the bare Au(111) electrode. [20, 21]

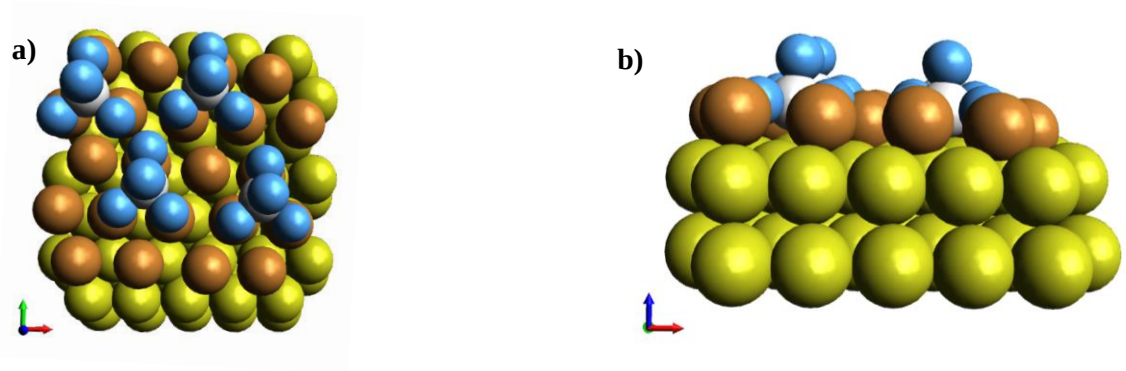

Figure 6.3 *Schematic of the (1 x 1) copper structure with the ($\sqrt{3}$ x $\sqrt{7}$)R19.1° sulphate anion structure.* ***a)*** *top view,* ***b)*** *side view. Gold: Au(111), Brown: Copper, White: Sulphur, Blue: Oxygen.*

Copper UPD on gold electrodes in acetonitrile has hardly ever been investigated. [22] In aqueous solutions, copper cations are reduced from Cu(II) to Cu(0) very fast but some researchers have claimed that the formation of Cu(I) as an intermediate during copper deposition on gold surfaces was possible but only in the OPD (Over-Potential Deposition) region. [4, 23, 24] Conversely, Omar *et al.* stated that Cu(II) can be reduced to Cu(I) in the UPD region and the strong repulsive interaction between the monovalent copper adatoms is counterbalanced by the co-adsorption of sulphate anions. [25] Additionally, Shi and Lipkowski claimed that the oxidation state of Cu^+ is the result of polar character of a chemisorption bond rather than a result of the formation of an intermediate in a step-by-step redox reaction. [26] On the other hand, Cu^+ ions can be stabilised in presence of acetonitrile by forming a $[Cu(AcN)_4]^+$ complex. [27] Hence, a difference in copper deposition process is expected. [28]

This Chapter will firstly examine the Cu UPD in pure sulphuric acid and the results providing information on the resulting structure, the transfer kinetics and the nucleation and growth and afterwards the results will be compared to the addition of 10 mM and 4 M acetonitrile.

6.2. Experimental Procedure

All chemicals: sulphuric acid, 99.999%, copper (II) sulphate pentahydrate and anhydrous acetonitrile, 99.8% were provided by Sigma-Aldrich®. All solutions were prepared by diluting solutions in volumetric flasks to the desired concentration with MilliQ water.

A three-electrode cell setup connected to a VersaStat potentiostat (Princeton Applied Research) was used for all the electrochemical experiments. Au(111) disk electrode, 10 mm diameter, obtained from Mateck, was the working electrode. A gold wire was employed as a counter electrode and a Ag/AgCl (3.4 M KCl) electrodes as a reference (E = 0.21V vs. SHE). The reference electrode was placed in a bridge tube filled with the same electrolyte as the cell to avoid any possible leaking chloride ions contaminating the electrochemical cell. All the potentials reported here are quoted against this reference electrode. The Au(111) was placed in a collet and put on a crystal holder for better handling. The crystal was mounted on the electrolyte in a "hanging meniscus" method so only the surface of the crystal was in contact.

Surface x-ray diffraction measurements were performed in the I-07 beamline of the Diamond Light Source in Didcot, Oxfordshire with photon energy of 18.5 keV and a grazing incidence angle of 0.3º. Surface coordinates of the Au(111) surface: a = b = 2.88 Å, c = 7.06 Å, $\alpha = \beta = 90^{o}$, $\gamma = 120^{o}$. For the X-Ray measurements the specifically modified thin layer cell was employed. The preparation for the Au(111) single crystal for both electrochemical and x-ray measurements has been outlined in *Section 3.1.3*.

6.3. Copper in Sulphuric Acid

6.3.1. Electrochemical Characterisation

6.3.1.1. Cyclic Voltammetry

For the general characterisation of the copper deposition process and for comparison with literature reports, a cyclic voltammogram (CV) was recorded in 0.1 M H_2SO_4 / 1 mM $CuSO_4$ solution in various scan rates (*Figure 6.4.*). Two peak pairs are observed in both the anodic and the cathodic potential sweeps. Peaks A_1 and A_2 correspond to the lifting and the formation of the $(\sqrt{3}$ x $\sqrt{3})R30^o$ copper structure respectively. In relation, peaks B_1 and B_2 are associated with the lifting and deposition of the pseudomorphic (1 x 1) copper monolayer. The shape of the cyclic voltammograms is in good agreement with other CVs reported in literature. [1, 3, 5, 13, 19] Cu deposition and desorption are completely reversible with no noticeable changes in succeeding voltammograms. Finally, the variation of the scan rate did not produce any significant alterations to the shape of the resulting CVs showing the stability of the system.

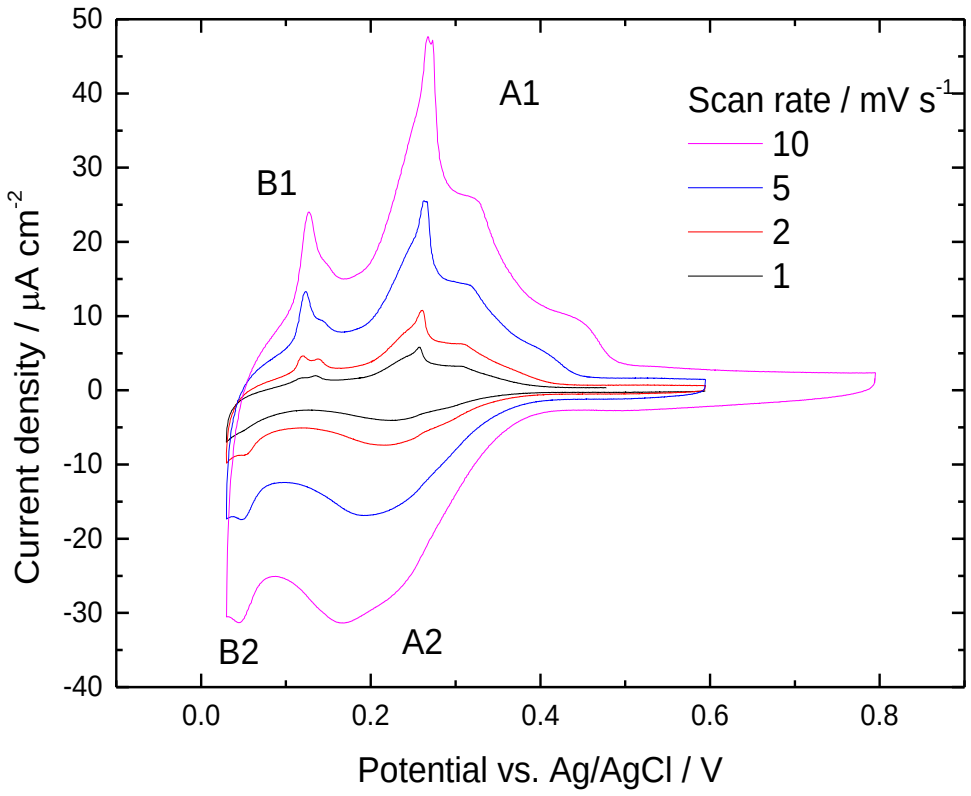

Figure 6.4 *Cyclic voltammograms of Au(111) in 1 mM $CuSO_4$ / 0.1 M H_2SO_4 at different scan rates.*

The small hysteresis between peaks B_1 and B_2 is due to the strong interaction of copper and sulphate adatoms and the strong adsorption of the $(\sqrt{3} \times \sqrt{7})R19.1^{o}$ sulphate structure on top of the (1 x 1) copper layer necessitating a large overpotential. This phenomenon is an indication of an instantaneous nucleation with 2D growth [3] which will be further evaluated in the next section.

6.3.1.2. Chronoamperometry

In order to monitor the development of copper coverage as a function of the potential; after obtaining the cyclic voltammograms a series of chronoamperometric transients were obtained in the same setup. (*Figure 6.5*) These are defined as the current responses to potential steps from 0.6 V, a potential where there are no copper is deposited, to more negative potential values. Initially, the potential was held at 0.6 V for 20 seconds and then immediately switched to a different potential which was then held for 60 seconds. It must be noted here that the shape of the chronoamperometric curves depends largely on the value of the final potential.

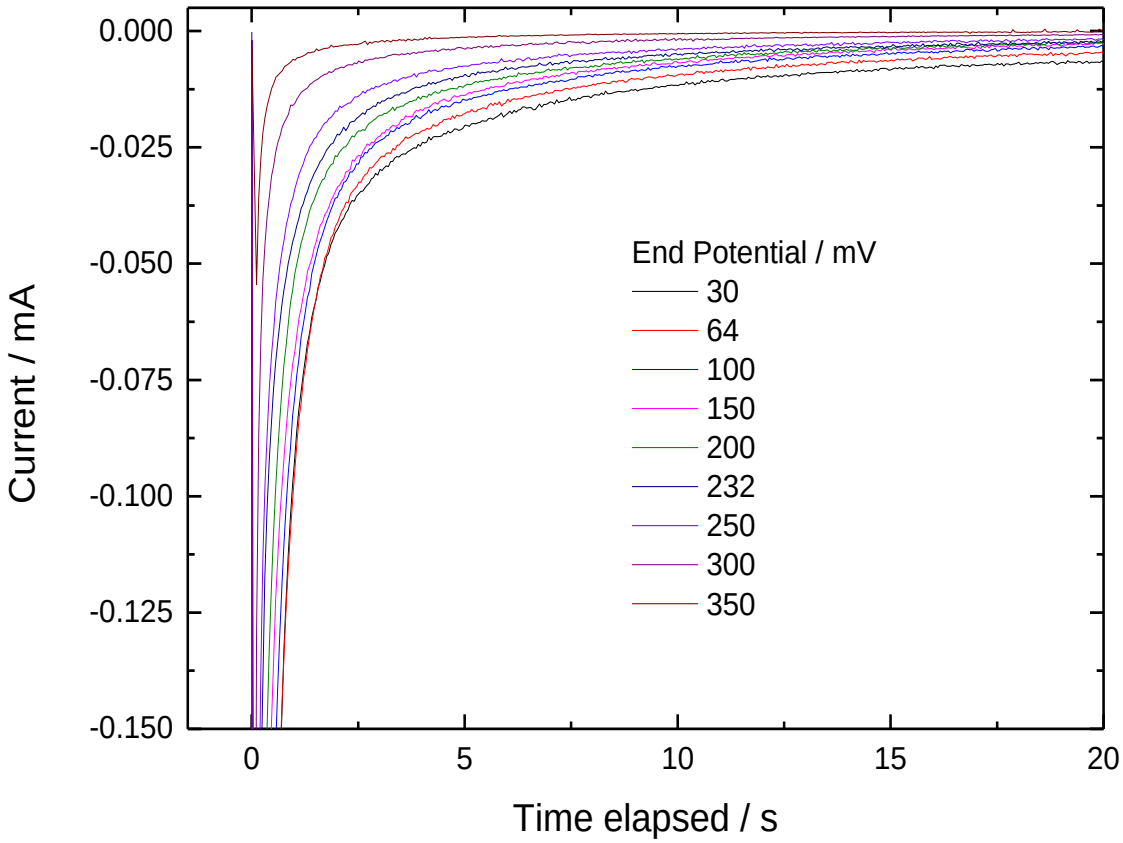

Figure 6.5 *Chronoamperometric curves of Au(111) in 1 mM $CuSO_4$ / 0.1 M H_2SO_4 for potential steps from 0.6 V to the final values indicated on the figure.*

Immediately following the potential step a very fast current transient peak is visible on all the chronoamperometric curves whose average charge and time scale correspond to the charging of the double layer. It is also evident that the current transients start to decay more slowly as the potential is stepped to more negative values due to higher charge on the surface.

The chronoamperometric curves presented in *Figure 6.5* were fit according to the Avrami equation (*Equation 6.1*) to determine the copper coverage, the electron transfer rate and the nucleation type

$$j_n(t) = S_n k_n m_n t^{(m_n-1)} e^{(-k_n t^{m_n})} \tag{6.1}$$

This equation has been explained in *Section 2.1.6.* The charge, S_n, and time constant, k_n, were left as free parameters and the exponents' values, m_n, were fixed, depending on the respective nucleation process. It is a requirement for m_n values to be an integer as they dictate the nucleation type.

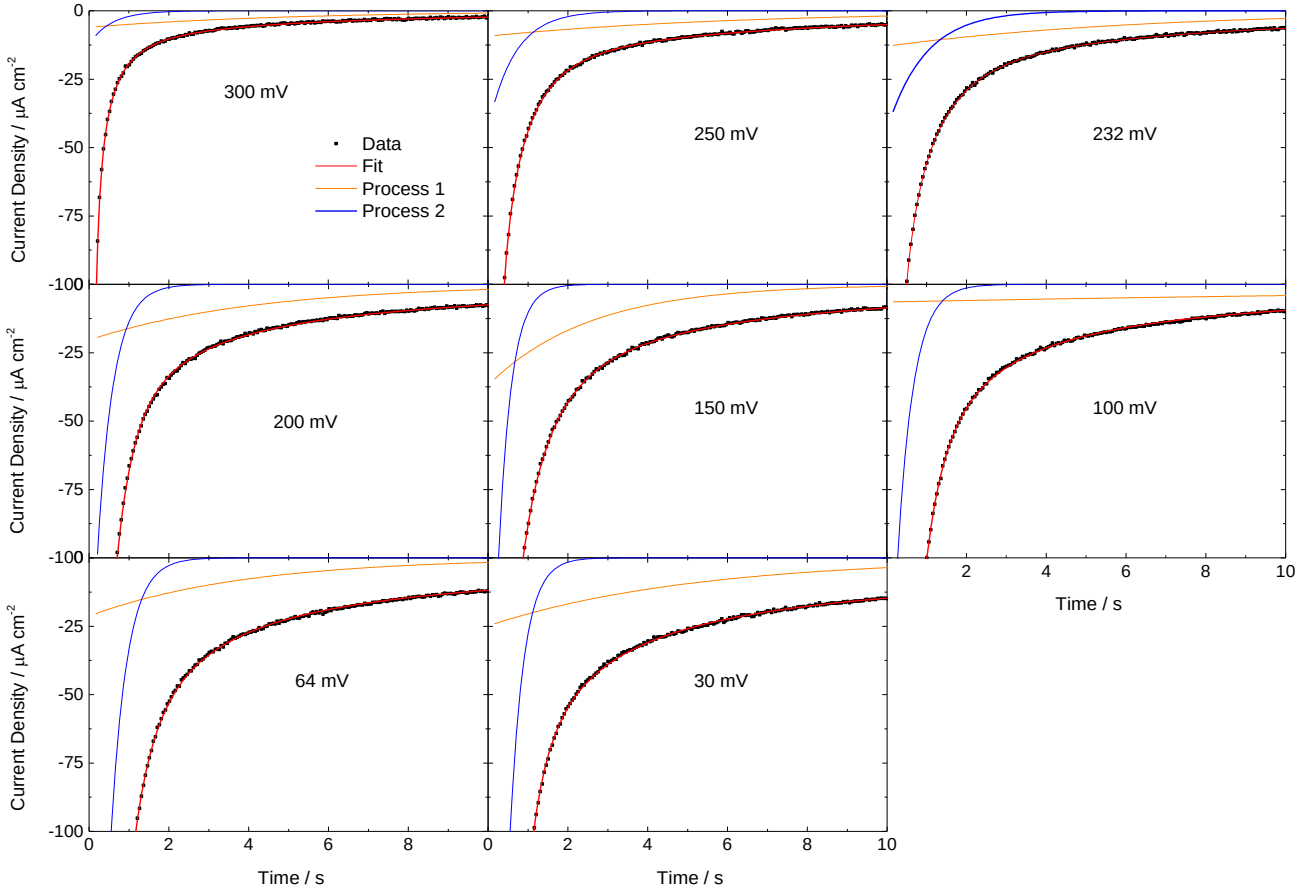

Figure 6.6 *Current transients after potential steps from 600 mV to more negative potentials in 0.1 M H_2SO_4 + 1 mM $CuSO_4$. The experimental data is shown together with best fits, obtained by assuming two separate nucleation and growth processes, each described by the Avrami equation.*

For the 0.1 M H_2SO_4 / 1 mM $CuSO_4$ system studied herein, the chronoamperometry transients could not be modelled with only one nucleation process. However, modelling them with two nucleation processes gave good fits to the data for all the transients and both processes were assigned to copper deposition. The presence of two separate processes implies that copper atoms deposit on different activation sites with different electron transfer rate. In *Figure 6.6* the obtained experimental data along with the best fits and the contribution of each of the two separate processes are shown.

A third process, $j_3(t)$, was attributed to the charging of the double layer. For this process, all parameters were left free and during modelling the best fit gave for the exponent value, m_3, a very low value which was very close to zero, thus rendering $j_3(t) \sim 0$ and the process practically negligible in the overall contribution.

The summary of the copper coverage percentage as a function of applied potential and the electron transfer rate extracted from the fits is presented in *Table 6.1*. The potentials were the two stages of Cu UPD occur are highlighted with a red frame. The best fits were obtained when the exponents' values were fixed at $m_1 = m_2 = 1$, thus it can be confirmed that both processes have instantaneous nucleation growth with surface diffusion. The resulting copper coverage was calculated by taking into account the crystal surface electrode area, as explained below.

	Process 1		Process 2		Proc. 1	Proc.2	**Total**	χ^2
$E_{fin.}$ / mV	S_1 / A s^{-1}	k_1 / s^{-1}	S_2 / A s^{-1}	k_2 / s^{-1}	%Coverage			
350	-7.9200e^{-6}	0.2211	-2.6020e^{-7}	1.7186	4.360	0.143	**4.503**	**1.7**
300	-2.3963e^{-5}	0.1978	-5.3468e^{-6}	1.7852	13.192	2.943	**16.135**	**1.2**
250	-4.6193e^{-5}	0.1578	-2.2379e^{-5}	1.0600	25.429	12.319	**37.749**	**0.9**
232	-6.6259e^{-5}	0.1540	-3.2462e^{-5}	1.5010	36.475	17.870	**54.346**	**0.7**
200	-6.7258e^{-5}	0.2382	-5.2485e^{-5}	2.4932	37.025	28.893	**65.918**	**1.6**
150	-7.3790e^{-5}	0.3931	-5.7348e^{-5}	3.0731	40.621	31.570	**72.191**	**1.9**
100	-7.9850e^{-5}	0.0455	-6.2817e^{-5}	2.4922	61.551	34.581	**78.923**	**0.3**
64	-6.5602e^{-4}	0.2548	-1.2572e^{-4}	2.4733	69.208	36.114	**105.322**	**0.8**
30	-1.0066e^{-4}	0.1938	-1.3438e^{-4}	2.8632	73.976	55.413	**129.389**	**0.2**

Table 6.1 *Summary of the fit models after the analysis of every current transient using the Avrami equation.*

To determine the coverage we consider that the charge is given by:

$$Q = I\,t \tag{6.2}$$

Then, dividing each charge by the charge of one electron (Q_e = 1.602 x 10^{-19} C) the total number of electrons exchanged, n_e can be determined. Since Cu^{2+} yields two electrons at deposition, the total number of electrons is divided by two and thus, the number of electrons per atom can be calculated:

$$\frac{n_{e-(atom)}}{2} = \frac{n_{e-total}}{n_{surface}} \tag{6.3}$$

Where $\mathbf{n_{surface}}$ is the number of the crystal surface atoms. To find out this value we need to take into account the structure of the *fcc*(111) crystal surface (*Figure 6.7*)

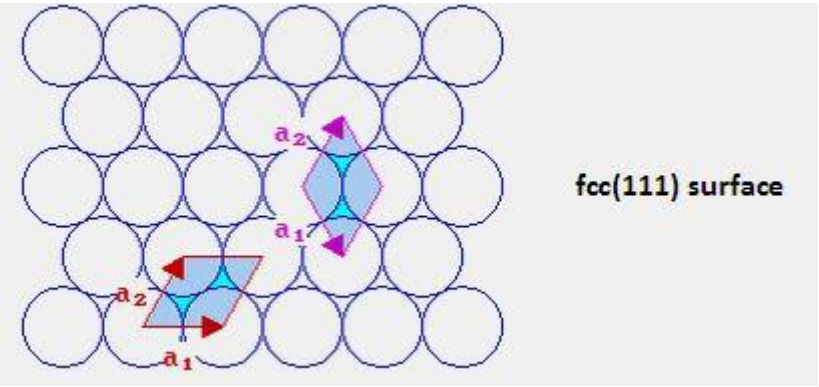

Figure 6.7 *Schematic depiction of the fcc(111) surface.*

Both gold and copper have *fcc* packing and for the (111) surface and the atomic ordering we have $|\alpha_1| = |\alpha_2|$ and the area can be estimated as:

$$\alpha = 2|\alpha_1| \Leftrightarrow |\alpha_1| = \left(\frac{\alpha}{\sqrt{2}}\right)^2 \tag{6.4}$$

Where α is the lattice constant of the respective metal, which in the case of Au, is α_{Au} = 4.0782 Å. Also, because the crystal is circularly shaped the surface area is given by

$$A_{sur.} = \pi r^2 \tag{6.5}$$

under the assumption of a perfect crystal and does not take surface roughness into account. So the number of the crystal surface atoms calculated is shown in *Equation 6.6*.

$$n_{surface} = \frac{A_{sur.}}{|\alpha_1|^2 \, sin120^o} \quad (6.6)$$

Finally, the coverage, Θ_{Cu}, for copper is calculated as the ratio of the total Cu atoms on the surface against the number of atoms on the crystal surface:

$$\Theta_{Cu} = \frac{n_{e-(Cu)}}{n_{surface}} \quad (6.7)$$

Copper coverage was calculated at Θ_{Cu} = 0.659 ML and at Θ_{Cu} = 1.053 ML (*red frames in Table 5.1*) at the first and second UPD peaks at 200 and 64 mV respectively. These values are in agreement with those stated in literature. (0.67 and 1.00 ML respectively). [1, 12, 19, 30] With both processes holding an instantaneous nucleation with surface diffusion, it signifies that throughout the whole deposition process, all copper atoms deposit on the top of Au(111) surface simultaneously forming initially the ($\sqrt{3}$ x $\sqrt{3}$)R30° structure and then the (1 x 1).

The results from *Table 6.1* are shown in *Figure 6.8* as a function of potential together with the 10 mV s^{-1} CV (*Figure 6.8a*). The graph depicts how the coverage (*Figure 6.8b*) and the time constant (*Figure 6.8c*) change during copper UPD. The manner the total copper coverage shown in *Figure 6.8b* (*blue points*) develops on the Au(111) surface with respect to the applied electrode potential is similar to the one reported by Frittmann *et al.* [30] However, in their analysis the determination of copper evolution is based on extrapolation of their analysis on the two copper UPD stages whereas a full copper coverage evolution on Au(111) is presented in this analysis. Also, at 64 mV where the second stage of the Cu UPD occurs the coverage of the second process (*red points*) dramatically increases, most probably due to copper atoms substituting the sulphate ions of the ($\sqrt{3}$ x $\sqrt{3}$)R30° structure to form the (1 x 1) structure. We have attributed the two processes to the two different nucleation processes of copper as reported by Hölzle *et al.* [3] One is taking place on surface defects and the second on well-ordered (111) terraces with the nucleation on defects being more energetically preferred. This phenomenon is dependent on the surface quality of the Au(111) crystal. In *Figure 6.8c* it is evident that the $j_2(t)$ nucleation process is faster than $j_1(t)$ for the whole potential region. It has been reported that the surface defects serve as starting nucleation sites for the ($\sqrt{3}$ x $\sqrt{3}$)R30° structure serve as starting nucleation sites [3] therefore, it is presumed that the process with higher transfer kinetics ($k_2 > 1$), in this case $j_2(t)$, is the one taking place on the surface defects and correspondingly, $j_1(t)$, the process with slower transfer kinetics ($k_1 < 1$) to deposition on well-ordered (111) terraces.

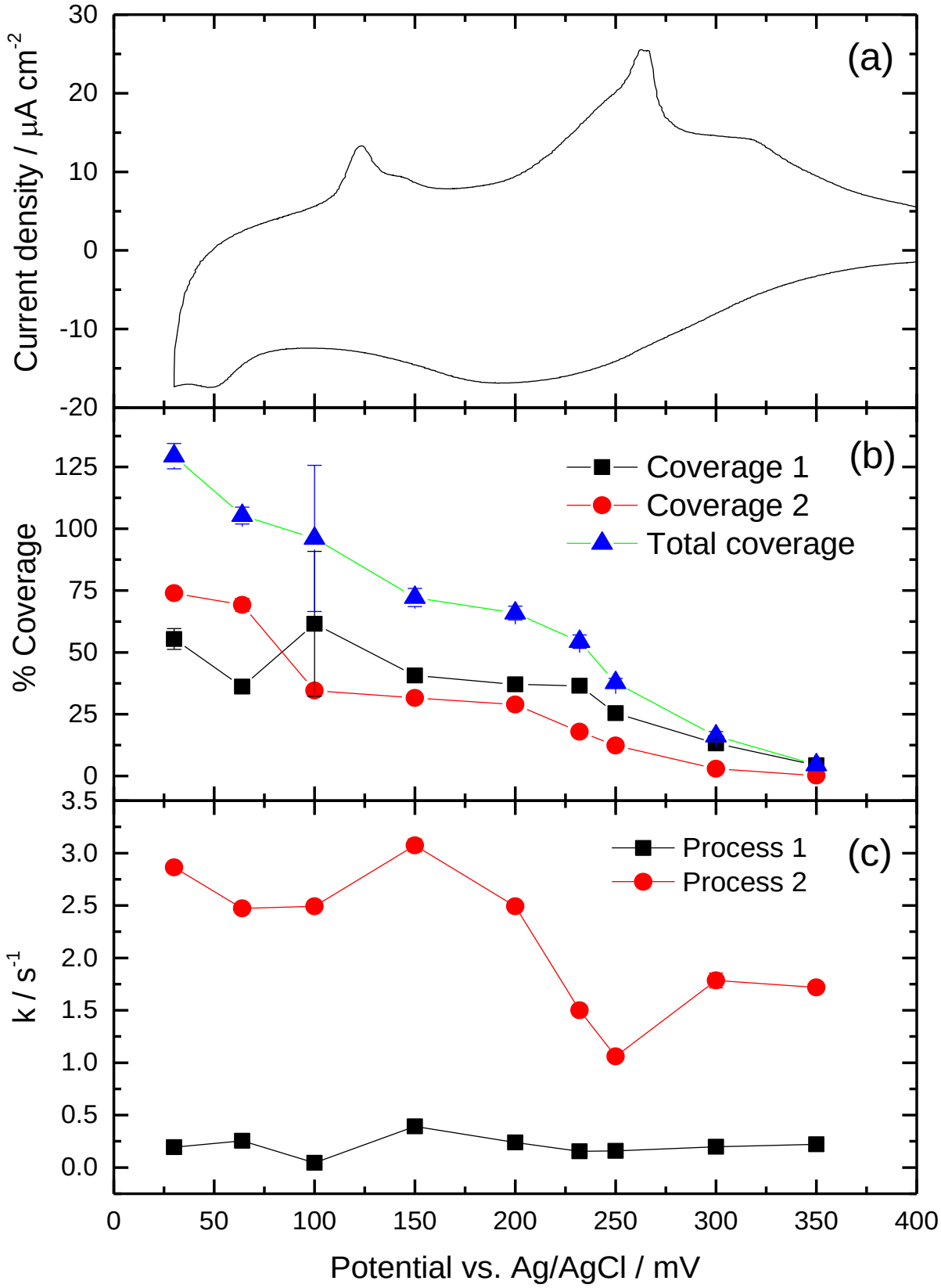

Figure 6.8 a) *Cyclic voltammetry of the of Au(111) in 1 mM $CuSO_4$ / 0.1 M H_2SO_4.* ***b)*** *Total coverage (blue) obtained from the fits to the transients by process 1 (black) and process 2 (red).* ***c)*** *Time constants obtained from the same fits by process 1 (black) and process 2 (red).*

6.3.2. Surface X-Ray Diffraction Analysis

Along with the electrochemical characterisation, *in situ* XRV scans were taken to observe any structural changes. As mentioned in *Section 2.2.8.*, in XRV the scattered intensity from the X-Rays is measured as a function of the applied electrochemical potential at specific reciprocal-lattice points along the Au(111) crystal truncation rods (CTRs). These points are sensitive to structural changes at the interface. [31]

6.3.2.1. X-Ray Voltammetry

XRV scans were obtained for the 1 mM $CuSO_4$ / 1 M H_2SO_4 system on Au(111). In *Figure 6.9* the intensities measured at ($^2/_3$ $-$ $^1/_3$ 1.2), (0 0 1.8), (1 0 3.6) and (0 0 3.3) positions are depicted together with the 5 mV s^{-1} scan CV from *Figure 5.1*. The scans started at 0.6 V where no significant features were observed at the cyclic voltammogram, scanning cathodically up to 0.03 V and then reversing the potential back to the starting point. A common trend observed in all the XRVs is the change in intensity at 0.2 V which coincides with the completion of the ($\sqrt{3}$ x $\sqrt{3}$)R30° honeycomb structure and has been highlighted with a blue dashed line.

The position at ($^2/_3$ $-$ $^1/_3$ 1.2) is specifically sensitive to the ($\sqrt{3}$ x $\sqrt{3}$)R30° structure and the intensity is stable starting from the most positive underpotentials until 0.2 V which corresponds to the first Cu UPD peak and afterwards, the intensity increases. In the anodic direction the intensity follows a similar pattern where it decreases sharply after 0.2 V and then remaining stable until the positive end. The sharp change observed at 0.2 V is a confirmation of the formation and lifting of the ($\sqrt{3}$ x $\sqrt{3}$)R30° structure. Also, it needs to be mentioned that the sharp change in intensity at this potential was reported by Nakamura *et al.* [32] (*Figure 6.9a*)

Additionally, the (0 0 1.8) position on the specular CTR (0 0 L) is sensitive to the electron density profile and mass transport of metal adatoms and monitors any adsorption/desorption processes. At the (0 0 1.8) (*Figure 6.9b*) position the intensity begins to increase gradually up to 0.2 V and directly after this potential it drops drastically as well. The sharpness of the peak implies that the ($\sqrt{3}$ x $\sqrt{3}$)R30° structure formed is present over a narrow potential window range. Thus, it can be further implied that a well-ordered ($\sqrt{3}$ x $\sqrt{3}$)R30° structure is formed up to 0.2 V.

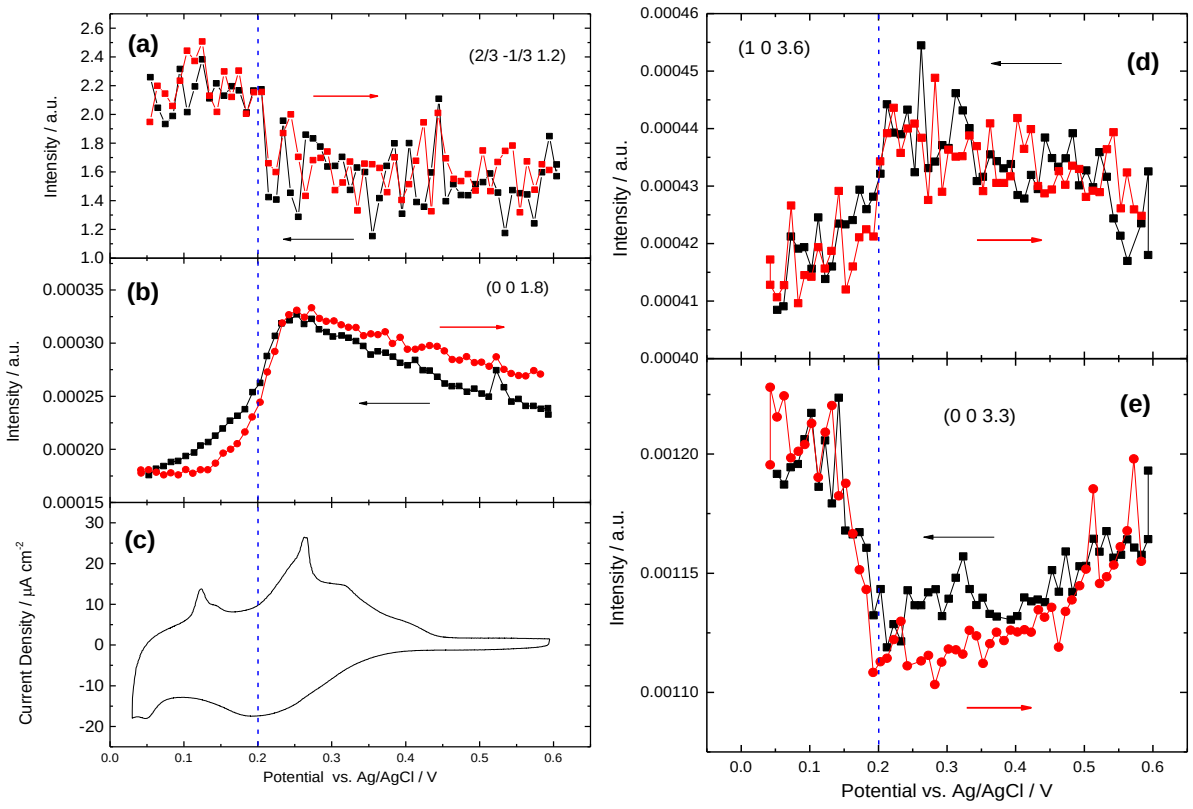

Figure 6.9 *X-Ray Voltammetry of Au(111) in 0.1 M H_2SO_4 + 1 mM $CuSO_4$, obtained* ***(a)*** *at the (2/3 -1/3 1.2) position, sensitive to the (√**3** x √**3**)R30º structure,* ***(b)*** *at the specular anti-Bragg position (0 0 1.8), shown together with* ***(c)*** *the corresponding cyclic voltammogram taken in the electrochemical cell. XRV, obtained at the* ***(d)*** *(1 0 3.6) and* ***(e)*** *(0 0 3.3) positions in the same electrolyte. All data was measured at a scan rate of 5 mV s^{-1}. The blue dashed line at 0.2 V indicates the sharp changes on the XRVs and attributed to the copper structural changes on Au(111).*

Moreover, the intensity at the (1 0 3.6), a position sensitive to surface relaxation, (*Figure 6.9d*) shows a drop in intensity after 0.2 V. This is an indication that the formation of the (√3 x √3)R30º structure is relaxing the top layers of the underlying substrate, the Au(111) single crystal, a phenomenon also reported by Nakamura *et al.* [32]

On the other hand, at the (0 0 3.3) position on the specular CTR (*Figure 6.9e*) we can observe a significant increase in intensity after 0.2 V, consequently after the first Cu UPD phase, possibly implying the formation of the (√3 x √7)R19.1º sulphate layer on top of the Cu – (1 x 1) structure.

6.3.2.2. Crystal Truncation Rods (CTRs)

In order to provide a structural model for the 1 mM $CuSO_4$ / 0.1 M H_2SO_4 system Crystal Truncation Rods (CTRs) were recorded at the I-07 beamline at Diamond Light Source. Two sets of CTRs were recorded along the specular (0 0 L) and non-specular, (0 1 L) and (1 0 L), directions; one at 0.58 V where according to the CVs (*Figure 6.4*) no copper is present on the Au(111) surface and the other one at 0.2 V where the first Cu UPD peak and the ($\sqrt{3}$ x $\sqrt{3}$)R30° structure is formed.

All three CTRs were modelled at the same time. The comparison of each CTR between the two potentials is shown in *Figure 6.10*. The solid line in every graph shows the best theoretical fit obtained for the experimental data points using a model including the expansion of the layers, ε_{ij}, the Debye-Waller factors, σ_i, the distance of the layers, d_i and the coverage, Θ_i for the adlayers. The coverage, Θ of the three top gold layers was fixed at 1 and each data point assumed a 10% systematic error. The best fits to the data were obtained after incorporating an oxygen adlayer and an error function for both potentials and for the 0.2 V potential a copper adlayer with a ($\sqrt{3}$ x $\sqrt{3}$)R30° structure. The parameters that gave the best fits from the CTRs are listed in *Table 6.2*

		0.58 V	0.2 V
Metal Layers	ε_{23} / Å	0.010 ± 0.006	0.017 ± 0.002
	ε_{12} / Å	-0.047 ± 0.009	-0.021 ± 0.002
	σ_2 / Å	0.07 ± 0.01	0.10 ± 0.01
	σ_1 / Å	0.21 ± 0.01	0.19 ± 0.01
($\sqrt{3}$ x $\sqrt{3}$)R30° Layer	Θ	N/A	0.67 ± 0.20
	d_{Cu} / Å		2.46 ± 0.32
	d_{SO4} / Å		0.88 ± 0.2
	σ_{Cu} / Å		0.05
	σ_{SO4} / Å		0.05
Oxygen Adlayer	Θ	0.68 ± 0.35	0.54 ± 037
	d / Å	5.67 ± 0.19	5.19 ± 0.37
	σ / Å	*0.1*	0.34 ± 0.07
Error Function	d / Å	6.68 ± 0.35	6.03 ± 1.50
	σ / Å	0.47 ± 0.56	1.04 ± 2.07
Reduced χ^2		3.49	3.98

Table 6.2 *Parameters giving best fits to the experimental data for the Au(111) / 1 mM $CuSO_4$ / 0.1M H_2SO_4 system. The left hand side (red background) show the parameters giving the best fit to the data at 0.58 V. The parameters on the right hand side (blue background) correspond to the parameters at 0.2 V.*

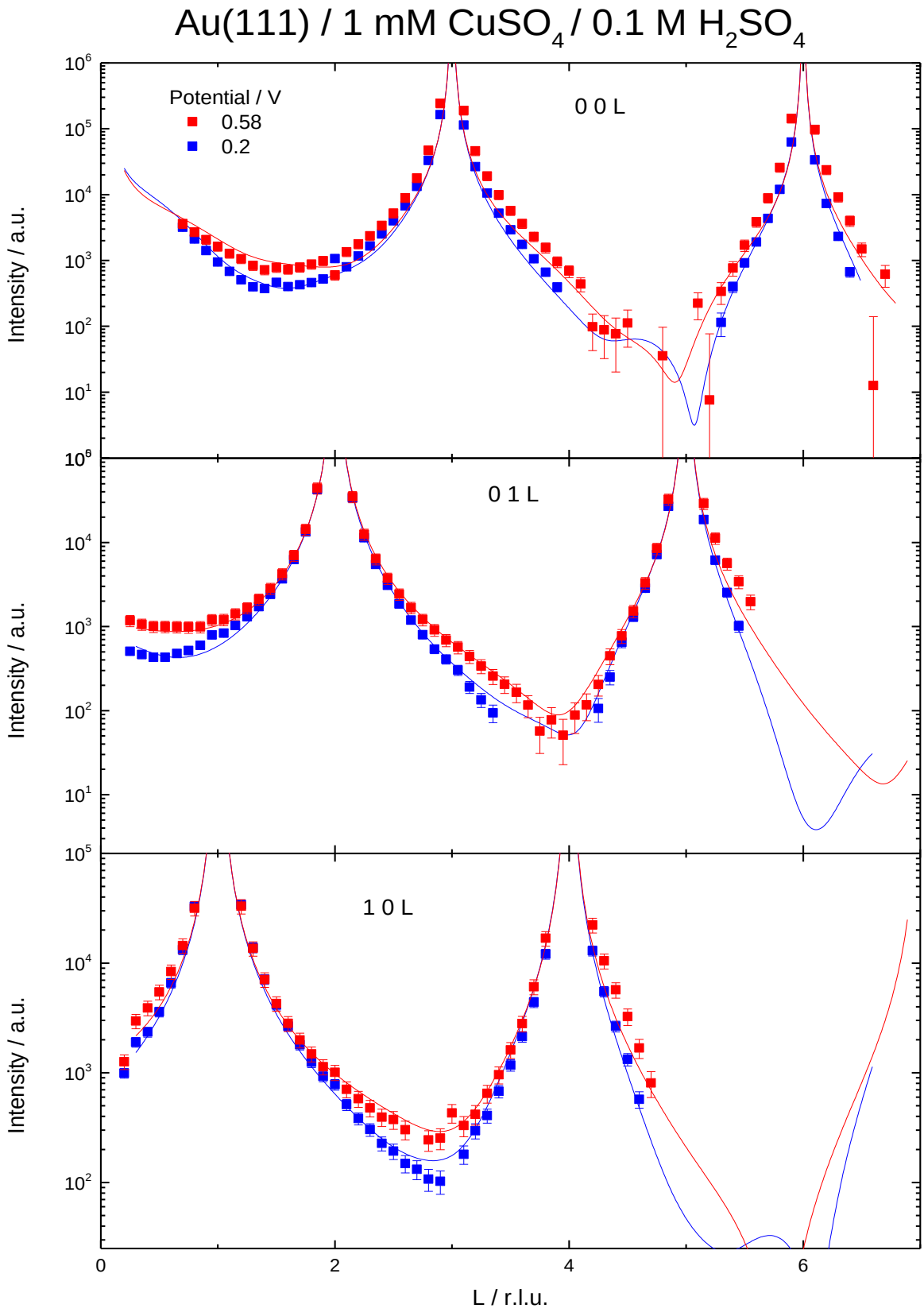

Figure 6.10 *Fits to specular (0 0 L) and non-specular (0 1 L) and (1 0 L) Crystal Truncation Rods for the Cu(111) / 1 mM $CuSO_4$ / 0.1M H_2SO_4 system. The red and blue points correspond to the data measured at 0.2 and 0.5 V respectively. The best fits to these are shown with the respective red and blue solid lines. Error bars include an assumed 10% systematic error.*

First of all, the adlayer coverage of the ($\sqrt{3}$ x $\sqrt{3}$)R30^o honeycomb structure at 0.2 V provided was at 0.67 ± 0.20 a value which is in agreement with the respective one obtained after the analysis of the chronoamperometry transients in *Section 6.3.1.2.* and is also within error with the value reported by Toney *et al.* [12] Furthermore, the spacing of Au – Cu and Cu – S were found at 2.46 ± 0.36 Å and 0.88 ± 0.3 Å which is in good agreement with the literature. [32]

Then, the interlayer spacing between the top two gold layers, ε_{12} had an *inwards* relaxation of -0.021 Å which after the formation of the ($\sqrt{3}$ x $\sqrt{3}$)R30^o copper structure decreased to -0.047 Å. This further confirmed the assumption from *Section 6.3.2.1.* that the ($\sqrt{3}$ x $\sqrt{3}$)R30^o structure is *inwards* relaxing the top Au layers of the underlying substrate.

It is therefore determined from the SXRD analysis the presence of the ($\sqrt{3}$ x $\sqrt{3}$)R30^o copper structure at 0.2 V with a 0.67 ML coverage. The existence of this structure instigates an *inwards* relaxation effect on the top Au layers. Finally, it must be noted that the two different copper structures formed on Au(111) have diverse contributions on the top gold layers and the resulting intensity as in all the XRVs presented in *Figure 6.9* there is a change in intensity at 0.2 V which is the onset potential value for the rearrangement of the copper atoms.

6.4. Acetonitrile Addition

6.4.1. Electrochemical Characterisation

To study the influence of acetonitrile on Cu UPD, the same electrochemical techniques were used in the addition of 10 mM and 4 M of AcN, respectively to the 1 mM $CuSO_4$ / 0.1 M H_2SO_4 to characterise the systems. The acetonitrile concentrations reported here were chosen to show the influence of a slight addition and in excess of the organic additive. 1 M acetonitrile was investigated as well. Nevertheless, due to poor quality of the data it was discounted and not presented in this thesis.

6.4.1.1. Cyclic Voltammetry

Initially, as with the study of Cu UPD in pure sulphuric acid, cyclic voltammograms at different scan rates were recorded after adding the two aforementioned concentrations and presented in *Figure 6.11* to determine any impact acetonitrile has on copper UPD and how the changes vary with acetonitrile concentration increase.

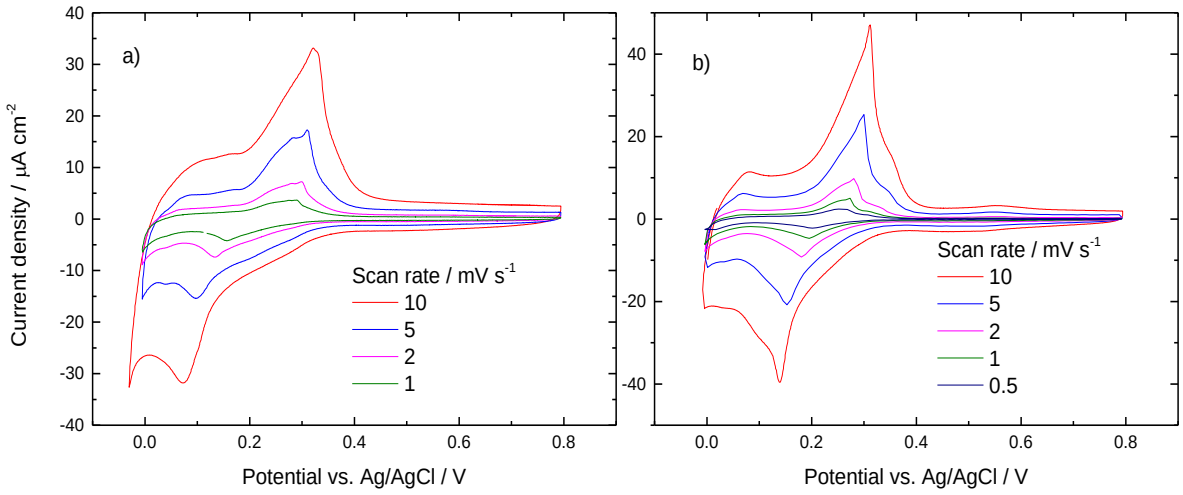

Figure 6.11 *Cyclic voltammograms of Au(111) in 1 mM $CuSO_4$ / 0.1 M H_2SO_4 / x M Acetonitrile in different scan rates.* ***a)*** *x = 0.01,* ***b)*** *x = 4.*

The comparison between different scan rates at the 10 mM and 4 M acetonitrile concentration is shown in *Figure 6.11*. The most prominent feature of the CVs is that the deposition and desorption peaks are at different potential values at varying scan rates. A major difference between the CVs in *Figures 6.4* and *6.11* is that, under the presence of acetonitrile, as the scan rate decreases the peak separation also decreases for both additions.

The difference between the deposition and desorption peak position values from *Figure 6.11* are given in *Table 6.3*. The difference between the two potentials, ΔE, is summarised at different scan rates and the data is presented in *Figure 6.13*. It becomes evident that the lowest value is obtained at 4 M addition and scan rate of 0.5 V s^{-1}, where the difference between the two peaks obtain a value of ΔE = 50 mV which leads to the assumption that copper deposits faster at slower scan rates in higher acetonitrile concentrations. As a result, it is suggested that increase in acetonitrile concentration leads to an increased deposition rate of copper and additionally, reduction of the scan rate produces also an increased copper deposition rate irrespective of acetonitrile concentration.

Scan rate / mV s^{-1}	**+ 10 mM Acetonitrile**			**+ 4 M Acetonitrile**		
	$E_{desorption}$ / V	$E_{deposition}$ / V	ΔE / V	$E_{desorption}$ / V	$E_{deposition}$ / V	ΔE / V
10	0.323	0.074	0.249	0.312	0.140	0.172
5	0.309	0.097	0.212	0.300	0.153	0.147
2	0.301	0.134	0.167	0.281	0.180	0.101
1	0.29	0.154	0.136	0.274	0.195	0.079
0.5	N/A			0.252	0.202	0.050

Table 6.3 *Summary of the peak separation values showed in Figure 6.11*

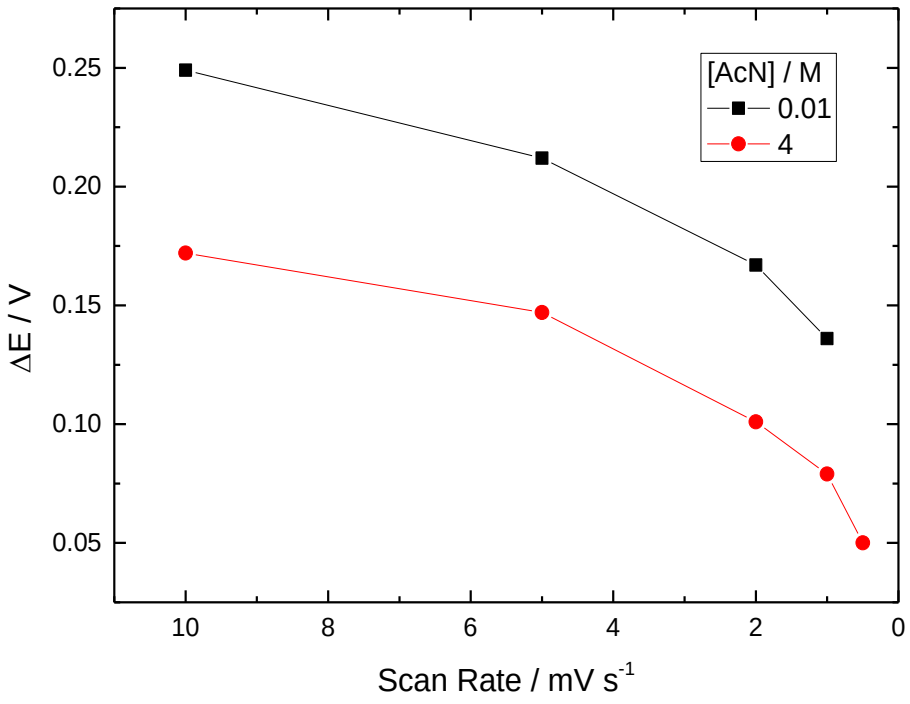

Figure 6.12 *Peak separation between deposition and dissolution of copper UPD as a function of the scan rate for acetonitrile additions for 0.01 M (black) and 4 M (red) acetonitrile concentration.*

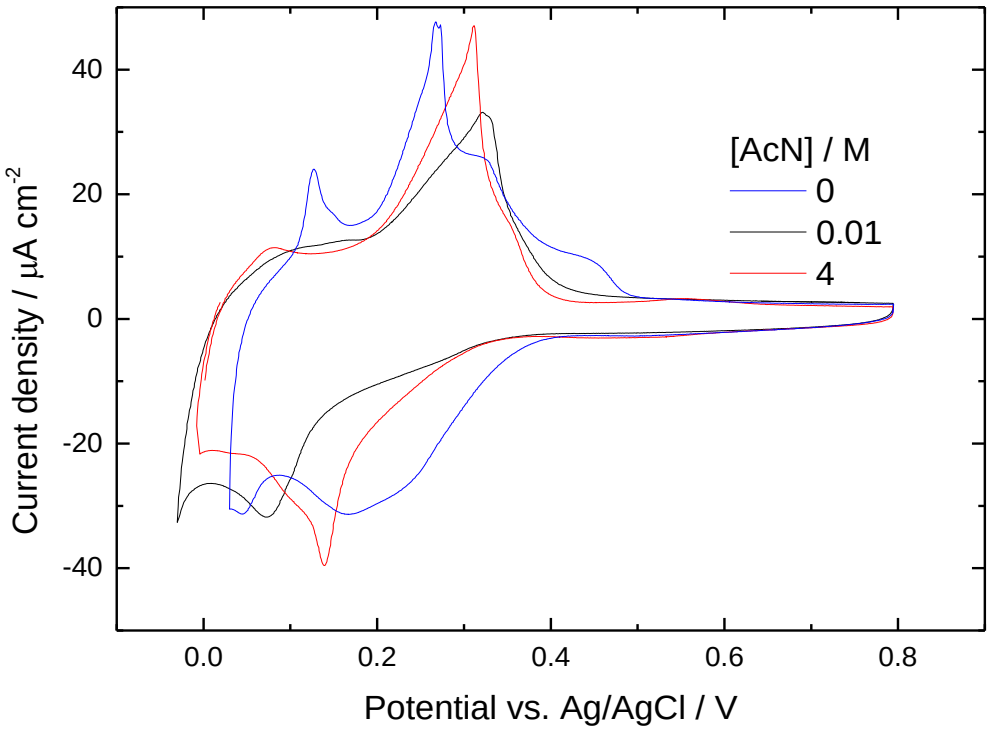

Figure 6.13 *Cyclic voltammogram of Au(111) in 1 mM $CuSO_4$ / 0.1 M H_2SO_4 in different concentrations of Acetonitrile. Scan rate: 10 mV s^{-1}*

Figure 6.13 shows the CV comparison between acetonitrile concentrations as well as a scan where no acetonitrile was incorporated for comparison. The scan rate of 10 mV s^{-1} was chosen for this comparison as the features discussed below are more noticeable.

Initially, the addition of 10 mM of acetonitrile inhibits Cu deposition, evident by: firstly, the negative shift of the cathodic peak from 0.2 V to 0.074 V due to Cu atoms having to displace AcN ions and also, by the positive shift of the anodic peak from 0.25 V to 0.323 V due to acetonitrile molecules adsorbed on top of the copper adatoms. Afterwards, the addition of 4 M acetonitrile causes a positive shift of the cathodic deposition peak to 0.14 V while the anodic stripping is slightly shifted to 0.312 V.

Addition of Acetonitrile instigates a peak separation between deposition and desorption peaks in comparison to when the organic molecule was not present in the solution. The large peak separation observed for 10 mM acetonitrile indicates slow electron transfer kinetics. However, increasing acetonitrile concentration to 4 M decreases the peak separation and indicates that the transfer kinetics become faster. [34] This occurrence has further established the hypothesis that copper deposits faster with increasing acetonitrile concentration. It can also be observed that with acetonitrile a single deposition peak is present in comparison to the two peaks in pure sulphuric acid, suggesting that only one copper structure is formed.

6.4.1.2. Chronoamperometry

After obtaining cyclic voltammograms for each acetonitrile addition, chronoamperometric transients were recorded in the respective system. The potential was held at 0.6 V since no copper was present on the Au(111) surface for 20 seconds and then switched to a more negative potential which was then held for 60 seconds. The shape of the chronoamperometric curves depend largely on the value of the final potential.

In *Figure 6.14* the current transients (*black dots*) more negative than 150 mV have a bump indicating that at least one of the nucleation processes is either instantaneous without surface diffusion or progressive. In the same manner with the 0.1 M H_2SO_4 + 1 mM $CuSO_4$, presented in *Section 6.3.1.2.* the chronoamperometry transients could be modelled with two processes. The chronoamperometric curves presented in *Figure 6.5* were fit according to the Avrami equation (*Equation 6.1*) to determine the copper coverage, the electron transfer rate and the nucleation type. For better explanation and easier follow, this section will be split into two sub-sections, one for each addition.

a) 10 mM Acetonitrile

+ 10 mM Acetonitrile								
	Process 1		Process 2		Proc. 1	Proc.2	**Total**	χ^2
$E_{fin.}$ / mV	S_1 / A s^{-1}	k_1 / s^{-1}	S_2 / A s^{-1}	k_2 / s^{-1}	%Coverage			
300	-1.1290e^{-5}	0.3795	-5.8600e^{-6}	2.2090	6.215	6.452	**12.667**	**1.22**
250	-2.8369e^{-5}	0.2308	-9.3810e^{-6}	1.4170	15.617	10.328	**25.945**	**1.64**
200	-5.9944e^{-5}	0.1814	-1.5191e^{-5}	1.2628	32.999	16.725	**49.724**	**0.84**
150	-2.2367e^{-4}	0.0700	-2.6573e^{-5}	0.9210	123.130	29.257	**152.386**	**0.28**
100	-2.1864e^{-4}	0.1313	-3.4828e^{-5}	0.0046	120.361	38.345	**158.706**	**0.59**
50	-2.6254e^{-4}	0.1328	-5.9770e^{-5}	0.1056	144.527	65.806	**210.333**	**0.82**
20	-2.7172e^{-4}	0.1980	-4.3261e^{-5}	0.2440	149.581	47.630	**197.211**	**0.28**
0	-2.7393e^{-4}	0.2630	-3.4116e^{-5}	0.4510	150.798	37.561	**188.359**	**0.28**

Table 6.4 *Summary of the fit models after the analysis of every current transient using the Avrami equation for the 0.1 M H_2SO_4 + 1 mM $CuSO_4$ + 10 mM Acetonitrile.*

In *Figure 6.14* the obtained current transients for the 1 mM $CuSO_4$ / 0.1 M H_2SO_4 / 10 mM acetonitrile system on Au(111) along with the best fits and the contribution of each of the two separate processes are presented. The best fits were acquired when the exponent's value for the first process, $j_1(t)$, was fixed at $m_1 = 1$ throughout the whole deposition potential region.

But, for the second process, $j_2(t)$, the exponent's value was varying, ranging from $m_2 = 1$ for the higher underpotentials before the UPD peak at 100 mV to a larger integer value, $m_2 = 2$ or 3, for the lower underpotentials after the UPD peak. At this point, it must be noted that acetonitrile in aqueous solution obtain a +1 transfer charge in the form of CH_3CN^+ [33] and thus for the calculation of the acetonitrile coverage one electron transfer is assumed.

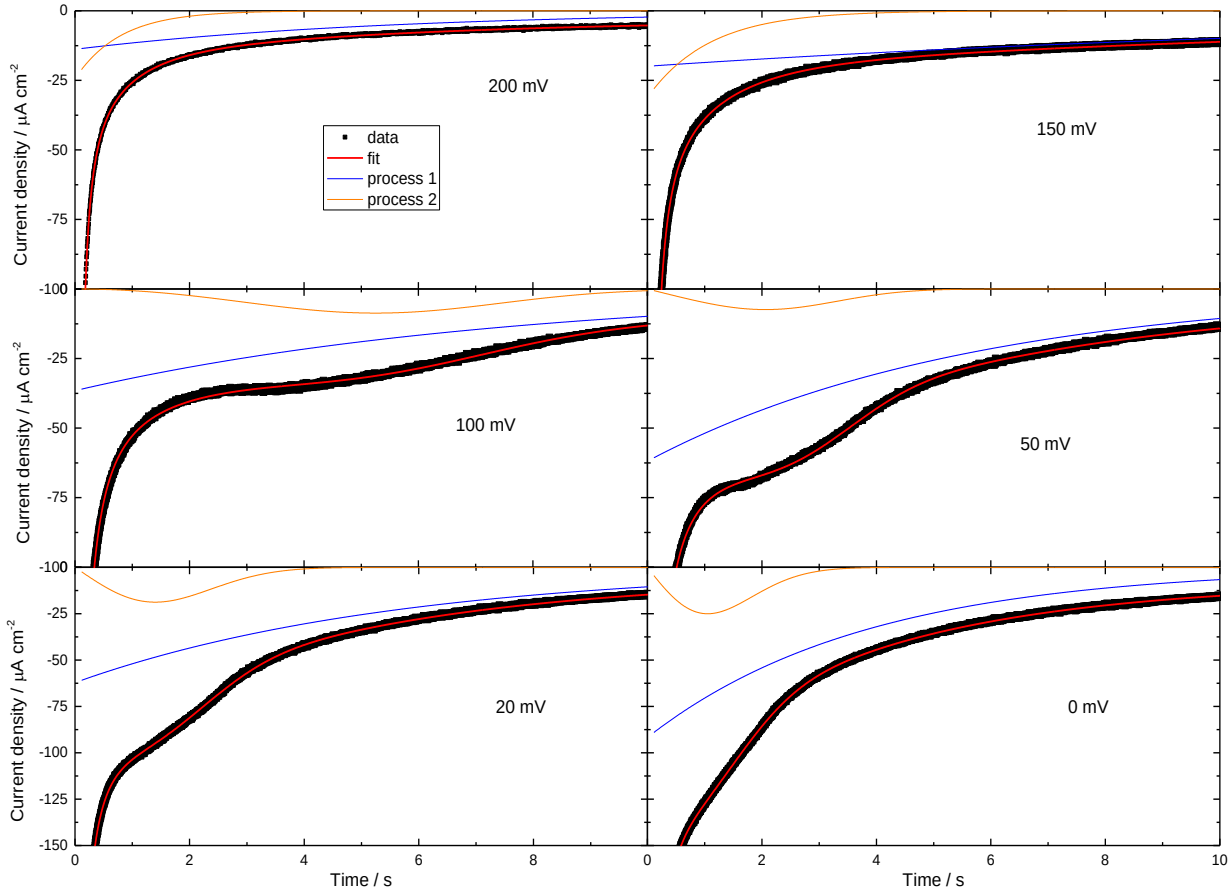

Figure 6.14 *Current transients after potential steps from 600 mV to more negative potentials in 0.1 M H_2SO_4 + 1 mM $CuSO_4$ + 10 mM Acetonitrile. The experimental data is shown together with best fits, obtained by assuming two separate processes, each described by the Avrami equation.*

From the data presented in *Table 6.4*, the first process, $j_1(t)$, can be allocated to the copper ions and the second process, $j_2(t)$, to acetonitrile adsorption ions. According to Rudnev *et al.*, in presence of acetonitrile, the Cu UPD is hindered due to blocking of electrode surface with organic molecules that are strongly adsorbed. [34] Until the UPD peak, for both acetonitrile concentrations, both processes have instantaneous nucleation growth with surface diffusion suggesting a simultaneous adsorption and competition for the adsorption sites on the Au(111) crystal surface. Afterwards, as the potential is stepped to values more negative than the UPD peak the exponent value of $j_2(t)$ changed to $m_2 = 3$, the nucleation of the process becomes

progressive and directly afterwards, on the next potential step after the UPD peak the nucleation turns into instantaneous ($m_2 = 2$) and therefore not limited by surface diffusion.

The results from *Table 6.4* are shown in *Figure 6.15* as a function of potential together with the 10 mV s^{-1} CV (*Figure 6.15a*). The graph depicts how the coverage (*Figure 6.15b*) and the time constant (*Figure 6.15c*) change during copper UPD. It is observed in *Table 6.4* and *Figure 6.15b* that in presence of acetonitrile the final copper coverage exceeds the limit of 1 ML at the UPD potential region and reaches a final value of Θ_{Cu} of 1.5 ML at 0 mV. While the coverage of copper constantly increases, the coverage of acetonitrile gradually increases until the deposition peak potential at 50 mV and then decreases again. Thus, by evaluating the coverage values of the two processes it becomes immediately evident that the presence of acetonitrile enhances the copper deposition rate as and after the peak deposition potential more copper ions replace acetonitrile molecules.

Regarding the transfer kinetics of the two processes, presented in *Table 6.4*, the hindrance of the copper deposition can be confirmed by observing the time constants (*Figure 6.15c*). $j_2(t)$ attributed to acetonitrile ions begins as a faster process than $j_1(t)$, which has a low time constant ($k_1 < 1$) throughout the whole UPD potential region, and due to the competitiveness for the adsorption sites between the two processes, k_2 value is decreasing until the UPD peak and then begins to increase.

Therefore, it can be speculated that under the presence of acetonitrile, the organic molecules adsorb on the Au(111) surface rather quickly and faster than copper ions, but simultaneously, in the beginning of the UPD process. As the copper ions begin to compete for the adsorption sites, CH_3CN^+ ion deposition transfer kinetics gradually become slower and at the UPD peak potential it begins to increase again. Also, it is suggested that after the formation of a copper monolayer, more copper atoms are deposited on top of the monolayer and simultaneously acetonitrile molecules are bonded with the deposited copper atoms as exhibited in Chapter 5. Furthermore, the possibility of a complex formation in the solution between copper and acetonitrile atoms and its deposition either on the Au(111) crystal or the copper monolayer is also taken into account since both CH_3CN^+ and copper complexes with acetonitrile yield one electron at adsorption/deposition processes. Finally, both assumptions would justify the alteration of the nucleation type from instantaneous to progressive.

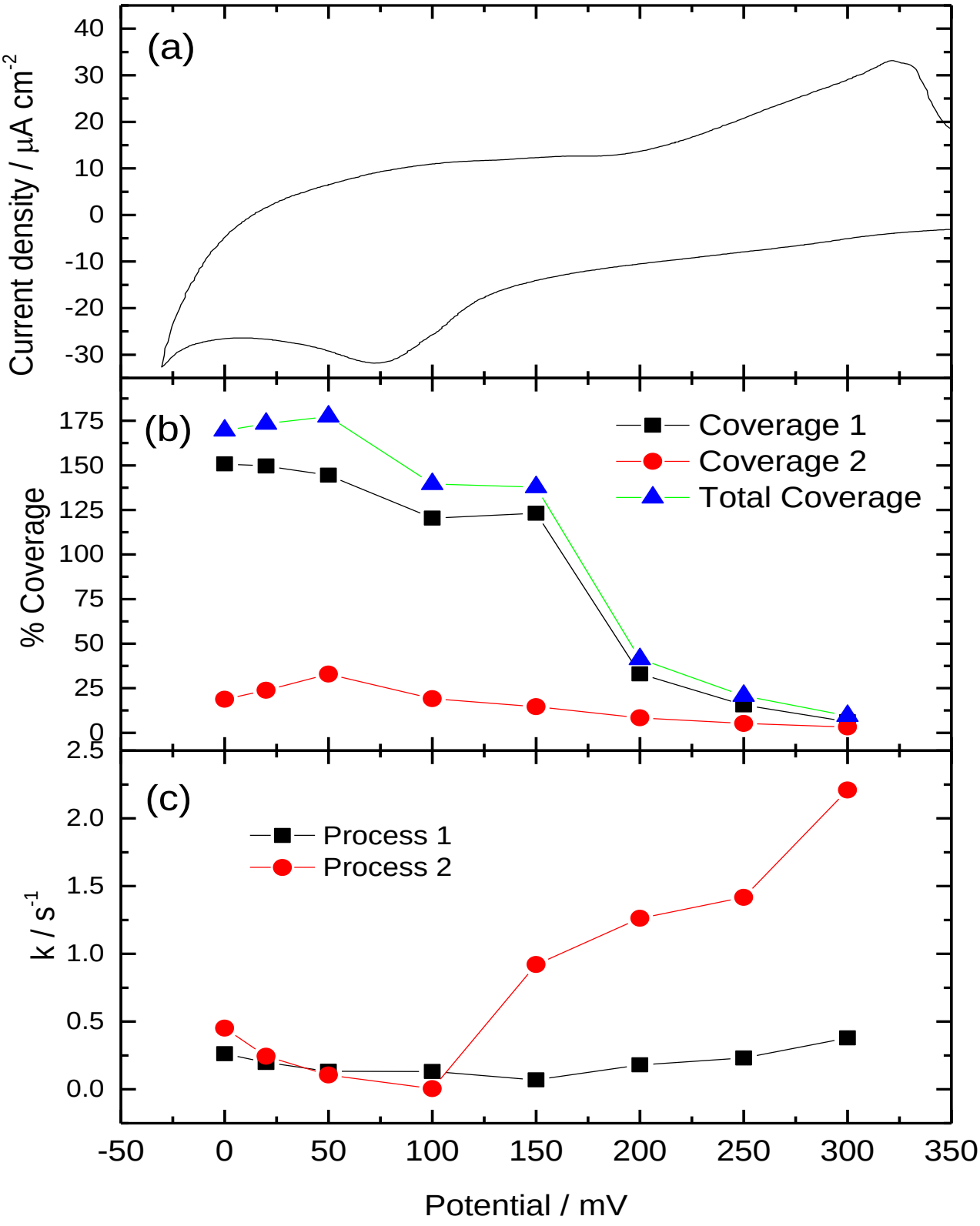

Figure 6.15 ***a)*** *Cyclic voltammetry of the of Au(111) in 1 mM $CuSO_4$ / 0.1 M H_2SO_4 /10 mM Acetonitrile at 10 mV s^{-1} scan rate.* ***b)*** *Total coverage (blue) obtained from the fits to the transients by process 1 (black) and process 2 (red).* ***c)*** *Time constants obtained from the same fits by process 1 (black) and process 2 (red).*

b) 4 M Acetonitrile

+ 4 M Acetonitrile								
	Process 1		Process 2		Proc. 1	Proc.2	**Total**	χ^2
$E_{fin.}$ / mV	S_1 / A s^{-1}	k_1 / s^{-1}	S_2 / A s^{-1}	k_2 / s^{-1}	%Coverage			
300	-8.3741e^{-6}	0.3742	-5.4940e^{-6}	2.5985	4.610	6.049	**10.659**	**4.546**
250	-2.8160e^{-5}	0.1910	-1.3630e^{-5}	1.0520	15.502	15.007	**30.509**	**1.038**
200	-1.4280e^{-4}	0.0812	-2.3600e^{-5}	0.6958	78.611	25.983	**104.594**	**0.449**
150	-1.7633e^{-4}	0.2140	-1.5037e^{-5}	0.0023	97.053	16.556	**113.608**	**0.831**
130	-2.1343e^{-4}	0.1793	-2.1090e^{-5}	0.00466	117.493	23.220	**140.713**	**1.023**
100	-2.1832e^{-4}	0.1920	-2.6420e^{-5}	0.05794	120.173	29.088	**149.262**	**1.742**
40	-2.4059e^{-4}	0.3060	-3.0322e^{-5}	0.7680	132.444	33.384	**165.828**	**2.085**
10	-2.3488e^{-4}	0.3250	-4.2860e^{-5}	1.8000	129.300	47.189	**176.489**	**2.064**

Table 6.5 *Summary of the fit models after the analysis of every current transient using the Avrami equation for the 0.1 M H_2SO_4 + 1 mM $CuSO_4$ + 4 M Acetonitrile. The concentration of Acetonitrile is shown on the table.*

In this section, the results of the chronoamperometric transients for the 1 mM $CuSO_4$ / 0.1 M H_2SO_4 / 4 M acetonitrile system on Au(111) are explained. In *Figure 6.16* the obtained current transients for the aforementioned system along with the best fits and the contribution of each of the two separate processes are presented. The outcome of the fits is presented in *Table 6.5*.

As previously mentioned, in the presence of acetonitrile, the process of copper deposition is impeded due to electrode surface blocking by CH_3CN^+ adsorption. [34] In a similar trend with the 10 mM acetonitrile addition, both processes begin with instantaneous nucleation growth with surface diffusion ($m_1 = m_2 = 1$) for high underpotentials until right before the UPD peak at $E_{fin.}$ = 200 mV. At $E_{fin.}$ = 150 mV, the potential of the UPD peak, the exponent value of $j_2(t)$ changed to $m_2 = 3$ obtaining a progressive nucleation and then to $m_2 = 2$ with an instantaneous nucleation for the rest of the potential steps.

A noticeable difference between the two additions is that at higher acetonitrile concentration, the complexation occurs at higher potentials implying faster complexation at the increase of acetonitrile concentration.

In *Figure 6.16* the obtained current transients for the 1 mM $CuSO_4$ / 0.1 M H_2SO_4 / 4 M acetonitrile system on Au(111) along with the best fits and the contribution of each of the two separate processes are presented. The best fits were acquired when the exponent's value for

the first process, $j_1(t)$, was fixed at $m_1 = 1$ throughout the whole deposition potential region. But, for the second process, $j_2(t)$, the exponent's value was varying, ranging from $m_2 = 1$ for the higher underpotentials before the UPD peak at 100 mV to a larger integer value, $m_2 = 2$ or 3, for the lower underpotentials after the UPD peak. At this point, it must be noted that acetonitrile in aqueous solution obtain a +1 transfer charge in the form of CH_3CN^+ [33] and thus for the calculation of the acetonitrile coverage one electron transfer is assumed.

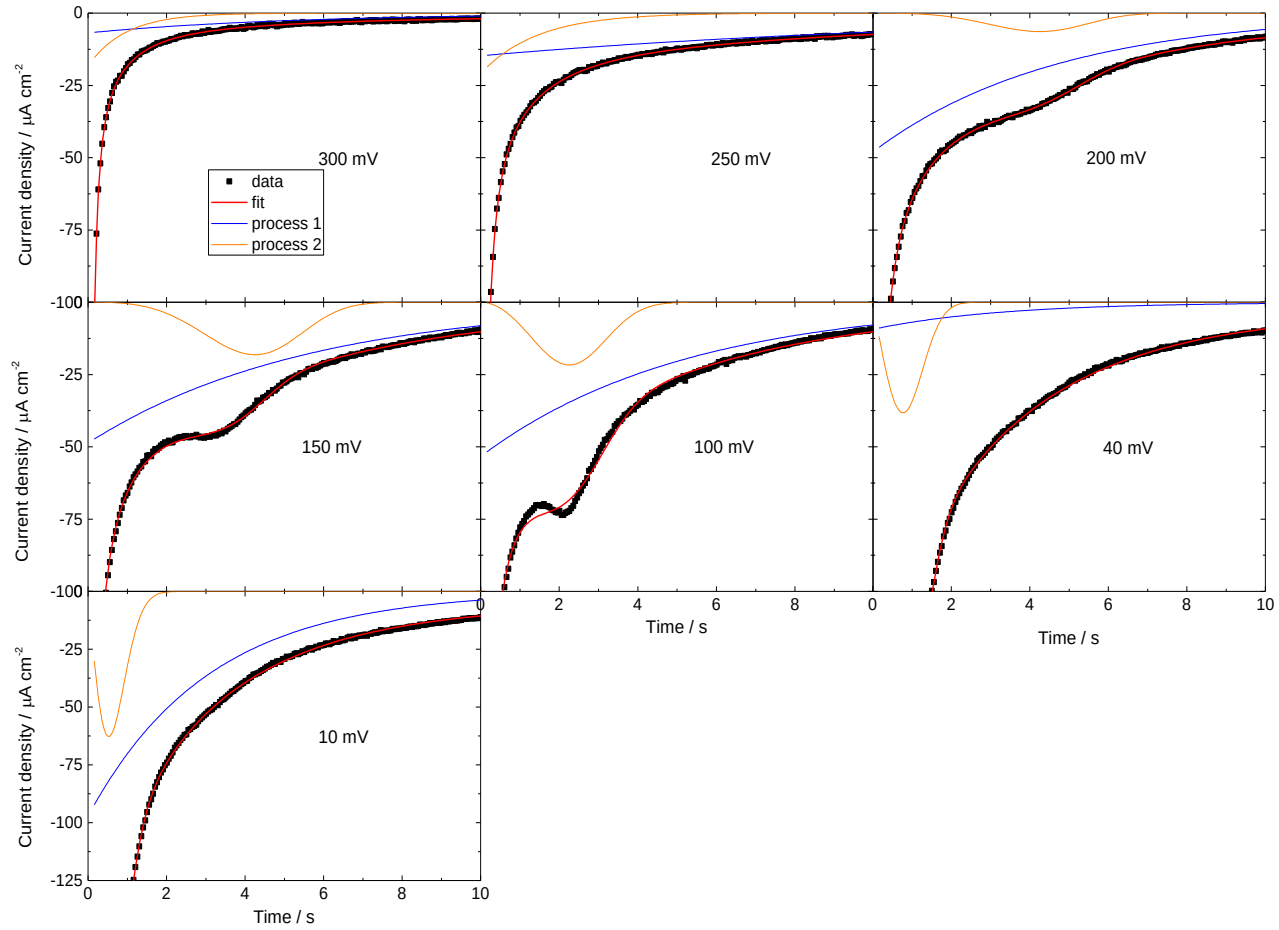

Figure 6.16 *Current transients after potential steps from 600 mV to more negative potentials in 0.1 M H_2SO_4 + 1 mM $CuSO_4$ + 4 M Acetonitrile, The experimental data is shown together with best fits, obtained by assuming two separate processes, each described by the Avrami equation.*

Similarly to the addition of 10 mM acetonitrile the results from *Table 6.5* are shown in *Figure 6.17* as a function of potential together with the 10 mV s^{-1} CV (*Figure 6.17a*). The graph depicts how the coverage (*Figure 6.17b*) and the time constant (*Figure 6.17c*) change during copper UPD.

Similarly to the addition of 10 mM acetonitrile the data presented in *Table 6.5* and *Figure 6.17b* shows that the final copper coverage exceeds one monolayer at the UPD potential region and reaches a final value of Θ_{Cu} of 1.3 ML at 10 mV. On the other hand, in contrast to 10 mM acetonitrile, in presence of 4 M acetonitrile in the most negative region the acetonitrile coverage increases while the copper coverage is decreasing. This is likely happening to due to a considerably larger amount of acetonitrile present in the solution. Thus, in this instance the acetonitrile molecules are substituting the copper atoms.

However, regarding the transfer kinetics of the two processes, presented as well in *Table 6.5*, there are similar results with those reported for 10 mM acetonitrile (*Figure 6.15c*). The time constants of the two processes have comparable values and the hindrance of the copper deposition is further confirmed as the $j_2(t)$ nucleation process, associated to the acetonitrile ions has a larger time constant at positive potentials, hence a faster process. The $j_1(t)$ nucleation process, which is attributed to copper atoms has a low time constant ($k_1 < 1$) throughout the whole UPD region. But, due to the competitiveness for the adsorption sites between the two processes, the k_2 value is gradually decreasing until the UPD peak where the nucleation process associated with copper deposition, $j_1(t)$ becomes faster as the $j_2(t)$ process obtains lower time constants for this region and after the deposition peak potential k_2 begins to increase.

Therefore, as already explained the acetonitrile molecules adsorb on the Au(111) surface rather quickly and faster than copper ions, in the beginning of the underpotential deposition. Then, as the electrochemical potential is scanned in the negative region, the copper ions begin to compete for the adsorption sites, and acetonitrile deposition transfer kinetics gradually become slower and afte the UPD peak potential it begins to increase again. Also, it is suggested that after the formation of a copper monolayer, more copper atoms are deposited on top of the monolayer and simultaneously acetonitrile molecules are bonded with the deposited copper atoms as exhibited in Chapter 5. Furthermore, the possibility of a complex formation in the solution between copper and acetonitrile atoms and its deposition either on the Au(111) crystal or the copper monolayer is also taken into account since both CH_3CN^+ and copper complexes with acetonitrile yield one electron at adsorption/deposition processes. Finally, both assumptions would justify the alteration of the nucleation type from instantaneous to progressive.

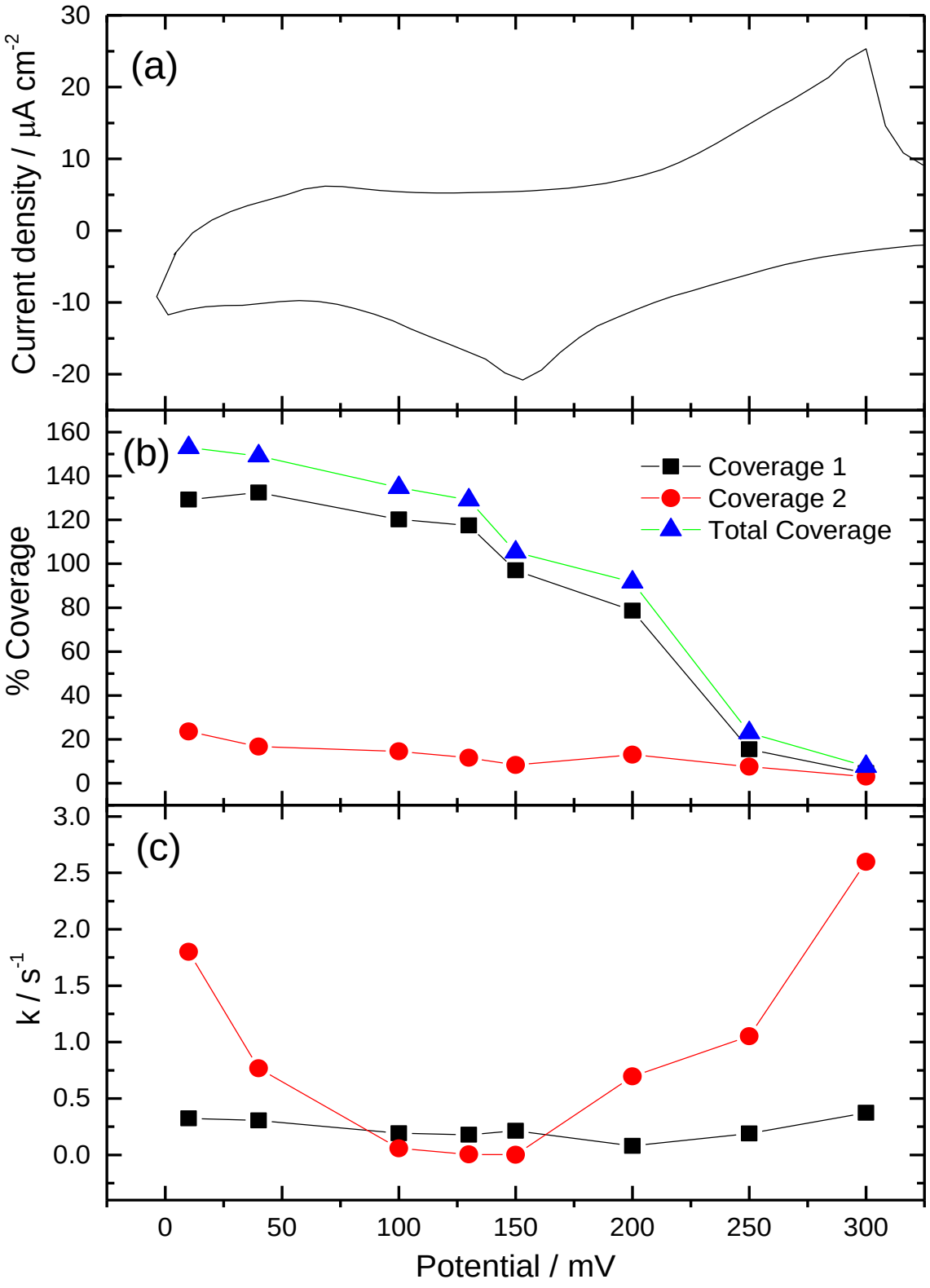

Figure 6.17 a) *Cyclic voltammetry of the of Au(111) in 1 mM $CuSO_4$ / 0.1 M H_2SO_4 /4 M Acetonitrile at 10 mV s^{-1} scan rate.* ***b)*** *Total coverage (blue) obtained from the fits to the transients by process 1 (black) and process 2 (red).* ***c)*** *Time constants obtained from the same fits by process 1 (black) and process 2 (red).*

6.4.2. Surface X-Ray Diffraction Analysis

6.4.2.1. X-Ray Voltammetry

In a similar fashion presented in *Section 6.3.2.1.* x-ray voltammograms (XRV) were taken for the 1 mM $CuSO_4$ / 0.1 M H_2SO_4 / 10 mM Acetonitrile system to express the influence of the organic molecule on the copper structure formed and any further structural changes observed on the Au(111) crystal. No x-ray data has been measured for the addition of 4 M acetonitrile and hence, it will not be presented.

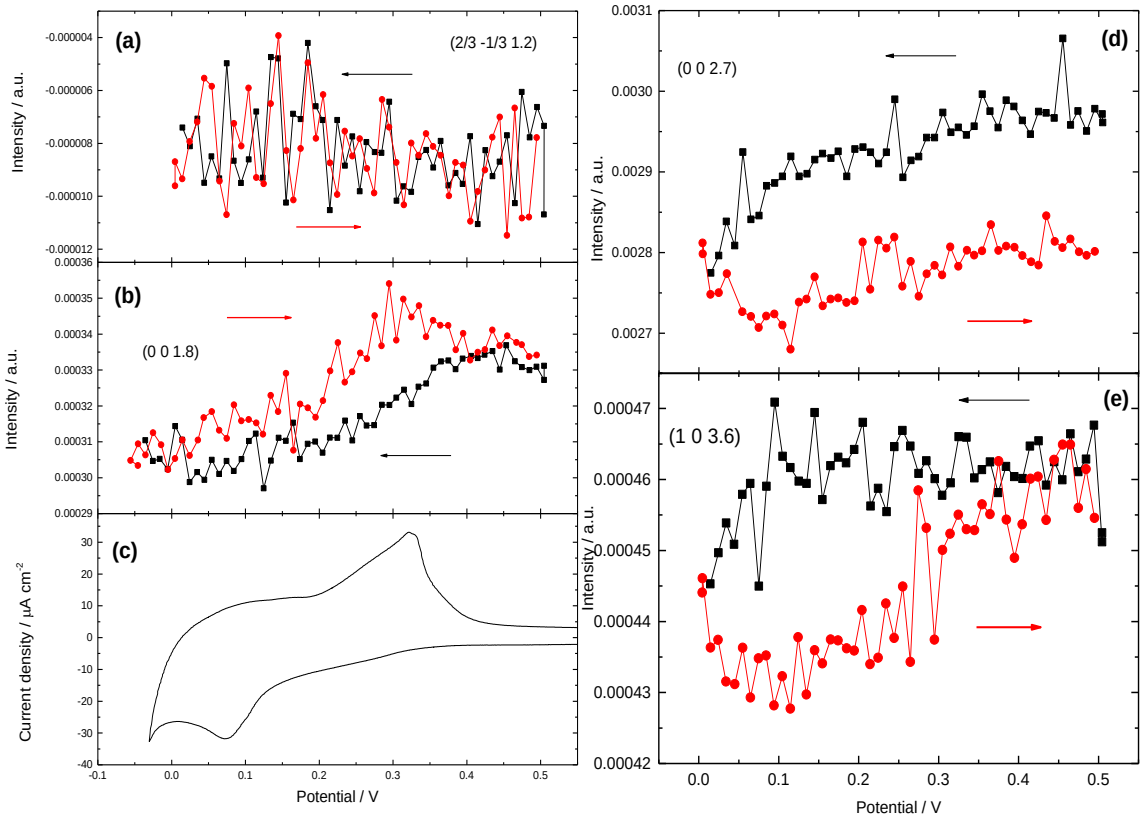

Figure 6.18 *X-Ray Voltammetry of Au(111) in 0.1 M H_2SO_4 + 1 mM $CuSO_4$ + 10 mM Acetonitrile, obtained* ***(a)*** *at the (2/3 -1/3 1.2) position, sensitive to the ($\sqrt{3}$ x $\sqrt{3}$)R30° structure,* ***(b)*** *at the specular anti-Bragg position (0 0 1.8), shown together with* ***(c)*** *the corresponding cyclic voltammogram. XRV, obtained at the* ***(d)*** *(0 0 2.7) and* ***(e)*** *(1 0 3.6) positions in the same electrolyte. All data was measured at a scan rate of 5 mV s^{-1}.*

In *Figure 6.18*, the X-Ray Voltammograms recorded at the same reciprocal lattice positions as with the 0.1 M H_2SO_4 / 1 mM $CuSO_4$ which were presented in *Figure 6.9* are shown. The most noticeable observation is at the ($^2/_3$ $-$ $^1/_3$ 1.2) position, where the intensity is very low with no significant changes for the whole potential region. (*Figure 6.18a*) This is an indication that under the presence of acetonitrile the ($\sqrt{3}$ x $\sqrt{3}$)R30° structure is absent

possibly due to the $[Cu(CH_3CN)_4]^+$ complex, formed by copper and acetonitrile atoms, hindering the formation of the honeycomb structure. [28] The intensity at the (0 0 1.8) position in *Figure 6.18b* steadily decreases as the potential is scanned towards the negative region and then when the potential scan is reversed increases to its initial intensity. This change in intensity is assumed to be caused by an ordering effect on the surface, in this instance copper deposition on Au(111). The same effect can also be concluded for the (0 0 2.7) position (*Figure 6.18d*) with a major difference being that the intensity does not return to its initial value, thus indicating an irreversible change on the Au(111) surface. Finally, at the (1 0 3.6) position (*Figure 6.18e*) it has been noticed a more prominent change in intensity accompanied with considerable hysteresis in comparison to the respective graph taken in the absence of acetonitrile (*Figure 6.7e*). This is indicative of a larger relaxation of the underlying Au(111) substrate.

Therefore, it is been proven that even a small amount of acetonitrile concentration is sufficient enough to alter the structure of the deposited copper on Au(111) and cause significant changes. The $(\sqrt{3} \times \sqrt{3})R30^o$ structure which is existent in the absence of the organic molecule was not detected in the XRVs. In addition, irreversible changes are taking place in presence of acetonitrile and a larger relaxation on the top gold layers has been detected.

6.4.2.2. Crystal Truncation Rods (CTRs)

To obtain a better understanding of the influence of acetonitrile on the process of copper under-potential deposition on Au(111) in sulphuric acid Crystal Truncation Rods (CTRs) were recorded at the I-07 beamline at Diamond Light Source. In a similar manner to *Section 6.3.2.2.*, two sets of CTRs were recorded along the specular (0 0 L) and non-specular, (0 1 L) and (1 0 L), directions. The first set was acquired at 0.58 V similarly to the pure sulphuric acid where according to the CVs (*Figure 6.11a*) no copper is present on the Au(111) surface. The other one at 0.2 V where the first the $(\sqrt{3} \times \sqrt{3})R30^{o}$ copper structure was formed in the absence of acetonitrile. The latter potential was chosen for direct comparison with the 1 mM $CuSO_4$ / 0.1 M H_2SO_4 system.

All three CTRs were modelled at the same time. The comparison of each CTR between the two potentials is shown in *Figure 6.19*. The solid line in every graph shows the best theoretical fit obtained for the experimental data points using a model including the expansion of the layers, ε_{ij}, the Debye-Waller factors, σ_i, the distance of the layers, d_i and the coverage, Θ_i for the adlayers. The coverage, Θ of the three top gold layers was fixed at 1 and each data point assumed a 10% systematic error. The best fits to the data were obtained after incorporating a carbon adlayer instead of oxygen due to the presence of acetonitrile and an error function for both potentials and for the 0.2 V potential two copper adlayers. The parameters that gave the best fits from the CTRs are listed in *Table 6.6.* The numbers in italics indicate the values that were fixed during the fitting procedure.

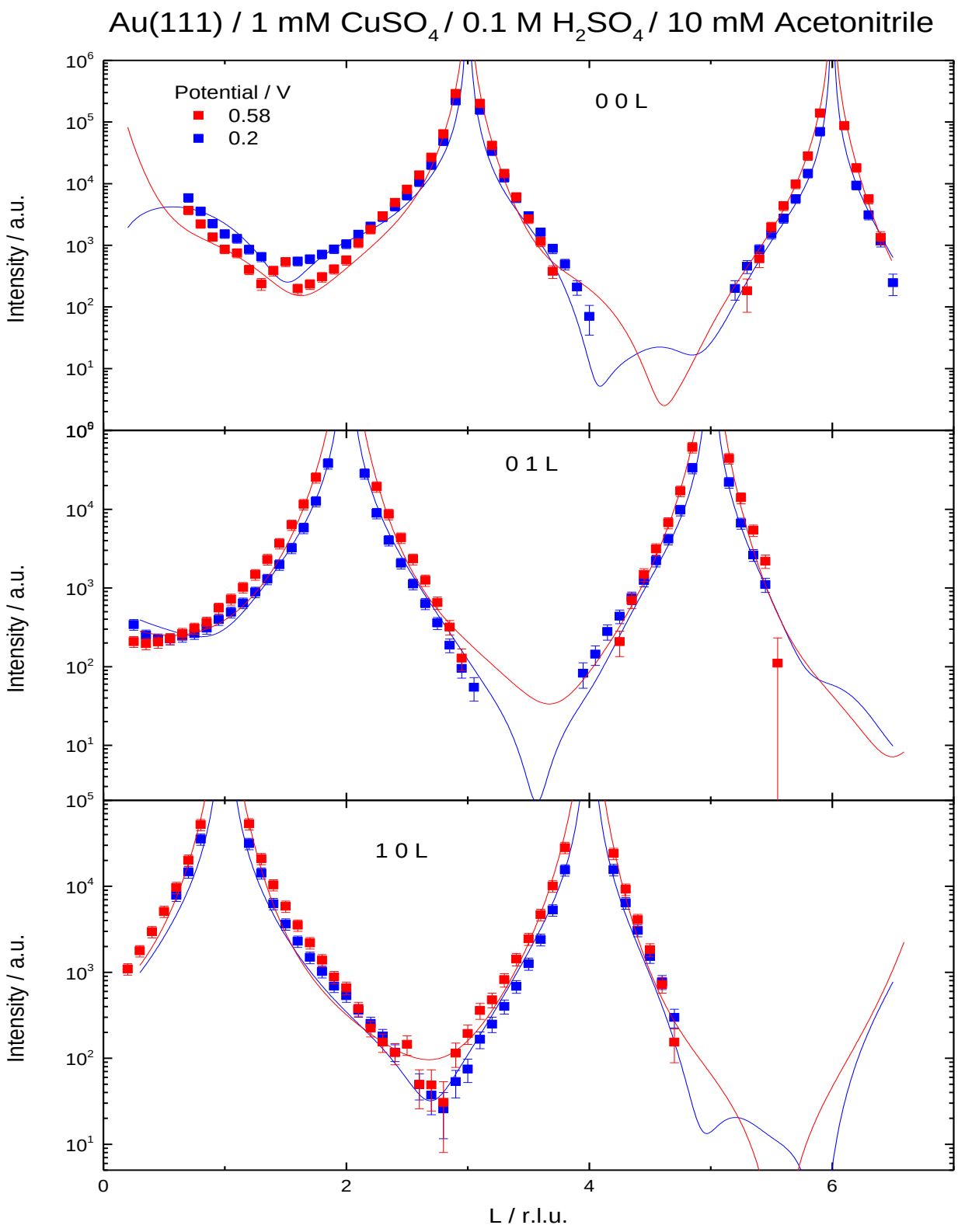

Figure 6.19 *Fits to specular (0 0 L) and non-specular (0 1 L) and (1 0 L) Crystal Truncation Rods for the Cu(111) / 1 mM $CuSO_4$ / 0.1M H_2SO_4 system. The red and blue points correspond to the data measured at 0.2 and 0.5 V respectively. The best fits to these are shown with the respective red and blue solid lines. Error bars include an assumed 10% systematic error.*

		0.58 V	0.2 V
Metal Layers	ε_{23} / Å	0.02 ± 0.01	0.000 ± 0.001
	ε_{12} / Å	-0.01 ± 0.01	0.014 ± 0.002
	σ_2 / Å	0.07 ± 0.03	0.100 ± 0.003
	σ_1 / Å	0.25 ± 0.02	0.22 ± 0.02
Copper Layer 1	Θ	N/A	0.82 ± 0.02
	d / Å		2.516 ± 0.07
	σ / Å		0.21 ± 0.11
Copper Layer 2	Θ		0.13 ± 0.07
	d / Å		3.07 ± 0.27
	σ / Å		*0.1*
Carbon Adlayer 1	Θ	1.05 ± 1.75	1.78 ± 2.33
	d / Å	1.09 ± 0.42	2.99 ± 0.7
	σ / Å	*0.15*	*0.15*
Carbon Adlayer 1	Θ	1.99 ± 1.33	1.99 ± 2.17
	d / Å	3.22 ± 4.98	3.59 ± 0.5
	σ / Å	*0.15*	*0.15*
Error Function	d / Å	0.07 ± 0.32	5.53 ± 0.35
	σ / Å	*0.5*	*0.5*
Reduced χ^2		3.73	5.11

Table 6.6 *Parameters giving best fits to the experimental data for the Au(111) / 1 mM $CuSO_4$ / 0.1M H_2SO_4 / 10 mM acetonitrile system. The left hand side (red background) show the parameters giving the best fit to the data at 0.58 V. The parameters on the right hand side (blue background) correspond to the parameters at 0.2 V. Numbers in italics indicate the values of the parameters that were fixed during the fitting procedure.*

Initially, the addition of acetonitrile initiates an *outwards* relaxation of the top two Au layers at 0.2 V potential by 0.014 Å in contrast to the *inwards* relaxation observed in the pure sulphuric acid. As with the chronoamperometric results there is a significant increase on the copper coverage, Θ_{Cu} deposited on Au(111) at the positive potential. As previously discussed in the electrochemical characterisation and in the XRV analysis in *Sections 6.4.1.1.* and *6.4.2.1.* respectively, the presence of acetonitrile molecules prevents the formation of the ($\sqrt{3}$ x $\sqrt{3}$)R30° honeycomb structure, due to competition of the molecules with the copper atoms, and thus, the co-adsorption of copper and (bi)sulphate ions in order for the honeycomb structure to be formed is prevented.

Furthermore, there is further evidence that acetonitrile enhances the deposition rate of copper on Au(111). At 0.2 V the value of copper coverage was calculated at 0.82 and 0.13 for the first and second copper layers with a total coverage of Θ_{Cu} = 0.95. The differences in the

copper coverages values between chronoamperometry and CTR analysis are attributed to the fact that the measurements were taken in different experiments. Thus, there might be a small deviation on the potential values resulting in this substantial copper coverage difference.

In both potentials the acetonitrile adsorption on Au(111) is apparent for both potentials. In addition, at 0.2 V the acetonitrile coverage has slightly increased as evidenced by the increase of the first carbon adlayer coverage.

However, the acetonitrile coverage calculated from the chronoamperometric transients was significantly less thus, presumably, this big difference in the calculations is attributed to the fact that chronoamperometry is a measure of electron transfer on the electrode surface whereas CTR profiles are sensitive to the structural changes occurring at the electrode/electrolyte interface and therefore, it is suggested the deposition of a copper-acetonitrile complex in the form of $[Cu(CH_3CN)_4]^+$. Along these lines, the suggested process could justify the large coverages of the carbon adlayers associated with the acetonitrile molecules. It must be noted, however, that a different approach to the model might potentially yield a better structural model.

6.5. Summary

The electrochemical characterisation of the analysis of the 0.1 M H_2SO_4 / 1 mM $CuSO_4$ system revealed a calculated copper coverage at 0.67 ML at the first and 1 ML at the second UPD peak at 0.2 V and 0.064 V vs. Ag/AgCl respectively. [1, 5, 12, 19] We have identified two separate copper processes where both contain instantaneous nucleation and 2D growth. The process with faster kinetics is taking place on surface defects and the slower process on well-ordered (111) terraces. [3] SXRD analysis further confirmed the existence of a $(\sqrt{3} \times \sqrt{3})R30^o$ honeycomb structure with a 0.67 ML coverage and additionally, the copper atoms produce an *inwards* relaxation effect on the top Au layers.

The addition of acetonitrile, even with a low concentration of 10 mM, has a clear effect on the copper deposition process. There is a noticeable peak separation in the cyclic voltammograms between copper desorption and deposition peaks caused by the hindrance of the acetonitrile molecules and the competition of the latter for the adsorption sites. This hysteresis decreased with slower scan rates and also with increase of acetonitrile concentration to 4 M suggesting that increase of acetonitrile concentration leads to an increase of the copper growth rate on Au(111) and reduction of the scan rate also produces an increase of the aforementioned growth rate independently of the acetonitrile concentration.

The increase of copper deposition rate at presence of acetonitrile was further evaluated by modelling the respective chronoamperometry transients. It was shown that the copper coverage exceeded 1 ML obtaining values of 1.5 ML and 1.3 ML for 10 mM and 4 M acetonitrile concentration respectively. The time constant of copper deposition was very low at the presence of acetonitrile and the time constant for the process of acetonitrile ions was considerably faster at high underpotentials and decreased at the UPD peak potential, irrespective of its concentration. The nucleation of copper ions remained instantaneous throughout the whole deposition process in every acetonitrile addition and on the other hand, the nucleation for acetonitrile ions began instantaneously at low underpotentials and became progressive at the UPD potential. It has been suggested that these observations are attributed to the $[Cu(CH_3CN)_4]^+$ complex formation.

The XRVs of copper deposition in pure sulphuric acid revealed that the two different copper structures produce a different effect in the underlying gold layers and furthermore, acetonitrile produces changes in the resulting copper structure as the $(\sqrt{3} \times \sqrt{3})R30^o$ structure

which exists at high underpotentials in pure sulphuric acid, in the 10 mM acetonitrile addition is not detectable. Furthermore, the relaxation effect on the top Au layers appears to be more prominent in presence of acetonitrile.

CTR analysis in presence of acetonitrile further established that the organic additive enhances copper deposition as the copper coverage value increased in comparison to pure sulphuric acid. However, there was contradiction regarding the final coverage values of copper and acetonitrile atoms between electrochemical characterisation and SXRD analysis due to different experimental setups and different techniques but both procedures indicated the possible formation of a copper-acetonitrile complex.

6.6. References

1. Herrero, E., Buller, L.J., Abruna, H.D., *Chem Rev.,* **2001,** *101,* 1897-1930
2. Szabos, S., *Int. Rev. Phys. Chem.,***1991,** *10,* 207-248
3. Hölze, M.H., Zwing, V., Kolb, D.M., *Electrochim. Acta,* **1995,** *40,* 1237-1247
4. Hölze, M.H., Retter, U., Kolb, D.M., *J. Electroanal. Chem.,* **1994,** *371,* 101-109
5. Shi, Z., Wu, S., Lipkowski, J., *J. Electroanal. Chem.,* **1995,** *384,* 171-177
6. Magnussen, O.M., Hotlos, J., Nichols, R.J., Kolb, D.M., Behm, R.J., *J. Vac. Sci. Technol. B.,* **1991,** *9,* 969-975
7. Hachiya, T., Honbo, H., Itaya, K., *J. Electroanal. Chem.,* **1991,** *135,* 275-291
8. Manne, S., Hansma, P.K., Massie, J., Elings, V.B., Gewirth, A.A., *Science,* **1991,** *251,* 183-186
9. Podgaynyy, N., Wezila, S., Molls, C., Iqbal, S., Baltruschat, H., *Beilstein J. Nanotechnol.,* **2015,** *6,* 820-830
10. Wu, S., Lipkowski, J., Tyliczak, T., Hitchcock, A.P., *Prog. Surf. Sci.,* **1995,** *50,* 227-236
11. Lee, J.R., O'Malley, R.L., O'Conell, T.J., Vollmer, A., Rayment, T., *J. Phys. Chem. C,* **2009,** *113,* 12260-12271
12. Toney, M.F., Howard, J.N., Richer, J., Borges, G.I., Gordon, J.G., Melroy, O.R., *Phys. Rev. Lett.,* **1995,** *75,* 4472-4475
13. Kolb, D.M., *Z. Phys. Chem.,* **1987,** *154,* 179-199
14. Zhan, J., Sung, Y.-E., Rikvold, P.A., Wieckowski, A., *J. Chem. Phys.,* **1996,** *104,* 5699-5712
15. Watanabe, M., Uchida, H., Miura, M., Ikeda, N., *J. Electroanal. Chem.,* **1995,** *384,* 191-195
16. Nakamura, M., Endo, O., Ohta, T., Ito, M., Yoda, Y., *Surf. Sci.,* **2002,** *514,* 227-233
17. Lennartz, M., Broekmann, P., Arenz, M., Stuhlmann, C., Wandelt, K., *Surf. Sci.,* **1999,** *442,* 215-222
18. Magnussen, O.M., Hagenböck, J., Hotlos, J., Behm, R., *Faraday Discuss.,* **1992,** *94,* 329-338
19. Madry, B., Wandelt, K., Nowicki, M., *Electrochimica Acta,* **2016,** *217,* 249-261
20. Zei, M.S., Qiao, G., Lehmpfuhl, G., Kolb, D.M., *Berichte der Bunsengesellschaft für physikalische Chemie,* **1987,** *91,* 349-353
21. Mrozek, P., Han, M., Sung, Y.-E., Wieckowski, A., *Surf. Sci.,* **1994,** *319,* 21-33
22. Vaskevich, A., Rubinstein, I., *J. Electroanal. Chem.,* **2000,** *491,* 87

23. Dickertmann, D., Koppitz, F. D., Schultze, J. W., *Electrochimica Acta,* **1976,** *21,* 967-971
24. Xing, X., Scherson, D.J., *Electroanal. Chem.,* **1989,** *270,* 273-279
25. Omar, I.H., Pauling, H.J., Juttner, K., *J. Electroanal. Chem.,* **1993,** *140,* 2187
26. Shi, Z., Lipkowski, J., *J. Electronal. Chem.,* **1994,** *365,* 303
27. Liang, H.-C., Kim, E., Incarvito, C.D., Rheingold, A.L., Karlin, K.D., *Inorg. Chem.,* **2002,** *41,* 2209-2212
28. Pekmez, K., Avci, E., Baumgartel, H. G., Donner, C., *Z. Phys. Chem.,* **2012,** *226,* 953-963
29. Palomar-Pardavé, M., Miranda-Hernández, M., González, I., Batina, N., *Surf. Sci.,* **1998,** *399,* 80-95
30. Frittmann, S., Schuster, R., *J. Phys. C.,* **2016,** *120,* 21522-21535
31. Lucas, C.A., Markovic, N.M., Ross, P.N., *Phys. Rev. B.,* **1997,** *56,* 3651-3654
32. Nakamura, M., Endo, O., Ohta, T., Ito, M., Yoda, Y., *Surface Science,* **2002,** *514,* 227-233
33. de Petris, G., Fornarini, S., Crestoni, M. E., Troiani, A., Mayer, P. M., *J. Phys. Chem. A,* **2005,** *109,* 4425-4427
34. Rudnev, A.V., Molodkina, E.B., Danilov, A.I., Polukarov, Y.M., Feliu, J.M., *Electrochem. Communications,* **2008,** *10,* 502-505

CHAPTER 7

Conclusions and Further Work

In this thesis electrochemical and *in situ* surface x-ray diffraction techniques have been used to explore several systems of technological importance.

Silicene, a novel synthetic silicon 2D allotrope with a honeycomb structure, offers exciting prospects to setting new boundaries in miniaturisation with direct compatibility with the current silicon technology. In this study, firstly imaging techniques and then, SXRD were employed to study in detail the atomic position of the (4 x 4) silicene structure grown on Ag(111) which is unanimously the most dominant structure of this 2D material. The confirmation of the buckling of the silicene layer was reported leading to an sp^3 hybridisation of the material. Additionally, it became evident that the buckling of the silicene layer causes a deformation on the top two layers of the Ag(111) single crystal substrate. The interlayer spacing between the silver atoms is highly dependent on the temperature as different values were observed at room temperature, presented in this thesis, and the growth temperature while the buckling of silicene is independent of temperature. This was attributed to silver having a much larger thermal expansion coefficient than the silicon respective one. There remains more to be done in this study of silicene structures. The FORs and the CTRs of the 70 minutes deposition time, where multilayer silicene was reported to be present and an additional structure is formed, can be modelled and provide further information on the interaction between the 2D material and the Ag(111) layers. In addition, it will be interesting to determine the atomic positions of the silicon atoms in the (4 x 4) structure at this specific silicene deposition time and observe any changes in the underlying substrate as well.

From the application point of view, novel approaches need to be employed to stabilise the as-grown silicene because of its high sensitivity to environmental conditions. At the single-layer scale, interactions with the underlying substrate significantly affect experimental observations, and consequently, there is a plethora of unexpected challenges in growing free-standing atomically thin silicene. In conclusion, there will be numerous exciting opportunities in developing the growth of high-quality silicene and other 2D materials of atomic thickness. Such 2D systems will not only expand our understanding of the underlying physics but also potentially lead to the discovery of unimagined phenomena and applications. It is believed that the ability to harness such unique properties and phenomena will surely lead to exciting technological advances.

The technique of SXRD has been extended to the study of the interaction of a non-aqueous solvent with single crystal electrodes, an important feature in the field of semiconductors and organometallic complex formation of transition metals. Non-aqueous systems are becoming important is modern electrochemistry as their electrochemical window is much wider than aqueous solutions. This thesis was focused on the substance of acetonitrile, a polar aprotic solvent, miscible with water with the ability to back donate its lone pair of electrons and its behaviour on two noble metal single crystal electrodes: Cu(111) and Ag(111) in presence of perchlorate anions.

It was presented that acetonitrile strongly interacts with the surface of Cu(111), where this interaction is directly proportional to the acetonitrile concentration, and weakly with Ag(111) under the presence of perchlorate anions. In Cu(111) it has been suggested that acetonitrile molecules have a perpendicular orientation to the copper surface and bond with the surface atoms via the nitrile group of acetonitrile and at high concentrations the organic molecules dissociate which leads to the formation of a cyanocopper(I) complex. On the other hand the orientation of acetonitrile is parallel to the Ag(111) crystal interacting weakly via the π orbital

of the nitrile group. It has been assumed that the redeposited copper atoms bonded with either acetonitrile or cyanide ions form a (511) structure due to the twinning effect observed in the CTRs. Further SXRD studies couples with other techniques such as X-Ray Photoemission Spectroscopy (XPS) or STM may be able to confirm the existence of this structure. In this thesis, the study of the behaviour of a non-aqueous solution was extended to the electrodeposition of copper on Au(111).

Electrodeposition of metals from non-aqueous solutions has attracted attention in the last few years. Conventional aqueous solutions cannot be always used as electrolytes due to the narrow electrochemical windows, low thermal stability and evaporation. These are the reasons why there has been an interest for new non-aqueous solutions to electrodeposit metals. The role of non-aqueous electrolytes in technology has become more and more important. Facing serious problems concerning the environment and energy scientists have found out new possibilities in electrochemical applications using non-aqueous electrolytes. In this thesis, the behaviour of the underpotential deposition of copper on Au(111) single crystal in acetonitrile was studied. Cu UPD on Au(111) is one of the most studied systems in the field of metal electrodeposition and thus, it is established as a principal system for fundamental electrochemical investigations.

Electrochemical characterisation of copper underpotential deposition in sulphuric acid on Au(111) in presence of acetonitrile indicates that the latter enhances the deposition rate of copper. By modelling chronoamperometric transients at different potential intervals it was shown that acetonitrile dramatically enhances the copper deposition as the copper coverage on the electrode exceeded 1 ML obtaining values of approximately 1.4 ML. Acetonitrile has a clear impact on the deposition process as it alters the kinetics and the resulting copper structure, as evidenced by chronoamperometric and SXRD analysis. However, the resulting copper structure in the presence of acetonitrile still remains unclear. A more detailed analysis

of the SXRD data can determine the resulting copper structure and confirm the presence of a complex formation between copper and acetonitrile atoms.

The subject of the fundamental electrochemistry of non-aqueous solutions and electrodeposition in presence of these solvents is very interesting, reflected by the increasing number of investigations in the last years. The development of technologies of obtaining the solid and dense metallic coatings from non-aqueous solutions may facilitate achieving new materials of specific properties. At present many such technologies are still in the stage of fundamental investigations, because of the difficulties to overcome, such as lack of knowledge on the effect of non-aqueous solutions and higher costs of the production of coatings, in relation to the classical electrolysis of aqueous solutions. However, the application of non-aqueous solutions in the electrodeposition of metals is definitely more economic than the formation of coatings with methods such as plasma spray or chemical vapour deposition.

CHAPTER 8

Appendices

Python Code for the Calculation of a CTR Profile

```
import lmfit as lf
import numpy as np
import sys
import scipy
import os
import time
from scipy.integrate import quad
from scipy.special import erf
from scipy.special import erfc
from TF import TF
from read_data import read_data
from f_atom_0496A import f_atom
from read_parameters import read_parameters
from residual import residual
from  diamondcorr import corr_factors
from  model111 import model
from time import gmtime, strftime
global expEy, expAy, amcorr1, fthick,  ial import erfc
from TF import TF
from read_data import read_data
from f_atom_0496A import f_atom
from read_parameters import read_parameters
from residual import residual
from  diamondcorr import corr_factors
from  model111 import model
from time import gmtime, strftime
global expEy, expAy, amcorr1, fthick,  specular, constants

import datetime
print datetime.datetime.now()
params,fmethod,tol, specularrod, atoms, constants, file1, syserror, folder = read_parameter
s('para001.py')
folder='data/'
#file1=filea
data = read_data(folder+file1)
data = np.asarray(data)
data = data.astype(np.float64)

#put cols in seperate numpy lists
h = abs(np.around(data[:,0],decimals=2))
k = abs(np.around(data[:,1],decimals=2))
l = np.around(data[:,2]/5,decimals=2)*5

hnew=np.array([])
knew=np.array([])
hnew=h[0]
```

```
46. knew=k[0]
47. 
48. for i in range(len(l)):
49. 
50.         if i>0:
51. 
52.                 if (h[i]!=h[i-1]) or (k[i]!=k[i-1]):
53.                         hnew=np.append(hnew,h[i])
54.                         knew=np.append(knew,k[i])
55. 
56. 
57. expA = np.around(data[:,3],decimals=2)
58. #expE = np.around(data[:,4],decimals=2)+2*abs((np.around(data[:,3],decimals=2)-
    np.around(data[:,5],decimals=2)))
59. expE =  np.sqrt((np.around(data[:,4],decimals=2))**2 + (syserror*expA)**2)
60. 
61. expAa = np.around(data[:,5],decimals=2)
62. #expE = np.around(data[:,4],decimals=2)+2*abs((np.around(data[:,3],decimals=2)-
    np.around(data[:,5],decimals=2)))
63. expEa =  np.sqrt((np.around(data[:,6],decimals=2))**2 + (syserror*expAa)**2)
64. 
65. for i in range(len(expE)):
66.         if h[i] ==  1 or k[i]==1:
67.                expA[i] = expAa[i]
68.                expE[i] = expEa[i]
69. 
70. #perform the fit
71. result = lf.Minimizer(residual, params,  fcn_args=(h,k,l,expA,expE,specularrod,atoms,consta
    nts))
72. 
73. result.prepare_fit()
74. 
75. if fmethod == "leastsq":
76.     result1=result.leastsq(xtol = tol[0], ftol = tol[1], maxfev = tol[2])
77. if fmethod == "lbfgsb":
78.     result.lbfgsb(maxfun = tol[2])
79. if fmethod == "nelder":
80.     result.fmin(xtol = tol[0], ftol = tol[1], maxfun = tol[2])
81. 
82. #calculate chi squared
83. params=result1.params
84. final = np.zeros(len(l))
85. final1 = np.zeros(len(l))
86. expAx = np.zeros(len(l))
87. expEx= np.zeros(len(l))
88. chisq = 0
89. for i in range(len(l)):
90.         final1[i],expAx[i],expEx[i],nichts = model(h[i],k[i],l[i],expA[i],expE[i],params, a
    toms,constants)
91. 
92.         if specularrod == 0 and final1[i]>0:
93.            if h[i] > .1 or k[i] > .1:
94.                 chisq = chisq + ((expA[i] - final1[i])/expE[i])**2
95.         else:
96.           chisq = chisq + ((expA[i] - final1[i])/expE[i])**2
97. # write error report
98. lf.report_fit(params)
99. 
100.       # plot results!
101.       #convert y to log scale and seperate the different rods
102.       kcount=1
103.       ichange=0
104. 
105.       for i in range(len(hnew)):
106.               local_namespace=locals()
107.               name='ytheory'+str(hnew[i])[0]+str(knew[i])[0]
```

```
108.                local_namespace['ytheory'+str(hnew[i])[0]+str(knew[i])[0]]=[]
109.                local_namespace['yexp'+str(hnew[i])[0]+str(knew[i])[0]]=[]
110.                local_namespace['yerr'+str(hnew[i])[0]+str(knew[i])[0]]=[]
111.                local_namespace['l'+str(hnew[i])[0]+str(knew[i])[0]]=[]
112.                local_namespace['l'+str(hnew[i])[0]+str(knew[i])[0]+'theo']=[]
113.        #ytheory00 = []
114.        #ytheory01 = []
115.        #ytheory10 = []
116.
117.        ltheo = []
118.        h1 = []
119.        h2 = []
120.        h3 = []
121.        h4 = []
122.        k1 = []
123.        k2 = []
124.        k3 = []
125.        k4 = []
126.        l1 = []
127.        l2 = []
128.        l3 = []
129.        l4 = []
130.        l1=np.arange(0.2,max(l)+0.2,.01)
131.        l2=np.arange(0.2,max(l)+0.2,.01)
132.        steps=len(l1)
133.        #for i in range(len(hnew))
134.        h1=np.ones(len(l1))*hnew[0]
135.        k1=np.ones(steps)*knew[0]
136.        h2=np.ones(steps)*hnew[1]
137.        k2=np.ones(steps)*knew[1]
138.
139.        if len(hnew)>2:
140.                h3=np.ones(steps)*hnew[2]
141.                k3=np.ones(steps)*knew[2]
142.                l3=np.arange(0.2,max(l)+0.2,.01)
143.
144.        if len(hnew)>3:
145.                h4=np.ones(steps)*hnew[3]
146.                k4=np.ones(steps)*knew[3]
147.                l4=np.arange(0.2,max(l)+0.2,.01)
148.        llayer=np.arange(0.05,7,.01)
149.
150.        ltheo=np.concatenate([l1, l2,l3,l4])
151.        htheo=np.concatenate([h1, h2,h3,h4])
152.        ktheo=np.concatenate([k1, k2,k3,k4])
153.        finaltheo = np.zeros(len(ltheo))
154.
155.        for i in range(len(htheo-2)):
156.                finaltheo[i] = model(htheo[i],ktheo[i],ltheo[i],ltheo[i],ltheo[i],params, a
    toms,constants)[3]#/corr_factors(htheo[i],ktheo[i],ltheo[i],params,constants)
157.                #finaltheo[i]=amcorr1
158.        ftot1=0
159.        temp=0
160.
161.         #oxygen layers
162.        shift = 0
163.        for i in range(1,4):
164.                                cov = params['Ocoverage'+str(i)].value
165.                                shift = params['Oeps'+str(i)].value
166.                                flayer = (6)*np.exp(-
    (llayer**2*params['Odwf'+str(i)].value**2)/2) *cov#*np.exp(1j*llayer)
167.                                ftot1 += flayer*np.exp(2*np.pi/7.063*1j*params['Oeps'+str(i
    )].value*llayer)
168.                #layered water structure
169.
170.        if(params['Lcoverage'].value > 0):
```

```
171.                                #print "LAYERED MODEL INCLUDED!"
172.                                temp = np.exp(-
    (llayer**2*params['Lsigmabar'].value**2)/2)*np.exp(1j*llayer*params['Lcw'].value)
173.                                flayer1 = params['Lcoverage'].value*np.exp(-
    (llayer**2*params['Lsigma0'].value**2)/2)*np.exp(2*np.pi/7.063*1j*(params['Ldist'].value-
    params['Lcw'].value)*llayer)
174.
175.                                ftot1 += flayer1/(1-temp)
176.        if(params['Lcoverage1'].value > 0):
177.                                #print "LAYERED MODEL INCLUDED!"
178.                                temp = np.exp(-
    (llayer**2*params['Lsigmabar1'].value**2)/2)*np.exp(1j*llayer*params['Lcw1'].value)
179.                                flayer1 = params['Lcoverage1'].value*np.exp(-
    (llayer**2*params['Lsigma01'].value**2)/2)*np.exp(2*np.pi/7.063*1j*(params['Ldist'].value-
    params['Lcw'].value)*llayer)
180.
181.                                ftot1 += flayer1/(1-temp)
182.                #error function
183.        if(params['Ecoverage'].value > 0):
184.                               # print "ERROR FUNCTION INCLUDED!"
185.                                flayer1 = 1j*(params['Ecoverage'].value)*np.exp(-
    ((llayer*params['Esigma'].value)**2/2))/llayer*np.exp(2*np.pi/7.063*1j*params['Edist'].valu
    e*llayer)
186.                                ftot1 = ftot1 +flayer1
187.
188.                #calculate complex conjugate
189.
190.        amp1 = np.log10(abs(ftot1*np.conjugate(ftot1)))
191.
192.
193.
194.        #for i in range(len(l)):
195.        #        if h[i] == 0 and k[i] == 0:
196.        #                l00.append(l[i])
197.        #                yexp00.append(np.log10(expAx[i]))
198.        #                yerr00.append(0.434*(expEx[i]/expAx[i]))
199.        #
200.        #        if h[i] == 0 and k[i] == 1:
201.         #               l01.append(l[i])
202.         #               yexp01.append(np.log10(expAx[i]))
203.        #                yerr01.append(0.434*(expEx[i]/expAx[i]))
204.         #       if h[i] == 1 and k[i] == 0:
205.         #               l10.append(l[i])
206.         #               yexp10.append(np.log10(expAx[i]))
207.         #               yerr10.append(0.434*(expEx[i]/expAx[i]))
208.
209.        for i in range(len(htheo)):
210.          for j in range(len(hnew)):
211.                if htheo[i] == hnew[j] and ktheo[i] == knew[j]:
212.                        local_namespace['l'+str(hnew[j])[0]+str(knew[j])[0]+'theo'].append(
    ltheo[i])
213.                        local_namespace['ytheory'+str(hnew[j])[0]+str(knew[j])[0]].append(n
    p.log10(finaltheo[i]))
214.
215.
216.        for i in range(len(l)):
217.          for j in range(len(hnew)):
218.                if h[i] == hnew[j] and k[i] == knew[j]:
219.                        local_namespace['l'+str(hnew[j])[0]+str(knew[j])[0]].append(l[i])
220.                        local_namespace['yexp'+str(hnew[j])[0]+str(knew[j])[0]].append(np.l
    og10(expAx[i]))
221.                        local_namespace['yerr'+str(hnew[j])[0]+str(knew[j])[0]].append(0.43
    4*(expEx[i]/expAx[i]))
222.
223.
224.        xlayer=[]
```

```
225.        ylayer=[]
226.        xlayer=np.arange(-3,50,.01)
227.        yerrlayer=(1+erf((xlayer-
    params['Edist'].value)/params['Esigma'].value))/2*params['Ecoverage'].value
228.        ylayerlayer1=0
229.        ylayerlayer2=0
230.        ylayerlayer=0
231.
232.        for i in range(1,30):
233.             ylayerlayer1 +=    np.exp(-(xlayer-(i)*params['Lcw'].value-
    (params['Ldist'].value-
    params['Lcw'].value))**2/(2*(params['Lsigma0'].value+(i)*params['Lsigmabar'].value)**2))/(2
    *(params['Lsigma0'].value+(i)*params['Lsigmabar'].value)/np.sqrt(2*np.pi))*params['Lcoverag
    e'].value
234.             ylayerlayer += np.exp(-(xlayer-(i)*params['Lcw'].value-(params['Ldist'].value-
    params['Lcw'].value))**2/(2*(params['Lsigma0'].value+(i)*params['Lsigmabar'].value)**2))/(2
    *(params['Lsigma0'].value+(i)*params['Lsigmabar'].value)/np.sqrt(2*np.pi))*params['Lcoverag
    e'].value
235.             ylayerlayer2 += np.exp(-(xlayer-(i)*params['Lcw1'].value-
    (params['Ldist1'].value-
    params['Lcw1'].value))**2/(2*(params['Lsigma01'].value+(i)*params['Lsigmabar1'].value)**2))
    /(2*(params['Lsigma01'].value+(i)*params['Lsigmabar1'].value)/np.sqrt(2*np.pi))*params['Lco
    verage1'].value
236.
237.             ylayerlayer += np.exp(-(xlayer-(i)*params['Lcw1'].value-
    (params['Ldist1'].value-
    params['Lcw1'].value))**2/(2*(params['Lsigma01'].value+(i)*params['Lsigmabar1'].value)**2))
    /(2*(params['Lsigma01'].value+(i)*params['Lsigmabar1'].value)/np.sqrt(2*np.pi))*params['Lco
    verage1'].value
238.        oxlayer=0
239.        for i in range(1,3):
240.             oxlayer += np.exp(-(xlayer-
    params['Oeps'+str(i)].value)**2/(2*(params['Odwf'+str(i)].value)**2))/(2*(params['Odwf'+str
    (i)].value)/np.sqrt(2*np.pi))*params['Ocoverage'+str(i)].value
241.
242.        ylayer=yerrlayer+ylayerlayer+oxlayer
243.        print
244.        print "Fit Succeeded"
245.        print file1
246.        print "--------------------"
247.        print   "Chi Squared:", chisq
248.        if fmethod == "leastsq":
249.                        print   "Degrees of Freedom:", result1.nfree
250.                        print   "Reduced Chi Squared:", chisq/result1.nfree
251.
252.        import pylab
253.        from matplotlib.ticker import NullFormatter,MultipleLocator, FormatStrFormatter
254.
255.
256.        myxlim= [0.2,7.2]
257.
258.        xmax=max(l)+0.2
259.        #xmax=6
260.        xmin=min(l)-0.2
261.        myxlim= [xmin,xmax]
262.
263.
264.        for j in range(len(hnew)):
265.              local_namespace['myylim'+str(hnew[j])[0]+str(knew[j])[0]]= [abs(min(local_na
    mespace['yexp'+str(hnew[j])[0]+str(knew[j])[0]])-
    0.2),max(local_namespace['yexp'+str(hnew[j])[0]+str(knew[j])[0]])+0.2]
266.        #myylim00= [min(yexp00)-0.2,max(yexp00)+0.2]
267.        #myylim10= [min(yexp10)-0.2,max(yexp10)+0.2]
268.        #myylim01= [min(yexp01)-0.2,max(yexp01)+0.2]
269.        myylimwater=[min(ylayer)-0.2,max(ylayer)+0.2]
270.        #myylimwater=[min(ylayer)-0.2,5.2]
```

```
271.        myxlimwater=[min(xlayer)-0.2,max(xlayer)+0.2]
272.        pylab.figure()
273.
274.        #subplots_adjust(hspace=0.000)
275.        number_of_subplots=len(hnew)+2
276.        myylim00=[1,5]
277.        myylim10=[1,5]
278.        myylim11=[.2,5]
279.        myylim20=[1,5]
280.
281.        for i,v in enumerate(xrange(len(hnew))):
282.            v = v+1
283.            ax1 = pylab.subplot(number_of_subplots,1,v)
284.
285.            pylab.plot(local_namespace['l'+str(hnew[i])[0]+str(knew[i])[0]], local_namespac
    e['yexp'+str(hnew[i])[0]+str(knew[i])[0]], "ro", label='Experiment', markersize=2)
286.            pylab.errorbar(local_namespace['l'+str(hnew[i])[0]+str(knew[i])[0]], local_name
    space['yexp'+str(hnew[i])[0]+str(knew[i])[0]],  local_namespace['yerr'+str(hnew[i])[0]+str(
    knew[i])[0]],fmt="none",)
287.            pylab.plot(local_namespace['l'+str(hnew[i])[0]+str(knew[i])[0]+'theo'], local_n
    amespace['ytheory'+str(hnew[i])[0]+str(knew[i])[0]], "b-", label='Theory')
288.            pylab.xlim(myxlim)
289.            pylab.ylim(local_namespace['myylim'+str(hnew[i])[0]+str(knew[i])[0]])
290.            pylab.text(0.5,3,str(hnew[i])[0]+str(knew[i])[0]+"l",fontdict={'fontsize':20})

291.
292.            ax1.xaxis.set_major_formatter( NullFormatter() )
293.        pylab.suptitle(file1  + '\n Reduced-
    Chi^2: '+str(chisq/result1.nfree),fontdict={'fontsize':8})
294.        ax4 = pylab.subplot(len(hnew)+2,1,len(hnew)+1)
295.        pylab.plot(llayer, amp1, "b-", label='Theory')
296.        myyliml= [min(amp1)-0.3,max(amp1)+0.2]
297.        pylab.xlim(myxlim)
298.        #pylab.xlim(3)
299.        pylab.ylim(myylimwater)
300.        ax4.xaxis.set_major_formatter( NullFormatter() )
301.
302.
303.        ax5 = pylab.subplot(len(hnew)+2,1,len(hnew)+2)
304.        pylab.plot(xlayer, ylayer, "r-", label='Error', markersize=2)
305.        pylab.plot(xlayer, ylayerlayer1, "y-", label='Error', markersize=2)
306.        pylab.plot(xlayer, ylayerlayer2, "g-", label='Error', markersize=2)
307.        pylab.plot(xlayer, oxlayer, "b-", label='Error', markersize=2)
308.        pylab.xlim(myxlimwater)
309.        pylab.ylim(myylimwater)
310.
311.
312.        pylab.text(0.5,4,"water",fontdict={'fontsize':20})
313.        pylab.subplots_adjust(wspace=0,hspace=0)
314.        pylab.savefig('fit/'+file1+'fits'+strftime(" %d_%b_%Y_%H_%M", gmtime())+'.png')
315.        #pylab.ion()
316.
317.
318.
319.        #Save to fit to a log
320.        def writelog(filename, paramw, chisq,rchi):
321.                localtime = time.asctime( time.localtime(time.time()))
322.                FILE = open(filename,"a") #Open the file in write mode
323.                FILE.write('fit/'+file1+'\n')
324.                FILE.write("-------------------------------------------------------------
    \n")
325.                FILE.write("FIT LOG:"+localtime+"\nCHISQ: "+str(chisq)+"\nRed-
    CHISQ: "+str(rchi)+"\n")
326.                FILE.write("-------------------------------------------------------------
    \n")
327.                FILE.write(lf.fit_report(params)+'\n')
```

```
328.                FILE.close
329.
330.        writelog('fit/'+file1+strftime(" %d_%b_%Y_%H_%M", gmtime())+'.log', params, chisq,
    chisq/result1.nfree)
331.
332.
333.
334.        #output the results
335.        def writecal(h,k,l, y,e):
336.          for i in range(len(hnew)):
337.
338.
339.                if h == hnew[i] and k == knew[i]:
340.                        FILE = open('fit/'+file1+str(hnew[i])[0]+str(knew[i])[0] +strftime(
    " %d_%b_%Y_%H_%M", gmtime())+'.exp',"a")
341.                        FILE.write(str(h)+"\t"+str(k)+"\t"+str(l)+"\t"+str(y)+"\t"+str(e)+"
    \n")
342.                        FILE.close
343.
344.        def writetheo(h,k,l, y):
345.          for i in range(len(hnew)):
346.                if h == hnew[i] and k == knew[i]:
347.                        FILE = open('fit/'+file1+str(hnew[i])[0]+str(knew[i])[0] +strftime(
    " %d_%b_%Y_%H_%M", gmtime())+'.cal',"a")
348.
349.                        FILE.write(str(h)+"\t"+str(k)+"\t"+str(l)+"\t"+str(y)+"\n")
350.                        FILE.close
351.
352.        def writewater(x,y1,y2,y,o):
353.           for i in range(len(hnew)):
354.                FILE = open('fit/'+file1+'watermodel'+strftime(" %d_%b_%Y_%H_%M", gmtime())
    +'.dat',"a")
355.
356.                FILE.write(str(x)+"\t"+str(y1)+"\t"+str(y2)+"\t"+str(y)+"\t"+str(o)+"\n")
357.                FILE.close
358.
359.
360.
361.        for i in range(len(l)):
362.                writecal(h[i], k[i], l[i], expAx[i], expEx[i])
363.
364.        for i in range(len(htheo)):
365.                writetheo(htheo[i], ktheo[i], ltheo[i], finaltheo[i])
366.
367.        #for i in range(len(xlayer)):
368.               # writewater(xlayer[i], oxlayer[i], ylayerlayer1[i],ylayerlayer2[i],ylayer[i
    ])
369.
370.        import datetime
371.        print datetime.datetime.now()
372.
373.        pylab.show()
```

Python Code for Modelling the Chronoamperometry Transients

```
1.  import lmfit as lf
2.  import numpy as np
3.  import sys
4.  import scipy
5.  import os
6.  import time
7.  import scipy.optimize as optimization
8.
9.  #This function just returns True or False depending on the input
10. def TF(tocheck):
11.         if tocheck == "T":
12.                 return True
13.         if tocheck == "t":
14.                 return True
15.         if tocheck == "F":
16.                 return False
17.         if tocheck == "f":
18.                 return False
19.         else:
20.
21.                 print "George Perpe mou klaneis mia mantra"
22.                 quit()
23.
24. #Function to read the parameters file
25. def read_parameters(filename):
26.
27.         params = lf.Parameters()
28.         line = []
29.         raw = 1
30.
31.         f = open(filename, 'r')
32.
33.         #skip first two lines
34.         [f.readline() for i in xrange(2)]
35.
36.         #read parameters from file
37.         while raw:
38.                 raw = f.readline()
39.                 line = raw.split()
40.                 if len(line) >1 and line[0] == "P":
41.                         params.add(line[1],   value= float(line[2]),  min=float(line[3]), m
    ax=float(line[4]),vary=TF(line[5]))
42.                 if len(line) >1 and line[0] == "M":
43.                         method = line[1]
44.                 if len(line) >1 and line[0] == "T":
45.                         tol = float(line[1])
46.
47.         return params, method, tol
48.
49. #function to read in a list of HKL values, structure factors, and errors
50. #since this program only treats the specular rod H and K should be zero
51. def read_data(filename):
52.
53.         f = open(filename, 'r')
54.         line = []
55.         data = []
56.         raw = 1
57.
58.         #skip first line
59.         f.readline()
60.
```

```
61.         #read parameters from file
62.         while raw:
63.                 raw = f.readline()
64.                 if len(raw.split()) > 1:
65.                         data.append(raw.split())
66.         return data
67.
68.
69. def model1(t,params):
70.     S1=params['S1'].value
71.     k1=params['k1'].value
72.     m1=params['m1'].value
73.     off=params['offset'].value
74.     current1=S1*m1*k1*np.power(t,(m1-1))*np.exp(-np.power(t,m1)*k1)
75.     return current1
76.
77. def model2(t,params):
78.     S2=params['S2'].value
79.     k2=params['k2'].value
80.     m2=params['m2'].value
81.     off=params['offset'].value
82.     current2=S2*m2*k2*np.power(t,(m2-1))*np.exp(-np.power(t,m2)*k2)
83.     return current2
84.
85. def model3(t,params):
86.     S3=params['S3'].value
87.     k3=params['k3'].value
88.     m3=params['m3'].value
89.     off=params['offset'].value
90.     current3=(S3*m3*k3*np.power(t,(m3-1))*np.exp(-np.power(t,m3)*k3))#*np.power(10,6)
91.     return current3
92.
93. def model4(t,params):
94.     S4=params['S4'].value
95.     k4=params['k4'].value
96.     m4=params['m4'].value
97.     t4=params['t4'].value
98.     off=params['offset'].value
99.     current4=(S4*m4*k4*np.power((t-t4),(m4-1))*np.exp(-np.power((t-
    t4),m4)*k4))#*np.power(10,6)
100.            return current4
101.
102.       def model5(t,params):
103.           S5=params['S5'].value
104.           k5=params['k5'].value
105.           m5=params['m5'].value
106.           t5=params['t5'].value
107.           off=params['offset'].value
108.           current5=(S5*m5*k5*np.power((t-t5),(m5-1))*np.exp(-np.power((t-
    t5),m5)*k5))#*np.power(10,6)
109.           return current5
110.
111.       def model(t,params):
112.           S1=params['S1'].value
113.           k1=params['k1'].value
114.           m1=params['m1'].value
115.           S2=params['S2'].value
116.           k2=params['k2'].value
117.           m2=params['m2'].value
118.           S3=params['S3'].value
119.           k3=params['k3'].value
120.           m3=params['m3'].value
121.           S4=params['S4'].value
122.           k4=params['k4'].value
123.           m4=params['m4'].value
124.           t4=params['t4'].value
```

```
125.            S5=params['S5'].value
126.            k5=params['k5'].value
127.            m5=params['m5'].value
128.            t5=params['t5'].value
129.            off=params['offset'].value
130.            #current=np.log((S1*np.power(t,(m1-1))*np.exp(-t*m1*k1)+S2*np.power(t,(m2-
    1))*np.exp(-t*m2*k2)+S3*np.power(t,(m3-1))*np.exp(-t*m3*k3)))+off
131.            current=((S1*m1*k1*np.power(t,(m1-1))*np.exp(-
    np.power(t,m1)*k1)+S2*m2*k2*np.power(t,(m2-1))*np.exp(-
    np.power(t,m2)*k2)+S3*k3*m3*np.power(t,(m3-1))*np.exp(-
    np.power(t,m3)*k3))+(S4*m4*k4*np.power((t-t4),(m4-1))*np.exp(-np.power((t-
    t4),m4)*k4))+(S5*m5*k5*np.power((t-t5),(m5-1))*np.exp(-np.power((t-
    t5),m5)*k5))+params['offset'].value)
132.
133.            return current
134.
135.
136.        #import numdifftools as ndt
137.
138.
139.
140.
141.        def residual(params, t, expA,experror):
142.
143.                points = len(t)
144.
145.                mod = np.zeros(points)
146.                for i in range(points):
147.                        mod[i] = model(t[i],params)
148.
149.                return (expE - mod)**2#./np.power(experror,2)#/np.power(expE,0.8)
150.                #fitting criteria-
    > if later part activated, weighted by value of data (lower values give lower discrepance w
    hich means fit more weighted towards fitting those well)
151.
152.        #epsfcn=np.finfo(np.float64).eps
153.        params,fmethod,tol = read_parameters('params.py')
154.        data = read_data('lisa.txt')
155.        data = np.asarray(data)
156.        data = data.astype(np.float64)
157.        #texp = data[20:200,0]
158.        #expE = data[20:200,1]
159.        texp = data[1:len(data[:,0]),0]
160.        expE = data[1:len(data[:,0]),1]
161.        experror=abs(0.025*(expE))
162.
163.        #preform the fit
164.        result = lf.Minimizer(residual, params,  fcn_args=(texp,expE,experror))
165.        #optimization.curve_fit(model(texp,params),texp,expE,experror)
166.        result.prepare_fit()
167.
168.        if fmethod == "leastsq":
169.                result.leastsq(xtol = tol, ftol = tol, maxfev = 999999999)
170.        if fmethod == "lbfgsb":
171.                result.lbfgsb()
172.        if fmethod == "nelder":
173.                result.fmin(ftol = tol, xtol = tol, maxfun=999999999)
174.        if fmethod == "anneal":
175.                result.anneal(xtol = tol, ftol = tol, maxfev = 999999999)
176.        if fmethod == "bent":
177.                result.leastsq(xtol = tol, ftol = tol, maxfev = 999999999,full_output=1)
178.                #result.leastsq(xtol = tol, ftol = tol, maxfev = 999999999,full_output=1.,
    Dfun = jac_errfunc)
179.
180.        #calculate chi squared
181.        theory = np.zeros(len(texp))
```

```
182.        theory1 = np.zeros(len(texp))
183.        theory2 = np.zeros(len(texp))
184.        theory3 = np.zeros(len(texp))
185.        theory4 = np.zeros(len(texp))
186.        theory5 = np.zeros(len(texp))
187.        final = np.zeros(len(texp))
188.        chisq = 0
189.        res=np.zeros(len(texp))
190.        #for i in range(len(texp)):
191.        for i in range(len(texp)):
192.
193.                theory[i] = model(texp[i],params)
194.                theory1[i] = model1(texp[i],params)+params['offset'].value
195.                theory2[i] = model2(texp[i],params)+params['offset'].value
196.                theory3[i] = model3(texp[i],params)+params['offset'].value
197.                theory4[i] = model4(texp[i],params)+params['offset'].value
198.                theory5[i] = model5(texp[i],params)+params['offset'].value
199.                final[i] = model(texp[i],params)
200.                res[i]=final[i]-expE[i]
201.                chisq = chisq + ((expE[i] - final[i])/experror[i])**2
202.
203.        #for i in range(len(texp)):
204.        #        theory[i]=model[texp[i],params]
205.        # write error report
206.        lf.report_fit(params)
207.
208.
209.        # plot results!
210.        #convert y to log scale and seperate the different rods
211.
212.        print
213.        print "Fit Succeeded"
214.        print "--------------------"
215.        print   "Chi Squared:", chisq
216.        if fmethod == "leastsq":
217.                        print   "Degrees of Freedom:", result.nfree
218.                        print   "Reduced Chi Squared:", chisq/result.nfree
219.
220.        import pylab
221.        from matplotlib.ticker import NullFormatter,MultipleLocator, FormatStrFormatter
222.        import math
223.
224.        #myxlim=[0.2,2]
225.        #myxlim=[-0.1,5]
226.        pylab.figure()
227.        pylab.errorbar(texp, expE, experror,fmt='bx',)
228.        pylab.plot(texp, (expE), "bo", label='Experiment', markersize=4)
229.        pylab.plot(texp, theory, "r-", label='Theory')
230.        #pylab.xlim(myxlim)
231.        pylab.show()
232.
233.        #pylab.savefig("testfig.jpg", format='jpg', dpi=700)
234.        #myxlim=[0.2,3]
235.        #set range x axis
236.        #myylim=[-1,0.1]
237.        #set range y axis
238.        pylab.figure()
239.        pylab.plot(texp, (expE), "bo", label='Experiment', markersize=4)
240.        #pylab.errorbar(texp, expE, experror,fmt='bx',)
241.        pylab.plot(texp, theory, "r-", label='Theory')
242.        pylab.plot(texp, theory1, "b-", label='1')
243.        pylab.plot(texp, theory2, "c-", label='2')
244.        #pylab.plot(texp, theory3, "g-", label='3')
245.        #pylab.plot(texp, theory4, "y-", label='4')
246.        #pylab.plot(texp, theory5, "m-", label='5')
247.        #pylab.xlim(myxlim)
```

```
248.        #pylab.ylim(myylim)
249.        #pylab.text(0.5,0.5,"001",fontdict={'fontsize':20})
250.        pylab.text(2,0.0005,'Reduced-
    Chi^2: '+str(chisq/result.nfree),fontdict={'fontsize':12})
251.        pylab.show()
252.
253.        #pylab.savefig("testfig2.jpg", format='jpg', dpi=700)
254.
255.        #res is normal residuals (exp.value-theo.value)
256.        #myxlim=[0,5]
257.        #set range x axis
258.        #myylim=[-1,1]
259.        #set range y axis
260.        pylab.figure()
261.        #myxlim=[0.2,2]
262.        #myylim=[-190,190]
263.        pylab.plot(texp, res, "ro", label='Residuals', markersize=3)
264.        pylab.plot(texp, experror, "bx", label='ExpError', markersize=3)
265.        #pylab.xlim(myxlim)
266.        #pylab.ylim(myylim)
267.        #pylab.text(0.5,0.5,"001",fontdict={'fontsize':20})
268.        pylab.show()
269.
270.        #Save to fit to a log
271.        def writelog(filename, paramw, chisq,rchi):
272.                localtime = time.asctime( time.localtime(time.time()) )
273.                FILE = open(filename,"a") #Open the file in write mode
274.                FILE.write("-------------------------------------------------------------
    \n")
275.                FILE.write("FIT LOG:"+localtime+"\nCHISQ: "+str(chisq)+"\nRed-
    CHISQ: "+str(rchi)+"\n")
276.                FILE.write("-------------------------------------------------------------
    \n")
277.                FILE.write(str(params))
278.                FILE.close
279.
280.        writelog('fit_150mV.log', params, chisq, chisq/result.nfree)
281.
282.
283.
284.        #output the results
285.        def writecal(t, y,e):
286.
287.
288.                FILE = open('avrami_10mm_sulphuric',"a")
289.
290.                FILE.write(str(t)+"\t"+str(y)+"\t"+str(e)+"\n")
291.                FILE.close
292.
293.
294.        #rewrite files with headers
295.        FILE = open('avrami_10mm_sulphuric',"w") #Open the file in write mode
296.        FILE.write("")
297.        FILE.close
298.
299.        for i in range(len(texp)):
300.                writecal(texp[i],  theory[i],expE[i])
```

ROD Files for the Structural Characterisation of (4 x 4) Silicene

Below are the final files for the determination of the atomic positions of Si and Ag atoms on the (4 x 4) silicene structure as described in *Chapter 4*. The files were extracted from the ROD program by E. Vlieg. Three files were necessary for the theoretical fit to our experimental data: 1) a bulk file, 2) a surface file and 3) a parameters file

i) Bulk file

```
4x4 my attempt (Takagi)
 11.5400 11.5400 7.0670  90.0  90.0  120.0
Ag  0.00000  0.00000  0.00000
Ag  0.00000  0.25000  0.00000
Ag  0.00000  0.50000  0.00000
Ag  0.00000  0.75000  0.00000
Ag  0.25000  0.00000  0.00000
Ag  0.25000  0.25000  0.00000
Ag  0.25000  0.50000  0.00000
Ag  0.25000  0.75000  0.00000
Ag  0.50000  0.00000  0.00000
Ag  0.50000  0.25000  0.00000
Ag  0.50000  0.50000  0.00000
Ag  0.50000  0.75000  0.00000
Ag  0.75000  0.00000  0.00000
Ag  0.75000  0.25000  0.00000
Ag  0.75000  0.50000  0.00000
Ag  0.75000  0.75000  0.00000
Ag  0.08333  0.16666 -0.33333
Ag  0.08333  0.41665 -0.33333
Ag  0.08333  0.66664 -0.33333
Ag  0.08333  0.91663 -0.33333
Ag  0.33332  0.16666 -0.33333
Ag  0.33332  0.41665 -0.33333
Ag  0.33332  0.66664 -0.33333
Ag  0.33332  0.91663 -0.33333
Ag  0.58331  0.16666 -0.33333
Ag  0.58331  0.41665 -0.33333
Ag  0.58331  0.66664 -0.33333
Ag  0.58331  0.91663 -0.33333
Ag  0.83333  0.16666 -0.33333
Ag  0.83333  0.41665 -0.33333
Ag  0.83333  0.66664 -0.33333
Ag  0.83333  0.91663 -0.33333
Ag  0.16666  0.08333 -0.66666
Ag  0.16666  0.33332 -0.66666
```

```
Ag  0.16666  0.58331  -0.66666
Ag  0.16666  0.83333  -0.66666
Ag  0.41665  0.08333  -0.66666
Ag  0.41665  0.33332  -0.66666
Ag  0.41665  0.58331  -0.66666
Ag  0.41665  0.83333  -0.66666
Ag  0.66664  0.08333  -0.66666
Ag  0.66664  0.33332  -0.66666
Ag  0.66664  0.58331  -0.66666
Ag  0.66664  0.83333  -0.66666
Ag  0.91663  0.08333  -0.66666
Ag  0.91663  0.33332  -0.66666
Ag  0.91663  0.58331  -0.66666
Ag  0.91663  0.83333  -0.66666
```

ii) Surface file

```
#4x4 my attempt (Takagi)
  11.5400  11.5400  7.0670  90.0  90.0  120.0
Si  0.11111  1.0  1  0.0  0  0.22222  1.0  1  0.0  0  2.3252  1.0  5  0.0  0  1  1  1
Si  0.11111  1.0  1  0.0  0  0.55555  1.0  1  0.0  0  2.3252  1.0  6  0.0  0  1  1  1
Si  0.11111  1.0  1  0.0  0  0.88888  1.0  1  0.0  0  2.3252  1.0  7  0.0  0  1  1  1
Si  0.22222  1.0  1  0.0  0  0.11111  1.0  1  0.0  0  2.3252  1.0  8  0.0  0  1  1  1
Si  0.22222  1.0  1  0.0  0  0.44444  1.0  1  0.0  0  2.4327  1.0  9  0.0  0  1  1  1
Si  0.22222  1.0  1  0.0  0  0.77777  1.0  1  0.0  0  2.4327  1.0 10  0.0  0  1  1  1
Si  0.44444  1.0  1  0.0  0  0.22222  1.0  1  0.0  0  2.4327  1.0 11  0.0  0  1  1  1
Si  0.44444  1.0  1  0.0  0  0.55555  1.0  1  0.0  0  2.3252  1.0 12  0.0  0  1  1  1
Si  0.44444  1.0  1  0.0  0  0.88888  1.0  1  0.0  0  2.3252  1.0 13  0.0  0  1  1  1
Si  0.55555  1.0  1  0.0  0  0.11111  1.0  1  0.0  0  2.3252  1.0 14  0.0  0  1  1  1
Si  0.55555  1.0  1  0.0  0  0.44444  1.0  1  0.0  0  2.3252  1.0 15  0.0  0  1  1  1
Si  0.55555  1.0  1  0.0  0  0.77777  1.0  1  0.0  0  2.4327  1.0 16  0.0  0  1  1  1
Si  0.77777  1.0  1  0.0  0  0.22222  1.0  1  0.0  0  2.4327  1.0 17  0.0  0  1  1  1
Si  0.77777  1.0  1  0.0  0  0.55555  1.0  1  0.0  0  2.4327  1.0 18  0.0  0  1  1  1
Si  0.77777  1.0  1  0.0  0  0.88888  1.0  1  0.0  0  2.3252  1.0 19  0.0  0  1  1  1
Si  0.88888  1.0  1  0.0  0  0.11111  1.0  1  0.0  0  2.3252  1.0 20  0.0  0  1  1  1
Si  0.88888  1.0  1  0.0  0  0.44444  1.0  1  0.0  0  2.3252  1.0 21  0.0  0  1  1  1
Si  0.88888  1.0  1  0.0  0  0.77777  1.0  1  0.0  0  2.3252  1.0 22  0.0  0  1  1  1
Ag  0.00000  1.0  1  0.0  0  0.00000  1.0  1  0.0  0  1.9878  1.0 25  0.0  0  7  7  1
Ag  0.00000  1.0  1  0.0  0  0.25000  1.0  1  0.0  0  2.0137  1.0 27  0.0  0  7  7  1
Ag  0.00000  1.0  1  0.0  0  0.50000  1.0  1  0.0  0  1.9878  1.0 25  0.0  0  7  7  1
Ag  0.00000  1.0  1  0.0  0  0.75000  1.0  1  0.0  0  1.9878  1.0 25  0.0  0  7  7  1
Ag  0.25000  1.0  1  0.0  0  0.00000  1.0  1  0.0  0  2.0143  1.0 26  0.0  0  7  7  1
Ag  0.25000  1.0  1  0.0  0  0.25000  1.0  1  0.0  0  1.9878  1.0 25  0.0  0  7  7  1
Ag  0.25000  1.0  1  0.0  0  0.50000  1.0  1  0.0  0  2.0137  1.0 27  0.0  0  7  7  1
```

Ag 0.25000 1.0 1 0.0 0 0.75000 1.0 1 0.0 0 1.9878 1.0 25 0.0 0 7 7 1
Ag 0.50000 1.0 1 0.0 0 0.00000 1.0 1 0.0 0 1.9878 1.0 25 0.0 0 7 7 1
Ag 0.50000 1.0 1 0.0 0 0.25000 1.0 1 0.0 0 2.0143 1.0 26 0.0 0 7 7 1
Ag 0.50000 1.0 1 0.0 0 0.50000 1.0 1 0.0 0 1.9878 1.0 25 0.0 0 7 7 1
Ag 0.50000 1.0 1 0.0 0 0.75000 1.0 1 0.0 0 2.0137 1.0 27 0.0 0 7 7 1
Ag 0.75000 1.0 1 0.0 0 0.00000 1.0 1 0.0 0 1.9878 1.0 25 0.0 0 7 7 1
Ag 0.75000 1.0 1 0.0 0 0.25000 1.0 1 0.0 0 1.9878 1.0 25 0.0 0 7 7 1
Ag 0.75000 1.0 1 0.0 0 0.50000 1.0 1 0.0 0 2.0143 1.0 26 0.0 0 7 7 1
Ag 0.75000 1.0 1 0.0 0 0.75000 1.0 1 0.0 0 1.9878 1.0 25 0.0 0 7 7 1
Ag 0.08333 1.0 1 0.0 0 0.16666 1.0 1 0.0 0 1.6665 1.0 24 0.0 0 6 6 1
Ag 0.08333 1.0 1 0.0 0 0.41665 1.0 1 0.0 0 1.6665 1.0 29 0.0 0 6 6 1
Ag 0.08333 1.0 1 0.0 0 0.66664 1.0 1 0.0 0 1.6665 1.0 24 0.0 0 6 6 1
Ag 0.08333 1.0 1 0.0 0 0.91663 1.0 1 0.0 0 1.6665 1.0 24 0.0 0 6 6 1
Ag 0.33332 1.0 1 0.0 0 0.16666 1.0 1 0.0 0 1.6665 1.0 28 0.0 0 6 6 1
Ag 0.33332 1.0 1 0.0 0 0.41665 1.0 1 0.0 0 1.6665 1.0 24 0.0 0 6 6 1
Ag 0.33332 1.0 1 0.0 0 0.66664 1.0 1 0.0 0 1.6665 1.0 29 0.0 0 6 6 1
Ag 0.33332 1.0 1 0.0 0 0.91663 1.0 1 0.0 0 1.6665 1.0 24 0.0 0 6 6 1
Ag 0.58331 1.0 1 0.0 0 0.16666 1.0 1 0.0 0 1.6665 1.0 24 0.0 0 6 6 1
Ag 0.58331 1.0 1 0.0 0 0.41665 1.0 1 0.0 0 1.6665 1.0 28 0.0 0 6 6 1
Ag 0.58331 1.0 1 0.0 0 0.66664 1.0 1 0.0 0 1.6665 1.0 24 0.0 0 6 6 1
Ag 0.58331 1.0 1 0.0 0 0.91663 1.0 1 0.0 0 1.6665 1.0 29 0.0 0 6 6 1
Ag 0.83333 1.0 1 0.0 0 0.16666 1.0 1 0.0 0 1.6665 1.0 24 0.0 0 6 6 1
Ag 0.83333 1.0 1 0.0 0 0.41665 1.0 1 0.0 0 1.6665 1.0 24 0.0 0 6 6 1
Ag 0.83333 1.0 1 0.0 0 0.66664 1.0 1 0.0 0 1.6665 1.0 28 0.0 0 6 6 1
Ag 0.83333 1.0 1 0.0 0 0.91663 1.0 1 0.0 0 1.6665 1.0 24 0.0 0 6 6 1
Ag 0.16666 1.0 1 0.0 0 0.08333 1.0 1 0.0 0 1.3332 1.0 23 0.0 0 5 5 1
Ag 0.16666 1.0 1 0.0 0 0.33332 1.0 1 0.0 0 1.3332 1.0 23 0.0 0 5 5 1
Ag 0.16666 1.0 1 0.0 0 0.58331 1.0 1 0.0 0 1.3332 1.0 23 0.0 0 5 5 1
Ag 0.16666 1.0 1 0.0 0 0.83333 1.0 1 0.0 0 1.3332 1.0 23 0.0 0 5 5 1
Ag 0.41665 1.0 1 0.0 0 0.08333 1.0 1 0.0 0 1.3332 1.0 23 0.0 0 5 5 1
Ag 0.41665 1.0 1 0.0 0 0.33332 1.0 1 0.0 0 1.3332 1.0 23 0.0 0 5 5 1
Ag 0.41665 1.0 1 0.0 0 0.58331 1.0 1 0.0 0 1.3332 1.0 23 0.0 0 5 5 1
Ag 0.41665 1.0 1 0.0 0 0.83333 1.0 1 0.0 0 1.3332 1.0 23 0.0 0 5 5 1
Ag 0.66664 1.0 1 0.0 0 0.08333 1.0 1 0.0 0 1.3332 1.0 23 0.0 0 5 5 1
Ag 0.66664 1.0 1 0.0 0 0.33332 1.0 1 0.0 0 1.3332 1.0 23 0.0 0 5 5 1
Ag 0.66664 1.0 1 0.0 0 0.58331 1.0 1 0.0 0 1.3332 1.0 23 0.0 0 5 5 1
Ag 0.66664 1.0 1 0.0 0 0.83333 1.0 1 0.0 0 1.3332 1.0 23 0.0 0 5 5 1
Ag 0.91663 1.0 1 0.0 0 0.08333 1.0 1 0.0 0 1.3332 1.0 23 0.0 0 5 5 1
Ag 0.91663 1.0 1 0.0 0 0.33332 1.0 1 0.0 0 1.3332 1.0 23 0.0 0 5 5 1
Ag 0.91663 1.0 1 0.0 0 0.58331 1.0 1 0.0 0 1.3332 1.0 23 0.0 0 5 5 1
Ag 0.91663 1.0 1 0.0 0 0.83333 1.0 1 0.0 0 1.3332 1.0 23 0.0 0 5 5 1
Ag 0.00000 1.0 1 0.0 0 0.00000 1.0 1 0.0 0 0.9999 1.0 2 0.0 0 2 2 1
Ag 0.00000 1.0 1 0.0 0 0.25000 1.0 1 0.0 0 0.9999 1.0 2 0.0 0 2 2 1
Ag 0.00000 1.0 1 0.0 0 0.50000 1.0 1 0.0 0 0.9999 1.0 2 0.0 0 2 2 1
Ag 0.00000 1.0 1 0.0 0 0.75000 1.0 1 0.0 0 0.9999 1.0 2 0.0 0 2 2 1

Ag	0.25000	1.0	1	0.0	0	0.00000	1.0	1	0.0	0	0.9999	1.0	2	0.0	0	2	2	1
Ag	0.25000	1.0	1	0.0	0	0.25000	1.0	1	0.0	0	0.9999	1.0	2	0.0	0	2	2	1
Ag	0.25000	1.0	1	0.0	0	0.50000	1.0	1	0.0	0	0.9999	1.0	2	0.0	0	2	2	1
Ag	0.25000	1.0	1	0.0	0	0.75000	1.0	1	0.0	0	0.9999	1.0	2	0.0	0	2	2	1
Ag	0.50000	1.0	1	0.0	0	0.00000	1.0	1	0.0	0	0.9999	1.0	2	0.0	0	2	2	1
Ag	0.50000	1.0	1	0.0	0	0.25000	1.0	1	0.0	0	0.9999	1.0	2	0.0	0	2	2	1
Ag	0.50000	1.0	1	0.0	0	0.50000	1.0	1	0.0	0	0.9999	1.0	2	0.0	0	2	2	1
Ag	0.50000	1.0	1	0.0	0	0.75000	1.0	1	0.0	0	0.9999	1.0	2	0.0	0	2	2	1
Ag	0.75000	1.0	1	0.0	0	0.00000	1.0	1	0.0	0	0.9999	1.0	2	0.0	0	2	2	1
Ag	0.75000	1.0	1	0.0	0	0.25000	1.0	1	0.0	0	0.9999	1.0	2	0.0	0	2	2	1
Ag	0.75000	1.0	1	0.0	0	0.50000	1.0	1	0.0	0	0.9999	1.0	2	0.0	0	2	2	1
Ag	0.75000	1.0	1	0.0	0	0.75000	1.0	1	0.0	0	0.9999	1.0	2	0.0	0	2	2	1
Ag	0.08333	1.0	1	0.0	0	0.16666	1.0	1	0.0	0	0.6666	1.0	3	0.0	0	3	3	1
Ag	0.08333	1.0	1	0.0	0	0.41665	1.0	1	0.0	0	0.6666	1.0	3	0.0	0	3	3	1
Ag	0.08333	1.0	1	0.0	0	0.66664	1.0	1	0.0	0	0.6666	1.0	3	0.0	0	3	3	1
Ag	0.08333	1.0	1	0.0	0	0.91663	1.0	1	0.0	0	0.6666	1.0	3	0.0	0	3	3	1
Ag	0.33332	1.0	1	0.0	0	0.16666	1.0	1	0.0	0	0.6666	1.0	3	0.0	0	3	3	1
Ag	0.33332	1.0	1	0.0	0	0.41665	1.0	1	0.0	0	0.6666	1.0	3	0.0	0	3	3	1
Ag	0.33332	1.0	1	0.0	0	0.66664	1.0	1	0.0	0	0.6666	1.0	3	0.0	0	3	3	1
Ag	0.33332	1.0	1	0.0	0	0.91663	1.0	1	0.0	0	0.6666	1.0	3	0.0	0	3	3	1
Ag	0.58331	1.0	1	0.0	0	0.16666	1.0	1	0.0	0	0.6666	1.0	3	0.0	0	3	3	1
Ag	0.58331	1.0	1	0.0	0	0.41665	1.0	1	0.0	0	0.6666	1.0	3	0.0	0	3	3	1
Ag	0.58331	1.0	1	0.0	0	0.66664	1.0	1	0.0	0	0.6666	1.0	3	0.0	0	3	3	1
Ag	0.58331	1.0	1	0.0	0	0.91663	1.0	1	0.0	0	0.6666	1.0	3	0.0	0	3	3	1
Ag	0.83333	1.0	1	0.0	0	0.16666	1.0	1	0.0	0	0.6666	1.0	3	0.0	0	3	3	1
Ag	0.83333	1.0	1	0.0	0	0.41665	1.0	1	0.0	0	0.6666	1.0	3	0.0	0	3	3	1
Ag	0.83333	1.0	1	0.0	0	0.66664	1.0	1	0.0	0	0.6666	1.0	3	0.0	0	3	3	1
Ag	0.83333	1.0	1	0.0	0	0.91663	1.0	1	0.0	0	0.6666	1.0	3	0.0	0	3	3	1
Ag	0.16666	1.0	1	0.0	0	0.08333	1.0	1	0.0	0	0.3333	1.0	4	0.0	0	4	4	1
Ag	0.16666	1.0	1	0.0	0	0.33332	1.0	1	0.0	0	0.3333	1.0	4	0.0	0	4	4	1
Ag	0.16666	1.0	1	0.0	0	0.58331	1.0	1	0.0	0	0.3333	1.0	4	0.0	0	4	4	1
Ag	0.16666	1.0	1	0.0	0	0.83333	1.0	1	0.0	0	0.3333	1.0	4	0.0	0	4	4	1
Ag	0.41665	1.0	1	0.0	0	0.08333	1.0	1	0.0	0	0.3333	1.0	4	0.0	0	4	4	1
Ag	0.41665	1.0	1	0.0	0	0.33332	1.0	1	0.0	0	0.3333	1.0	4	0.0	0	4	4	1
Ag	0.41665	1.0	1	0.0	0	0.58331	1.0	1	0.0	0	0.3333	1.0	4	0.0	0	4	4	1
Ag	0.41665	1.0	1	0.0	0	0.83333	1.0	1	0.0	0	0.3333	1.0	4	0.0	0	4	4	1
Ag	0.66664	1.0	1	0.0	0	0.08333	1.0	1	0.0	0	0.3333	1.0	4	0.0	0	4	4	1
Ag	0.66664	1.0	1	0.0	0	0.33332	1.0	1	0.0	0	0.3333	1.0	4	0.0	0	4	4	1
Ag	0.66664	1.0	1	0.0	0	0.58331	1.0	1	0.0	0	0.3333	1.0	4	0.0	0	4	4	1
Ag	0.66664	1.0	1	0.0	0	0.83333	1.0	1	0.0	0	0.3333	1.0	4	0.0	0	4	4	1
Ag	0.91663	1.0	1	0.0	0	0.08333	1.0	1	0.0	0	0.3333	1.0	4	0.0	0	4	4	1
Ag	0.91663	1.0	1	0.0	0	0.33332	1.0	1	0.0	0	0.3333	1.0	4	0.0	0	4	4	1
Ag	0.91663	1.0	1	0.0	0	0.58331	1.0	1	0.0	0	0.3333	1.0	4	0.0	0	4	4	1
Ag	0.91663	1.0	1	0.0	0	0.83333	1.0	1	0.0	0	0.3333	1.0	4	0.0	0	4	4	1

iii) Parameters file

```
!Silicene Parameters
!files used: data4x4_5_err.dat ag111_4x4_1.bul ag111_si_1.fit
scale       4.0599    0.0000    0.0000  YES
beta        0.1317    0.0000    0.0000  YES
surffrac    1.0000    0.0000    0.0000  NO
displace  1   0.0000    0.0000    0.0000  NO
displace  2  -0.0017    0.0000    0.0000  NO
displace  3  -0.0010    0.0000    0.0000  NO
displace  4  -0.0005    0.0000    0.0000  NO
displace  5   0.0000    0.0000    0.0000  NO
displace  6   0.0000    0.0000    0.0000  NO
displace  7   0.0000    0.0000    0.0000  NO
displace  8   0.0000    0.0000    0.0000  NO
displace  9   0.0000    0.0000    0.0000  NO
displace  10   0.0000    0.0000    0.0000  NO
displace  11   0.0000    0.0000    0.0000  NO
displace  12   0.0000    0.0000    0.0000  NO
displace  13   0.0000    0.0000    0.0000  NO
displace  14   0.0000    0.0000    0.0000  NO
displace  15   0.0000    0.0000    0.0000  NO
displace  16   0.0000    0.0000    0.0000  NO
displace  17   0.0000    0.0000    0.0000  NO
displace  18   0.0000    0.0000    0.0000  NO
displace  19   0.0000    0.0000    0.0000  NO
displace  20   0.0000    0.0000    0.0000  NO
displace  21   0.0000    0.0000    0.0000  NO
displace  22   0.0000    0.0000    0.0000  NO
displace  23  -0.0023    0.0000    0.0000  NO
displace  24  -0.0034    0.0000    0.0000  NO
displace  25  -0.0040    0.0000    0.0000  NO
b1      1   6.6540    0.0000    0.0000  NO
b1      2   0.1432    0.0000    0.0000  NO
b1      3   0.0891    0.0000    0.0000  NO
b1      4   0.0357    0.0000    0.0000  NO
b1      5   0.1929    0.0000    0.0000  NO
b1      6   0.3268    0.0000    0.0000  NO
b1      7   0.3816    0.0000    0.0000  NO
b2      1   6.6780    0.0000    0.0000  NO
b2      2   1.7187    0.0000    0.0000  NO
b2      3   0.9964    0.0000    0.0000  NO
b2      4   0.4728    0.0000    0.0000  NO
b2      5   2.6767    0.0000    0.0000  NO
b2      6   3.5555    0.0000    0.0000  NO
```

b2 7 4.1529 0.0000 0.0000 NO
occupancy 1 1.0000 0.0000 0.0000 NO
return return